

ABSTRACT

BOWMAN, MICHELLE KATHLEEN. Controlling Sub-Microdomain Structure in Microphase-Ordered Block Copolymers and Their Nanocomposites. (Under the direction of Richard J. Spontak.)

Block copolymers exhibit a wealth of morphologies that continue to find ubiquitous use in a diverse variety of mature and emergent (nano)technologies, such as photonic crystals, integrated circuits, pharmaceutical encapsulents, fuel cells and separation membranes. While numerous studies have explored the effects of molecular confinement on such copolymers, relatively few have examined the sub-microdomain structure that develops upon modification of copolymer molecular architecture or physical incorporation of nanoscale objects. This work will address two relevant topics in this vein: (i) bidisperse brushes formed by single block copolymer molecules and (ii) copolymer nanocomposites formed by addition of molecular or nanoscale additives. In the first case, an isomorphic series of asymmetric poly(styrene-*b*-isoprene-*b*-styrene) (S_1IS_2) triblock copolymers of systematically varied chain length has been synthesized from a parent SI diblock copolymer. Small-angle x-ray scattering, coupled with dynamic rheology and self-consistent field theory (SCFT), reveals that the progressively grown S_2 block initially resides in the I-rich matrix and effectively reduces the copolymer incompatibility until a critical length is reached. At this length, the S_2 block co-locates with the S_1 block so that the two blocks generate a bidisperse brush (insofar as the S_1 and S_2 lengths differ). This single-molecule analog to binary block copolymer blends affords unique opportunities for materials design at sub-microdomain length scales and provides insight into the transition from diblock to triblock copolymer (and thermoplastic elastomeric nature). In the second case, I explore the distribution of molecular and

nanoscale additives in microphase-ordered block copolymers and demonstrate via SCFT that an interfacial excess, which depends strongly on additive concentration, selectivity and relative size, develops. These predictions are in agreement with experimental findings. Moreover, using a poly(styrene-*b*-methyl methacrylate) (SM) diblock copolymer with an order-disorder transition temperature (T_{ODT}) of 186°C, we find that the addition of clustered and discrete nanoparticles of varying size and surface selectivity can cause T_{ODT} to generally decrease, but occasionally increase. Also experimenting with a poly(styrene-*b*-isoprene) (SI) diblock copolymer with an T_{ODT} of 116°C, we find that the addition of smaller nanoparticles at small volume fractions effect the T_{ODT} more profoundly. The latter unexpected results are likewise predicted by SCFT and provide a unique strategy by which to improve the nanostructure stability of block copolymers by physical means.

Controlling Sub-Microdomain Structure in Microphase-Ordered Block
Copolymers and Their Nanocomposites

by
Michelle Kathleen Bowman

A dissertation submitted by the Graduate Faculty
of North Carolina State University
in partial fulfillment of the
requirements of the Degree of
Doctor of Philosophy

Materials Science and Engineering

Raleigh, NC

2008

APPROVED BY:

Richard J. Spontak
Chair of Advisory Committee

Jan Genzer

Russell E. Gorga

Carl C. Koch

Tzy-Jiun Mark Luo

Steve D. Smith

DEDICATION

I dedicate my dissertation to my parents, Philip and Zoretta, my brother Michael, and my fiancé Osie L. Gaines III, for all of your love and support.

BIOGRAPHY

Michelle Kathleen Bowman was born in Royal Oak, Michigan on November 16, 1980. She is the beloved daughter of Philip and Zoretta Bowman, and has one brother, Michael. Always interested in math and science, she decided to pursue here B. S. degree in Chemical Engineering at Michigan State University. While at Michigan State, she worked several internships at 3M. Here is where she discovered her desire for doing research, and began to grow a true appreciation for materials development. After earning her undergraduate degree in 2003, she relocated to North Carolina to embark on her dream of earning her Ph.D. Michelle decided at that point to move in a new direction with her studies. She enrolled in the college as a Materials Science and Engineering major, and built an entirely new knowledge base from her previous studies. In graduate school, Michelle began to explore how far she could crawl down “the rabbit hole.” She learned about polymer materials, developing research techniques, and moved entirely out of her comfort zone to understand novel technologies in a wide range of areas. She worked under the direction of Professor Richard J. Spontak, while exploring her exciting new world of polymers.

ACKNOWLEDGEMENTS

I would like to take this opportunity to acknowledge many groups and individuals that have been instrumental in my development to become a Ph.D.

I would like to thank my advisor Professor Richard Spontak for his direction, support, and insight, while pursuing my degree. His enthusiasm has been contagious and his wealth of knowledge has been invaluable, as I journeyed here at NC State. I am thankful for all the opportunities he initiated such as presenting at conferences, international travel, international and domestic research collaboration, internships, national laboratory exposure, and journal publishing. I would also like to thank Jon Samseth and SINTEF for providing funding for my research, and for my exposure to Norway. I am also grateful for the GEM and NOBBChE fellowships in providing funding during my graduate career.

I would like to thank Dr. Saad Khan, Dr. Russell Gorga, Steve Smith, Mark Hamersky, Kim Rasmussen, Russell Thompson, Michael Bockstaller, Jack Douglas, Alamgir Karim, Ronald Jones, Justin Smith, Dr. Christine Grant, Dr. Jane Griffith, Dr. Jan Genzer, Dr. Carl Koch, Dr. Mark Luo, and Dr. Joe Tracy for providing equipment, materials, resources, valuable conversations, collaborations, and for serving on my thesis committee. Each professor played a major role in the development of my research, and I am very grateful for their help. I would also like to thank the members of the polymer morphology group for being such wonderful and supportive team members.

Finally, I am grateful for my family and friends for their love, support, prayers, and belief in me. I am especially thankful for my mom and Dad, for being the incredible parents that they are. Also, thank both Michael and Osie for being such a loving support.

TABLE OF CONTENTS

LIST OF TABLES.....	ix
LIST OF FIGURES.....	x
CHAPTER 1 THE PHASE BEHAVIOR OF INORGANIC NANOPARTICLES IN MULTI-COMPONENT POLYMER SYSTEMS.....	
	1
Abstract.....	1
1.1 Introduction.....	3
1.2 Polymer Phase Behavior.....	6
1.3 Binary Blends.....	9
1.4 Multi-Component Blends.....	20
1.5 Structured Blends.....	33
1.6 Conclusions.....	46
1.7 References.....	48
1.8 List of Figure Captions.....	58
CHAPTER 2 MOLECULARLY ASYMMETRIC TRIBLOCK COPOLYMERS AS A SINGLE-MOLECULE ROUTE TO ORDERED BI-DISPERSE POLYMER BRUSHES.....	
	100
Abstract.....	100
2.1 Introduction.....	101
2.2 Experimental.....	103
2.3 Results and Discussion.....	104
2.4 Conclusions.....	109
2.5 Acknowledgements.....	110

2.6 References.....	111
2.7 List of Figure Captions.....	114
CHAPTER 3 SELECTIVITY- AND SIZE-INDUCED SEGREGATION OF MOLECULAR AND NANOSCALE SPECIES IM MICROPHASE-ORDERED TRIBLOCK COPOLYMERS.....	
	120
Abstract.....	120
3.1 Introduction.....	122
3.2 Methods.....	124
3.3 Results and Discussion.....	126
3.4 Conclusions.....	130
3.5 Acknowledgements.....	130
3.6 References.....	131
3.7 List of Figure Captions.....	136
CHAPTER 4 NANOPARTICLE-REGULATED PHASE BEHAVIOR OF ORDERD BLOCK COPOLYMERS	
	145
Abstract.....	145
4.1 Introduction.....	146
4.2 Experimental.....	148
4.3 Results and Discussion.....	149
4.4 Conclusions.....	154
4.5 Acknowledgements.....	154
4.6 References.....	156
4.7 List of Figure Captions	159

CHAPTER 5 COLLOIDAL NETWORK FORMATION IN NANOSTRUCTURED POLYMER MATRICES	165
Abstract.....	165
5.1 Introduction.....	166
5.2 Experimental.....	168
5.3 Results and Discussion.....	169
5.4 Conclusions.....	175
5.5 Acknowledgements.....	176
5.6 References.....	177
5.7 List of Figure Captions	180
CHAPTER 6 FRUSTERATING THE LAMELLAR ORDERING TRANSITION OF POLYSTYRENE- <i>BLOCK</i> -POLYISOPRENE WITH C ₆₀ BUCKEYBALLS.....	186
Abstract.....	186
6.1 Introduction.....	188
6.2 Experimental.....	192
<i>Materials</i>	192
<i>Sample Preparation</i>	192
<i>Sample Characterization</i>	193
6.3 Results.....	194
6.4 Discussion.....	200
6.5 Conclusions.....	206
6.6 Acknowledgements.....	207
6.7 References.....	208
6.8 List of Table Captions.....	215
6.9 List of Figure Captions.....	217

CHPATER 7 CONCLUSIONS AND FUTURE WORK.....	226
7.1 A ₁ BA ₂ Asymmetric Triblock Copolymers.....	226
7.2 Block Copolymer Molecular-Composites.....	228
7.3 Block Copolymer Nanocomposites.....	231
7.4 References.....	235
7.5 List of Figure Captions.....	236

LIST OF TABLES

Table 6.1.	Measured values of T_{ODT} from BCP2 materials modified with C_{60} nanoparticles according to dynamic shear rheology.....	216
------------	--	-----

LIST OF FIGURES

CHAPTER 1 THE PHASE BEHAVIOR OF INORGANIC NANOPARTICLES IN MULTI-COMPONENT POLYMER SYSTEMS

- Figure 1.1. SEM images showing fracture surfaces of PS/SiO₂ nanocomposites. a) 15 wt% untreated SiO₂/PS nanocomposite. Nanoparticles reside inside voids indicating dewetting of PS from SiO₂ surfaces. b) 2wt% SiO₂-g-PS/PS nanocomposite. In contrast to the untreated surface, the particle surface of the SiO₂-g-PS is well adhered to the PS. (Scale bar = 200 nm)..... 65
- Figure 1.2. TEM images of C₆₀ buckyballs in PMMA homopolymer self-assemble into large aggregates, small clusters, anisotropic shapes which also include vesicles..... 67
- Figure 1.3. TEM images of aluminum NP in PS, demonstrating the dispersion of non-adsorbing NP in a polymer matrix as NP concentration increases. a) 5 wt% aluminum NP loading shows uniform dispersion of the aggregates on a micron-scale. b) 5 wt% aluminum NP loading shows that the aluminum NP cluster in large aggregates under a higher resolution, and that they are not completely dispersed at the nanoscale. c) At 30 wt% NP loading, the aggregates are larger and we can see their morphology..... 68
- Figure 1.4. Gold NP in PEO self-assembly. a) TEM image of Au surface functionalized NP in PEO at 0.4wt% PEO (materials are dissolved in water). b) DSC traces of (a) pure PEO and (b) PEO containing functionalized Au NP..... 71
- Figure 1.5. ESEM images of self-assembled hydrogels stimulated by pH. Negatively charged microgel particles swell at high pH and shrink and low pH. When subjected to positively charged CdTe NP, they either self assemble into the core microgel particles (low pH) (a & b), or they phase separate from the swollen microgel particles (high pH) (c). This figure shows the two different morphologies observed, captured from ESEM (Scale bar = 5μm)..... 73
- Figure 1.6. SCFT calculations on polymer-NP suspensions. These figures show the specific heat requirement in order for the NP form a network. a) Compares particle-polymer size ratio with increasing NP concentration b) Displays the phase behavior of the nanocomposites over time..... 76

- Figure 1.7. Sequence of 100 μm x 100 μm height and phase angle AFM images show the surface roughness of PS/poly vinyl methyl ether (PVME) thin film blends containing different sizes of clay layered silicates. The PVME has been washed away with methanol and the PS domains remain in these images. a) At $d_{\text{NP}} = 30 \text{ nm}$, the spinodal domains appear pinned due to NP exfoliation in the blend. b) At $0.5 \mu\text{m} < d_{\text{NP}} < 1.0 \mu\text{m}$, a similar domain morphology appears as in part a, due to partial NP intercalation. c) When $d_{\text{NP}} = 5 \mu\text{m}$, there does not seem to be a change in the domain morphology compared to the neat PS/PVME blend..... 78
- Figure 1.8. TEM Images of PMMA/SAN blends, which show phase separation at 0 % NP loading (a-c) and 2 wt % silica NP (trimethyl silane functionalized) loading (d-f). (a-b) & (d-e) reflect the surface features. (c) & (f) show the interface morphology after removing PMMA. The hills in (a) & (d) measure $\sim 10 \text{ nm}$ high. The rings in (b) & (e) are artifacts resulting from abrupt changes in height. The hills form from capillary driven flow of PMMA during early stage. The hills have been measured to have a higher modulus than the surrounding phase, representative of NP partitioning. The inset is the fast-Fourier Transform (FFT) of the interface morphology. These images show that PMMA domains become smaller as a result of NP partitioning to the PMMA. The kinetics of the phase separation also show that the phase separation is slowed down by the presence of the NP, due to the localization of NP at the domain/matrix interface reducing the driving force for PMMA flow..... 81
- Figure 1.9. AFM images of PMMA/SAN blends with 5 wt % silica NP loading of 2 different surface functionalities – trimethyl silane & PMMA grafts (P2K). a) Larger PMMA phase domains of MEK nanocomposites. b) Smaller PMMA phase domains of P2K nanocomposites, domains are stabilized by the localization of NP at the domain/matrix interface. c) MEK nanocomposite after long annealing time shows domain rupturing. d) Shows that P2K nanocomposites remain phase separated and stable at long annealing times..... 82
- Figure 1.10. UCST behavior of epoxy/PS blend containing epoxy functionalized NP. This figure highlights the cloud point temperature as a function of epoxy composition. Each plot varies with increasing NP loading: a) $\phi_{\text{P}} = 0.01$, b) $\phi_{\text{P}} = 0.04$, c) $\phi_{\text{P}} = 0.1$, d) $\phi_{\text{P}} = 0.18$, e) $\phi_{\text{P}} = 0$. As NP loading increases the two-phase region decreases. NP loading does not appear to have any effect on the location of the spinodal..... 83
- Figure 1.11. Phase map showing the magnitude of the stable region as a function of composition of homopolymer A in an AB binary homopolymer blend with $\chi_{\text{AP}} > 0$ & $\chi_{\text{BP}} > 0$ NP. Blue, Red, and Green lines represent $\chi_{\text{AB}} = 0.01$,

0.0244, and 0.025, respectfully. These data provide evidence that increasing the segregation between A and B homopolymers drastically decreases the stability of the blend. ($\phi_{NP} = 0.18$)..... 84

Figure 1.12. CryoTEM imaging of the morphology of ternary blends of glycerol, amphiphilic block copolymer, and glycerol precursor-NP. (a) As the block copolymer concentration increases, the morphology of the particles changes from one large cubic particle with a disordered interior accompanied by vesicles to a mixture of vesicles, L_3 particles, and cubic particles with a disordered interior. At the highest concentration, there were only vesicles and L_3 particles. The diblock copolymer concentration influenced the size and number of cubic particles with a disordered interior. (b) Morphology of blends containing triblock copolymer with increasing lipid-mimetic anchors. At low hydrophobic asymmetry, foam-like partially fused unilamellar vesicle agglomerates are observed, with a disordered interior. As hydrophobicity increases, unilamellar vesicles and thread-like or band-like particles appear. The thread-like structures represent some sort of copolymer/GMO mixed micelles in an L_1 phase and the vesicles represent a dispersion of the lamellar phase in it. (Scale bar = 100 nm)..... 85

Figure 1.13. CDS model used to analyze the phase segregation in a homopolymer/block copolymer/NP blend of varying interaction strength. This figure shows how the interaction between the NP and one of the blocks in the copolymer affects the microphase separation which affects the macrophase separation of the blend. The NP are not pictured. The block copolymer is represented by the black and gray strips and the white region is the homopolymer. As NP-block copolymer interaction strength increases from a) 0.000001, b) 0.008, to c) 0.028, the block copolymer phase domains increase in long-range-order..... 87

Figure 1.14. a) Density profiles of colloidal-polymer blends show the phase transitions, with increasing concentration of colloidal particles. (a) disordered liquid, (b) sparse square, (c) hexagonal (or mixed square-hexagonal), (d) sparse square, (e) cylindrical structures in plane. b) The phase diagram of the colloidal-polymer blend as a function of polymer grafting density and colloidal concentration. S_2 : sparse square structure, M_2 : hexagonal structure, C_2 : cylindrical structure, S_3 : three-layer spherical structure, CS_3 : three-layer cylindrical-spherical mixed structure, C_3 : three-layer cylindrical structure. Arrow represents the direction taken to generate Fig 14a..... 88

Figure 1.15. An illustration of how careful specification of interaction behavior and temperature play a role in developing a well-positioned A-phase microdroplet

- between two asperities (two surfaces). Red represents A-phase and Dark Blue represents the B-phase. The NP are in white..... 90
- Figure 1.16. Neutron scattering samples of PEO-PPO-PEO triblock copolymer micelles and silica NP are shown. It has been demonstrated that adding more silica NP to the PEO-water matrix causes a polymer phase transition from face-centered-cubic (FCC) to body-centered-cubic (BCC). The triblock copolymer concentration in water is 30%..... 91
- Figure 1.17. Dependence of the order-disorder transition temperature (T_{ODT}) measured by isochronal dynamic rheology on nanoparticle concentration (ϕ_p) for clustered nanoparticles with -OH, -C8, and -MA surface functionalities..... 92
- Figure 1.18. Bi-functionalized NP (~ amphiphilic surfactants) induce a phase transition in polystyrene-*b*-poly-2-vinylpyridine (PS-*b*-P2VP) diblock copolymer from lamellar to the double gyroid (Ia3d space group) bicontinuous morphology. TEM images show PS-partially coated NP volume fractions (ϕ_p): (a) 0.04, (b) 0.07, (c) 0.09, and (d) 0.28. The scale bar is 100 nm. A well ordered lamellar nanostructure can be observed at 4 % loading, while a dramatic change in the morphology occurs at 9 % loading (bicontinuous)..... 93
- Figure 1.19. SST was used to investigate the importance of entropy and enthalpy on a diblock copolymer, containing A-selective bi-disperse NP. (a) 2D & 3D probability density profiles of symmetric diblock copolymer, displaying a cylindrical morphology due to the entropic effects of the small NP ($R_2 = 0.1R_0$). The large NP ($R_1 = 0.2R_0$) localize at the center of the A-microphase cylinders. (b) The free energy contribution of translational entropy (black), enthalpy (red), and steric interactions (blue). This shows that small particles have the potential for more steric interactions and translational entropy combats it by allowing them to spread to energetically unfavorable B. The inset demonstrates that the larger particles are located in a different microphase from most of the small particles, even though they have been tailored to have the same attractive interaction towards the A-block..... 94
- Figure 1.20. PS-coated Au NP in PS-*b*-P2VP asymmetric ($\phi_{ps} < 0.5$) diblock copolymer show hexagonal cylinder disordering as NP concentration increases, due to increased surface roughness between NP and PS interfaces. (a) TEM data at $\phi_p = 0.09$; $\phi_p = 0.27$. (b) Small Angle X-Ray Scattering (SAXS) data shows a disappearing of the hexagonally-closed-packed cylinder peak positions as NP concentration increases..... 96

Figure 1.21. SCFT/DFT calculations show how selective NP concentration and NP geometry can affect the ODT and the microphase stability of a diblock copolymer. (a) Critical value of the segregation factor (ODT) plotted as a function of reduced particle radius. ϕ is the volume fraction of NP. This plot shows how increasing NP concentration causes the ODT to decrease. (b) Critical value of the segregation factor (ODT) is plotted as a function of effective radius. As the aspect-ratio of the NP becomes large compared to the polymer brush length (NP surface area increases), the ODT increases. It shows that NP with a high aspect ratio exhibit the most change in the ODT and the microphase stability of the copolymer..... 98

CHAPTER 2 MOLECULARLY ASYMMETRIC TRIBLOCK COPOLYMERS AS A SINGLE-MOLECULE ROUTE TO ORDERED BI-DISPERSE POLYMER BRUSHES

Figure 2.1. SAXS patterns acquired at ambient temperature from the isomorphic A_1B diblock and molecularly asymmetric A_1BA_2 triblock copolymer series under investigation. The patterns have been shifted vertically to facilitate viewing, and the copolymers are identified by the listed value of M_{A_2} . The dashed line marks the principal peak position (q_m) of the parent A_1B copolymer..... 116

Figure 2.2. The microdomain period (D) of A_1BA_2 triblock copolymers measured by SAXS, normalized with respect to that of the parent A_1B copolymer and presented as a function of M_{A_2} . The solid line corresponds to SCFT predictions, and the dotted horizontal line denotes $D/D_0 = 1$. The dashed vertical line shows where the A_1BA_2 copolymer becomes molecularly symmetric ($M_{A_1} = M_{A_2}$). Schematic cross-sections of the A-rich cylinders (a-e) show the arrangement of the A_1 (blue), B (red) and A_2 (yellow) blocks, as well as B/ A_2 (orange) and A_1/A_2 (green) mixtures..... 117

Figure 2.3. Segmental density distributions generated by SCFT for six copolymers in the 9-46- A_2 series under investigation wherein M_{A_2} (in kDa) is systematically increased: (a) 0.0, (b) 2.0, (c) 3.4, (d) 6.5, (e) 8.2 and (f) 11.8. The A_1 , B and A_2 species are labeled in (a) and (b)..... 118

Figure 2.4. In (a), the A_2 core density evaluated from SCFT in the A_1 microdomain and B matrix (labeled) as a function of M_{A_2} . The dashed lines identify the condition of molecular symmetry ($M_{A_2} = M_{A_1}$), and the arrow shows where the core densities are equal. The inset displays the density field of the A_2 block in the copolymer with $M_{A_2} = 3.4$ kDa. High and low concentrations are denoted by red and dark blue, respectively. The elastic modulus (G') is presented as a function of M_{A_2} at 100°C in (b). The solid lines are guides for the eye. The

dotted line identifies the value of G' measured from the parent A_1B copolymer, and the dashed lines show where $M_{A2} = M_{A1}$ 119

CHAPTER 3 SELECTIVITY- AND SIZE-INDUCED SEGREGATION OF MOLECULAR AND NANOSCALE SPECIES IN MICROPHASE-ORDERED TRIBLOCK COPOLYMERS

Figure 3.1. In (a), solvent volume-fraction distributions generated by SCFT of a highly incompatible ($\alpha_{AB} = 100$), compositionally and molecularly symmetric ABA triblock copolymer containing three different concentrations of a moderately B-selective solvent ($\epsilon = 1.0$). Variation in the copolymer interfacial width, which broadens with increasing solvent concentration, is not depicted here for simplicity. Half of one $\Phi_S(x)$ distribution (SCFT calculations as circles and the nonlinear regression as the solid line), along with its individual contributions generated by Eqs. 1 (dashed line) and 2 (heavy solid line) in the text, is depicted in (b). The interfacial excess (ϕ^*) is labeled..... 138

Figure 3.2. Dependence of the interfacial excess (ϕ^*) on bulk solvent concentration (Φ_S) for systems differing in solvent selectivity (ϵ): (a) 0.5, nonselective; (b) 1.0, slightly B-selective; and (c) 1.5, strongly B-selective. Note the change in Φ_S range in (c). The inset in (c) with calculations for $\epsilon = 2.0$ has the same ϕ^* and Φ_S ranges as (c). The copolymer incompatibility (α_{AB}) values examined include 25 (solid line), 50 (dashed line), 75 (dotted line) and 100 (heavy solid line)..... 139

Figure 3.3. Interfacial excess (ϕ^*) as a function of solvent selectivity (ϵ) at $\Phi_S = 0.10$ for four copolymer incompatibility (α_{AB}) values (labeled). The solid lines are linear regressions to calculations at constant α_{AB} with three or more points..... 141

Figure 3.4. Solvent volume-fraction distributions generated by SCFT of a microphase-ordered ABA triblock copolymer ($\alpha_{AB} = 50$) swollen with 10 vol% of a nonselective solvent ($\epsilon = 0.5$) in (a) and a moderately B-selective solvent ($\epsilon = 1.0$) in (b). The relative solvent volume (v_r) is varied by two orders of magnitude — 0.001 (dotted line), 0.01 (dashed line), 0.05 (solid line) and 0.1 (heavy solid line) — to illustrate the effect of solvent size on solvent segregation..... 142

Figure 3.5. In (a), bright-field transmission electron microscopy (TEM) image of an unstained PS-PEP-PS/AuPS composite with ~ 2 vol% Au particles, which appear as dark dots within the PS domains. Shown in the inset is an

enlargement that illustrates the enrichment of small particles along the lamellar interfaces. Imaging has been performed on a JEOL 2000FX electron microscope operated at 200 kV. The spatial distribution of Au particles with $R_p < 3$ nm measured along the [001] direction is provided in (b) and reveals that the particles uniformly distribute within the PS lamellae, but preferentially locate along the PS/PEP interfaces. The analogous distribution of particles with $R_p > 5$ nm measured along the [001] direction is included in (c) and confirms that these particles tend to segregate along the center plane of the PS domains, as observed in (a)..... 143

CHAPTER 4 MICROPHASE SPERATION PAPER

- Figure 4.1. Segmental density profiles of the A block (solid line), B block (dotted line) and nanoparticle (p , bold solid line) as a function of distance (x) perpendicular to the lamellar microdomains in an ordered block copolymer and normalized with respect to the microdomain period (D). These results are generated by a hybrid SCF/DF theory for AB diblock copolymers ($\chi_{AB}N = 25$, $N_A = N_B$) modified with (a,b) small ($R/R_g = 0.05$) and (c,d) large ($R/R_g = 0.50$) nanoparticles varying in selectivity: (a,c) neutral ($\chi_{Ap}N = \chi_{Bp}N$) and (b,d) A-selective ($\chi_{Ap}N = 0$). The enlargements below (a) and (b) show the corresponding nanoparticle density profiles..... 161
- Figure 4.2. The order-disorder transition temperature (T_{ODT}) measured by isochronal dynamic rheology as a function of nanoparticle mass fraction (w_p) and block selectivity (i.e., nanoparticle surface chemistry, labeled) for clustered (FS) and discrete (CS) nanoparticles. The solid lines serve as guides for the eye, and the shaded region corresponds to the range over which T_{ODT} of the neat copolymer has been measured..... 162
- Figure 4.3. Predicted dependence of $(\chi_{AB}N)_{ODT}$ from SCF/DF analysis on the volume fraction of nanoparticles (ϕ_p), which vary in block selectivity (values of $\chi_{Ap}N$ are labeled) at $R/R_g = 0.40$. The dashed line identifies $(\chi_{AB}N)_{ODT}$ for the neat copolymer, and the arrowheads denote minima in the curves. The inset shows the explicit effect of nanoparticle selectivity on copolymer phase behavior at two different concentrations ($\phi_p = 0.05$ and 0.10)..... 163
- Figure 4.4. Predicted dependence of $(\chi_{AB}N)_{ODT}$ from SCF/DF analysis on ϕ_p for A-selective nanoparticles ($\chi_{Ap}N = 0$) varying in R/R_g . The inset shows the explicit effect of nanoparticle size on copolymer phase behavior at two different concentrations ($\phi_p = 0.05$ and 0.10), and the illustration depicts the observed¹⁶ localization of nanoparticles in the large R/R_g

limit..... 164

CHAPTER 5 COLLOIDAL NETWORK FORMATION IN NANOSTRUCTURED POLYMER MATRICES

- Figure 5.1 Temperature dependence of the dynamic shear moduli (G' , open; G'' , filled) for SM nanocomposites containing 20 wt% of three different nanoscale additives: hydroxyl-terminated colloidal silica (CS, circles), hydroxyl-terminated fumed silica (FS-OH, triangles) and octyl-terminated fumed silica (FS-C8, squares). The dotted vertical line identifies an abrupt change in G' that occurs in the case of the hydroxyl-terminated nanoparticles..... 182
- Figure 5.2 Dependence of G' (a,c) and $\tan\delta$ (b,d) on nanoparticle concentration for three nanoparticle species — CS (●), FS-OH (△), FS-C8 (□) and FS-MA (○) — at two temperatures (in °C): 160 (a,b) and 200 (c,d). The solid and dashed lines serve as guides for the eye for the FS-MA and CS data, respectively; whereas the shaded region shows the range in G' over which nanoparticle concentration generally has little effect on nanocomposite mechanical properties. The vertical dotted line identifies the concentration vicinity beyond which the nanocomposites behave solid-like, and the horizontal dotted line (c,d only) signifies where $\tan\delta = 1$ 183
- Figure 5.3 Isothermal frequency spectra acquired for G' (○) and G'' (●) at the following conditions: (a) 0.5 wt% FS-C8 at 140°C, (b) 10 wt% FS-C8 at 140°C and (c) 10 wt% FS-C8 at 200°C..... 184
- Figure 5.4 TEM images acquired at three different tilt angles (labeled) from SM/FS-MA nanocomposites containing 5 and 20 wt% FS-MA (top and bottom rows, respectively). In each case, the FS-MA nanoparticles appear as electron-opaque (dark) aggregate features, whereas the styrenic lamellae of the SM copolymer are likewise dark due to selective staining. The arrow shows the location of lamellae comprising the copolymer nanostructure, whereas the circled region highlights copolymer lamellae that appear distorted or partially discontinuous..... 185

CHAPTER 6 FRUSTERATING THE LAMELLAR ORDERING TRANSITION OF POLYSTYRENE-*BLOCK*-POLYISOPRENE WITH C₆₀ BUCKYBALLS

- Figure 6.1. Thermal treatment protocols adopted in the SAXS measurements for: (a) BCP1a (neat PS-*b*-PI); (b) BCP1b with 0.387 wt% C₆₀; (c) BCP1c with 1 wt% C₆₀. The arrows marked in *a* and *b* denote the corresponding values of T_{ODT} : 163-161°C and 149-146°C, respectively..... 218

Figure 6.2.	Temperature dependence of the SAXS profiles near the first-order peaks for BCP1a at various temperatures (a) and at $T > T_{ODT}$ (b).....	219
Figure 6.3.	Temperature dependence of the SAXS profiles near the first-order peaks for BCP1b at various temperatures (a) and at $T > T_{ODT}$ (b).....	220
Figure 6.4.	Temperature dependence of the SAXS profiles near the first order peaks for BCP1c at various temperatures.....	221
Figure 6.5.	I_m^{-1} and (b) σ_q^2 presented as functions of T^{-1} for BCP1a, BCP1b and BCP1c. (c) I_m^{-1} and (d) σ_q^2 plotted as functions of $T^{-1}-T_{ODT}^{-1}$ for BCP1a and BCP1b.....	222
Figure 6.6.	Isochronal temperature sweeps of the dynamic storage modulus (G') for the BCP2 series varying in C_{60} concentration from 0 to 0.5 wt% (see key).....	223
Figure 6.7.	Variation of D with T^{-1} for BCP1a, BCP1b and BCP1c.....	224
Figure 6.8.	Scattering profiles near the first-order peak for BCP1a, BCP1b and BCP1c evaluated at 180°C.....	225

CHAPTER 7 CONCLUSIONS AND FUTURE WORK

Figure 7.1.	Two-dimensional probability density profiles of selective solvent in an ABA triblock copolymer. The images show that with increasing Φ_S , phase transitions can be induced. a) $\Phi_S = 0.10$ – lamellae, b) $\Phi_S = 0.66$ – lamellae, c) $\Phi_S = 0.67$ – cylinders, d) $\Phi_S = 0.68$ – cylinders, e) $\Phi_S = 0.69$ – spheres, $\Phi_S = 0.70$ – disorders. ($\chi_{AB}N = 50$; $\varepsilon = 1.0$).....	238
Figure 7.2.	Two-dimensional probability density profiles of nonselective solvent in an ABA triblock copolymer. The images show that with increasing Φ_S and less solvent–B-block interaction, fewer phase transitions can be induced. a) $\Phi_S = 0.10$ – lamellae, b) $\Phi_S = 0.62$ – lamellae, c) $\Phi_S = 0.63$ – cylinders, d) $\Phi_S = 0.68$ – swollen lamellae, e) $\Phi_S = 0.69$ – disorders. ($\chi_{AB}N = 50$; $\varepsilon = 0.5$).....	239
Figure 7.3.	Dynamic temperature sweeps of PS- <i>b</i> -PI diblock copolymer (sample II) nanocomposites, with increasing C_{60} concentration. These show evidence of first order ODT disappearance at high C_{60} concentrations, and cross-linking behavior at temperatures past 110°C.....	240

- Figure 7.4. FTIR data of Neat, 0.02wt%, 1 wt%, & 4 wt% nanocomposites before thermal treatment, to investigate the source of cross-linking behavior. The 1wt% and 4 wt% samples show evidence of –OH groups ($\sim 3440\text{ cm}^{-1}$), the emergence of C–O bond (1068 cm^{-1}), and presence of a CH=CH-R bond ($\sim 904\text{ cm}^{-1}$). These peaks describe the nanocomposite’s interaction with water, causing alcohols to form and bonding to occur between either the PI double bond and/or the PS benzene ring..... 241
- Figure 7.5. FTIR data of Neat, 0.02 wt%, 1 wt%, & 4 wt% nanocomposites after thermal treatment, to continue investigating the source of cross-linking behavior. 1 wt% and 4 wt% samples show a reduction in the $[2990\text{-}2850]\text{ cm}^{-1}$ triplet, indicating a reduced signal for the aliphatic groups in PI. The –OH peak and the C–O peaks reduced and the CH=CH peak ($\sim 680\text{ cm}^{-1}$) remained strongest peak. Heating the nanocomposites may have reduced the number of cross-links formed between the C_{60} NP and the PI and PS double bonds..... 242
- Figure 7.6. DSC traces of Neat, 0.02 wt%, 1 wt%, & 4 wt% nanocomposites before thermal treatment. These data show the nanoparticles’ affect on the glass-transition temperature, T_g . The fullerenes show no influence on PS, but cause PI’s T_g to increase with C_{60} concentration. The fullerenes act like an anti-plasticizer, reducing in mobility of the PI blocks..... 243
- Figure 7.7. DSC traces of Neat, 0.02 wt%, 1 wt%, & 4 wt% nanocomposites after thermal treatment. These data so no evidence of change from the non-thermally treated samples..... 244

CHAPTER 1

THE PHASE BEHAVIOR OF INORGANIC NANOPARTICLES ON MULTI-COMPONENT POLYMER SYSTEMS

Abstract

Polymer composites have risen to the forefront as preferred materials for a variety of consumer and industrial products because they are flexible, easily fabricated, and cost-effective materials. Reducing the size of additives to the *nanoscale* has shown a profound effect on the material properties, projecting polymer nanocomposites to be the bridge towards expanding the scope of product development beyond technologies that have already been conceived. Although many have successfully added nanoinclusions to polymer matrixes and created new materials, one must stop to consider the supramolecular interactions occurring at the surface of the nanoparticle and the polymer chains and how they impact the structure and the material properties of the nanocomposite. Nanocomposites are primarily developed from a bottom-up approach, which rely on spontaneous interactions between the components to form the equilibrium microstructure of the material. In order to optimize development and to be able to control

the phase behavior in nanocomposites, it is necessary to fully understand and be able to tune these thermodynamic supramolecular functions at the nanoscale. Therefore, it is necessary to gain a full understanding of the phase behavior of nanoinclusions in polymers. The following is a review on the phase behavior of nanoinorganic materials in polymer systems.

1.1 Introduction

Polymers have emerged as attractive alternatives to metal and ceramic materials, and have also pioneered in several industries. Some examples include rubber tires, adhesives, coatings, and packaging materials. With the inclusion of additives, polymers have become the forerunner of the materials industry as soft, flexible resources, perfect for housing reinforcements. They are ideal matrix materials because they can be easily processed, fabricated, and are economically feasible, while reinforcements and additives enhance the material properties and create multi-functional composites. Many industries have been instrumental in developing polymer composite technology such as: personal care products, paints & coatings, disposable consumer products, food storage & enrichment, fiber optics, computer chips, military devices, automobiles & transportation, and athletic equipment.

Over the last ten to twenty years, polymer technology has taken a new spin – the inclusion of nano-sized fillers. In a review done by Bockstaller and coworkers on block copolymer nanotechnology, they explain that reducing the size of the additives among polymer molecules further influences the material properties of the matrix for several important reasons: a) particle-particle correlation increases, b) ultra-low percolation thresholds ($< \sim 1$ vol.), c) large particle number densities up to $\sim 10^{20} \text{ cm}^{-3}$, d) extensive interfacial area per volume of particles ($\sim 10^7 \text{ cm}^2 \text{ cm}^{-3}$), e) short particle-particle distances, and g) comparable length scales between particle size, distances between particles, and the typical relaxation volume of a polymer chain ($\sim R_g^3$, $R_g = \sim 10 \text{ nm}$ for typical molecular weights) ¹. Some of the major advantages of including nanoparticles

(NP) are the monumental enhancement of properties, optical transparency, and less material requirement to create the desired effect. General Motors has already introduced nanotechnology to their 2002 GMC Safari and Chevrolet Astro vans by adding exfoliated clay reinforcements to enhance the toughness of polyolefin resins ². Multi-component nanocomposite polymer blends are incorporated as photovoltaic junctions for semiconductors, light-emitting displays, integrated circuits, and storage devices, and as heterogeneous electrolytes for ideal Lewis acid-base surface chemistry to take place in solid-state lithium batteries ³⁻⁴. Block copolymers have been identified as ideal materials for templating nanoadditives. Some technologies being developed require hybrid materials, such as a block copolymer containing polymer segments that are chemically distinct, and NP provide further versatility of material functions. Block copolymers provide the double benefit of monitoring NP spatial separation and fulfilling more functionality with its chemical distinctness. Examples of these emergent technologies include lithography ⁵, membrane technology ⁶⁻⁷, solid state Li batteries ⁸, drug encapsulation ⁹⁻¹⁰, catalysis ¹¹, and optoelectronics ¹². In nature, the microstructure of biomacromolecules such as proteins and lipids exist naturally as nano-architectures that ultimately make up soft and hard tissues in living organisms ¹³. Genetic engineers have seen these natural materials as excellent avenues for mimicking nano-structured materials, while investigating methods for synthetically modifying their structures for applications in nano- and biotechnology ¹³.

Now that the size-scale of the additives has been reduced, intimate contact between the polymer molecules and the fillers cause surface interactions to become very

important. As discussed previously, it has been determined that these new materials can be fabricated for the various desired products. A lot of work has been done to understand how the NP behave in the polymer as these nanocomposites are generated, with improved mechanical properties, emergent electronic properties of low-dimensional semiconductors, developed magnetic properties of single-domain particles, and predictable solution properties of colloidal suspensions. However, the common denominator for all these material property areas is phase behavior & microstructure formation¹³. Nanomaterial synthesis has followed two main directions – top-down, and bottom-up. Top-down requires transposing conventionally sized materials to micro-scale dimensions. The bottom-up approach relies on molecular interactions at the surface of nano-scale materials to drive self-assembly, forming structures on a molecular level. It is the most attractive approach towards developing nanomaterials because it is not limited by resolution, the as the top-down approach is, and occurs spontaneously. Although much progress has been made in developing nanotechnology, the realization of the full potential of nanotechnological systems has so far been limited due to the difficulties in their synthesis and subsequent assembly into useful functional structures and devices¹³. In particular, we still need to determine how the existing nanoadditives affect the molecular behavior and interactions between themselves and the polymer molecules, occurring at the surface. The best way to look at these aspects is to identify the phase behavior of these nanomaterials. Nanoresearch has been caught up, to a large extent on understanding the supramolecular behaviors and nanostructured ordering of the nanoparticulates in the polymer matrix. There has been little focus on the flip-side of the

argument, which understands how nano-restructuring occurs with the polymer molecules in the nanocomposite matrix. Understanding the phase diagram of the polymer matrix is important in understanding the full picture on how to improve the macroscopic properties of the polymer matrix for manufacturing ideal, functional nanocomposites¹⁴. In particular, it is important to understand how environmental aspects affect a polymer matrix (i.e. pH, temperature, mechanical mixing, solution-dissolution, and surface confinement) as well as how the presence NP influence the microstructural ordering of the polymer chains, so these scenarios can help predict and control the phase behavior of the nanocomposites as they are being developed for desired applications. This review will highlight how inorganics affect the equilibrium phase behavior of polymer systems, and how they correlate with other materials that have already been studied. The format of this review will follow II) Phase behavior of polymer systems, III) Phase behavior of binary blends (NP in unstructured polymers and copolymers), IV) Multi-component polymer blends (NP in multi-component polymer blends), V) Structured copolymer blends (NP in block, graft, crystalizable, and hybrid copolymers), VI) Conclusions. As we identify the trends in the thermodynamics and phase behavior of these materials, more industries will be able to benefit from being able to control the molecular interactions and formation of structures at the nano-scale.

1.2 Polymer Phase Behavior

There has been a lot of work done towards understanding the phase behavior of polymers in general. It is well understood how homopolymers & unstructured

copolymers¹⁵⁻¹⁷, polymer blends^{17-19,21}, and block copolymers behave thermodynamically^{17,20-25}. There are four main aspects that contribute to the enthalpy and entropy which govern equilibrium phase behavior: a) size – degree of polymerization (N) b) choice of monomers – segment-segment interaction, c) molecular architecture, and d) composition^{17,20,24}. In a very simple sense, unstructured polymers (homopolymers, random, and alternating copolymers) typically have one phase (neglecting crystallization). Polymer blends of two or more homopolymers typically undergo endothermic mixing and desire to macrophase separate into two or more separate phases within the mixture. Depending the condition of the blend, the phase separation is either metastable (governed by nucleation of small droplets of the minority phase and growth once the concentration of the supernatant has reached equilibrium) or unstable (governed by spinodal decomposition, where there is no free energy barrier to nucleate to a new phase)¹⁷⁻¹⁹. The sizes of the phase-domains, in the blend, are dictated by their desire to reduce their surface area to reduce interfacial tension, Ostwald ripening. For thin films of a polymer blend, the phase separation leads to nanostructuring of the film surface⁹. Block copolymers behave differently from random and alternating copolymers. Since they are composed to large sequences of chemically similar repeat units, they have the ability to pack like-chains with like-chains in an effort to reduce their surface area to reduce interfacial tension (~ to polymer blends). However, they are in a sense, two or more chemically distinct homopolymers covalently bonded to one another. Therefore, the most phase separation they can undergo is microphase separation, where the phase domains are governed by the size of the individual polymer chains.

As we consider changes to the environment, the phase behavior of the polymers change as a result of solvent addition^{17,26-29}, homopolymers^{18,30-34} (in block copolymers), changes in pH³⁵⁻³⁷, and surface confinement^{38,39}. These aspects change the enthalpic and entropic contributions of the system and affect how the polymer will behave thermodynamically and what its resulting phase behavior will be. Depending on the interaction (Flory-Huggins Interaction Parameter, χ) between the solvent molecules and the polymer chains, the polymer chain will either swell, pack tightly within itself, or show no impact at all¹⁵. Lodge and coworkers is one of many groups who have done extensive work on predicting the phase behavior of solvents in block copolymers. They found that they were able to shift the phase diagram and expand the range for several of the classical equilibrium morphologies for diblock copolymer systems, micelles, cylinders, and alternating lamellae, based on the type of solvent incorporated^{26,27}. Homopolymers have a similar behavior, although because they are much larger than solvent molecules, they can either behave as diluent wet-brushes, interpenetrating the brushes as polymer nanoinclusions, or as dry-brush polymer nanoparticles, only interacting with the surface of the polymer brushes³⁰⁻³⁴. Poly electrolyte *N*-isopropylacrylamide is known to swell and shrink as the pH of its solution changes from acidic to basic, and these behaviors result in a change in the polymer's film properties³⁵⁻³⁷. Neutral surface-confinement impact block copolymer microstructure in two ways: structure effect (interaction between the surfaces and the polymers) and structure frustration (commensurability between the size of confinement and the structure period)³⁸. Han and coworkers were able to determine that the spinodal point of the disordered

homogeneous phase shifted for a diblock copolymer confined to a spherical nanopore. It has been determined by Mayes, Russell, and others that the spinodal point for block copolymer thin films (polymer confined between air and silicon substrate) is strongly dependent on film thickness^{10,39}. Polymeric materials that are sandwiched between an air/water interface exhibit changing their microstructural ordering to accommodate the most relaxed orientation possible⁴⁰.

1.3 Binary Blends

Binary blends are specified as polymer nanocomposites that include inorganic NP in an unstructured polymer matrix. Examples of unstructured copolymers (neglecting crystallinity) include homopolymers, random copolymers, and alternating copolymers. The microstructure and the ordering behavior of these nanocomposites are still governed by the factors mentioned above: size ratio, particle-polymer interaction, molecular architecture, and composition, as changes to the environment are also considered. One of the most important of these variables in controlling the phase behavior of a system is particle-polymer interaction by tuning the interfacial interactions between the NP and the polymer chains. The polymer molecules desire to interact with one another at a particular energy of mixing ϵ_{MM} , the NP are interacting with one another at particular energy of mixing ϵ_{PP} , and the NP are also interacting with the polymer chains at a particular energy of mixing ϵ_{MP} . These values are used to develop the Flory-Huggins polymer segment-NP interaction parameter χ_{MP} according to equation 1.

$$\chi_{MP} = \frac{1}{k_B T} \left(\varepsilon_{MP} - \frac{1}{2} (\varepsilon_{MM} + \varepsilon_{PP}) \right) \quad (1)$$

χ makes up a large portion of the enthalpic contribution to the equilibrium phase behavior. If $\chi_{MP} \approx 0$, the nanoparticles are strongly attracted to the polymer molecules and will adsorb well within the polymer matrix. However, this scenario is not typical. Most of the time, the nanoparticles are more attracted to themselves than they are the polymer molecules, and they tend to aggregate. Most polymers are hydrophobic and their intramolecular forces are typically weak van der Waals forces (except polyelectrolytes which are governed by ionic bonding and polymers containing oxygen as an end-group [ethylene oxide] which are governed by strong hydrogen bonding). Their weak intramolecular forces are not strong enough to penetrate the stronger hydrophilic²⁵, dipole-dipole⁴¹, electrostatic^{42,43}, or affinitive intramolecular mechanisms which are more interactive than the interactions from the surrounding matrix material (also dependent on temperature and pH)⁴⁴. These strong intramolecular forces cause NP aggregation, causing poor dispersion in the polymer matrix⁴⁵. However, based on χ , the surrounding polymer chains can adsorb to some level to the nanoparticle aggregates, causing some level of dispersion.

There are ways of modifying the interaction parameter so that the nanoparticles are more likely to interact with the polymer matrix. The most popular way is to functionalize the outside of the nanofiller, causing the interaction between the nanoparticle and the polymer molecules to be governed by the ligands or polymer chains, grafted on the outside of the nanofiller^{1,6,7,102-106}, also causing a reduction in χ and an

increase in phase-mixing. Bansel and coworkers have looked at wettability, which illustrates the interaction between un-functionalized and polystyrene-coated SiO₂ nanoparticles in polystyrene ⁴⁶. They found that the un-functionalized SiO₂ dewetted from the polystyrene (PS) and inhabited the voids between the polymer aggregates, and that the SiO₂ nanoparticles with PS chains grafts mixed well within the PS matrix, and adhered to the polystyrene molecules (illustrated in Figure 1). They showed that dispersion and interaction between NP and polymer molecules not only influenced the dispersion of the NP in the polymer matrix, but that the polymer molecules' equilibrium structure was also affected by the presence of the nanoparticles.

In particular, Bansel and coworkers also discussed how the glass transition temperature (T_g) shifted according to NP interaction. For un-functionalized SiO₂, the T_g decreased with increasing NP loading. Therefore, the NP were increasing the mobility of the polymer chains and also causing polymer packing density to increase. These changes in the T_g affect how the polymer molecules order within the nanocomposite. Basel *et. al.* also determined that as the unmodified SiO₂ nanocomposites were solvent cast, the type of solvent used changed the size of the SiO₂ aggregates in the polymer matrix and also affected the PS's glass transition temperature. They discovered that unmodified SiO₂ nanocomposites cast in methylethylketone (MEK) formed smaller aggregates than the composites cast in tetrahydrofuran (THF). The polymer matrix also exhibited a larger drop in T_g when cast in MEK as SiO₂ content increased than the PS nanocomposites cast in THF. These differences result from the fact that SiO₂ is more interacted to MEK molecules than THF. Although the solvent molecules were eventually dissolved away

from the films, they still played a role in the film morphology as the nanocomposites were being fabricated in solution. These differences are important to note for material development.

Depending on the specific applications desired, un-modified nanoparticles can be satisfactorily incorporated in a polymer matrix for a single component blends. One example is fullerenes (buckyballs, C_{60}), which are capable of cross-linking to polymer chains via donor-acceptor interactions. These radical seeking inorganics can interact and cross-link with polymers that contain a double bond. When in contact with PS, an increase in packing density⁴⁷ and polymer chain mobility⁴⁸ has been observed. The C_{60} interacted with the PS and acted like a plasticizer, reducing the T_g of the materials, but also formed aggregates in the PS which caused the homopolymer chains to become more compact within the matrix. On the other hand, C_{60} in polymethyl methacrylate (PMMA) homopolymer behaved differently⁴⁹, where there was less opportunity for particle-polymer interaction. These materials showed a decrease in molecular chain packing, mobility, and an increase in T_g from the coexistence of both nanoscopic and micron-sized agglomerates. The buckyballs are interacting less with the homopolymer and more with themselves, resulting in agglomeration of the C_{60} . As the buckyball concentration continues to increase, the aggregates grow and take on a new phase behavior within the PMMA matrix. They begin to form micron-sized agglomerates, which were anisotropic and contain nanoscopic voids (Figure 2). Although un-modified C_{60} in PS and PMMA show two different trends in phase behavior resulting in two different trends in nanocomposite microstructure, both materials can be used for specific desired

applications such as improved or reduced permeability of gas molecules for gas separation.

There has been much work done to gain uniform displacement in a nanoparticle/polymer nanocomposite. We must remember that simultaneous control over nanoparticle size distribution and dispersion uniformity is difficult to achieve because agglomeration occurs during composite fabrication. Therefore, in order to get particles to become uniformly distributed in to a polymer matrix, more than just the particle-polymer interactions, χ , are considered. Biswas and coworkers have shown that in order to gain full uniform displacement of nanoparticles, the size of the nanoparticles must be restricted to a small size regime along with a narrow size distribution. They used individually assembled Ag nanocrystals held together within a Teflon matrix to create uniform nanocomposites via e-beam deposition. Composites with well dispersed Ag nanocrystals showed a most favorable increase in elastic properties⁵⁰. Mackey and coworkers have demonstrated that the thermodynamic stability of nanoparticles in a polymer liquid increases when the polymer radius of gyration, R_g , becomes much larger than the radius of the NP, R_{NP} ⁵¹. We have now introduced how the *size* and *concentration* influence the dispersion of a single-component polymer-adsorbing system, which changes the entropy of the system. It has been observed that nanoparticles with a particle-radius that is comparable to a polymer molecules' R_g tend to remain less disperse in the nanocomposite⁵⁰⁻⁵². Coupled with the nanoparticles' inherent desire to mix with themselves, the presence of "large" nanoparticles often also cause aggregation and macrophase separation. A similar trend has been observed in polymer blends and solutions. Large

homopolymer molecules tend to coil within themselves and interact less with polymer matrix (dry brush) or solvent molecules when mixed in a poor solvent, than smaller homopolymer molecules that tend to adsorb to the polymer matrix (wet brush) or swell in the presence of a good solvent. The size of NP can be considered from two different standpoints: by tailoring the diameter of the inorganic nanoparticles, or by controlling the length of the surface functional groups (ligand, self-assembled monolayer (SAM), or polymer graft). The microstructural dependence on varying the diameter of the inorganic core results in different behaviors than varying the length of the surface modification. One example was illustrated nicely by Mackey *et. al.* where three different size ratios (R_{NP}/R_g) were observed⁵¹. The smallest NP ($R_{NP}/R_g = 0.077, 0.10, 0.077$) were C_{60} in PS and were experimentally found to disperse well within the homopolymer. The largest NP ($R_{NP}/R_g = 1.15, 1.5, 2.14$) were polyethylene (PE) dendrites in PS, and were experimentally found to agglomerate in the PS matrix as a result of an increase in cohesive energy to the system. Intermediate sized NP were observed in a homopolymer melt, and their dispersion behavior was observed theoretically using polymer reference interaction site model (PRISM) calculations. They found a general crossover point where the particle size transcended from miscible to clustering was $R_{NP}/R_g \approx 1$. These observations align very well with what others have reported^{44, 52}. The effect of the different sized NP on the microstructural ordering behavior of the PS matrix was not reported by Mackey and coworkers, but based on the examples that have been previously discussed, it is expected that the glass-transition behavior would also vary with size. We can predict that the small, well dispersed fullerene NP might lower the T_g (as the NP also

interact with the PS), and that larger NP would continue to lower the T_g by aggregating and forcing the polymer chains to mix more with themselves. Had the case with the small C_{60} NP been dispersed in a non-adsorbing polymer such as PMMA, the T_g would have more than likely increased and disrupted the mobility of the surrounding polymer chains⁴⁸. An example where the length of the surface functionality resulted in different phase behaviors was illustrated by Lan *et. al.*, where silica NP were introduced to non-adsorbing polystyrene. They were surface-functionalized with PS polymer brushes of varying molecular weight ($0 \leq M_n \leq 48,000$)⁵⁴. We must also recognize that as the size of the NP is increasing with increasing M_n of PS grafts, the interaction is also increasing between the NP as the surrounding PS chains. Ultimately what was discovered was that particle clustering decreased with increasing PS graft M_n , which resulted in increasing NP dispersion. Based on the above discussion, it would be difficult to predict how the microstructural ordering behavior might behave. The larger silica NP have longer PS grafts and will interact more with the surrounding polymer chains. This could cause an increase in mobility (increase in molecular packing density and decrease in T_g) because of better dispersion or it could cause a decrease in mobility (decreasing in molecular packing density and increase in T_g) because the interactions between the PS matrix chains and the NP are so strong that they behave like cross-linked molecules.

Now considering the size of NP aggregates, the work done by Bansal and coworkers reminds us that the ordering behavior in the polymer matrix is affected. They showed that larger aggregates created in THF had less affect on the T_g of PS than the smaller aggregates created in MEK. With less change in the T_g , there was less

interference in the diffusion of the polymer chains around the aggregates, and less of an entropic penalty. The smaller aggregates remained dispersed and had more of an affect on the ordering behavior of the PS matrix. Figure 3 displays a second example on how NP aggregate size affects the distribution in a polymer matrix. As the concentration of aluminum NP increases from 5 wt % to 30 wt %, we see that the agglomerates remain dispersed in the PS matrix and as NP concentration increases, the size of the NP aggregates also increases⁵². Based on the previous discussion, one would expect there to be less influence on the glass-transition phase behavior of the copolymer as the agglomerate size increases. However, now we are also considering *concentration* and as the number of NP increases, the packing density increases, causing more molecular confinement of the polymer molecules. Therefore, there should be an exponential increase in the glass-transition phase behavior of the PS until the agglomerates become so large that they inhibit mobility of the polymer chains and create a colloidal network.

Uniform distribution, stabilized by the enthalpic interactions and the small size of the nanoparticles relative to the polymer molecules gives rise to a whole host of new properties possible in the nanocomposite. Depending on the chemistry of the nanoparticles, some of these include optical clarity, chemical resistance, wear resistance (scratch resistance), flame retardance, thermal conductivity, dewetting, and reflectivity. As the interactions between the particles and the polymers change and self-assembly of the particles occur (arrays and channels of NP forming in the polymer matrix) other material properties, such as mechanical toughness, electric conductivity, and magnetic ability, become possible or more enhanced depending on the chemistry of the particle.

Sometimes the interplay between the polymer chains and the nanoparticles can allow the polymer chains to stabilize the nanoparticles, allowing them to assemble into connecting arrays and flocculate throughout the matrix. These colloidal systems and even gels in some cases cause the mechanical properties to improve drastically and the viscosity to increase. Typically in these systems, the composition of the particle is high in the polymer matrix. Flocculation was already described earlier with the buckyballs in PMMA, where the self-assembly of aggregates increased with C₆₀ concentration. The geometry of the NP can play a role here, where anisotropic NP or aggregate structures can reduce the percolation threshold, allowing photonic⁵⁵, electronic⁵⁶, or magnetic³⁵ conductivity to flourish. However, how does the presence of these nanostructures affect the phase properties of the polymer matrix? Figure 4 shows gold NP, with hydrophilic molecules grafted to the outside, selective to the hydrophilic ethylene-oxide bonds in a polyethylene oxide (PEO) matrix⁵⁷. The NP self-assembled in the PEO causing the polymer's crystallization temperature (T_c) and T_g to shift. The T_c increased by ~ 5°C upon adding nanofiller, showing that the PEO crystallites must have interacted with the NP. They must have mostly formed around the NP, using them as nucleation sites for crystallization. The NP also caused PEO's heat of formation (ΔH_f) to increase, meaning that more heat was required to melt the PEO crystallites. The NP were interfering with PEO crystallinity and probably increasing the percentage of crystallization. As the concentration of NP increased, the T_c and ΔH_f would continue to increase until the concentration of NP became so high that PEO crystallites were inhibited in forming. Figure 5 displays how pH affects the morphology and phase behavior of a polymer

nanocomposite hydrogel (*N*-isopropylacrylamide) containing electrostatic inorganic CeTe nanocrystals⁴². Li and coworkers developed a nanocomposite hydrogel that responded to changes in pH. At low pH (Fig. 5a & b), the *N*-isopropylacrylamide polyelectrolyte matrix shrank and the attractive forces between the inorganic NP cores drove the assembly of branched, flocculating dendritic nanostructures. At high pH (Fig. 5c), the *N*-isopropylacrylamide swelled and the attractive forces between the polyelectrolyte molecules dominated. The nanocomposite structure resulted in a porous film with CeTe nanocrystals dispersed in it.

There has been much discussion on how the phase behavior of an unstructured polymer behaves in the presence of inorganic NP, but how do these observations compare with theory? Striolo used Monte Carlo simulations to explore the self-assembly of spherical NP in a non-adsorbing polymer matrix, induced by interactions which become anisotropic due to entropic effects. The spherical NP were attracted to each other by varying their square-well potential, which mimicked dispersive interactions. The anisotropic effects are induced by adding short polymer brushes to the NP, which are treated as tangent-hard-sphere chains. Monte Carlo calculations were conducted to examine the properties as a function of polymer brush length (entropy/geometry) and square-well potential depth (enthalpy/interactions). When the particle-particle interactions were very strong (NP were surface functionalized with long polymer brushes), the NP formed spherulites which stabilized at uniform dispersion. This phase behavior of NP aggregates forming uniformly dispersed agglomerates is similar to what was observed experimentally by Kausch and coworkers, when aluminum NP

agglomerates dispersed uniformly in a PS matrix⁵³. At intermediate lengths of polymer brushes, long one-dimensional anisotropic wires formed. These observations are consistent with experimental observations in Figures 2 & 4. Striolo showed that hard sphere colloids dissolved in non-adsorbing polymer experienced a depletion attraction, which may be coupled to a weak, mid-range repulsion when the polymer chains are short. If the R_g of the polymer is longer than the R_g of the short chains, they may become attractive at intermediate distances. When the side chains are short, they are only repulsive. These results are useful in creating reversible nanostructures yielding a variety of behaviors (uniformly dispersed spherulites or anisotropic wires).

In an adsorbing polymer matrix, Hooper and Schweiser used PRIM to examine the behavior of hard spheres, varying in size from monomeric to macroscopic⁵⁸. They also predicted, by changing the interaction between the NP and the surrounding polymer chains, three regimes of phase behavior the NP are I) small, non-interacting aggregates, II) miscible within the polymer matrix, or III) network forming. Hooper and Schweiser also found that increasing the NP concentration had a large affect on positioning of the surrounding the polymer matrix, causing it to reorganize on a length scale similar to the NP diameter. The response at the interface was having the contact layer of the polymer suppressed from the increased volume fraction of particles, which caused a build up of monomer near the particle surface. As the particle-polymer interaction decreased, more chain mobility was observed because there was less adhesion between the particles and the polymer. More NP also induced a phase transition from regime II (stable uniformly dispersed particles) to regime I (aggregates). These results are similar to the phase

behavior observed with hard spheres in a matrix of star polymer⁵⁹. What about gelation? Zhao and coworkers noted that at high particle-polymer adhesion, a network began to form between the star polymers and the NP, and the miscibility between the two was enhanced as the arm number increased and became longer. Figure 6 demonstrates, using Self Consistent Field Theory (SCFT), NP in a polymer matrix form a colloidal network⁶⁰. Figure 6 also shows the specific heat requirement necessary for the nanocomposite to form a gel. As NP loading increased, less specific heat was required to form a network between particles. As the particle-polymer size ratio increased and the particle diameters became comparable to the polymer's R_g , the specific heat requirement became larger because larger particles are less mobile than smaller particles and have less translational entropy, not requiring them to spread. Fig. 6b demonstrates that over time more specific heat is required to induce gelation. This implies that the gel is likely to lose its integrity over time.

1.4 Multi-Component Blends

Now that the phase behavior of a two-component system has been discussed, we will now focus our attention towards the phase behavior on polymer nanocomposites of multi-component polymer systems. Here, we will consider how more than one polymeric species behaves in the presence of inorganic NP. There are several examples of these types of systems: a) binary polymer blend containing inorganic NP, b) a blend of homopolymer, block copolymer, and inorganic NP, c) a blend of polymer, aqueous liquid, and inorganic (or organic) NP (also called an aqueous two-phase system [ATPS]),

d) a colloidal suspension of polymer, solvent, and inorganic (or organic) NP. All four multi-component systems exhibit trends in polymer phase behavior and nanostructured ordering. These details will be discussed as the physical parameters of the components in these systems are modified: a) interactions, b) size-scale, c) concentration, and d) geometry.

First we'll consider the case of inorganic NP in a binary blend of chemically distinct homopolymers. One of the first groups to pioneer in this research area is Tankana and coworkers⁶¹. Where glass beads that were attracted to one of the liquids in a blend of two liquids, acted as a compatibilizer between the macrophase separated domains. Physically, the selective glass beads reduced the interfacial tension and changed the interfacial curvature of the separated phase domains, by causing a wetting-induced depletion. Surfactants behave in the same fashion by partitioning between the oil and water interface in an organic/aqueous blend⁵². Since then, more blends have been analyzed to understand more about how the selectivity towards one of the homopolymers affects domain stability, domain size, and how it influences the location of the spinodal in the phase diagram. In spun-cast thin films of PMMA and PS, Minelli and coworkers discovered that the macrophase separated domains of PMMA became more stable when CoPt₃:Cu NP were added to the blend⁶². Using atomic force microscopy (AFM), they observed an increase in the height of the PMMA domains as NP loading, attributed to the increase in packing density of the PMMA phase from the spontaneous incorporation of NP. Minelli *et. al.* also observed a decrease in the size of the PMMA domains, which is consistent coarse-grain behavior. However, selective NP are not a requirement for

affecting the phase behavior of these blends. Spontak and coworkers incorporated NP that were equally selective to both homopolymers⁶³. Conversely, in a non-specific blend like this, the materials are expected to exhibit one-phase. Although there is no phase separation observed, the fumed silica (FS) NP formed a network, causing an increase in free volume due to frustrated chain packing.

As seen in binary blends, the geometry of the NP can influence the phase behavior of a multi-component blend. Clay NP have a large aspect-ratio and when exfoliated in a polymer matrix, one of its dimension's is on the nano size-scale. As with a binary blend, organoclays are favored for their ability to enhance the mechanical properties, thermal stability, and chemical resistance of a multi-component polymer blend⁶⁴. Yurekli and coworkers studied the influence of disk diameter on the phase-separated morphology of near-critical PS/poly vinyl methyl ether (PVME) blends⁶⁵. Surface roughness was compared over a temperature gradient, showing dramatic differences in late-stage morphology. In Figure 7, the blends evidence domain-pinning, an increase in the number of phase domains, and a higher fraction of near circular structures. The layered silicates are anisotropic disks ranging from nanometers in width to microns and were organically modified to interact with the polymer domains (not any one in particular but will interact more with the PVME). Blends of PS and PVME contain a morphology governed by spinodal decomposition of PS droplets in a PVME matrix. The addition of silicates appear to stabilize the thin polymer films on the silicon surface, and show a different morphology with smaller PS domains for the two smaller layered silicates. The results reveal a slower coarsening of domain structure for 30 nm and < 1.0 μm diameter

layered silica NP. The 30 nm clay layered silicates completely exfoliated while the < 1.0 μm became partially intercalated. The slowing down of the kinetics is related to the pinning-mechanism. This same trend of domain stabilization applies here for multi-component blends with inorganic NP. The change in geometry and size does not appear to any major difference in the morphology of the phase domains until the particles are on the micron size-scale.

Chung and coworkers observed the role of NP in phase separating a polymer blend of PMMA and poly styrene-ran-acrylonitrile (SAN) thin films ⁶⁶. Starting with a homogenous blend of silica NP (trimethyl silane functionalized) in the PMMA/SAN blend, the NP partitioned to the PMMA-rich phase and stratified during phase separation. The correlation length between phases was measured and showed that as NP were introduced the size of the PMMA-rich phase domains decreased. This behavior also agrees with the coalescence coarse-grain model. The kinetics of the blend were also explored and Chung *et. al.* determined that the NP were slowing down the phase separation of the polymers. These observations are in good agreement with the computational Ginzburg-Landau model, showing that wetting of NP and their partitioning into certain domains are what slows down the phase separation. PMMA/SAN blends undergo 3 stages in morphology evolution: a) Early stage, dominated by hydrodynamic-flow-driven wetting of PMMA through a 3D bicontinuous morphology to a free surface and substrate, b) Intermediate stage, PMMA-rich domains span the SAN-rich mid-layer and grow as 2D disks (coalescence model), and c) Late stage, PMMA/SAN/PMMA trilayer structure ruptures due to interfacial fluctuations resulting in

a rough film. Figure 8 shows the phase separation behavior occurring at the second stage of morphological evolution, with and without NP. The hills in (a) & (d) measure ~ 10 nm high. The rings in (b) & (e) are artifacts resulting from abrupt changes in height. The hills form from capillary driven flow of PMMA during early stage. The hills have been measured to have a higher modulus than the surrounding phase, representative of NP partitioning. The inset is the fast-Fourier transform (FFT) of the interface morphology. The mechanism for slowing down the phase separation showed that the NP move to the domain/matrix interface, reducing interfacial tension and therefore reducing the driving force for domain growth. The NP served as obstacles for polymer mobility.

So how is the mobility affected in a binary polymer blend containing NP? One example was demonstrated by Johnson *et. al.* where silica particles were incorporated in an epoxy resin with anhydride to help with curing⁶⁷. The silica was incorporated in-situ, using the sol-gel technique and became well dispersed within the matrix, as a result. Johnson and coworkers displayed that the T_g of the epoxy decreased with NP loading, and the modulus and toughness increased. This implies that the particles acted as diluents in the system, increased the mobility of the polymer chains, and acted like a plasticizer.

Returning to the same PMMA/SAN blend listed in Fig. 8, Chung *et. al.* explore NP localization at the domain/matrix interface incorporating two different surface functionalized NP with trimethyl silane (MEK) and PMMA brushes (PEK)⁶⁸. Chung and coworkers reported in SEM images that P2K NP segregated mostly to the domain/matrix interface, while MEK NP remained dispersed within the PMMA-rich phase. In Figure 9, AFM shows that PMMA-rich phase domains' decreased in diameter with increasing

MEK loading. The domain correlation length decreased drastically as well. 9 c illustrates at long heating times, the MEK and neat blends rupture and phase separation can no longer be observed. The P2K blends, however remain stable. It appears that there is a trend where NP reduce the size of phase domains in an effort to reduce interfacial tension. As a result, the domains become more stable.

Experiment compares very well with theory. The Campos group^{69,70} explored computationally epoxy/PS blends, with epoxy surface-functionalized or PS (phenyl group) surface-functionalized NP. They report that the NP partitioned to their respective phase domains and that the presence of the NP stabilized epoxy-rich or PS-rich phase domains. They demonstrate that the size of the NP play a role in compatibility. As the radius of the NP (R_p) becomes similar to the R_g of one of the polymers, the compatibility of the blend decreases. However, when $R_p > R_g$, compatibility and domain stabilization decrease. Campos and coworkers also show, in Figure 10, the USCT behavior of epoxy surface-functionalized NP in the epoxy/PS blend. The phase diagrams show a narrowing stabilization window with increasing NP loading, implying a decrease in polymer compatibilization. There was not much difference in the data when comparing the two NP surface-functionalities. Computational work done by He, Ginzberg, and Balazs, cover how polymer concentration, particle volume fraction, particle size, and interaction energies influence the phase stabilization in binary polymer blends containing NP⁷¹. Ginzberg's model is a modified version of Flory-Huggins theory where the χ values of each of the components is set and the χ value between the A block and the NP is = 0. Depending on the diameter of the NP and the R_g ratio, the presence of the NP either

stabilize or hinder polymer macrophase separation. The stable region for large χ_{AB} is smaller than smaller χ_{AB} values. For a symmetric case ($\phi_A = \phi_B$), at higher χ_{AB} and strong interactions between the particles and the homopolymer causes destabilization of the phase domains. For an asymmetric case ($\phi_A > \phi_B$), the central axis of the solid region is shifted along the $y = x$ axis. Systems containing neutral particles can become unstable when χ_{AB} is large and selective particles interact with one of the homopolymers, providing stabilization. When χ_{AB} , χ_{AP} , and χ_{BP} are all > 0 , all three components are incompatible and the blend behaves like an ABC ternary blend. However, χ_{AP} and χ_{BP} are both larger than χ_{AB} . At appropriate loadings of NP, the smaller segregation between A and B lead to stabilizing the blend (even with increasing NP loading). Also what helps stabilize the blend is the flip-side, where χ_{AP} and χ_{BP} are smaller than χ_{AB} and the NP are acting more like a traditional compatibilizing blend which is to reduce unfavorable interactions between A & B. The size of the stable region for asymmetric blends is larger than for symmetric blends. The phase diagram of the spinodal with increasing NP loading and varying NP size shows that the compatibilizing effect deteriorates, especially with asymmetric samples. It also shows that with increasing NP loading, compatibility between A & B increases. Figure 11 demonstrates how AB segregation influences the stability of the blend. For higher segregation values of χ_{AB} , symmetric blends cannot be stabilized with NP and the size of the stable region decreases drastically for these higher χ values. They become more stable as the blends become asymmetric. He, Ginzberg, and Balazs agree with previous examples that reducing the size of the NP can help compatibilize the blend (increases the stable region) and increasing the homopolymer

chain length also helps with stability. The major advantage of performing theoretical calculations is the ability to quickly simulate a wide range of experimental conditions, without needing the actual resources. These examples provide insight on how to direct creating the optimal conditions for forming a thermodynamically stable mixture, where the particles don't phase separate from the matrix material.

Now let's examine the phase behavior of ternary blends of homopolymer, block copolymer, and inorganic NP. These blends add a level of complexity by incorporating a microphase separating block copolymer. Almgren and coworkers created ternary blends of amphiphilic BCP, particles, & bicontinuous cubic phase of Glycerol Monooleate (GMO) and from a phase diagram was able to generate several different phase separated morphologies ⁷². Instead of the NP acting as the stabilizer/compatibilizer (as seen in previous examples) the BCP now serves the compatibilizer between dispersed particles in GMO. The phase behavior of this ternary system begins to resemble a colloid, which is a blend of suspended particles in a liquid. The BCP comes as a diblock copolymer of hydrophilic PEO and hydrophobic lipid-mimetic groups or as a triblock copolymer with a PEO mid-block and lipid-mimetic endblocks. Two avenues are being investigated: (1) The polymers' ability to swell the GMO phase in water and (2) The phase segregation of GMO and BCP in the presence particle dispersions, prepared via precursor dispersion of the GMO-polymer mixtures in glycerol. Figure 12 shows cryoTEM images of these blends in excess of water. Dispersed cubic particles were observed occasionally shaped as small cubes (low portions of polymer). At high polymer concentrations, particles with vesicles and various morphologies were observed. For the highest concentrations of

hydrophobic polymers, band-shaped micellar structures were observed with vesicles (micelles containing GMO and the polymer). The phase behavior of these blends were controlled by their interaction behavior and molecular weight of the polymers, packing behavior, and effect as steric stabilizers. In this example of a ternary blend, the particles were on the micron-scale instead of the nano-scale. They were also organic. However, similar phase separation principles apply. In some work done by Perlich *et. al.*, TiO₂ NP and PS homopolymer were blended with PS-*b*-PEO in an effort to have the homopolymer assist with templating the TiO₂ to the PEO phase ⁷³. The nanostructuring in this blend was controlled by the volume of homopolymer added.

Theoretical calculations performed by Zhang *et. al.* show the phase behavior of a homopolymer, a BCP, and NP ternary blends, where the NP are attracted to one of the blocks in the BCP, using the three-order-parameter (CDS) computational model ⁷⁴. By modifying the interactions between the NP, the formation of microphase and macrophase structures arise due to the interplay between the phase separation and the interactions from particle-particle attractions under a modulated potential. Microphase and macrophase morphology can be controlled by adjusting the interaction strength, the amplitude, and the period of the modulated potential. This work examines varying the wetting interactions in phase separations near the spinodal. Adding NP selective to one of the BCP blocks affects the microphase separation, which then affects the macrophase separation of the blend. The composition of selective particles is 5 wt % and the composition ratio of copolymer to homopolymer is 41.5 : 53.5. The orientation structures arise from the wettable NP in the presence of a modulated potential. As pictured in Figure

13, black domains are A-rich, gray domains are B-rich, and white domains C-rich. The black and gray domains represent the block copolymer. The NP are not shown in order to clearly display the microphase structures, but the NP are attracted to the B-rich phase. As wetting strength increases, the isotropy of the BCP microphase separation is broken down in the blend, and the blocks become more long range ordered. Increasing the modulation amplitude causes an increase in the wetting strength and improves microphase separation, resulting in the BCP domains becoming further ordered and less circular. When the modulation amplitude is large enough, the copolymer-homopolymer mixture is constrained to arrange itself to fit the modulation period. The macrodomains are controlled by the microdomains, which are controlled by the long-range correlation in the BCP. The amplitude has the largest affect on the domain growth, which most likely relates to the interaction between the copolymer and the homopolymer (the surrounding matrix material).

The phase behavior of an aqueous two-phase system (ATPS) containing NP becomes a little more simplified. In this system, there are only two-phase domains and they are visible to the naked eye. The NP occupy the interface between each the phases. PEG and dextran ATPS are attractive for purifying biomaterials (proteins, nucleic acids, organelles, or intact cells) for biomedical applications under low interfacial tension ^{75,76}. In one case ⁷⁵, a PEG/dextran blend incorporated gold NP with two different surface functionalities – horseradish peroxidase-(HRP) coated and protein-coated Au NP – to compare partitioning behavior. Long and Keating are working to use the PEG/dextran matrix as a primitive cytoplasm and controlling the phase behavior of the blend will be

necessary as the temperature and osmotic pressure controls its environment. The dextran-functionalized NP localized to the PEG-rich phase, and the protein-functionalized NP localized to the dextran-rich phase. Degree of localization was dependent on polymer concentration and molecular weight, NP diameter, and sometimes NP concentration. Improvement in localization seemed to result mostly in increased NP surface area, rather than interaction between the NP and the polymer. Another APTS blend was observed by the Keating group, comprising of PEG, dextran, water, and Au and Ag nanospheres and nanorods ⁷⁶. The NP partitioned between PEG-rich and dextran-rich phases. Larger nanospheres and nanowires localize at the interface, between the two aqueous phases. The NP had been functionalized with DNA, which directs their assembly in the blend. Nanospheres smaller than 80 nm partitioned between the PEG-rich and dextran-rich phases, and the large NP localized at the aqueous/aqueous interface. An increase in molecular weight or polymer concentration results a decrease in NP mobility at the interface. We may remember that a similar behavior was observed in the binary A B blends. Similar to an APTS blend but on a micro-macrophase separated size-scale, microemulsion droplets are oil and water blends useful for a range of biological applications. The micodroplets serve as a platform for NP synthesis ⁷⁷, a candidate for electrostatic NP stabilization ⁷⁸, or for foreign-body compatibilization ⁷⁹.

The last category of unique phase behavior in multi-component systems is colloidal suspensions of polymer, solvent, and inorganic (or organic) NP. Many are looking towards developing more strategies for stabilizing colloid suspensions. In this case, the NP are the colloidal particles and they are suspended in a polymer or solvent.

Zhang and coworkers examine silica NP suspended in cyclohexane⁸⁰. They add polyisoprene (PI) to the blend to provide further stability of the silica NP and to give the blend a protein limit ($q = R_g/R_p > 1$). Figure 14 displays a phase diagram, showing the blend's binodal, the boundary between miscible and immiscible blends. The critical colloid volume fraction is marked as 0.13, under good solvent conditions. This is the point of the phase boundary where, after phase separation, the volume of the two phases is equal. Below the binodal in the phase diagram, the blend is one-phase. Above the binodal, the blend phase-separates into a dense lower phase and a dilute upper phase. Less NP are required in order to reach the two-phase regime compared to a two-component system with NP and interacting. Also, the critical point can be controlled in this three-component system by changing the volume fraction of the NP and by changing the MW of the polymer. The phase behavior above the colloidal suspensions' protein limit can also be controlled by modifying the solvent concentration⁸¹. The phase behavior of the components in a colloidal suspension is very sensitive towards the type of solvent used. Good, ideal, and athermal solvents all add another element of dependency on the phase behavior and can be used to control the interaction behavior between the particles and the fluid⁸². Chen, Schweizer, and Fuchs, used computational simulations on a wide variety of cases to show trends in the interaction behavior of these materials. They reported that suspension miscibility worsens with increasing size asymmetry, for blends containing large polymers or small NP under ideal solvent conditions (opposite to athermal solvent behavior). They also found that over a range of intermediate size asymmetries, the spinodal curves are nearly constant and higher order contributions of

polymer concentration stabilize the miscible phase in both athermal and ideal solvents. The phase behavior of more complex colloidal networks was explored using self-consistent field theory (SCFT) and density functional theory (DFT), to evaluate the colloidal self-assembly of colloid-polymer films confined between two soft surfaces grafted by polymers⁸³. With increasing colloidal concentrations, the films undergo a series of phase transitions: disordered liquid → sparse square → hexagonal (or mixed square-hexagonal) → dense square → cylindrical structures in plane (Figure 14). These phase transitions result in entropic elasticity between polymer brushes and steric packing of colloidal particles, which give a new control mechanism to stabilize these morphologies. When grafting density is large, there is a larger liquid region and the phase structures are not two layered. A larger grafting density gives less phase separation (volume of phase domains).

Anna Balazs wrote a review summarizing the computational models developed to explain self-assembly in complex mixtures⁸⁴. She examines how thermodynamics and hydrodynamic effects can be exploited to create regular arrays of nanowires or monodisperse, particle-filled droplets. She also shows that an applied light source and a chemical reaction can be controlled to create hierarchically ordered patterns in ternary blends and that confining the walls and inducing a chemical reaction can create a swollen polymer gel, driven to form dynamically periodic structures. The examples used in her review show how coarse-grained models can be used to represent equilibrium phase behavior and the systems' dynamics. Figure 15 illustrates an example where NP become encapsulated in droplets, within microchannels. They start with A and B homopolymers,

where B is the minority component and the ordering parameter is in the nucleation-and-growth-regime. As the concentration of B increases, the fluid is quenched into the 2-phase spinodal region. When the wetting interactions are specified properly between the fluids and the surface, regular bands of A can be created. If the mixture is uniform before quenching, and the asperities are placed at equal distance apart, bands of equal volume are created (d). Being that the NP are A-selective, they partition into the A-domain. This example nicely equates all the principals discussed involving the self-assembly of multi-component polymer/NP blends.

1.5 Structured Blends

Up to this point, we have studied that NP affect the phase behavior and polymer chain ordering in unstructured, single and multi-component polymer systems. It is now time to focus on how NP affect the phase and chain packing behavior of polymers that exhibit their own structures at the nanoscale. An example of these are segmented copolymers, which are copolymers composed of hard and soft segments, able to phase separate into disordered microdomains within the blend. Examples of segmented copolymers include: polyurethanes, poly ether ester imides, and poly ether ester amides. In some work done by Liff and coworkers, the hard segments in a polyurethane were reinforced by clay platelets and were incorporated via solvent-exchange⁸⁵, increasing the toughness of the composite. It is expected that the presence of these particles would have an affect on the phase behavior of the polymer, even though polyurethanes don't order in any kind of periodic fashion. In another case, ZnO NP were added to a polyurethane and

the mechanical properties decreased dramatically ⁸⁶. The change in size and geometry caused a different behavior in the mechanical properties, and ultimately the phase behavior due to the spatial location of the NP in the polymer. The T_g increased by $\sim 11^\circ\text{C}$ meaning that the NP were decreasing the mobility of the polymer and acting like an anti-plasticizer. Contrary to the clay platelets, the spherical ZnO NP disrupted the phase separation of the polyurethane by not segregating to any particular hard or soft phase and by increasing the free volume in the polymer matrix. A second example of a structured copolymer blend includes hybrid copolymers. These are materials composed of inorganic segments covalently bonded to organic polymer segments. Hybrid copolymers can phase separate into microdomains, allowing for the blend to behave like a binary nanocomposite ⁸⁷⁻⁸⁹. The inorganic segment can be replaced with a chemically dissimilar organic segment, such as a DNA oligomer, to be used in biological applications ⁹⁰. In a random hybrid copolymer composed of a sulfonated monomer, PS, and a urethane acrylate non-ionomer compatibilizer was constructed by Kim and coworkers ⁹¹. They also incorporated NP within its phase separated hybrid mesostructure, and developed the films for sophisticated material separations for advanced membrane technology.

Pluronic triblock copolymers are structured copolymers that phase separate into microdomains with some degree of crystallinity. They are triblock copolymers composed of polyethylene oxide-*b*-poly propylene oxide-*b*-polyethylene oxide. (PEO-PPO-PEO). The molecular weight of each of the segments dictate the potential for crystallinity. Although this review has not focused much on crystallizable polymers, we will mention that incorporating NP to Pluronics also has an effect on the ordering behavior of the

copolymer as well as the degree of crystallinity. In some work done by Chen and coworkers, Pluronic copolymers were used to stabilize the hydrophobicity and aggregation of gold nanoclusters in water, in the formation of gold NP in polymer micelles⁹². They also incorporated Pluronic triblock copolymers in a colloidal suspension of poly (D, L-lactic-co-glycolic acid) PGLA NP, providing uniformly dispersed NP by self-assembling in the surface of the NP⁹³. Pozzo and coworkers examined how NP affect the ordering of the crystallites in Pluronic triblock copolymer cubic micelles⁹⁴. They added silica NP and found that the NP concentration affects the ordering behavior, which are organized by excluded volume interactions as they are driven into the interstitial cavities of the micelle cubic crystal. The triblocks were used to template the position of the NP¹², and they found that higher polymer concentrations in the matrix and temperatures above, the ODT gave favorable conditions for NP templating. Eventually, the increased NP concentration causes the morphology of the cubic micelles to transcend from body-centered-cubic (BCC) to face-centered-cubic (FCC) (Figure 16). Pozzo and coworkers demonstrates that incorporating NP at particular concentrations can be used to tune the morphology and nanostructure of Pluronic nanocomposites.

More generally, block copolymers have been identified as ideal nanostructured materials for directing the assembly of NP into ordered mesostructures^{95,96}. Block copolymers are composed of two or more chemically dissimilar homopolymers that thermodynamically order into periodic microphase-separated phase domains. What makes them so unique is that their individual polymer chains are similar in length to the diameter of NP, which allows the block copolymer to be capable of impregnating their

phase domains with NP while maintaining their microphase-separated morphologies. No other materials are capable of performing at such a minute level because the phase domains were never small enough to compete with the size of the individual NP. The ability to selectively incorporate NP into these microphase-separated phase domains, allowing one to control the location of the NP in the polymer matrix, will provide access to a wide range of new advanced technologies. As mentioned previously, there has been much work done towards understanding how the NP spatially locate in block copolymers, but being that the block copolymer dictates how the NP segregate, it is important to study how the block copolymer molecules behave in the presence of NP. In other words, it is necessary to determine how the thermodynamics of block copolymers are affected by NP interactions.

We will begin first with looking at how particle-polymer interactions play a role in segregation among a block copolymer. The interaction between the polymer chains and the NP can be tailored (as in the case with the binary and multi-component blends) to be attracted to one or more the polymer blocks. The best method is to functionalize the NP surface. When the NP are functionalized with polymer chains of the same chemistry as one of the blocks, the Flory-Huggins interaction parameter, χ , between the two becomes very low. This causes the enthalpic contribution to increase in the free energy term and typically causes the NP to spatially locate to its preferred microdomain^{1,54, 97-103}. But how do these NP affect the order of the block copolymer brushes, once next to the NP and their surface-functionalized ligands? Their behavior varies depending on the size of the NP and the length of their tethers compared to the R_g of the block copolymer

^{1,54, 97-103}. Kramer and coworkers showed that they could induce a microphase transition in morphology of PS-*b*-P2VP diblock copolymer from lamellae to hexagonally-closed-packed cylinders by introducing Au NP with small PS chains grafted to the surface of them ⁹⁸. They spatially located to the center of the PS microdomains and eventually with increasing concentration, the PS microphases swelled and caused the interfaces to curve and form cylinders ^{98,99}. The mechanical properties polysiloxane copolymers were maximized by carefully tailoring the surface-functionalities to meet the more efficient phase conditions ¹⁰³. The advantage was that presence of these NP did not change the impregnated block copolymer's microstructure, which maximized the efficiency of force fields by supramolecular structural units. There are other ways to control the functionality of the NP. Organoclays can become hydrophobic by solvent-ion exchange ¹, allowing them to be miscible in more organic polymers, and other NP can be surface-functionalized with other smaller ligands or other polymers, which are still chemically affinitive to one of the blocks ^{104,105}. The Spontak group shows an example of how fumed silica NP with three different surface functionalities (–OH, –C8, & –MA) affect the ODT in PS-*b*-PMMA diblock copolymer ¹⁰⁴. Figure 17 shows a plot of T_{ODT} as a function of NP concentration, ϕ_p . One can gather from this data that all three surface-functionalized fumed silica NP had little affect on the ODT at low concentrations, despite their affinity towards the PMMA block. Not until the concentration increased past 5 wt% did the NP begin to reduce the ODT, which indicates that the presence of NP has a decaying affect on the microphase stability of the BCP ¹⁰⁴.

In some work done by Kramer, Fredrickson, and coworkers, Au NP were functionalized to behave like surfactants, causing them to spatially locate to the interface of polystyrene-*b*-poly-2-vinyl pyridine (PS-*b*-P2VP) diblock copolymer¹⁰⁶. By adding small amounts of NP, they show a decrease in lamellar thickness as a result of decreasing interfacial tension and stabilizing the liquid film between the droplets preventing coalescence, eventually causing a phase transition from lamellae to a bicontinuous morphology. Figure 18 illustrates PS-*b*-P2VP impregnated with Au-coated NP behaving as surfactants because short PS chains were grafted to the surface of the Au NP via thiol linkages, exposing part of the bare Au surface to affinitive P2VP. This technique caused the NP to localize at the interface between the PS and P2VP polymer chains. In this case, the NP help stabilize the strongly-segregated block copolymer's equilibrium bicontinuous nanostructure as did the PMMA coated NP in the PMMA/SAN blend stabilized the PMMA domains in reference 68. Strong segregation models explain the decrease in lamellar thickness and increase in interfacial area by surfactant NP addition as resulting from a decrease in chain stretching and the binding attraction between the NP to each of the blocks. This same decrease in chain stretching was observed in very asymmetric triblock copolymers¹⁰⁷, observed by Spontak and coworkers. The Fredrickson and Kramer group also observed that NP coated with PS-*r*-P2VP polymer brushes initially localized at the PS/P2VP interface because the interfacial tension between the blocks was so high, but as NP concentration increased, the NP began to cluster and macrophase separate because they were mostly neutral to the system and because they were not enthalpically driven to localize at any particular place. Their entropic interactions

prevailed and allowed them to macrophase separate. Polymer blends can produce bicontinuous structures by quenching the structure below the spinodal and trapping the non-equilibrium structure, but further thermal processing or rapid solvent casting can destroy this structure. Microphase-separated block copolymers can exhibit a bicontinuous nanostructure naturally. Their work looks at methods towards providing morphological stabilization by adding NP at the interface.

The work done by the Fredrickson-Kramer group brought up an interesting new point, as the phase behavior of block copolymer nanocomposites is discussed. The entropic interactions also play a role in dictating the equilibrium morphology of the block copolymer and the NP. When considering block copolymers, it is well understood that their entropic interactions allow polymer chain packing to occur, reducing their free energy and causing an interface to form between dissimilar chains. Depending on the molecular weight of the block copolymers, the microdomains are typically small (tens of nanometers), and each polymer chain undergoes a range of conformations before it arrives at its ideal relaxed state. These principals are also true for regular polymers, but block copolymers are unique because they are also driven by their enthalpically unfavorable counterparts, which confine them to their preferred microdomain. Based in the fact that these polymer blocks are spatially constricted, the addition of a NP will have an affect on how they conform. Wiesner created hybrid materials, using BCP high NP concentrations of varying sizes ¹⁰⁸. The final morphology exhibited depended on the interplay between enthalpy and entropy within the system. The goal for these materials was to ‘exploit’ this interplay to create a desired structure, for a particular function ⁹⁷.

Wiesner and coworkers showed that particle size is a key player in determining the final morphology, proving good agreement with other studies^{97, 104}. First, the NP block-selective surface chemistry causes an enthalpic driving force towards diffusing themselves into its preferred block. Secondly, if the NP are smaller than the selective block's R_g (or the contour length – distance between the two polymer ends), then they disperse within the block's microphase and the overall structure is dictated by the BCP. If the R_p is larger than or equal to the selective block's R_g (contour length), the polymers must stretch around the particles to accommodate these materials. Lots of stretching lowers the entropy (degrees of freedom) of the polymer because the extended chains can undergo fewer conformations than relaxed coils. When the particles reach a critical size, the cost of free energy becomes too large and the particles macrophase separate and cluster. The structure of the particles now dictate the morphology of the system⁹⁷.

The Balazs group has done much theoretical work on tuning the block copolymer morphology by modifying the size of the NP. They use self-consistent-field theory (SCFT) to describe the thermodynamic equilibrium behavior of pure polymers and density functional theory (DFT) to cover particle ordering and phase behavior in colloidal systems. Large selective NP ($R_p = 3R_0$ and $\phi_p = 0.15$) localized to the midplane of its preferred block and smaller selective particles ($R_p = 2R_0$ and $\phi_p = 0.15$) located closer to the AB interface¹⁰⁹. Entropically, the polymer chains must stretch around the large dispersed spheres, resulting in a loss of conformational entropy. Stretching becomes reduced as NP loading increases as particles segregate. For smaller particles, less stretching is required and less conformational entropy is lost. Translational entropy

dominates and as NP loading increases, the spheres become more uniformly dispersed. The thermodynamics of the NP have also been confirmed as the same for strongly segregated block copolymers¹¹⁰. This group looked at the thermodynamics of NP and how they melt in a diblock copolymer in the low-temperature regime (near ODT), but similar observations were made using SST¹¹¹. In this second case, the particles had been designed to interact with both A & B blocks (neutral). Their presence was assumed to induce phase transitions, similar to the work done by the Fredrickson and Kramer group for bicontinuous morphologies. They found that variations in the particle size and interaction energies can cause phase transitions. They show a phase diagrams for two different sized NP, effectively showing that you can have two different morphologies at a fixed χ_{AP} , χ_{BP} , and ϕ . They also note that even with non-selective particles, NP with increasing radii can induce a phase transition from cylinders to lamellae, with the particles residing uniformly among both blocks and gathering slightly at the interface. The particles gather at the interface to reduce interfacial tension between the blocks, by reducing the number A & B contacts and reducing the enthalpic contribution. The large particles gather only at the interface to reduce interfacial tension, which is more important than the entropy loss of the particles' translational entropy. The large particles gather at the interface and bulge into the other microphases, altering the asymmetry of the BCP and causing a transition from cylinders to lamellae.

In a third interesting case, the Balazs group expand their study on to systems with two different sized NP (binary particle mixture)¹¹². They show that the system still undergoes nanoscale phase ordering and can induce phase transitions. They also show

that entropy drives the nanostructure of the system and it can be exploited to create very specifically ordered nanocomposites. Operating in the SST (chains are highly stretched), two sizes of NP are introduced. Both small and large particles are A-selective and the large particles localize at the midplane. The A-chains don't lose as much conformational entropy by having to stretch around the particles. The smaller particles are near the A-B interface, and to a large extent, in the incompatible B-phase. The particles form a "gradient layer" according to size, from the center to the edges of the cylinder. This behavior causes a phase transition from lamellae to cylinders. When the small A-particles move into the energetically unfavorable B-block, this increases the enthalpic contribution and would potentially increase the free energy. However, the increase in enthalpy is offset by an increase in translational entropy, which decreases the steric contribution (a measure of crowding of the hard particles). This shows that entropy dominates in the system, even with enthalpically unfavorable interactions. Figure 19 shows the morphology of bi-disperse NP in a BCP and demonstrates the role of translational entropy has on the system.

Reister and Fredrickson take another look at how NP size affects the microphase ordering behavior in a symmetric block copolymer¹¹³. Instead of simulating NP with hard surfaces, they simulate tiny NP with long monodisperse polymer chains tethered to their surface. The NP are modeled according to their grafted shell as star polymers and are assumed to be spheres. Reister and Fredrickson are looking at how the phase behavior changes when as the arm length and grafting density change on the NP. Qualitatively, the increase in star arms behaves the same as an increase in homopolymer length from

Matsen's work, where at high volume fractions the system becomes 2-phase³⁰. The number of star arms and length was summarized in a $\beta\sigma$ term, which remained constant. As the number of arms increased, their length became shorter. At lower $\beta\sigma$ and the case where the NP had longer arms but a lower number of arms, the lamellar phase was more stable at higher NP concentrations until the lamellae become infinitely swollen. The lamellar spacing seemed to increase with arm length. A similar behavior was observed experimentally by the Mathis group, where fullerene NP were surface functionalized with long PS grafts and the PS lamellae became swollen with increasing graft length¹⁰². Alternatively at higher $\beta\sigma$, increasing the arm density led to a narrower lamellar region. The NP were found to distribute uniformly in the A-block, and the polymer blocks localized near the interface. In this case, the polymer chains did not stretch around the NP. Instead, they coiled within themselves and located near the interface. The most influential factor governing whether macrophase separation occurred was the size-ratio of NP to the diblock copolymer. Small NP were able to remain segregated in the block copolymer's lamellar morphology at higher loadings than large NP. This concept is directly related to the entropic contribution.

There has been much discussion on the NP inducing phase transitions by swelling or shrinking the block copolymer microphase domains or whether the NP macrophase separate from the blocks, possibly reducing their impact on the block copolymer nanostructure or forcing the block copolymers to disorder. All of these arguments relate to interactions occurring between the particles and the polymer blocks and the particle-particle interactions. If the particles have soft surfaces due to functionalization

^{98,99,102,103,106,114} or addition of a selective solvent ^{115,116}, they will typically swell the blocks and induce order-order phase transitions (OOT). In some theoretical work done by Rasmussen and coworkers, lamellar swelling from selective NP in a block copolymer caused a decrease in the tensile modulus due to the displacement of polymer molecules and an increase in the free volume ¹¹⁷. On the contrary, if NP have short surface-functional groups and have a strong affinity to interact with one another, they can produce surface roughness between the soft polymer brush-surface and the hard NP surface ¹¹⁸. As the NP concentration increases unfavorable interactions increase surface roughness, causing the particles to macrophase separate and even break down the nanostructured morphology of the block copolymer ^{100,104,106,118}. Figure 20 depicts the disordering behavior of PS-coated Au NP in PS-*b*-P2VP copolymer. One can speculate that the actual order-disorder-transition might decrease with NP loading, regardless of surface roughness between the NP and copolymer. Balazs and coworkers display in Figure 21 how the ODT decreases with NP concentration ¹¹⁹. This behavior is expected, considering the entropic penalties the polymer chains take as they are required to stretch around the NP. The same behavior was predicted by Schultz and coworkers, using Monte Carlo simulations ¹²⁰. However, there are a few cases where the interplay between enthalpy and entropy was tuned precisely enough to show an increase in ODT and microphase stability. One was demonstrated by Han and coworkers, where hydrophilic nanoclays were placed in PS-*b*-P2VP diblock copolymer ²⁵. Because the NP were strongly attracted to the P2VP block via hydrogen bonding, and the clays had such a high aspect ratio, the ODT increased for those blends. An example where NP increased the

ordering stability of the microphase separated domains was shown by the Spontak group, where large, spherical silica PS-surface functionalized NP increased the T_{ODT} at low NP loadings¹⁰⁴. In this case, the nanoparticles had a larger R_p than the block copolymer R_g . Up until this point, it had been assumed that NP with a R_p greater than or equal to the polymer R_g will cause NP macrophase separation, immiscibility with the copolymer, and a decrease in the ordering behavior. The Spontak group has qualitatively demonstrated experimentally and theoretically that designing the selectivity and the size-ratio of particle to polymer can actually improve microphase stability. These discoveries lead us to believe that tuning the phase morphology of polymers is far more complicated than originally suspected. One last consideration includes how geometry affects block copolymer stability. The Balazs group describes in Figure 21b that increasing the aspect ratio of NP improves the microphase stability of the copolymers. This also may explain why Han saw an increase in ODT, by adding high-aspect ratio nanoclays to PS-*b*-P2VP block copolymer. Again, creating an exact case where an improvement in microphase stability can be observed is complicated and very sensitive upon each design parameter. Jain and coworkers observe a decrease in T_{ODT} for selective spherical, rod, and platelet NP at a fixed NP loading¹²¹, which demonstrates a case where geometry has no influence on improving the microphase stability. The previous examples imply that fine-tuning more of the parameters in the experiments conducted in reference 121, may reveal a window of increased microphase stability.

1.6 Conclusions

There has been a wide range of phase behaviors reviewed on polymer systems impregnated by inorganic nanoparticles. Although each system displays very different behaviors, several main concepts shine through. The interactions between all of the components in the system play a major role in how the nanostructures will form. Adsorbing polymers provide an avenue for NP to assemble within an unstructured polymer. Multi-component polymer blends contain unstructured, non-periodic macrophases, where at least one of the polymers may have an affinity towards the nanoparticles. The interacting nanoparticles may either be encapsulated by the microphases and/or reside at the interface between the two polymers, effectively reducing the number of A-B contacts at the interface. These favorable interactions have demonstrated more stable macrophases and also exhibited the ability to change the interfacial curvature of one of the phases, causing smaller microphases to form. Structured copolymer blends illustrated similar behaviors, where the interactions between one of their segments and the inorganic nanoparticles permitted impregnation of their microphases. For block copolymers in particular, the interaction between one or more of the blocks played a large role in where most of the nanoparticles would spatially locate.

The other critical factor governing the phase behavior of these polymer systems were the size-ratio of nanoparticles (R_p) to polymer (R_g). For all three cases, it has been found that shrinking the size of the nanoparticles or increasing the molecular weight of the polymer molecules caused the nanoparticles to become more miscible and dispersed within the polymer matrix. Smaller particles displayed a natural tendency to form smaller

aggregates than larger particles because smaller particles have an inherent desire to spread to reduce steric crowding but cause an increase in translational entropy. Larger particles have less translational entropy, surface area, and crowding, which allows them to remain stable as larger agglomerates. Larger particles have demonstrated a greater possibility of macrophase separating from the polymer nanostructure. The size-ratio of inorganic particles to polymer molecules (R_p/R_g) becomes most interesting in block copolymers, where small-selective particles spatially locate near the interface and larger particles segregate near the midplane. In both instances, the polymer's periodic nanostructure is governed by the polymer molecules. The nanoparticles only influence the polymer's nanostructure, by causing it to disorder or macrophase separate from the block copolymer's microphases, if the surface roughness is high or if the nanoparticle concentration is high. Several groups have also demonstrated that tailoring the interaction behavior (by reducing the number of A-B contacts or strongly interacting with one of the microphases), size-ratio, and geometry of the nanoparticles can provide stabilization of the microphases in a block copolymer or macrophases in a polymer blend. Learning to tune these parameters will be critical in designing optimized nanocomposites for scaled-up applications.

1.7 References

1. Bockstaller M. R.; Mickiewicz, R. A.; Thomas, E. L. *Adv. Mater.* **2005**, 17, 1331-1349.
2. Frazer, L. *Environmental Health Perspectives* **2001**, 109, 11, A524-A525.
3. Aricò, A. S.; Bruce, P.; Scrosati, B.; Tarascon, J.; Schalkwijk, W. V. *Nature Materials* **2005**, 4, 366-377.
4. Bouclé, J.; Ravirajan, P.; Nelson, J. *J. Mater. Chem.* **2007**, 17, 3141-3153.
5. Park, C.; Yoon, J.; Thomas, E. L. *Polymer* **2003**, 44, 6725-6760.
6. Merkel, T. C.; Freeman, B. D.; Spontak, R. J.; He, Z.; Pinnau, I.; Meakin P.; Hill, A. J. *Science* **2002**, 0, 1-4.
7. Walls, H. J.; Riley, M W.; Singhal, R. R.; Spontak, R. J.; Fedkew, P. S.; Khan, S. A. *Adv. Func. Mater.* **2003**, 13, 710-717.
8. Li, Y.; Fedkiw, P. S. *J. Electro. Chem. Soc.* **2007**, 154, A1140-A1145.
9. Wang, Y.; Gao, S.; Ye, W.; Yoon, H. S.; Yang, Y. *Nature Materials* **2006**, 5, 791-796.
10. Granick, S.; Kumar, S. T.; Amis, E. J.; Antonielli, M; Balazs, A. C.; Chakraborty A. K.; Grest, G. S.; Hawker, C.; Janmey, P.; Kramer, E. J.; Nuzzo, R.; Russell, T. P.; Safinya, C. R. *J. Polym. Sci. Part B: Polym. Phys.* **2003**, 41, 2755-2793.
11. Shenhar, R.; Norsten, T. B.; Rotello, V. M. *Adv. Mater.* **2005**, 17, 657-669.
12. Corma, A.; Atienzar, P.; García, H.; Chane-Ching, J. *Nature Materials* **2004**, 3, 394-397.

13. Sarikaya M.; Tamerler, C.; Jen, A. K. -Y.; Schulten, K.; Baneyx, F. *Nature Materials* **2003**, 2, 577-585.
14. Striolo, A. *Small* **2007**, 3, 628-635.
15. F. Rodriguez, C. Cohen, C. K. Ober and L. A. Archer, *Principles of Polymer Systems*, 5th Ed., Taylor & Francis, New York, 2003.
16. Young, R. J. and P.A. Lovell, *Introduction to Polymers*, 2nd Ed., Nelson Thornes, United Kingdom, 2002.
17. Bates, F. *Science* **1991**, 251, 898-905.
18. Balsara, N. P.; Rappl, T. J.; Lefebvre, A. A. *J. Polym. Sci. B: Polym. Phys.* **2004**, 42, 1793-1809.
19. Spontak, R. J.; Patel, N. P. "Phase Behavior of Block Copolymer Blends" *Developments of Block Copolymer Science and Technology* I. W. Hamley, John Wiley & Sons, 2004, Chapter 5.
20. Hamley, I. W. *The Physics of Block Copolymers*; Oxford University Press: New York, 1998.
21. Bates, F. S.; Fredrickson, G. H. *Physics Today* **1999**, 52, 32-38.
22. Khandpur, A. K.; Forster, S.; Bates, F. S.; Hamley, I. W.; Ryan, A. J.; Bras, W.; Almdal, K. and Mortensen, K. *Macromolecules* **1995**, 28, 8796-8806.
23. Floudas, G.; Vazaiou, B.; Schipper, F.; Ulrich, R.; Wiesner, U.; Iatrou, H.; Hadjichristidis, N. *Macromolecules* **2001**, 34, 2947-2957.
24. Han C. D.; Kim, J. *Macromolecules* **1987**, 25, 1741-1764.
25. Lee, K. M.; Han, C. D. *Macromolecules* **2003**, 36, 804-815.

26. Lodge T. P.; Blazey, M. A.; Lui, Z. *Macromol. Chem. Phys.* **1997**, 198, 983-995.
27. Hanley, K. J.; Lodge, T. P.; Huang C-I *Macromolecules* **2000**, 33, 5918-5931.
28. Spontak, R. J.; Shankar, R.; Bowman, M. K.; Krishnan, A. S.; Hamersky, M. W.; Samseth, J.; Bockstaller, M. R.; Rasmussen, K. Ø. *Nano Lett* **2006**, 6, 2115-2120.
29. Shankar, R.; Ghosh, T. K.; Spontak, R. J. *Soft Matter* **2007**, 3, 1116-1129.
30. Matsen, M. W. *Macromolecules* **1995**, 28, 5765-5773.
31. a) Winey, K. I.; Thomas, E. L.; Fetters, L. J. *Macromolecules* **1991**, 24, 6182-6188. b) Winey, K. I.; Thomas, E. L.; Fetters, L. J. *J. Chem. Phys.* **1991**, 95, 9367-9375.
32. Court, F.; Hashimoto, T. *Macromolecules* **2002** 35, 2566-2575.
33. Epps, T. H.; Chatterjee, J.; Bates, F. S. *Macromolecules* **2005**, 38, 8775-8784.
34. Kim, J. U.; O'Shaughnessy, B. *Macromolecules* **2006**, 39, 413-425.
35. Riskin, M.; Basnar, B.; Huang, Y.; Willner, I. *Adv. Mater.* **2007**, 19, 2691-2695.
36. Khan, A. J. *Coll. Int. Sci.* **2007**, 313, 697-704.
37. Huang, G.; Hu, Z. *Macromolecules* **2007**, 40, 3749-3756.
38. Maio, B.; Yan, D.; Han, C. C. *J. Chem. Phys.* **2006**, 124, 144902.
39. Mayes, A. M.; Russell, T. P.; Satija, S. K.; Majkrzak, C. F. *Macromolecules* **1992**, 25, 6523-6531.
40. Wei, B.; Genzer, J., Spontak, R. J. *Langmuir*, **2004**, 20, 8659-8667.
41. Zolotukhin, I. V.; Yanchenko, L. I.; Belonogov, E. K. *JETP Lett.* **1998**, 67, 720-722.
42. Li, J.; Lui, B.; Li, J. *Langmuir* **2006**, 22, 528-531.

43. Zeynalov, E.; Azerbaijan, B.; Friedrich, J. F. *Polym. Mater.* **2007**, 49, 265-270.
44. Starr, F. W.; Douglas, J. F. *J. Chem. Phys.* 2003, 119, 1777-1788.
45. Barnes, K. A.; Karim A.; Douglas, J. F.; Nakatani, A. I.; Gruell, H.; Amis, E. J. *Macromolecules* **2000**, 33, 4177-4185.
46. Bansal, A.; Yang, H.; Li, C.; Cho, K.; Benicewicz, B. C.; Kumar, S. K.; Schadler, L.S. *Nature Materials* **2005**, 4, 693-698.
47. Gladchenko, S. V.; Polotskaya, G. A.; Griбанov, A. V.; Zgonnik, V. N. *Technical Physics* **2002**, 47, 105-109.
48. Sanz, A.; Ruppel, M.; Douglas, J. F.; Cabral, J. T. J. *Phys.: Condens. Matter.* **2008**, 20, *in press*.
49. Kropka, J. M.; Putz, K. W.; Pryamitsyn, V.; Ganesan, V.; Green, P. F. *Macromolecules* **2007**, 40, 5424-5432.
50. Biswas A.; Bayer I. S.; Marken, B.; Pounds, T. D.; Norton M. G. *Nanotechnology* **2007**, 18, 305602 (6pp).
51. Mackey, M. E.; Tuteja, A.; Duxbury, P. M.; Hawker, C. J.; Horn, B. V.; Guan, Z.; Chen, G.; Krishnan, R. S. *Science* **2006**, 311, 1740-1743.
52. Balazs, A.C.; Emrick, T.; Russell, T. P. *Science* **2006**, 314, 1107-1110.
53. Kausch, H. H.; Michler, G. H. *J. Appl. Polym. Sci.* **2007**, 105, 2577-2587.
54. Lan, Q.; Francis, L. F.; Bates, F. S. *J. Polym. Sci. Part B: Polym. Phys.* **2007**, 45, 2284-2299.
55. McDonald, S. A.; Konstantatos, G.; Zhang, S.; Cyr, P. W.; Klem, E. J. D.; Levina, L.; Sargent, E. H. *Nature Materials* 2005, 4, 138-142.

56. Sivaramakrishnan, S.; Chia, P.- J.; Yeo, Y.- C.; Chua, L.- L.; H., P. K. -H. *Nature Materials*, **2007**, 6, 149-155.
57. Bhattacharjee, R. R.; Mandal, T. K. *J. Coll. Int. Sci.* **2007**, 307, 288-295.
58. Hooper, J. B.; Schweizer, K. S.; *Macromolecules* **2007**, 40, 6998-7008.
59. Zhao, L.; Li, Y.- G.; Zhong, C. *J. Chem. Phys.* **2007**, 127, 154909.
60. Chen, Y. -L., Kobelev, V.; Schweizer, K. S. *Phys. Rev. E.* **2005**, 71, 041405.
61. Tanaka, H.; Lowinger, J.; Davis, D. D.; *Phys. Rev. Lett* **1994**, 72, 2581-2584.
62. Minelli, C.; Frommen, C.; Hinderling, C.; Pugin, R.; Heinzelmann, H.; Liley, M. *Colloid Polym. Sci.* **2006**, 284, 482-488.
63. Patel, N. P.; Aberg, C. M.; Sanchez, A. M.; Capracotta, M. D.; Martin, J. D.; Spontak, R. J. *Polymer* **2004**, 45, 5941-5950.
64. Sánchez-Solís, A.; Romero-Ibarra, I.; Estrada, M. R.; Calderas, F.; Manero, O. *Polym. Eng. Sci.* **2004**, 44, 1094-1102.
65. Yurekli, K.; Karim, A.; Amis, E. J.; Krishnamoorti, R. *Macromolecules* **2003**, 36, 7256-7267.
66. Chung, H. -J.; Taubert, A.; Deshmukh, R. D.; Composto, R. J. *Europhys. Lett.* **2004**, 68, 219-225.
67. Johnson, B. B.; Kinloch, A. J.; Mohammed, R. D.; Taylor, A. C.; Sprenger, S. *Polymer*, **2007**, 530-541.
68. Chung, H. -J.; Ohno, K.; Fukuda, T.; Composto, R. J. *Nano. Lett.* **2005**, 5, 1878-1882.

69. Gómez, C. M.; Porcar, I.; Monzo, I. S.; Abad, C.; Campos, A. *Eurp. Polym. J.* **2007**, 43, 360-373.
70. Figueruelo, J. E.; Gómez, C. M.; Monzó, I. S.; Abad, C.; Campos, A. *Macromol. Theory Simul.* **2007**, 16, 458-475.
71. He, G.; Ginzberg, V. V.; Balazs, A. C. *J. Polym. Sci. Part B: Polym. Phys.* **2006**, 44, 2389-2403.
72. Almgren, M.; Rangelov, S. *J. Dispersion Sci. Tech.* **2006**, 27, 599-609.
73. Perlich, J.; Schulz, L.; Kashem, M. M. A.; Cheng, Y. -J.; Memesa, M.; Gutmann, J. S.; Roth, S. V.; Müller-Buschbaum, P. *Langmuir* **2007**, 23, 10299-10306.
74. Zhang, J. -J.; Jin, G.; Ma, Y. *Eur. Phys. J. E.* **2005**, 18, 359-365.
75. Long, M. S.; Keating, C. D. *Anal. Chem.* **2006**, 78, 379-386.
76. Helfrich, M. R.; El-Kouedi, M.; Etherton, M. R.; Keating, C. D. *Langmuir* **2005**, 21, 8478-8486.
77. Note, C.; Ruffin, J.; Tiersch, B.; Koetz, J. *J. Disp. Polym. Sci. Tech.* **2007**, 28, 155-164.
78. Lepková, K.; Clohessy, J.; Cunnane, V. J. *J. Phys. : Condens. Matter* **2007**, 19, 375106.
79. Qiu, X.; Han, Y.; Zhuang, X.; Chen, X.; Li, Y.; Jing, X. *J. Nanopart. Res.* **2007**, 9, 901-908.
80. Zhang, Z.; Duijneveldt, J. S. van. *Langmuir* **2006**, 22, 63-66.
81. Kramer, T.; Schweis, R.; Huber, K. *Macromolecules* **2005**, 38, 9783-9793.
82. Chen, Y. -L.; Schweiser, K. S.; Fuchs, M. *J. Chem. Phys.* **2003**, 118, 3880-3890.

83. Ren, C. -i.; Ma, Y. -q. *J. Am. Chem. Soc.* **2006**, 128, 2733-2737
84. Balazs, A. C. *Annu. Rev. Phys. Chem.* **2007**, 58, 211-233.
85. Liff, S. M.; Kumar, N.; McKinley, G. H. *Nature Materials* **2007**, 6, 76-83.
86. Zheng, J.; Ozisik, R.; Siegel, R. W. *Polymer* **2005**, 46, 10873-10882.
87. Bronstein, L. M.; Ashcraft, E.; DeSanto II, P.; Karlinsey, R. L.; Zwanziger, J. W. *J. Phys. Chem. B* **2004**, 108, 5851-5858.
88. Zheng, L.; Hong, S.; Cardoen, G.; Burgaz, E.; Gido, S.; Coughlin, E. B. *Macromolecules* **2004**, 37, 8606-8611.
89. Dzhardimalieva, G. I.; Pomogailo, A. D.; Volpert, V. A. *J. Inorg. Organomet. Polym.* **2002**, 12, 1-21.
90. Kudley, A.; Gibbs, J. M.; Schatz, G. C.; Nguyen, S. T.; Olvera de la Cruz, M. J. *Phys. Chem. B* **2007**, 111, 1610-1619.
91. Kim, J. Y.; Mulmi, S.; Lee, C. H.; Park, H. B.; Chung, Y. S.; Lee, Y. M. *J. Membrane Sci.* **2006**, 283, 172-181.
92. Chen, S.; Guo, C.; Hu, G. -H.; Liu, H. -Z.; Liang, X. -F.; Wang, J.; Ma, J. -H.; Zheng, L. *Colloid Polym. Sci.* **2007**, 285, 1543-1552.
93. Santander-Ortega, M. J.; Jódar-Reyes, Csaba, N.; Bastos-González, D.; Ortega-Vinuesa, J. L. *J. Colloid Int. Sci.* **2006**, 302, 522-529.
94. Pozzo, D. C.; Walker, L. M. *Col. Surf. A: Physiochem. Eng. Aspects* **2007**, 294, 117-129.
95. Jain, A.; Wiesner, U. *Macromolecules* **2004**, 37, 5665-5670.

96. Thompson, R. B.; Ginzberg, V. V.; Matson, M. W.; Balazs, A. C. *Macromolecules* **2002**, 35, 1060-1071.
97. Balazs, A. C. *Nature Materials* **2007**, 6, 94-95.
98. Kim, B.J.; Chiu, J. J.; Yi, G. -R.; Pine, D. J.; Kramer, E. J. *Adv. Mater.* **2005**, 17, 2618-2622.
99. Sides, S. W.; Kim, B. J.; Kramer, E. J.; Fredrickson, G. H. *Phys. Rev. Lett.* **2006**, 96, 250601.
100. Tsutsumi, K.; Funaki, Y.; Hirokawa, Y.; Hashimoto, T. *Langmuir* **1999**, 15, 5200-5203.
101. Kashem, M. M. A.; Schulz, P. L.; Roth, S. V.; Petry, W.; Müller-Buschbaum, P. *Macromolecules* **2007**, 40, 5075-5083.
102. a) Mathis, C.; Schmaltz, B.; Brinkmann, M. *C. R. Chimie* **2006**, 9, 1075-1084. b) Schmaltz, B.; Brinkmann, Mathis, C. *Macromolecules* **2004**, 37, 9059-9063.
103. Voznyakovskii, A. P. *Phys. Solid State* **2004**, 46, 629-632.
104. Gaines, M. K.; Smith, S. D.; Samseth, J.; Bockstaller, M. R.; Thompson, R. B.; Rasmussen, K. Ø.; Spontak, R. J. submitted to ...
105. Park, S. C .; Kim, B. J.; Hawker, C. J.; Kramer, E. J.; Bang, J.; Ha, J. S. *Macomolecules* **2007**, 40, 8119-8124.
106. Kim, B. J.; Fredrickson, G. H.; Hawker, C. J.; Kramer, E. J. *Langmuir* **2007**, 23, 7804-7809.
107. Smith, S. D.; Hamersky, M. W.; Bowman, M. K.; Rasmussion, K. Ø.; Spontak, R. *J. Langmuir* **2006**, 22, 6465-6468.

108. Warren, S. C.; Disalvo, F. J.; Wiesner, U.; *Nature Materials* **2007**, 6, 156-161.
109. Thompson, R. B.; Ginzburg, V. V.; Matsen, M. W.; Balazs, A. C. *Science* **2001**, 292, 2469-2472.
110. Pryamitsyn, V.; Ganesan, V. *Macromolecules* **2006**, 39, 8499-8510.
111. Lee, J. Y.; Thompson, R. B.; Jasnow, D.; Balazs, A. C. *Macromolecules* **2002**, 35, 4855-4858.
112. Lee, J. -Y.; Thompson, R. B.; Jasnow, D.; Balazs, A. C. *Phys. Rev. Lett.* **2002**, 89, 155503.
113. Reister, E.; Fredrickson, G. H. *J. Chem. Phys.* **2005**, 123, 214903.
114. Lee, B.; Lo, C. -T.; Seifert, S.; Rago, N. L. D.; Winans, R. E.; Thiyagarajan, P. *Macromolecules* **2007**, 40, 4232-4243.
115. Lo, C. -T.; Lee, B.; Winans, R. E.; Thiyagarajan, P. *Macromolecules* **2007**, 40, 614-647.
116. Lo, C. -T.; Lee, B.; Winans, R. E.; Thiyagarajan, P. *Macromolecules* **2006**, 39, 6318-6320.
117. Thompson, R. B.; Rasmussen, K. Ø.; Lookman, T. *Nano Lett.* **2004**, 4, 2455-2459.
118. Lo, C. -T.; Lee, B.; Pol, V. G.; Rago, N. L. D.; Seifert, S.; Winans, R. E.; Thiyagarajan, P. *Macromolecules* **2007**, 40, 8302-8310.
119. Chervanyov, A. I.; Balazs, A. C. *J. Chem. Phys.* **2003**, 119, 3529-2534.
120. Schultz, A. J.; Hall, C. K.; Genzer, J. *Macromolecules* **2005**, 38, 3007-3016.

121. Jain, A.; Gutmann, J. S.; Garcia, C. B. W.; Zhang, Y.; Tate, M. W.; Gruner, S. M.; Wiesner, U. *Macromolecules* **2002**, 35, 4862-4865.

1.8 List of Figure Captions

Figure 1.1 SEM images showing fracture surfaces of PS/SiO₂ nanocomposites. a) 15 wt% untreated SiO₂/PS nanocomposite. Nanoparticles reside inside voids indicating dewetting of PS from SiO₂ surfaces. b) 2wt% SiO₂-g-PS/PS nanocomposite. In contrast to the untreated surface, the particle surface of the SiO₂-g-PS is well adhered to the PS⁴⁶ (Scale bar = 200 nm).

Figure 1.2 TEM images of C₆₀ buckyballs in PMMA homopolymer self-assemble into large aggregates, small clusters, and anisotropic shapes which also include vesicles.

49

Figure 1.3 TEM images of aluminum NP in PS, demonstrating the dispersion of non-adsorbing NP in a polymer matrix as NP concentration increases. a) 5 wt% aluminum NP loading shows uniform dispersion of the aggregates on a micron-scale. b) 5 wt% aluminum NP loading shows that the aluminum NP cluster in large aggregates under a higher resolution, and that they are not completely dispersed at the nanoscale. c) At 30 wt% NP loading, the aggregates are larger and we can see their morphology.⁵³

Figure 1.4 Gold NP in PEO self-assembly. a) TEM image of Au surface functionalized NP in PEO at 0.4wt% PEO (materials are dissolved in water). b) DSC traces of (a) pure PEO and (b) PEO containing functionalized Au NP.⁵⁷

Figure 1.5 ESEM images of self-assembled hydrogels stimulated by pH. Negatively charged microgel particles swell at high pH and shrink and low pH. When subjected to

positively charged CdTe NP, they either self assemble into the core microgel particles (low pH) (a & b), or they phase separate from the swollen microgel particles (high pH) (c). This figure shows the two different morphologies observed, captured from ESEM (Scale bar = 5 μ m).⁴²

Figure 1.6 SCFT calculations on polymer-NP suspensions. These figures show the specific heat requirement in order for the NP form a network. a) Compares particle-polymer size ratio with increasing NP concentration b) Displays the phase behavior of the nanocomposites over time.⁶⁰

Figure 1.7 Sequence of 100 μ m x 100 μ m height and phase angle AFM images show the surface roughness of PS/poly vinyl methyl ether (PVME) thin film blends containing different sizes of clay layered silicates. The PVME has been washed away with methanol and the PS domains remain in these images. a) At $d_{NP} = 30$ nm, the spinodal domains appear pinned due to NP exfoliation in the blend. b) At $0.5 \mu\text{m} < d_{NP} < 1.0 \mu\text{m}$, a similar domain morphology appears as in part a, due to partial NP intercalation. c) When $d_{NP} = 5$ nm, there does not seem to be a change in the domain morphology compared to the neat PS/PVME blend.⁶⁵

Figure 1.8 TEM Images of PMMA/SAN blends, which show phase separation at 0 % NP loading (a-c) and 2 wt % silica NP (trimethyl silane functionalized) loading (d-f). (a-b) & (d-e) reflect the surface features. (c) & (f) show the interface morphology after removing PMMA. The hills in (a) & (d) measure ~ 10 nm high. The rings in (b) & (e) are

artifacts resulting from abrupt changes in height. The hills form from capillary driven flow of PMMA during early stage. The hills have been measured to have a higher modulus than the surrounding phase, representative of NP partitioning. The inset is the fast-Fourier Transform (FFT) of the interface morphology. These images show that PMMA domains become smaller as a result of NP partitioning to the PMMA. The kinetics of the phase separation also show that the phase separation is slowed down by the presence of the NP, due to the localization of NP at the domain/matrix interface reducing the driving force for PMMA flow.⁶⁶

Figure 1.9 AFM images of PMMA/SAN blends with 5 wt % silica NP loading of 2 different surface functionalities – trimethyl silane & PMMA grafts (P2K). a) Larger PMMA phase domains of MEK nanocomposites. b) Smaller PMMA phase domains of P2K nanocomposites, domains are stabilized by the localization of NP at the domain/matrix interface. c) MEK nanocomposite after long annealing time shows domain rupturing. d) Shows that P2K nanocomposites remain phase separated and stable at long annealing times.⁶⁸

Figure 1.10 UCST behavior of epoxy/PS blend containing epoxy functionalized NP. This figure highlights the cloud point temperature as a function of epoxy composition. Each plot varies with increasing NP loading: a) $\phi_p = 0.01$, b) $\phi_p = 0.04$, c) $\phi_p = 0.1$, d) $\phi_p = 0.18$, e) $\phi_p = 0$. As NP loading increases the two-phase region decreases. NP loading does not appear to have any effect on the location of the spinodal.⁶⁹

Figure 1.11 Phase map showing the magnitude of the stable region as a function of composition of homopolymer A in an AB binary homopolymer blend with $\chi_{AP} > 0$ & $\chi_{BP} > 0$ NP. Blue, Red, and Green lines represent $\chi_{AB} = 0.01, 0.0244,$ and $0.025,$ respectively. These data provide evidence that increasing the segregation between A and B homopolymers drastically decreases the stability of the blend. ($\phi_{NP} = 0.18$)⁷¹

Figure 1.12 CryoTEM imaging of the morphology of ternary blends of glycerol, amphiphilic block copolymer, and glycerol precursor-NP. (a) As the block copolymer concentration increases, the morphology of the particles changes from one large cubic particle with a disordered interior accompanied by vesicles to a mixture of vesicles, L_3 particles, and cubic particles with a disordered interior. At the highest concentration, there were only vesicles and L_3 particles. The diblock copolymer concentration influenced the size and number of cubic particles with a disordered interior. (b) Morphology of blends containing triblock copolymer with increasing lipid-mimetic anchors. At low hydrophobic asymmetry, foam-like partially fused unilamellar vesicle agglomerates are observed, with a disordered interior. As hydrophobicity increases, unilamellar vesicles and thread-like or band-like particles appear. The thread-like structures represent some sort of copolymer/GMO mixed micelles in an L_1 phase and the vesicles represent a dispersion of the lamellar phase in it. (Scale bar = 100 nm)⁷²

Figure 1.13 CDS model used to analyze the phase segregation in a homopolymer/block copolymer/NP blend of varying interaction strength. This figure

Figure 1.14 a) Density profiles of colloidal-polymer blends show the phase transitions, with increasing concentration of colloidal particles. (a) disordered liquid, (b) sparse square, (c) hexagonal (or mixed square-hexagonal), (d) sparse square, (e) cylindrical structures in plane. b) The phase diagram of the colloidal-polymer blend as a function of polymer grafting density and colloidal concentration. S₂: sparse square structure, M₂: hexagonal structure, C₂: cylindrical structure, S₃: three-layer spherical structure, CS₃: three-layer cylindrical-spherical mixed structure, C₃: three-layer cylindrical structure. Arrow represents the direction taken to generate Fig 14a. ⁸³

Figure 1.15 An illustration of how careful specification of interaction behavior and temperature play a role in developing a well-positioned A-phase microdroplet between two asperities (two surfaces). Red represents A-phase and Dark Blue represents the B-phase. The NP are in white. ⁸⁴

Figure 1.16 Neutron scattering samples of PEO-PPO-PEO triblock copolymer micelles and silica NP are shown. It has been demonstrated that adding more silica NP to the

PEO-water matrix causes a polymer phase transition from face-centered-cubic (FCC) to body-centered-cubic (BCC). The triblock copolymer concentration in water is 30%.⁹⁴

Figure 1.17 Dependence of the order-disorder transition temperature (T_{ODT}) measured by isochronal dynamic rheology on nanoparticle concentration (ϕ_p) for clustered nanoparticles with $-OH$, $-C8$, and $-MA$ surface functionalities.¹⁰⁴

Figure 1.18 Bi-functionalized NP (\sim amphiphilic surfactants) induce a phase transition in polystyrene-*b*-poly-2-vinylpyridine (PS-*b*-P2VP) diblock copolymer from lamellar to the double gyroid (Ia3d space group) bicontinuous morphology. TEM images show PS-partially coated NP volume fractions (ϕ_p): (a) 0.04, (b) 0.07, (c) 0.09, and (d) 0.28. The scale bar is 100 nm. A well ordered lamellar nanostructure can be observed at 4 % loading, while a dramatic change in the morphology occurs at 9 % loading (bicontinuous).¹⁰⁶

Figure 1.19 SST was used to investigate the importance of entropy and enthalpy on a diblock copolymer, containing A-selective bi-disperse NP. (a) 2D & 3D probability density profiles of symmetric diblock copolymer, displaying a cylindrical morphology due to the entropic effects of the small NP ($R2 = 0.1R0$). The large NP ($R1 = 0.2R0$) localize at the center of the A-microphase cylinders. (b) The free energy contribution of translational entropy (black), enthalpy (red), and steric interactions (blue). This shows that small particles have the potential for more steric interactions and translational entropy combats it by allowing them to spread to energetically unfavorable B. The inset demonstrates that the larger particles are located in a different microphase from most of

the small particles, even though they have been tailored to have the same attractive interaction towards the A-block.¹¹²

Figure 1.20 PS-coated Au NP in PS-*b*-P2VP asymmetric ($\phi_{PS} < 0.5$) diblock copolymer show hexagonal cylinder disordering as NP concentration increases, due to increased surface roughness between NP and PS interfaces. (a) TEM data at $\phi_p = 0.09$; $\phi_p = 0.27$. (b) Small Angle X-Ray Scattering (SAXS) data shows a disappearing of the hexagonally-closed-packed cylinder peak positions as NP concentration increases.¹¹⁸

Figure 1.21 SCFT/DFT calculations show how selective NP concentration and NP geometry can affect the ODT and the microphase stability of a diblock copolymer. (a) Critical value of the segregation factor (ODT) plotted as a function of reduced particle radius. ϕ is the volume fraction of NP. This plot shows how increasing NP concentration causes the ODT to decrease. (b) Critical value of the segregation factor (ODT) is plotted as a function of effective radius. As the aspect-ratio of the NP becomes large compared to the polymer brush length (NP surface area increases), the ODT increases. It shows that NP with a high aspect ratio exhibit the most change in the ODT and the microphase stability of the copolymer.¹¹⁹

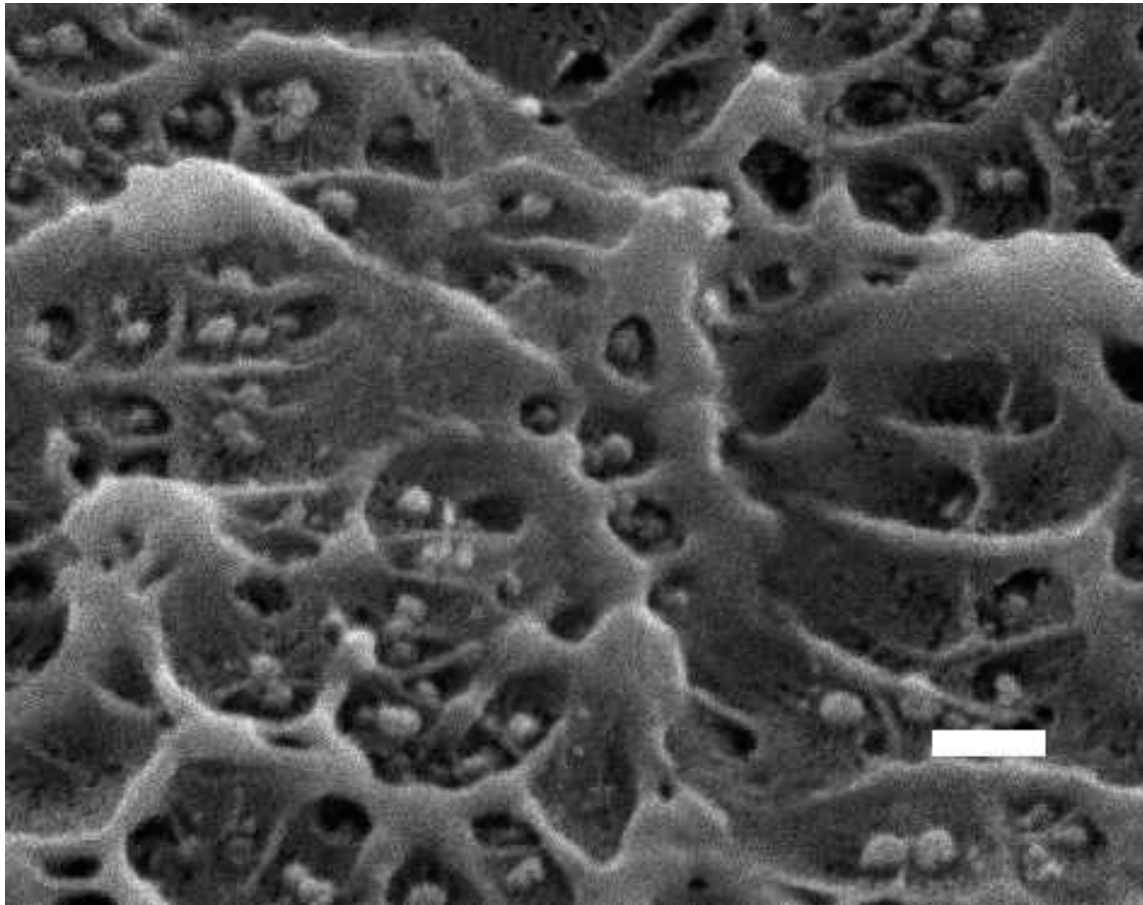


Figure 1.1. SEM images showing fracture surfaces of PS/SiO₂ nanocomposites. a) 15 wt% untreated SiO₂/PS nanocomposite. Nanoparticles reside inside voids indicating dewetting of PS from SiO₂ surfaces.⁴⁶

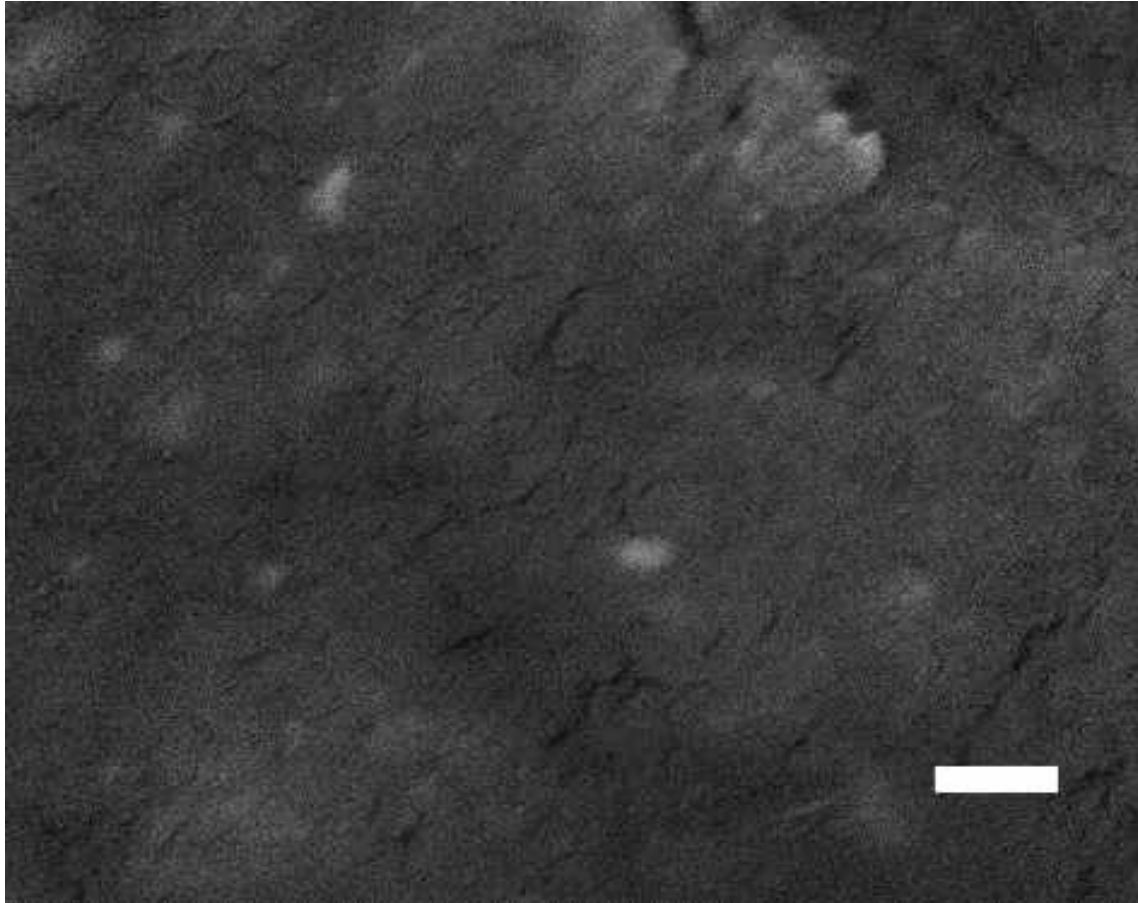


Figure 1.1b. SEM images showing fracture surfaces of PS/SiO₂ nanocomposites. b) 2wt% SiO₂-g-PS/PS nanocomposite. In contrast to the untreated surface, the particle surface of the SiO₂-g-PS is well adhered to the PS⁴⁵ (Scale bar = 200 nm).⁴⁶

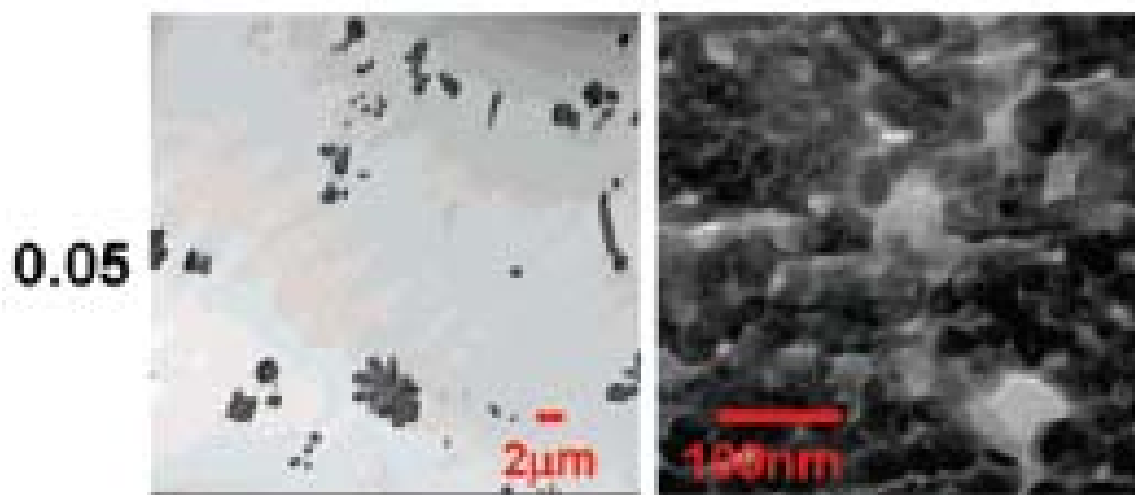


Figure 1.2. TEM images of C_{60} buckyballs in PMMA homopolymer self-assemble into large aggregates, small clusters, and anisotropic shapes which also include vesicles.⁴⁹

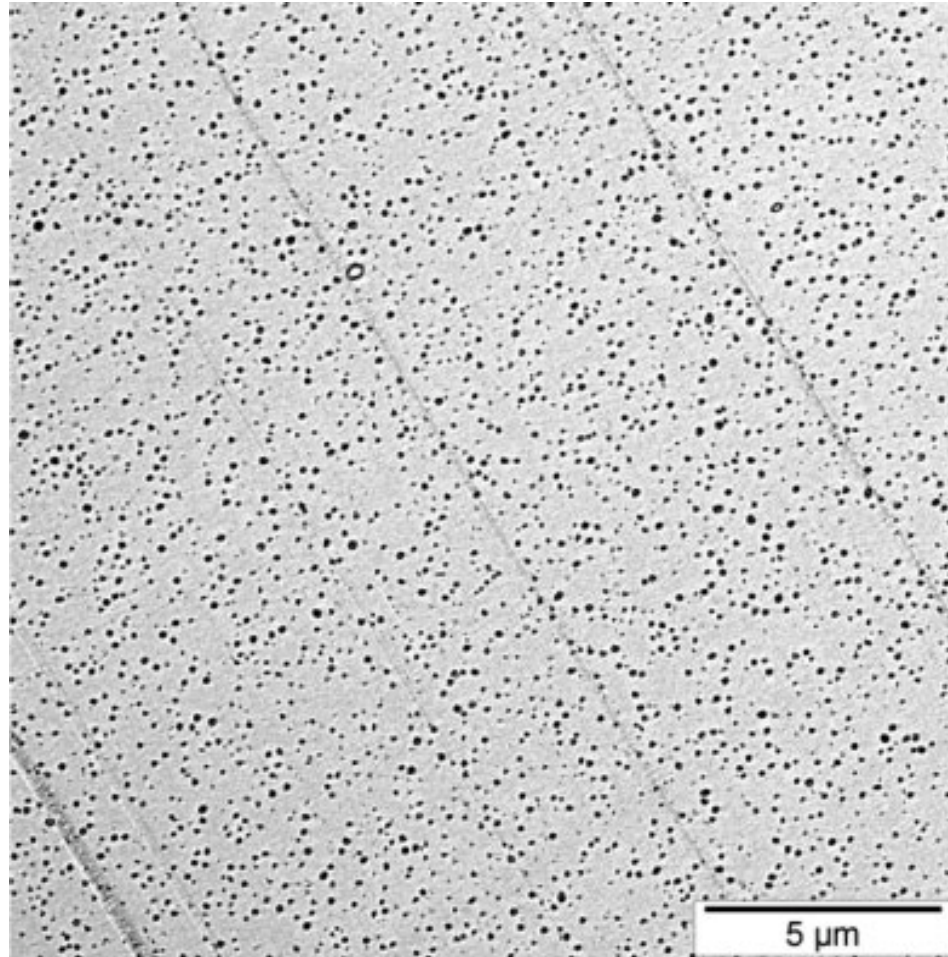


Figure 1.3. TEM images of aluminum NP in PS, demonstrating the dispersion of non-adsorbing NP in a polymer matrix as NP concentration increases. a) 5 wt% aluminum NP loading shows uniform dispersion of the aggregates on a micron-scale.⁵³

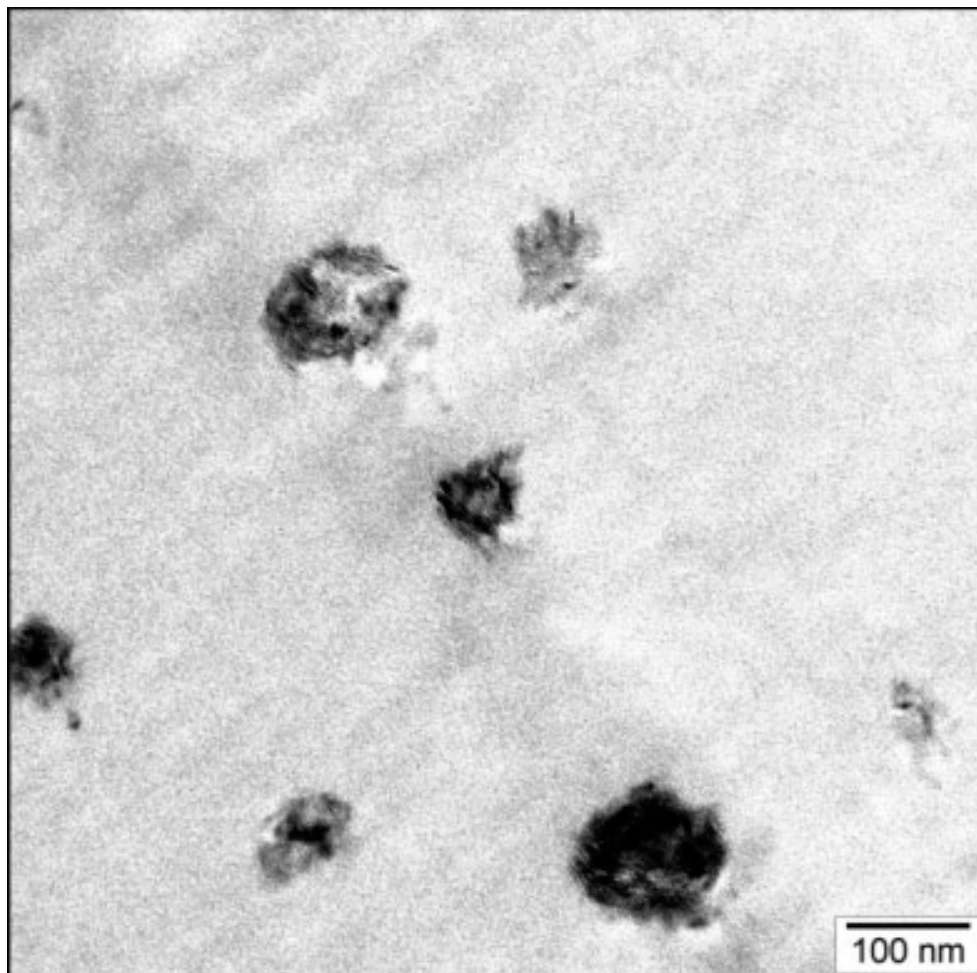


Figure 1.3b. TEM images of aluminum NP in PS, demonstrating the dispersion of non-adsorbing NP in a polymer matrix as NP concentration increases. b) 5 wt% aluminum NP loading shows that the aluminum NP cluster in large aggregates under a higher resolution, and that they are not completely dispersed at the nanoscale.⁵³

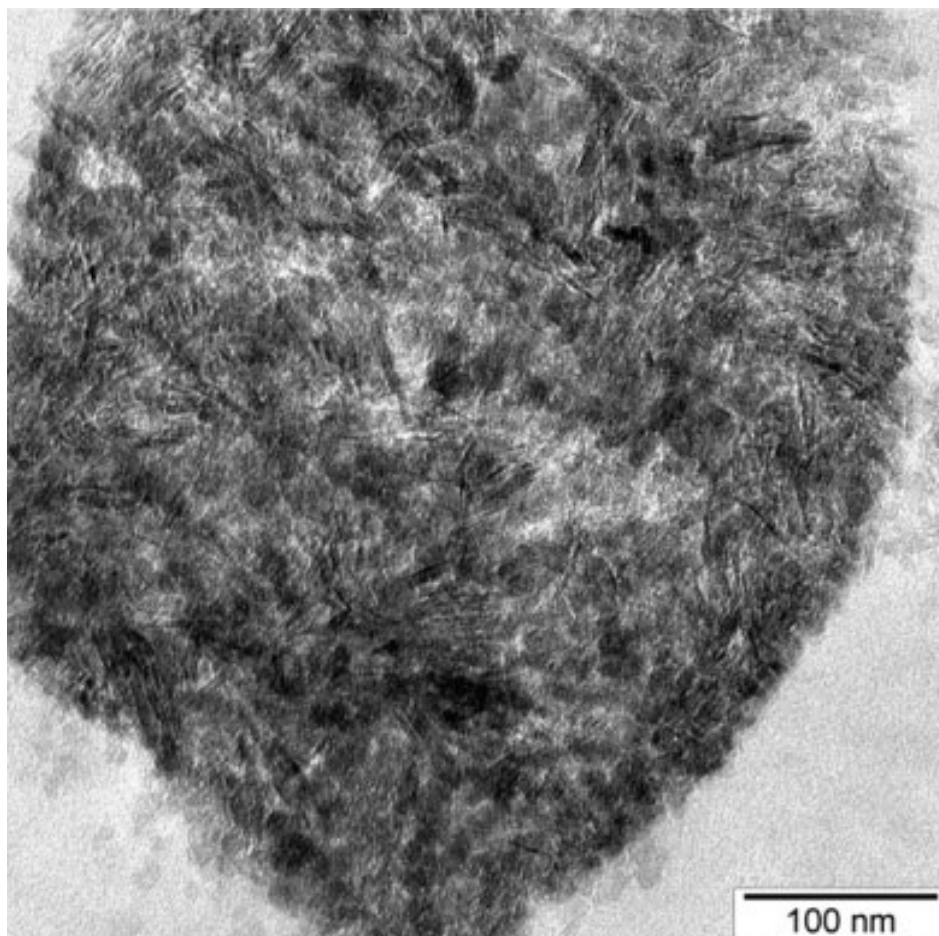


Figure 1.3c. TEM images of aluminum NP in PS, demonstrating the dispersion of non-adsorbing NP in a polymer matrix as NP concentration increases. c) At 30 wt⁰% NP loading, the aggregates are larger and we can see their morphology.⁵³

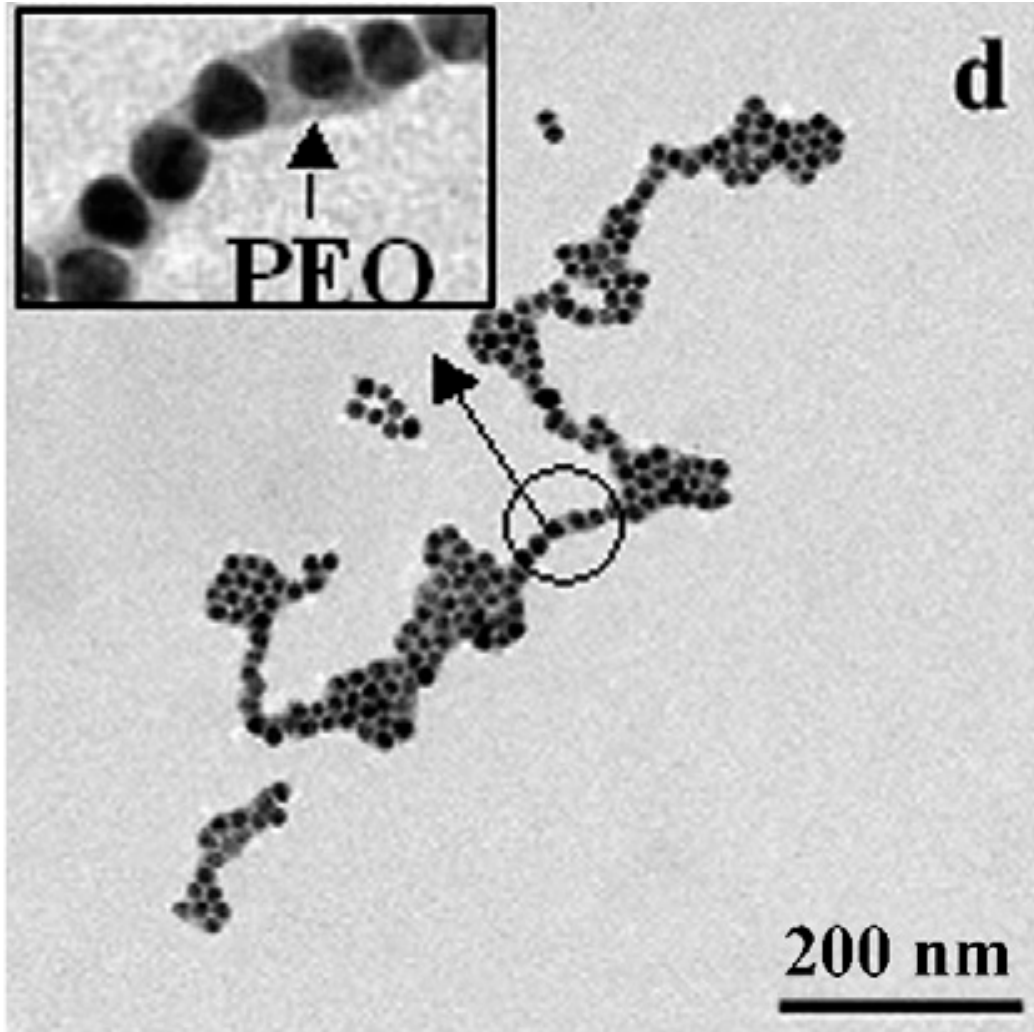


Figure 1.4. Gold NP in PEO self-assembly. a) TEM image of Au surface functionalized NP in PEO at 0.4wt% PEO (materials are dissolved in water).⁵⁷

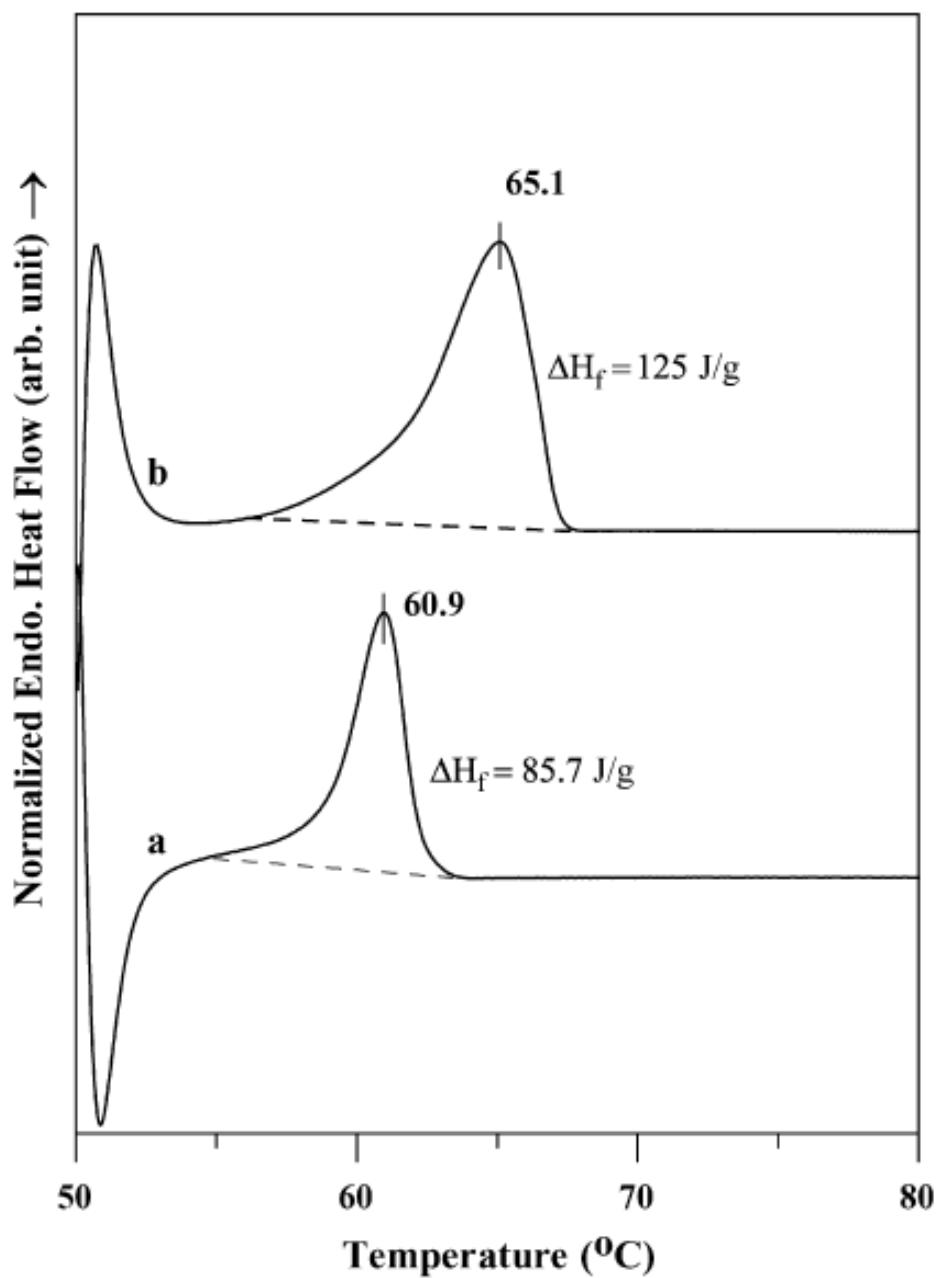


Figure 1.4b. Gold NP in PEO self-assembly. b) DSC traces of (a) pure PEO and (b) PEO containing functionalized Au NP.⁵⁷

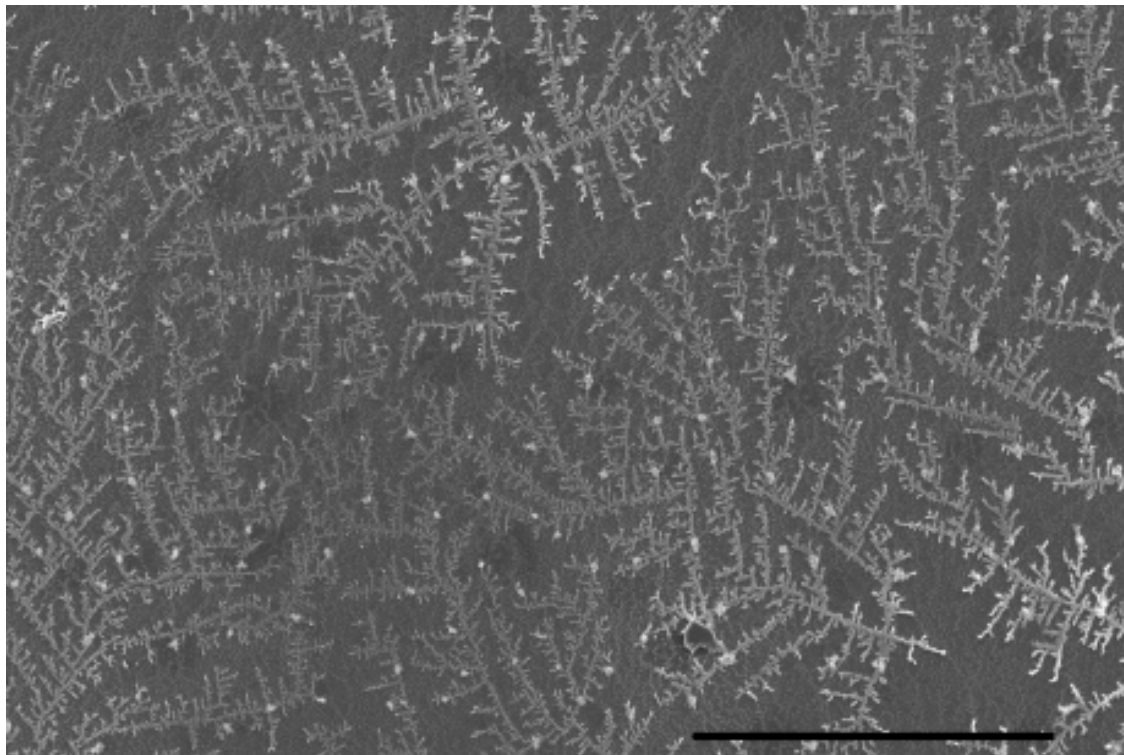


Figure 1.5. ESEM images of self-assembled hydrogels stimulated by pH. Negatively charged microgel particles swell at high pH and shrink and low pH. When subjected to positively charged CdTe NP, they either self assemble into the core microgel particles (low pH) (a & b), or they phase separate from the swollen microgel particles (high pH) (c). This figure shows the two different morphologies observed, captured from ESEM (Scale bar = 5 μ m).⁴²

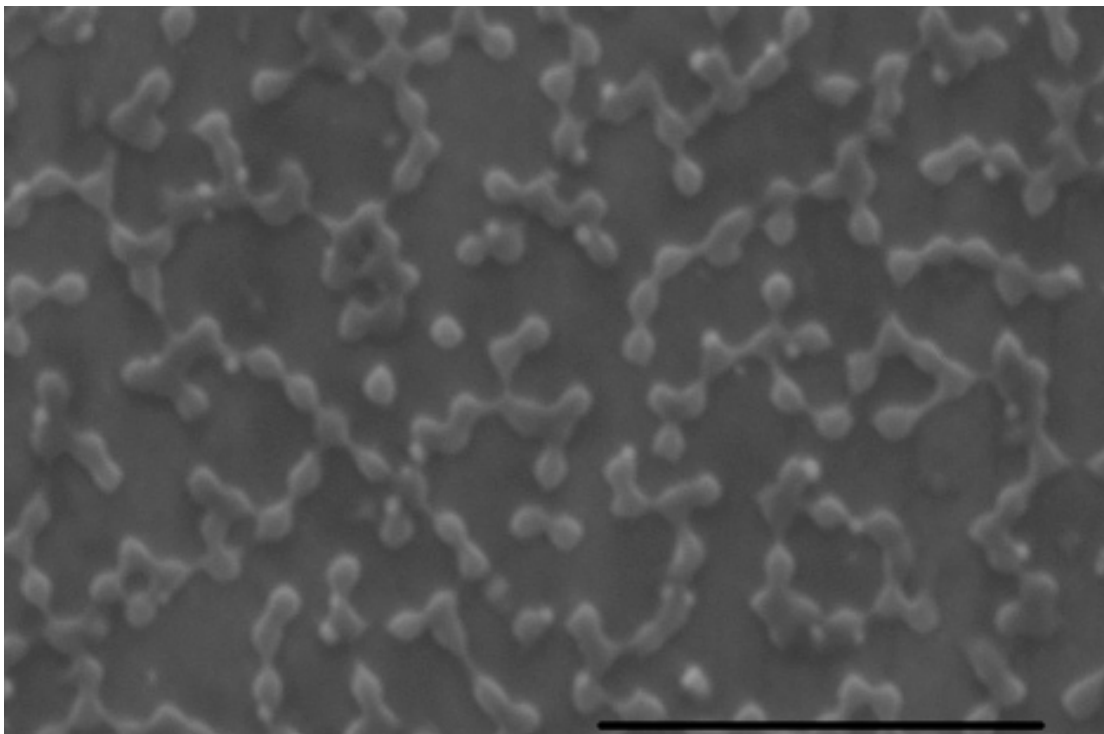


Figure 1.5b. ESEM images of self-assembled hydrogels stimulated by pH. Negatively charged microgel particles swell at high pH and shrink and low pH. When subjected to positively charged CdTe NP, they either self assemble into the core microgel particles (low pH) (a & b), or they phase separate from the swollen microgel particles (high pH) (c). This figure shows the two different morphologies observed, captured from ESEM (Scale bar = 5 μ m).⁴²

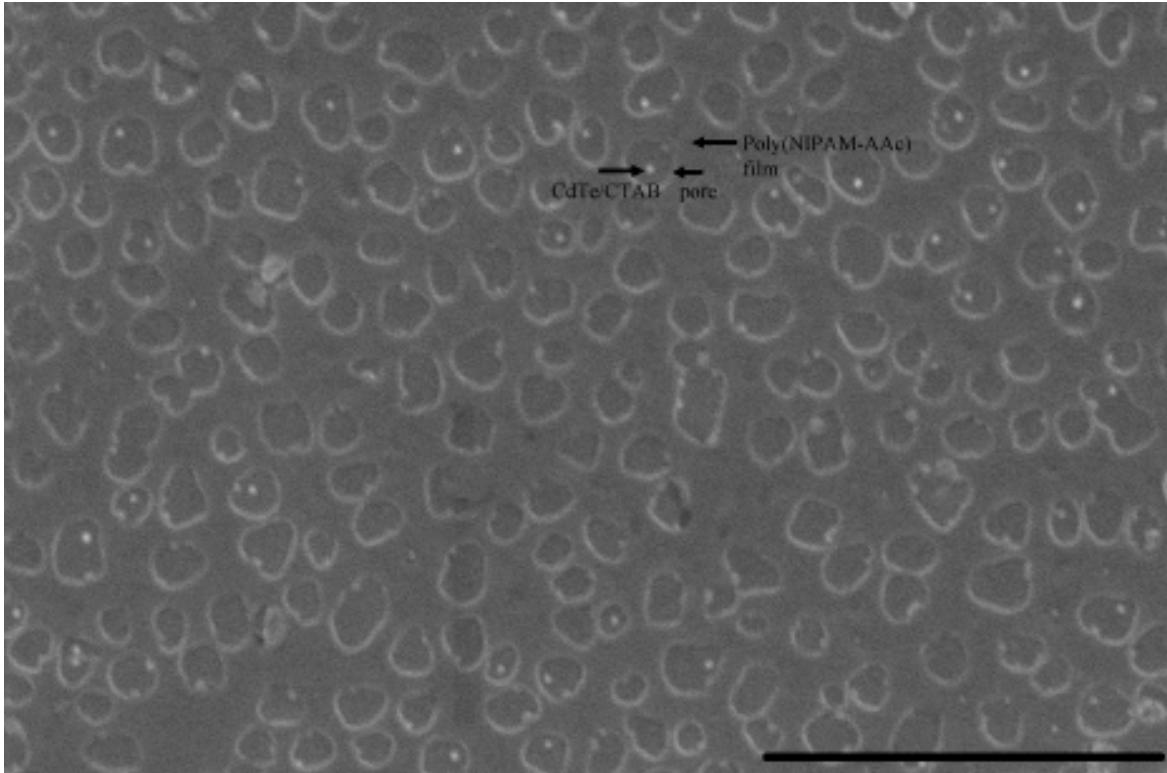


Figure 1.5c. ESEM images of self-assembled hydrogels stimulated by pH. Negatively charged microgel particles swell at high pH and shrink and low pH. When subjected to positively charged CdTe NP, they either self assemble into the core microgel particles (low pH) (a & b), or they phase separate from the swollen microgel particles (high pH) (c). This figure shows the two different morphologies observed, captured from ESEM (Scale bar = 5 μ m).⁴²

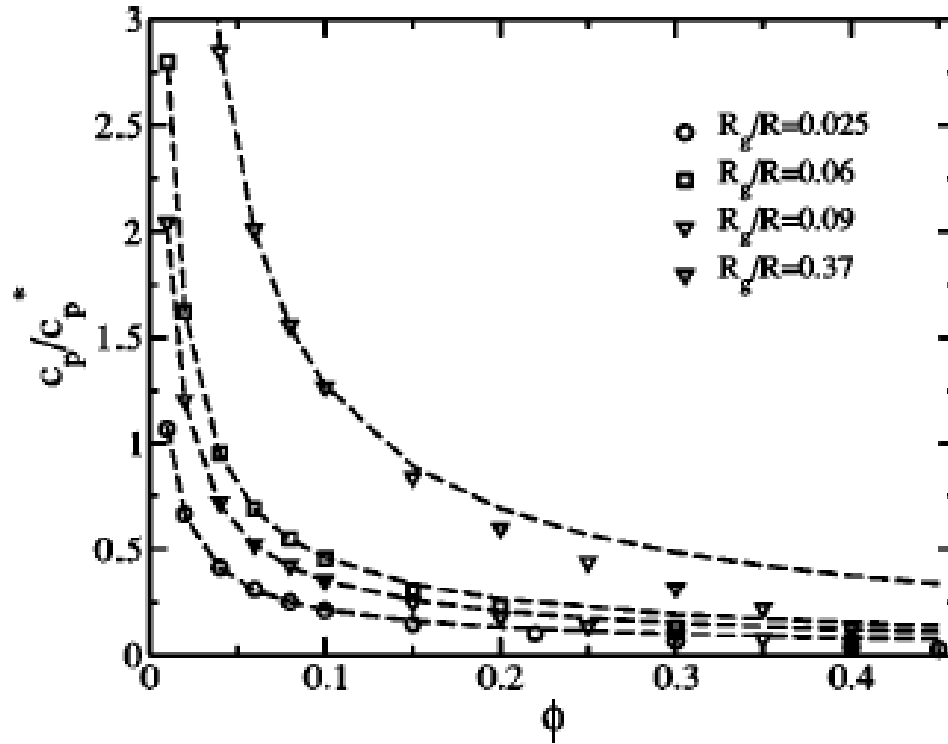


Figure 1.6. SCFT calculations on polymer-NP suspensions. These figures show the specific heat requirement in order for the NP form a network. a) Compares particle-polymer size ratio with increasing NP concentration.⁶⁰

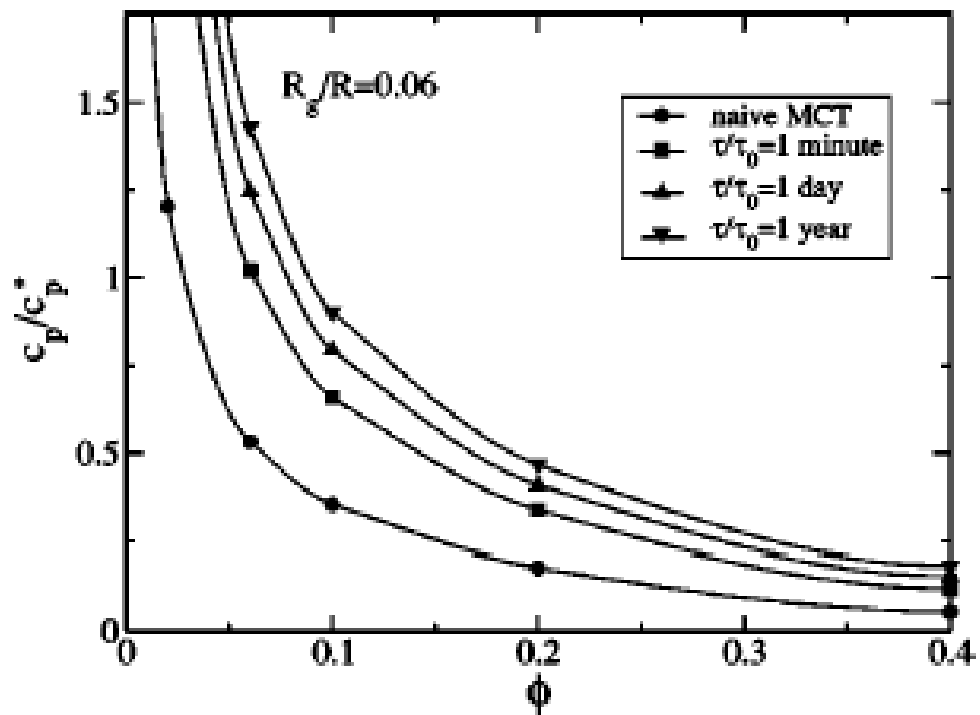


Figure 1.6b. SCFT calculations on polymer-NP suspensions. These figures show the specific heat requirement in order for the NP form a network. b) Displays the phase behavior of the nanocomposites over time.⁶⁰

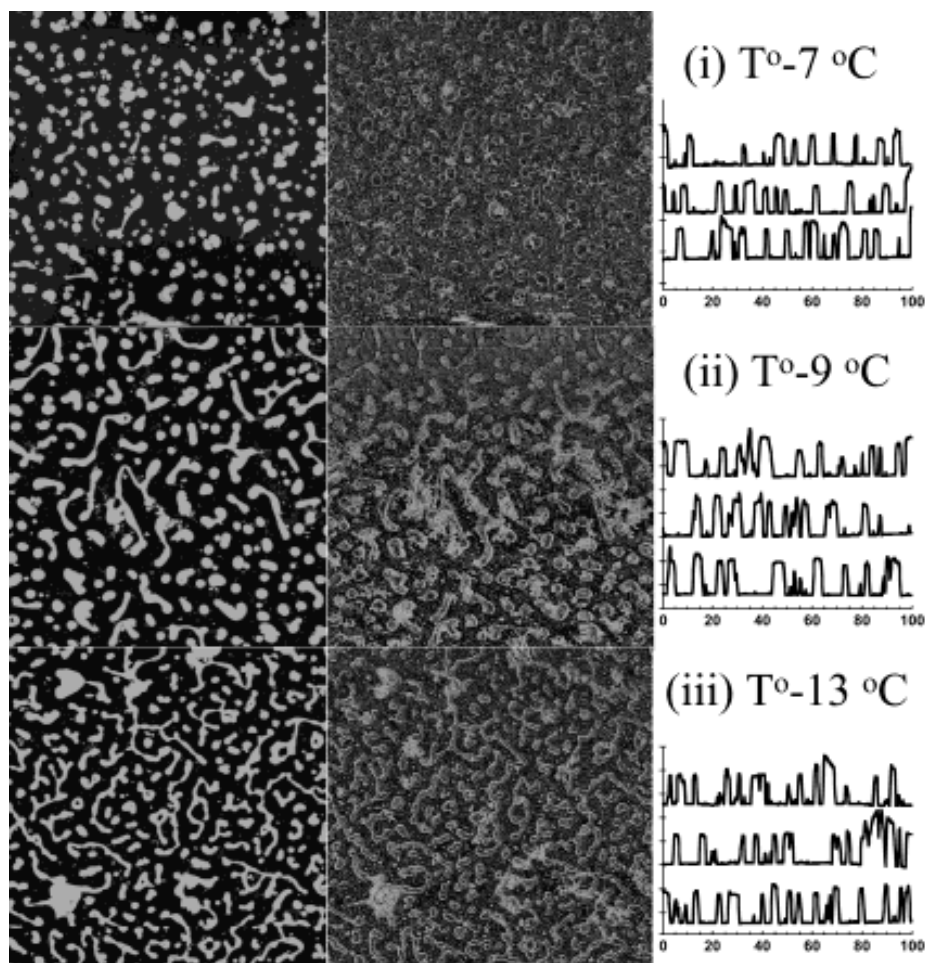


Figure 1.7. Sequence of 100 μm x 100 μm height and phase angle AFM images show the surface roughness of PS/poly vinyl methyl ether (PVME) thin film blends containing different sizes of clay layered silicates. The PVME has been washed away with methanol and the PS domains remain in these images. a) At $d_{\text{NP}} = 30$ nm, the spinodal domains appear pinned due to NP exfoliation in the blend.⁶⁵

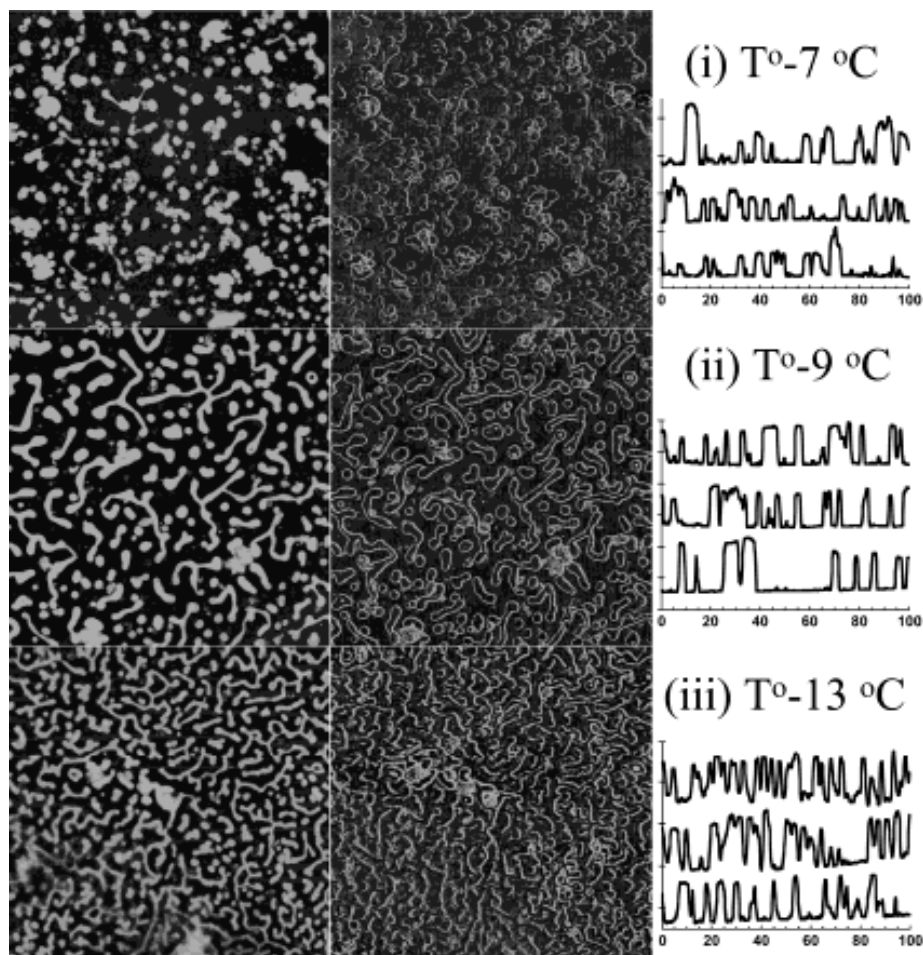


Figure 1.7b. Sequence of $100\ \mu\text{m} \times 100\ \mu\text{m}$ height and phase angle AFM images show the surface roughness of PS/poly vinyl methyl ether (PVME) thin film blends containing different sizes of clay layered silicates. The PVME has been washed away with methanol and the PS domains remain in these images. b) At $0.5\ \mu\text{m} < d_{\text{NP}} < 1.0\ \mu\text{m}$, a similar domain morphology appears as in part a, due to partial NP intercalation.⁶⁵

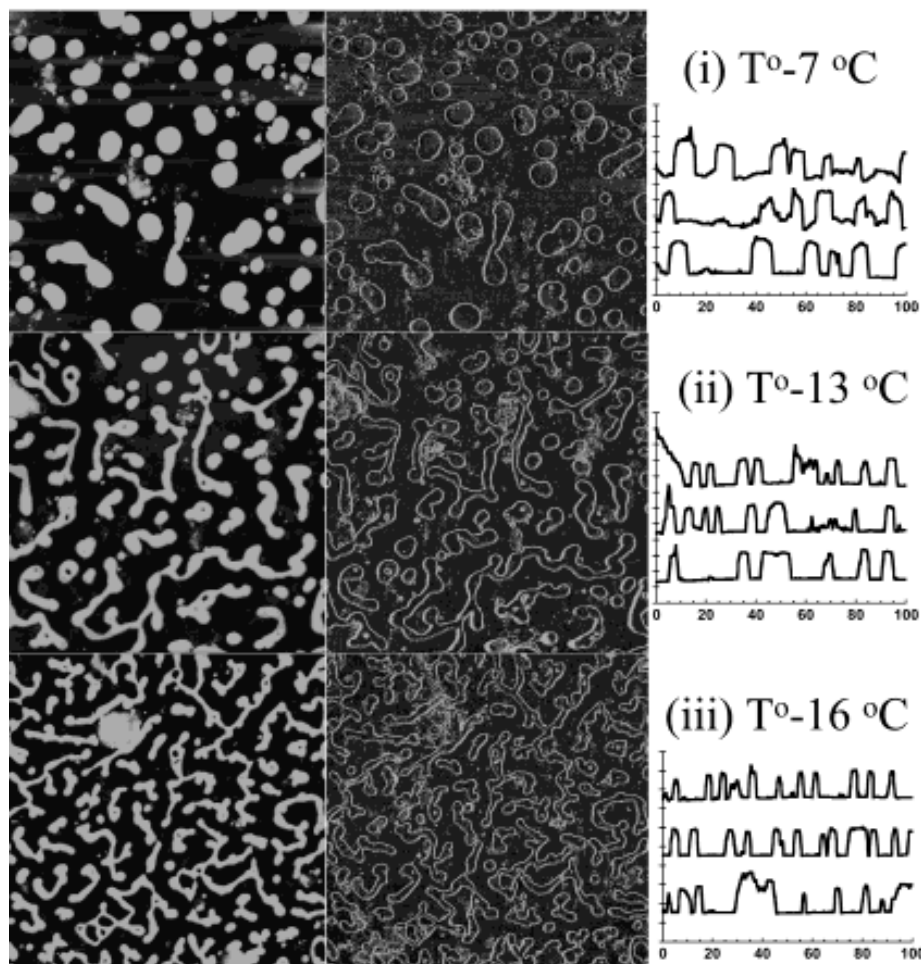


Figure 1.7c. Sequence of 100 μm x 100 μm height and phase angle AFM images show the surface roughness of PS/poly vinyl methyl ether (PVME) thin film blends containing different sizes of clay layered silicates. The PVME has been washed away with methanol and the PS domains remain in these images. c) When $d_{\text{NP}} = 5 \text{ nm}$, there does not seem to be a change in the domain morphology compared to the neat PS/PVME blend.⁶⁵

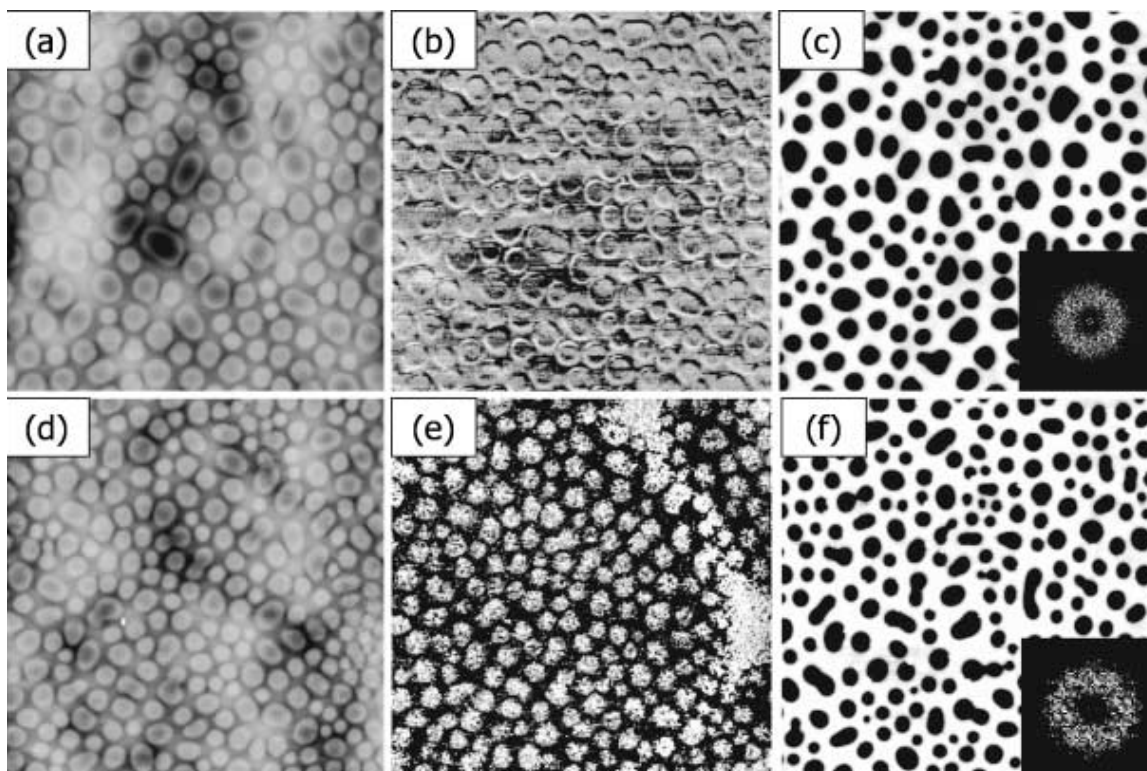


Figure 1.8. TEM Images of PMMA/SAN blends, which show phase separation at 0 % NP loading (a-c) and 2 wt % silica NP (trimethyl silane functionalized) loading (d-f). (a-b) & (d-e) reflect the surface features. (c) & (f) show the interface morphology after removing PMMA. The hills in (a) & (d) measure ~ 10 nm high. The rings in (b) & (e) are artifacts resulting from abrupt changes in height. The hills form from capillary driven flow of PMMA during early stage. The hills have been measured to have a higher modulus than the surrounding phase, representative of NP partitioning. The inset is the fast-Fourier Transform (FFT) of the interface morphology. These images show that PMMA domains become smaller as a result of NP partitioning to the PMMA. The kinetics of the phase separation also show that the phase separation is slowed down by the presence of the NP, due to the localization of NP at the domain/matrix interface reducing the driving force for PMMA flow.⁶⁶

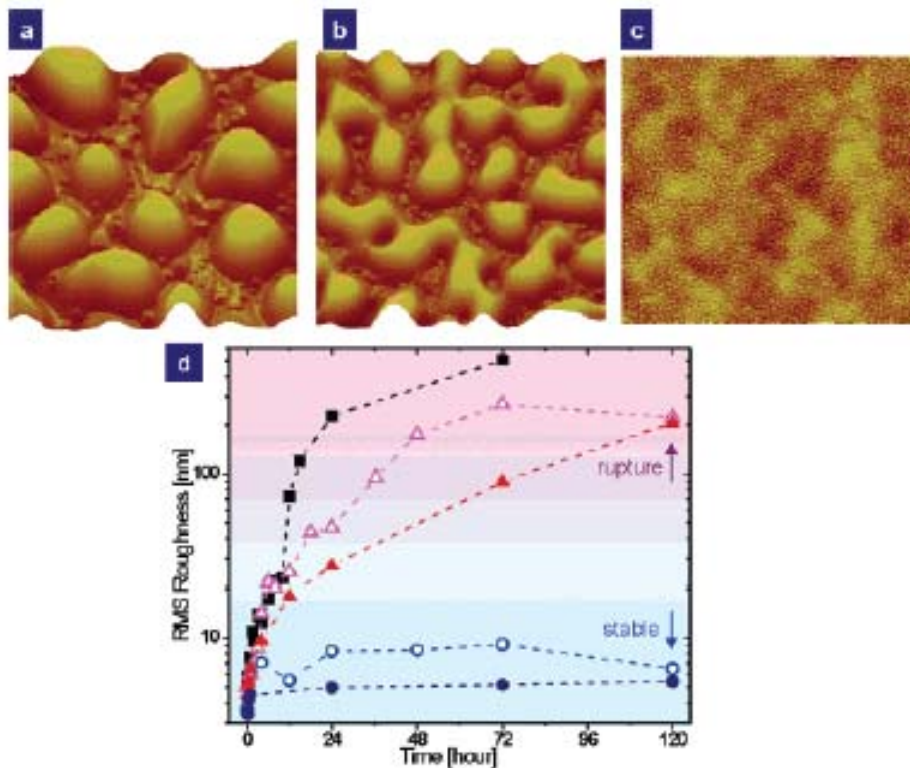


Figure 1.9. SFT was used to investigate the importance of entropy and enthalpy on a diblock copolymer, containing A-selective bi-disperse NP. (a) 2D & 3D probability density profile of symmetric diblock copolymer, displaying a cylindrical morphology due to the entropic effects of the small NP ($R_2 = 0.1R_0$). The large NP ($R_1 = 0.2R_0$) localize at the center of the A-microphase cylinders. (b) The free energy contribution of translational entropy (black), enthalpy (red), and steric interactions (blue). This shows that small particles have the potential for more steric interactions and translational entropy combats it by allowing them to spread to energetically unfavorable B. The inset demonstrates that the larger particles are located in a different microphase from most of the small particles, even though they have been tailored to have the same attractive interaction towards the A-block.⁶⁸

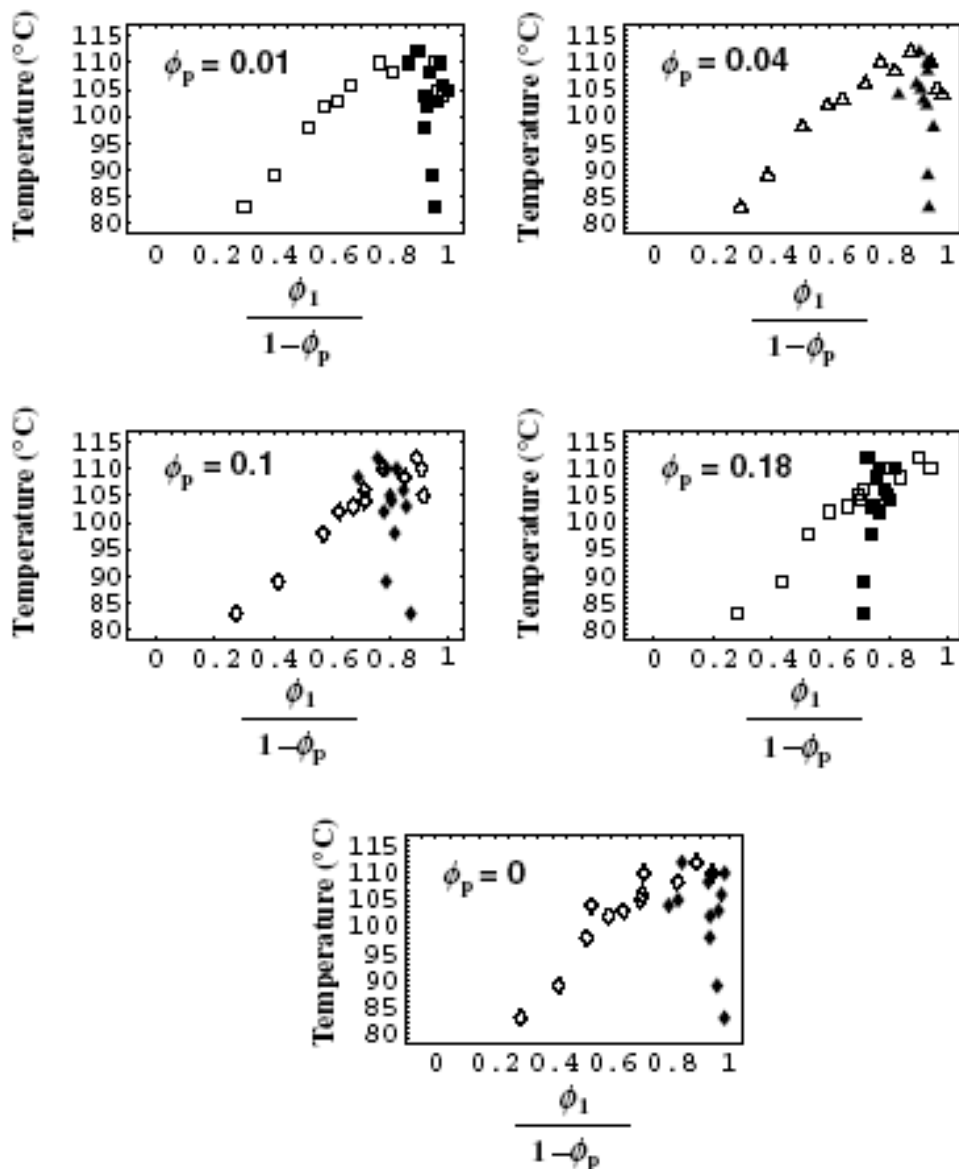


Figure 1.10 UCST behavior of epoxy/PS blend containing epoxy functionalized NP. This figure highlights the cloud point temperature as a function of epoxy composition. Each plot varies with increasing NP loading: a) $\phi_p = 0.01$, b) $\phi_p = 0.04$, c) $\phi_p = 0.1$, d) $\phi_p = 0.18$, e) $\phi_p = 0$. As NP loading increases the two-phase region decreases. NP loading does not appear to have any effect on the location of the spinodal.⁶⁹

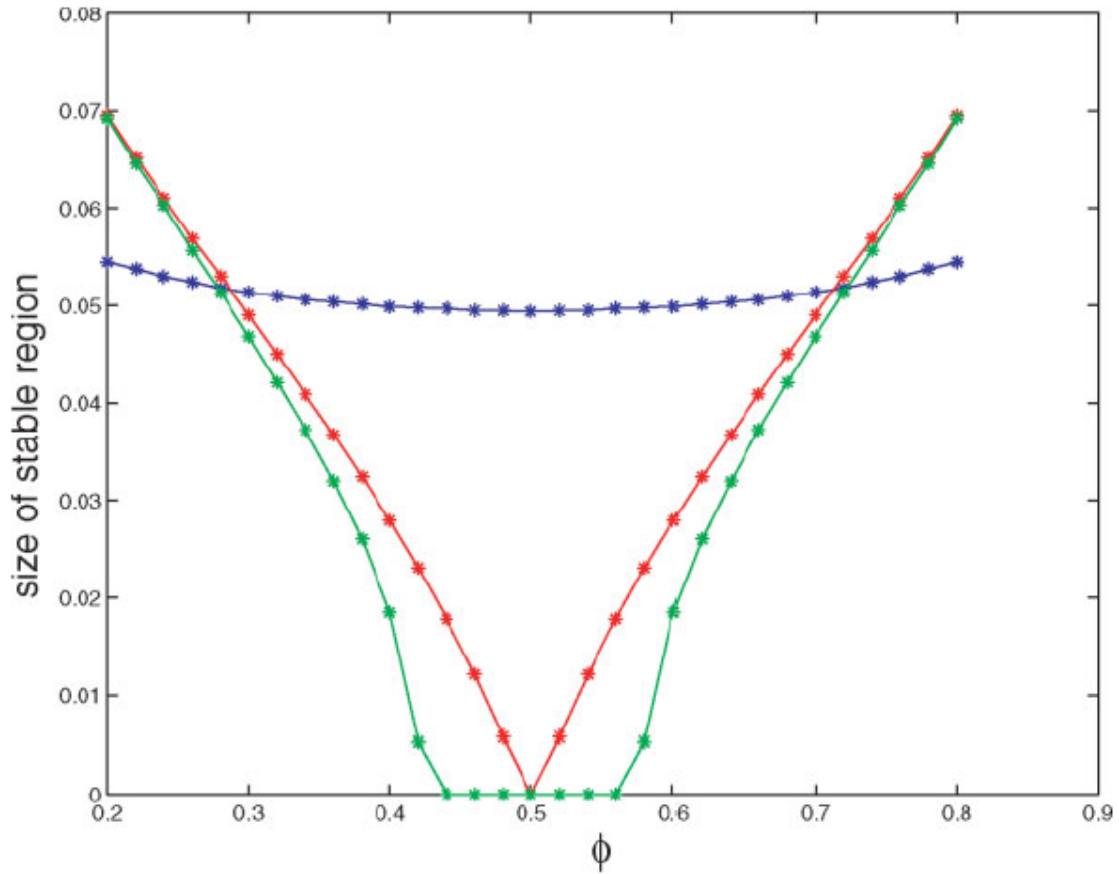


Figure 1.11. Phase map showing the magnitude of the stable region as a function of composition of homopolymer A in an AB binary homopolymer blend with $\chi_{AP} > 0$ & $\chi_{BP} > 0$ NP. Blue, Red, and Green lines represent $\chi_{AB} = 0.01, 0.0244,$ and $0.025,$ respectively. These data provide evidence that increasing the segregation between A and B homopolymers drastically decreases the stability of the blend. ($\phi_{NP} = 0.18$)⁷¹

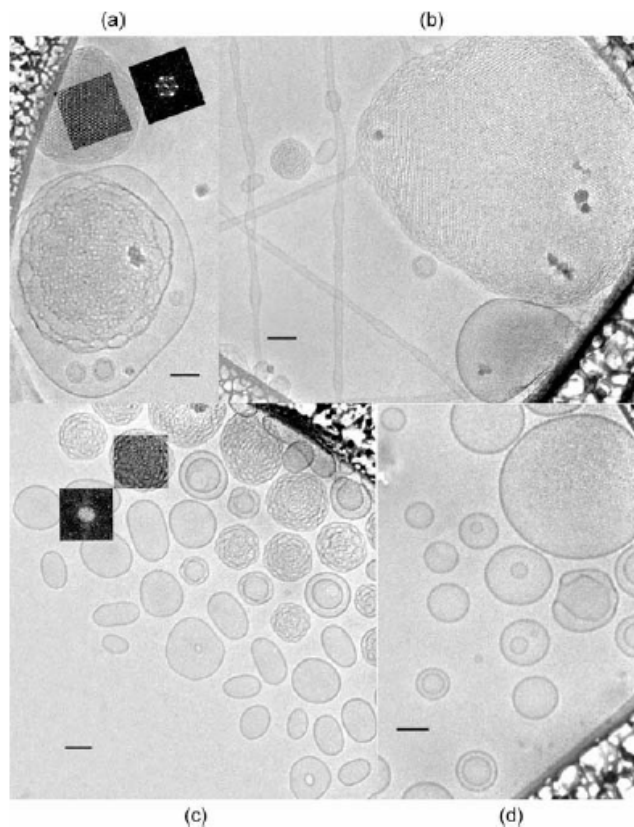


Figure 1.12. CryoTEM imaging of the morphology of ternary blends of glycerol, amphiphilic block copolymer, and glycerol precursor-NP. (a) As the block copolymer concentration increases, the morphology of the particles changes from one large cubic particle with a disordered interior accompanied by vesicles to a mixture of vesicles, L_3 particles, and cubic particles with a disordered interior. At the highest concentration, there were only vesicles and L_3 particles. The diblock copolymer concentration influenced the size and number of cubic particles with a disordered interior.⁷²

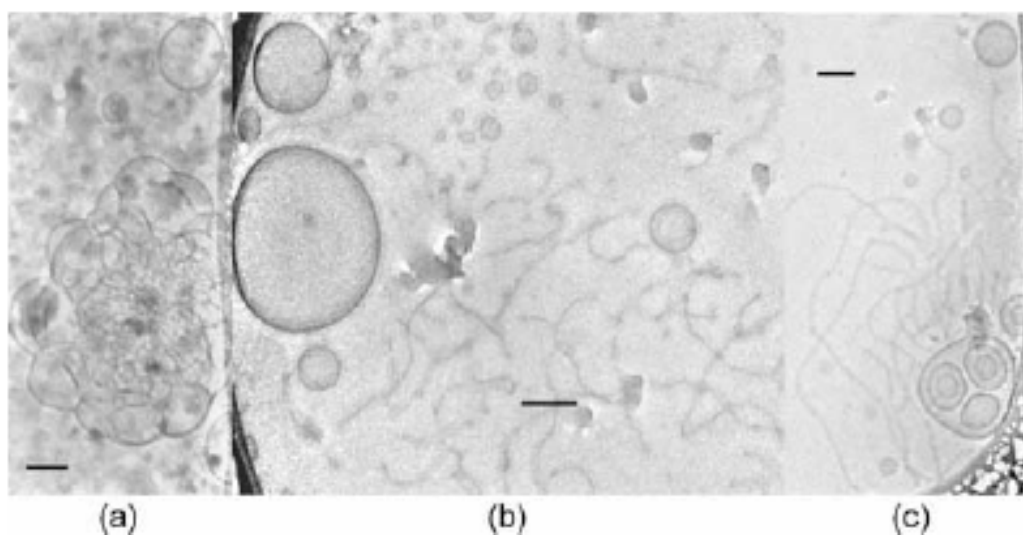


Figure 1.12b. CryoTEM imaging of the morphology of ternary blends of glycerol, amphiphilic block copolymer, and glycerol precursor-NP. (b) Morphology of blends containing triblock copolymer with increasing lipid-mimetic anchors. At low hydrophobic asymmetry, foam-like partially fused unilamellar vesicle agglomerates are observed, with a disordered interior. As hydrophobicity increases, unilamellar vesicles and thread-like or band-like particles appear. The thread-like structures represent some sort of copolymer/GMO mixed micelles in an L_1 phase and the vesicles represent a dispersion of the lamellar phase in it. (Scale bar = 100 nm)⁷²

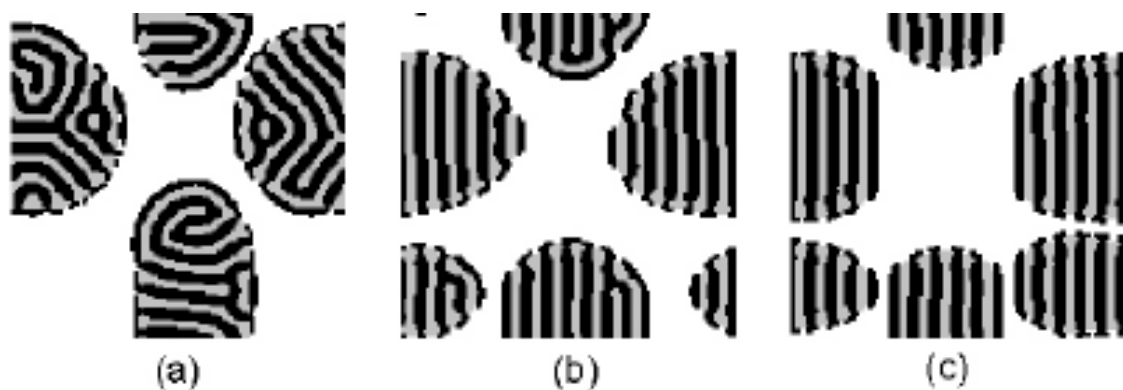


Figure 1.13. CDS model used to analyze the phase segregation in a homopolymer/block copolymer/NP blend of varying interaction strength. This figure shows how the interaction between the NP and one of the blocks in the copolymer affects the microphase separation which affects the macrophase separation of the blend. The NP are not pictured. The block copolymer is represented by the black and gray strips and the white region is the homopolymer. As NP-block copolymer interaction strength increases from a) 0.000001, b) 0.008, to c) 0.028, the block copolymer phase domains increase in long-range-order.⁷⁴

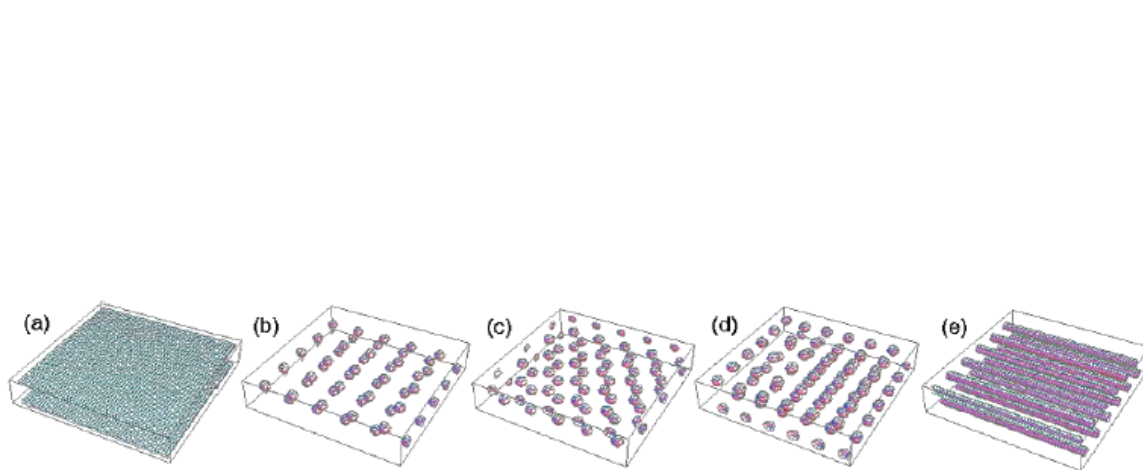


Figure 1.14. a) Density profiles of colloidal-polymer blends show the phase transitions, with increasing concentration of colloidal particles. (a) disordered liquid, (b) sparse square, (c) hexagonal (or mixed square-hexagonal), (d) sparse square, (e) cylindrical structures in plane.⁸³

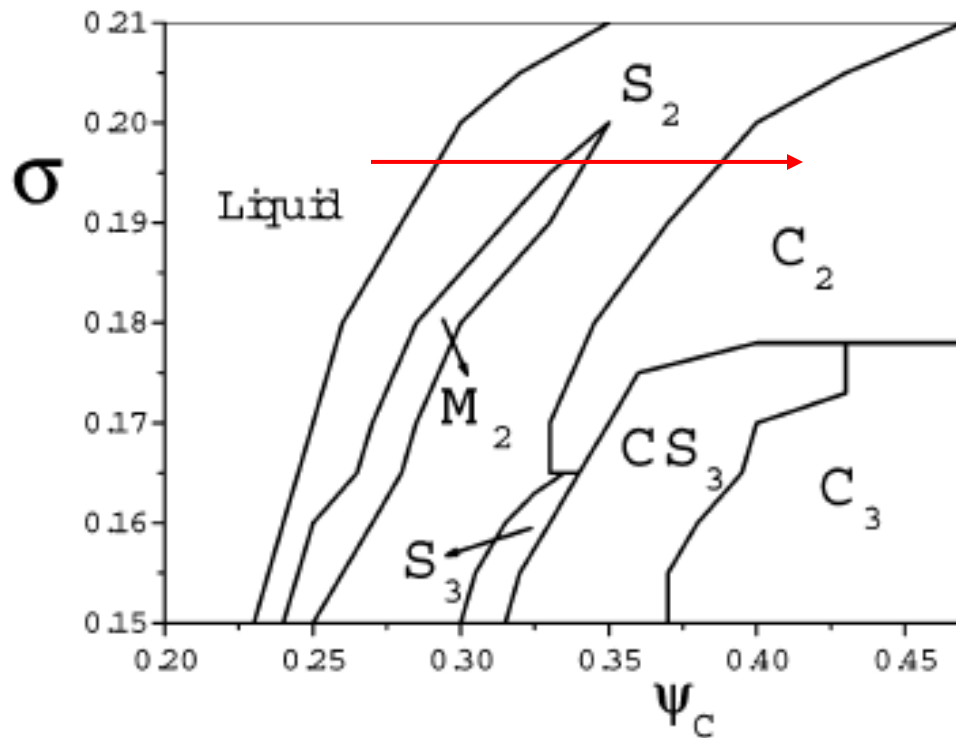


Figure 1.14b. b) The phase diagram of the colloidal-polymer blend as a function of polymer grafting density and colloidal concentration. S₂: sparse square structure, M₂: hexagonal structure, C₂: cylindrical structure, S₃: three-layer spherical structure, CS₃: three-layer cylindrical-spherical mixed structure, C₃: three-layer cylindrical structure. Arrow represents the direction taken to generate Fig 14a.⁸³

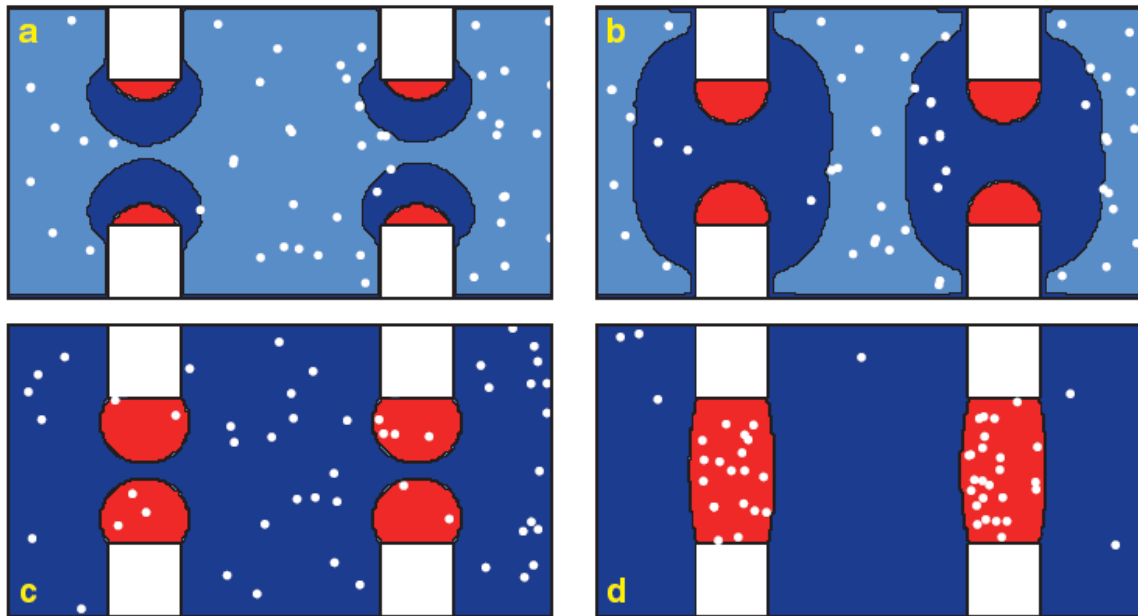


Figure 1.15. An illustration of how careful specification of interaction behavior and temperature play a role in developing a well-positioned A-phase microdroplet between two asperities (two surfaces). Red represents A-phase and Dark Blue represents the B-phase. The NP are in white.⁸⁴

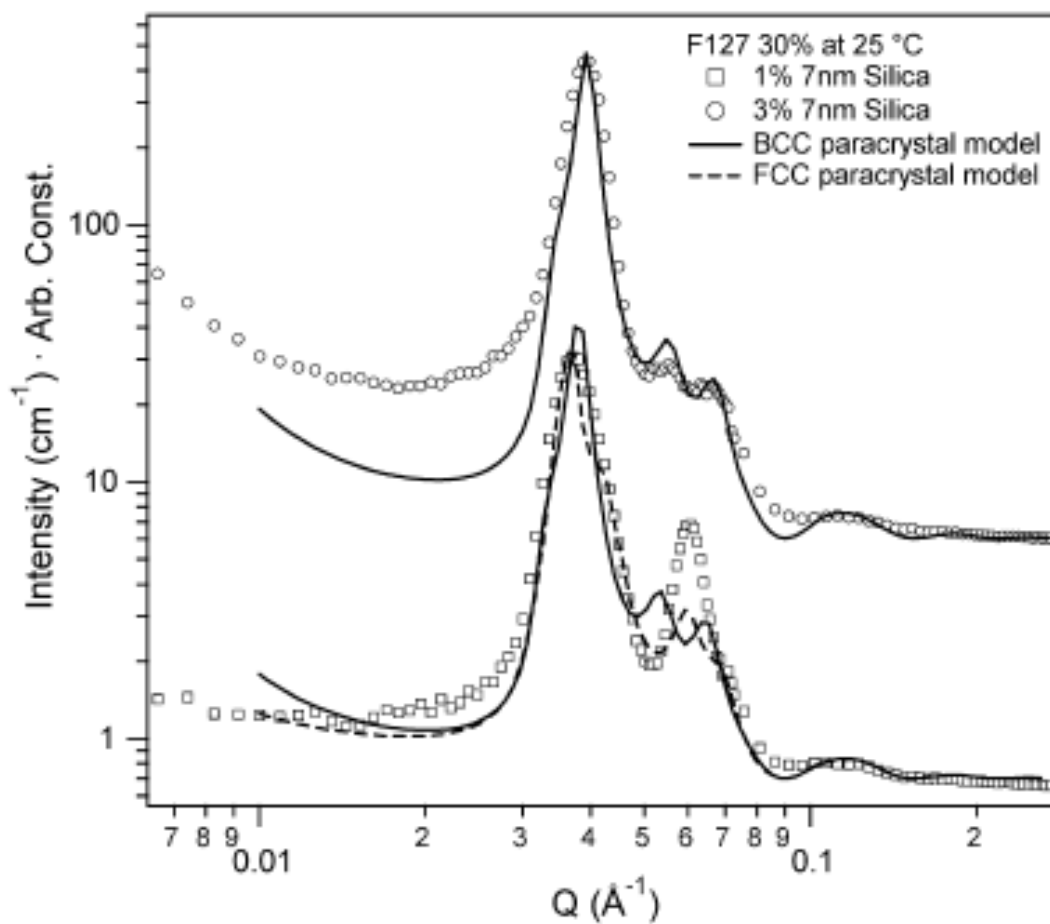


Figure 1.16. Neutron scattering samples of PEO-PPO-PEO triblock copolymer micelles and silica NP are shown. It has been demonstrated that adding more silica NP to the PEO-water matrix causes a polymer phase transition from face-centered-cubic (FCC) to body-centered-cubic (BCC). The triblock copolymer concentration in water is 30%.⁹⁴

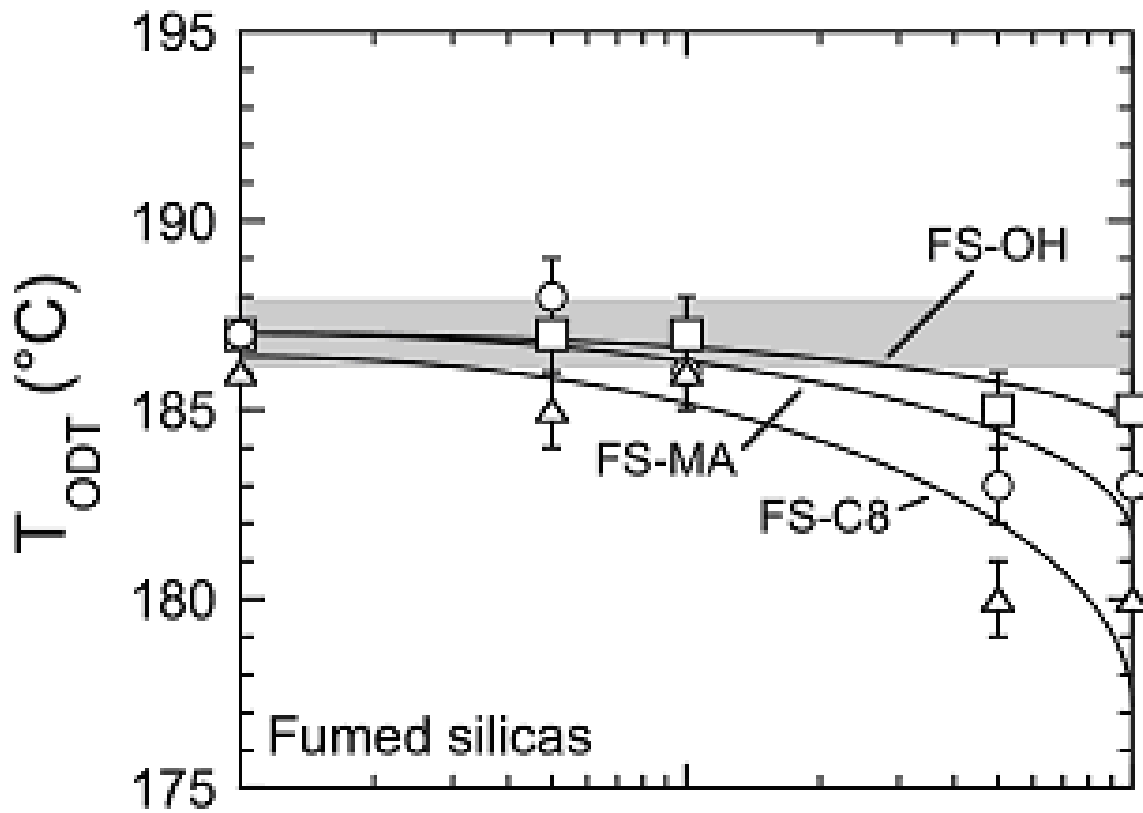


Figure 1.17. Dependence of the order-disorder transition temperature (T_{ODT}) measured by isochronal dynamic rheology on nanoparticle concentration (ϕ_p) for clustered nanoparticles with $-OH$, $-C8$, and $-MA$ surface functionalities.¹⁰⁴

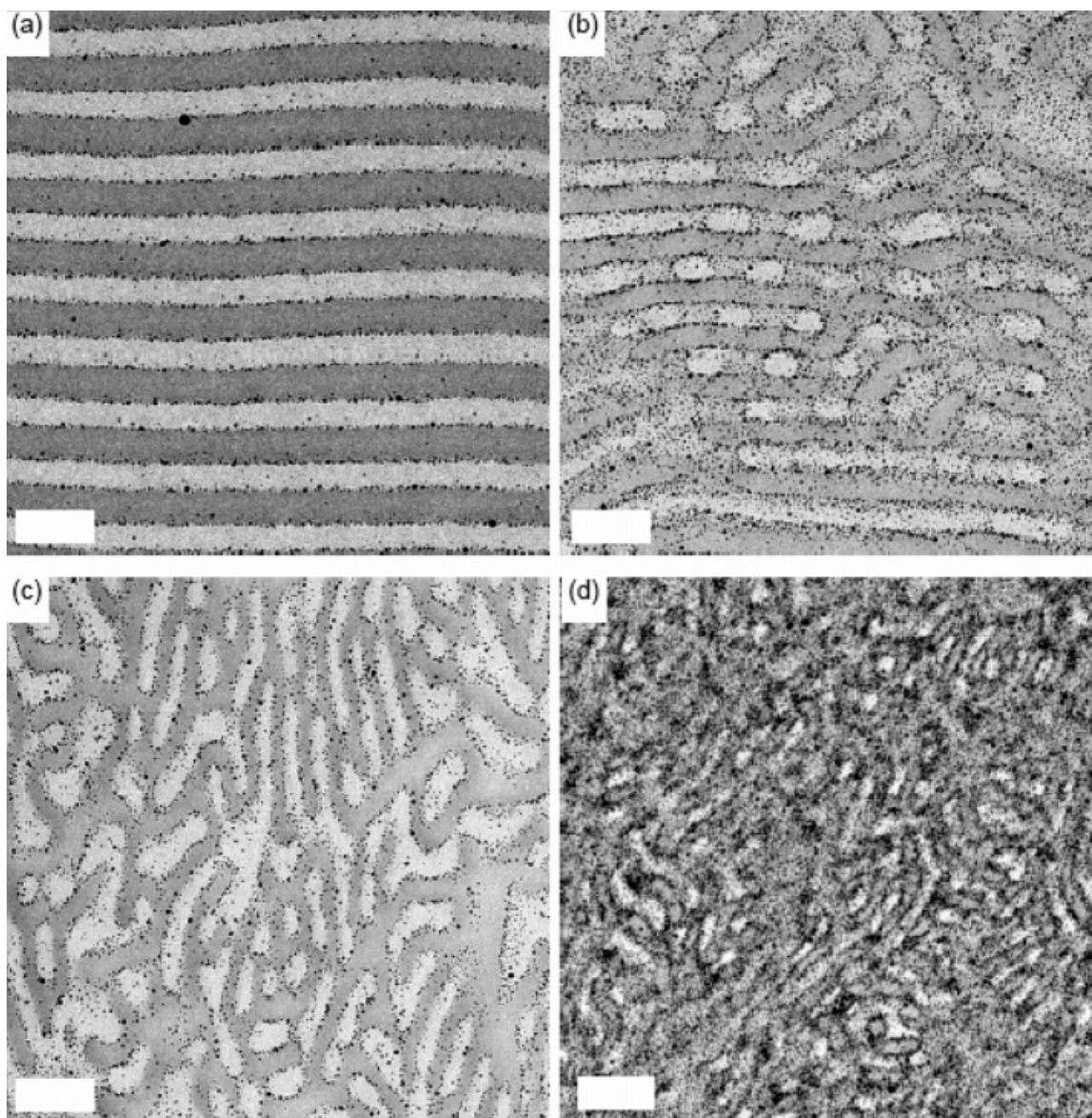


Figure 1.18. Bi-functionalized NP (\sim amphiphilic surfactants) induce a phase transition in polystyrene-*b*-poly-2-vinylpyridine (PS-*b*-P2VP) diblock copolymer from lamellar to the double gyroid (Ia3d space group) bicontinuous morphology. TEM images show PS-partially coated NP volume fractions (ϕ_p): (a) 0.04, (b) 0.07, (c) 0.09, and (d) 0.28. The scale bar is 100 nm. A well ordered lamellar nanostructure can be observed at 4 % loading, while a dramatic change in the morphology occurs at 9 % loading (bicontinuous).¹⁰⁶

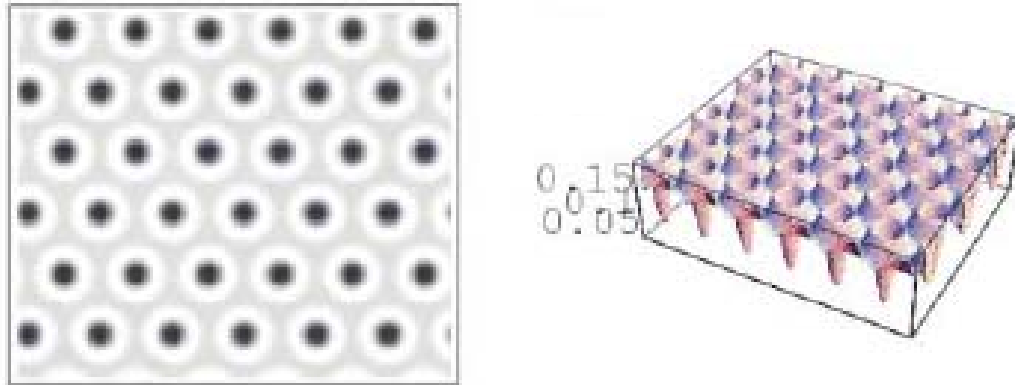


Figure 1.19. SST was used to investigate the importance of entropy and enthalpy on a diblock copolymer, containing A-selective bi-disperse NP. (a) 2D & 3D probability density profiles of symmetric diblock copolymer, displaying a cylindrical morphology due to the entropic effects of the small NP ($R_2 = 0.1R_0$). The large NP ($R_1 = 0.2R_0$) localize at the center of the A-microphase cylinders.¹¹²

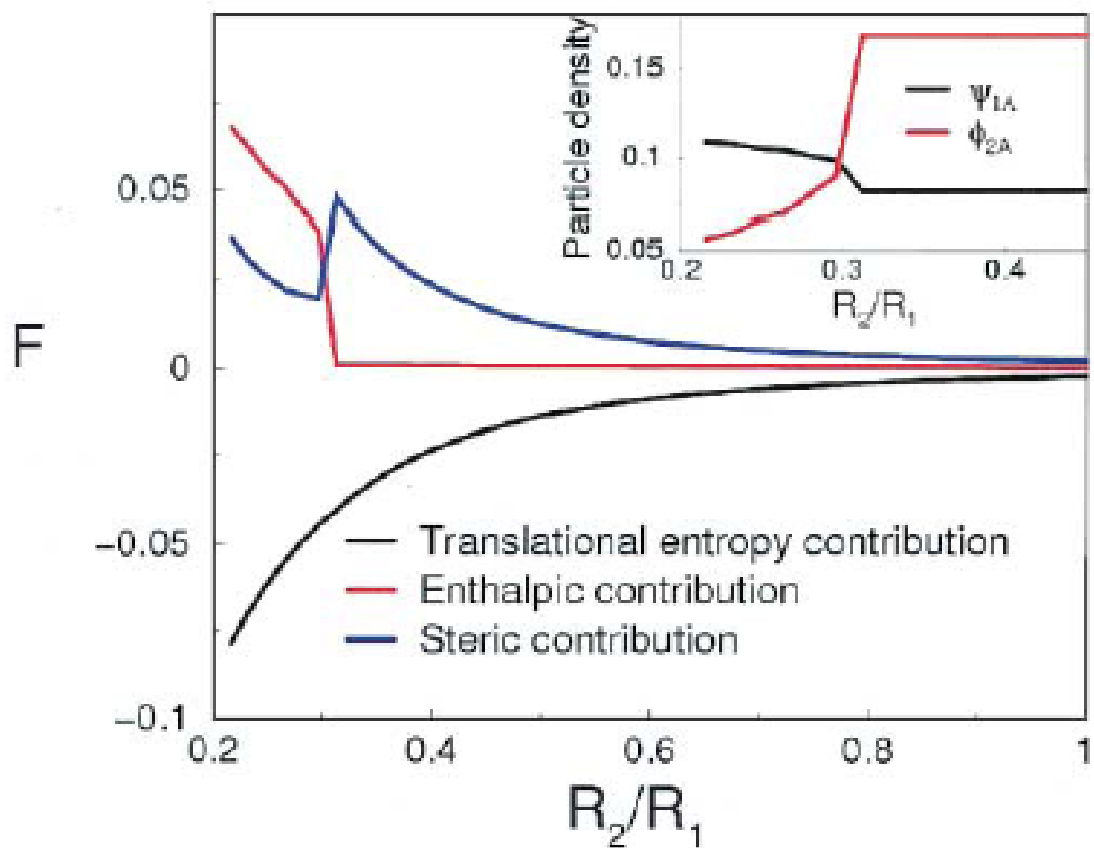


Figure 1.19b. SST was used to investigate the importance of entropy and enthalpy on a diblock copolymer, containing A-selective bi-disperse NP. (b) The free energy contribution of translational entropy (black), enthalpy (red), and steric interactions (blue). This shows that small particles have the potential for more steric interactions and translational entropy combats it by allowing them to spread to energetically unfavorable B. The inset demonstrates that the larger particles are located in a different microphase from most of the small particles, even though they have been tailored to have the same attractive interaction towards the A-block.¹¹²

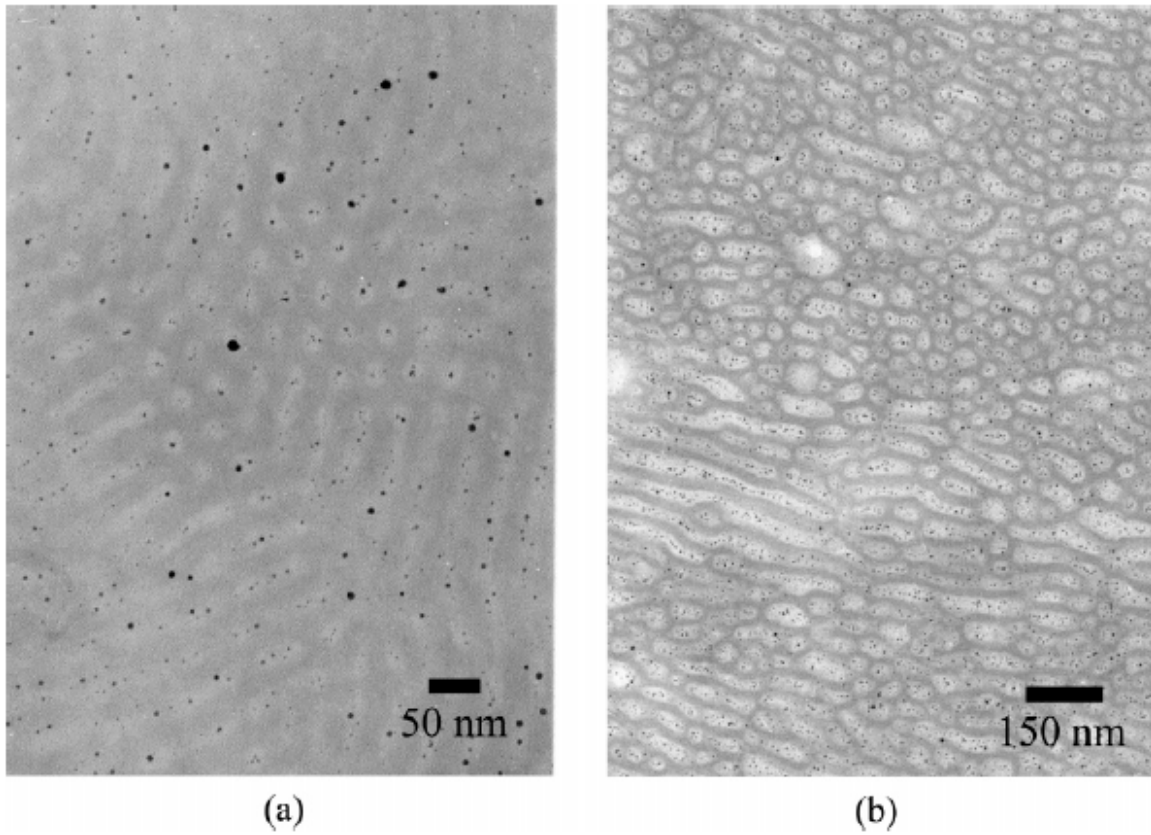


Figure 1.20. PS-coated Au NP in PS-b-P2VP asymmetric ($\phi_{PS} < 0.5$) diblock copolymer show hexagonal cylinder disordering as NP concentration increases, due to increased surface roughness between NP and PS interfaces. (a) TEM data at $\phi_P = 0.09$; $\phi_P = 0.27$.¹¹⁸

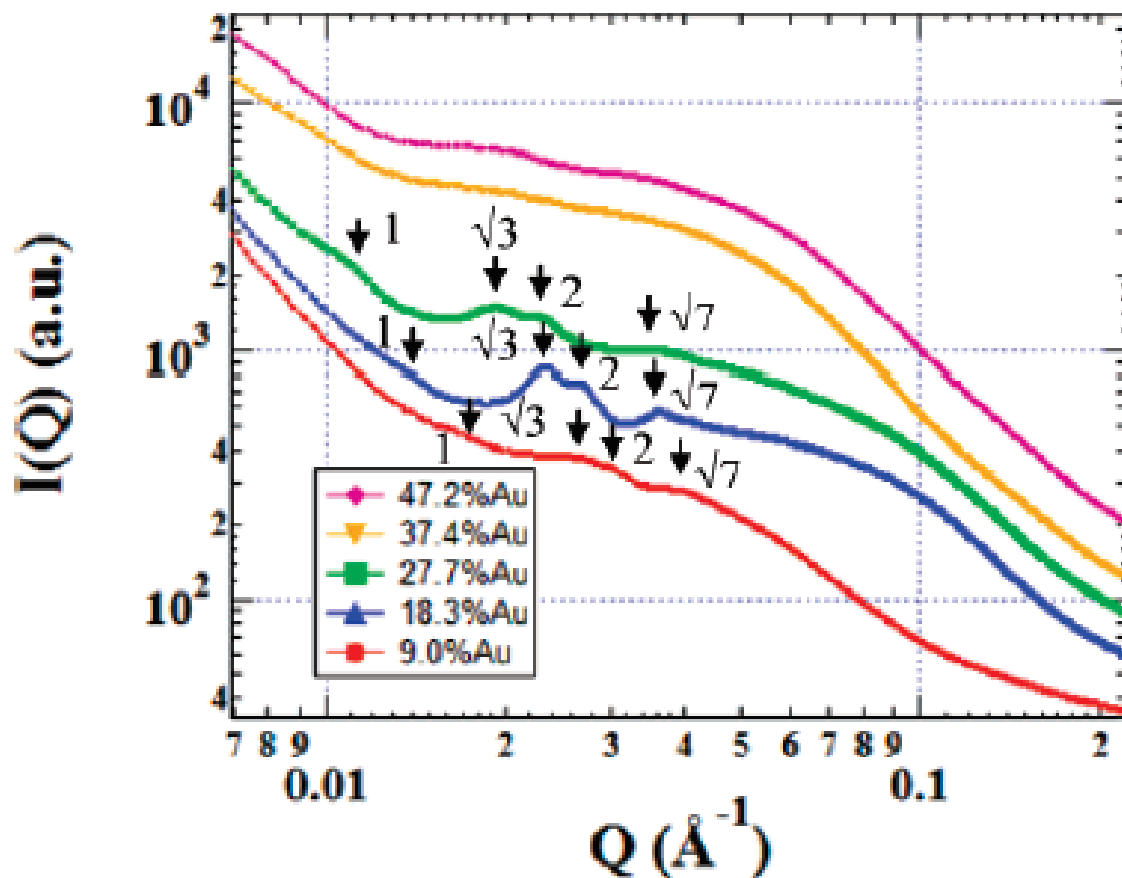


Figure 1.20b. PS-coated Au NP in PS-*b*-P2VP asymmetric ($\phi_{\text{PS}} < 0.5$) diblock copolymer show hexagonal cylinder disordering as NP concentration increases, due to increased surface roughness between NP and PS interfaces. (b) Small Angle X-Ray Scattering (SAXS) data shows a disappearing of the hexagonally-closed-packed cylinder peak positions as NP concentration increases.¹¹⁸

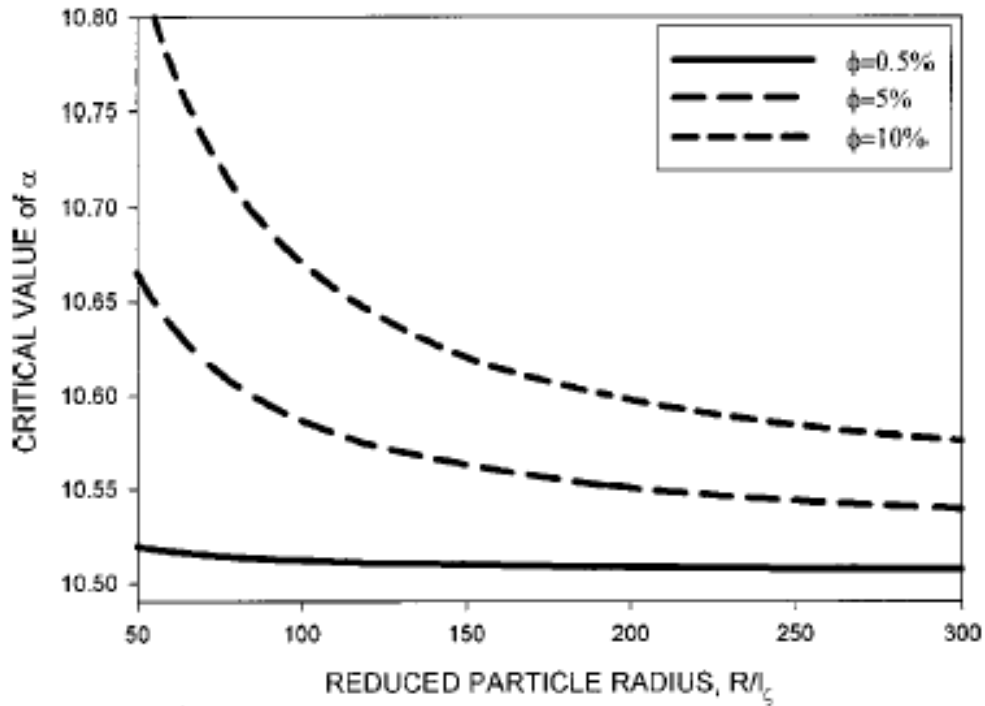


Figure 1.21. Balazs *et.al.* SCFT/DFT calculations show how selective NP concentration and NP geometry can affect the ODT and the microphase stability of a diblock copolymer. (a) Critical value of the segregation factor (ODT) plotted as a function of reduced particle radius. ϕ is the volume fraction of NP. This plot shows how increasing NP concentration causes the ODT to decrease.¹¹⁹

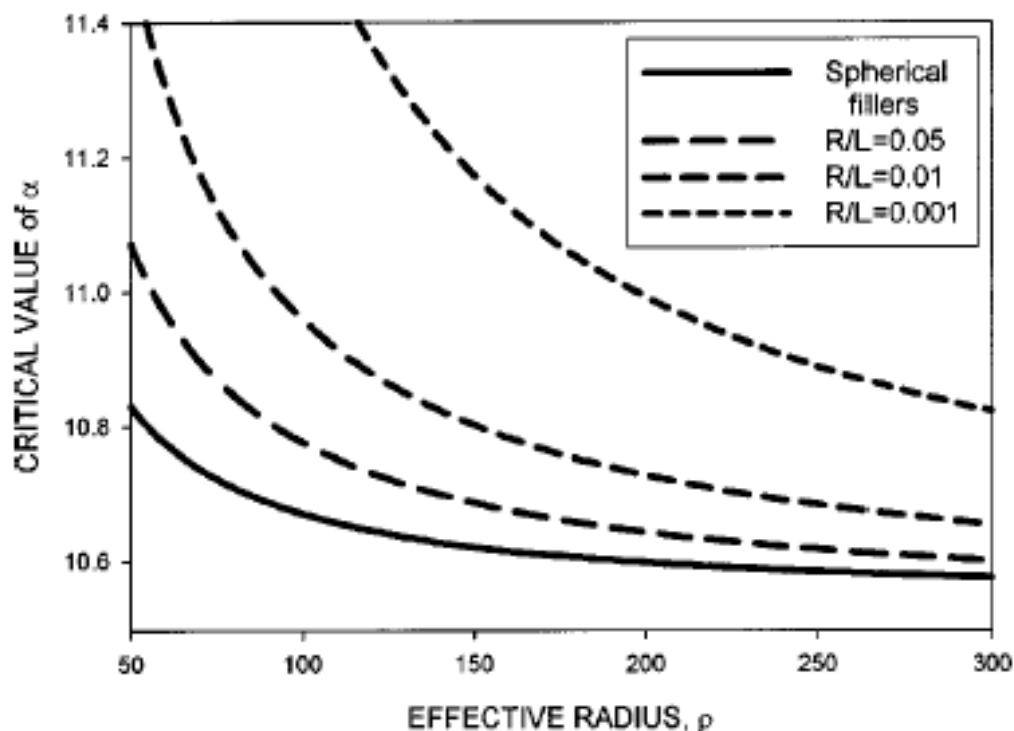


Figure 1.21 (b). Balazs *et.al.* SCFT/DFT calculations show how selective NP concentration and NP geometry can affect the ODT and the microphase stability of a diblock copolymer. (b) Critical value of the segregation factor, α (ODT) is plotted as a function of effective radius. As the aspect-ratio of the NP becomes large compared to the polymer brush length (NP surface area increases), the ODT increases. It shows that NP with a high aspect ratio exhibit the most change in the ODT and the microphase stability of the copolymer.¹¹⁹

CHAPTER 2

MOLECULARLY ASYMMETRIC TRIBLOCK COPOLYMERS AS A SINGLE-MOLECULE ROUTE TO ORDERED BIDISPERSE BRUSHES

Abstract

Conditions signaling the formation of bidisperse brushes in ordered block copolymers are investigated as an A_2 block is progressively grown onto an A_1B diblock copolymer to form a series of molecularly asymmetric, isomorphic A_1BA_2 triblock copolymers. Small-angle scattering and self-consistent field theory confirm that the microphase-ordered period decreases when the A_2 block is short relative to the A_1 block, but then increases as A_1+A_2 bidisperse brushes develop. Mechanical properties systematically follow the spatial distribution of the A_2 block.

(This chapter has been published in its entirety:
Smith, S. D.; Hamersky, M. W.; Bowman, M. K.; Rasmussen, K. Ø.; Spontak, R. J.
Molecularly Asymmetric Triblock Copolymers as a Single-Molecule
Route to Ordered Bidisperse Polymer Brushes. *Langmuir* **2006**, 22, 6465-6468)

2.1 Introduction

Unlike immiscible homopolymers that generally phase-separate at macroscopic length scales, incompatible diblock copolymers are capable of spontaneous molecular self-organization into various ordered morphologies at nanoscale dimensions. Classical block copolymer morphologies include spheres on a cubic lattice, cylinders on a hexagonal lattice and alternating lamellae.¹ Equilibrium or metastable complex morphologies such as the gyroid or perforated lamellae, respectively, consist of channels exhibiting long-range order and spatial symmetry. The ability to tune the morphologies of microphase-ordered block copolymers is critical to a broad range of emerging nanotechnologies² and depends sensitively on the conformational entropy associated with interfacial chain packing.³ Molecular factors governing interfacial chain packing include copolymer composition, repeat unit asymmetry⁴ and (liquid) crystallinity.^{5,6} The dependence of morphological development on interfacial chain packing is further amplified if a third block is added to a diblock copolymer, thereby forming a triblock copolymer. Incorporation of a dissimilar block results in the formation of an ABC triblock copolymer, which can greatly extend the assortment of experimentally accessible, and often hybrid, morphologies.⁷⁻¹⁰

In this work, we focus on ABA triblock copolymers wherein the third block is chemically identical to the first. Although copolymers of this general architecture have been experimentally found^{11,12} and theoretically predicted¹³⁻¹⁵ to exhibit the same morphologies as their AB counterparts, they can possess markedly different mechanical and flow properties¹⁶ due to the placement of the third block. If it resides in the same

microdomain as the first, the corresponding B midblock forms a loop. If, on the other hand, the third block locates in a different microdomain, the midblock connects two adjacent microdomains by forming a bridge. Experimental¹⁷⁻¹⁹ and theoretical^{15,19-22} studies have long sought to elucidate the conditions favoring, as well as the consequences of, molecular bridging in ABA triblock copolymer systems with limited success. These previous efforts have focused almost exclusively on molecularly (though not necessarily compositionally) symmetric copolymers wherein the A endblocks are of identical length and thus form A brushes of uniform thickness. Previous theoretical²³⁻²⁷ and experimental^{25,28,29} studies of polymer brushes composed of either short and long grafted chains on hard surfaces^{23,24,27} or blocks in physical mixtures of block copolymers^{25,26,28,29} have repeatedly demonstrated that such systems afford additional versatility in materials design through the formation of bidisperse (stratified) brushes. In this work, we provide a single-molecule avenue to bidisperse brushes in ordered block copolymer nanostructures through the synthesis of molecularly asymmetric A_1BA_2 triblock copolymers progressively grown from a single A_1B diblock copolymer.

We have recently shown³⁰ that such copolymers can be used to elucidate thermodynamic differences associated with the transformation from diblock to triblock copolymer. Comparison of the order-disorder transition (ODT) measured from two series of A_1BA_2 copolymers with mean-field theory¹³ reveals that the ODT is initially depressed when the A_2 block is short relative to the A_1 block. As the A_2 block length is increased further, however, the ODT increases, eventually exceeding that of the parent A_1B diblock copolymer. Moreover, this result is qualitatively consistent with the self-consistent field

theory (SCFT) of Matsen,³¹ who finds that molecular asymmetry in a triblock copolymer is capable of altering microdomain dimensions, as well as order-order transitions, due to the presence of short A_2 blocks that remain mixed upon microphase-ordering of the longer A_1 and B blocks. The objectives of this work are to (i) discern the morphological and property conditions signaling the onset of bidisperse (A_1+A_2) brush formation and (ii) the physical ramifications of A_1+A_2 brush bidispersity in a series of ordered A_1BA_2 triblock copolymers varying in A_2 block length from experimental and SCFT analyses.

2.2 Experimental

A parent poly(styrene-*b*-isoprene) A_1B diblock copolymer, along with a series of molecularly asymmetric A_1BA_2 triblock copolymers, was synthesized³⁰ via living anionic polymerization in cyclohexane at 60°C with *sec*-butyllithium as the initiator. Their molecular characteristics were measured by ^1H NMR and gel permeation chromatography. Since the block masses of the parent diblock were 9.4 kDa (styrene, A_1) and 46 kDa (isoprene, B), the copolymer series is designated 9-46- A_2 . The maximum polydispersity index in this series was 1.04. Specimens for small-angle x-ray scattering (SAXS) and rheometry were prepared by compression molding and subsequent annealing under vacuum at 170°C. The SAXS data were acquired using $\text{CuK}\alpha$ radiation ($\lambda = 0.154$ nm) from a Rigaku RU-300 rotating anode operated at 40 kV and 40 mA. Two-dimensional scattering patterns, collected with the Siemens HI-STAR wire detector, were azimuthally integrated to yield scattered intensity as a function of wave vector (q), where $q = (4\pi/\lambda)\sin(\theta/2)$ and θ is the scattering angle. Differential scanning calorimetry per-

formed with a Perkin-Elmer DSC-7 confirmed that the upper glass transition temperature (T_g) of all the copolymers was $<100^\circ\text{C}$. Dynamic shear measurements were obtained on an ARES strain-controlled rheometer equipped with 25 mm parallel plates separated by a 1 mm gap. Modulus values reported here used strain levels below 2-5% to ensure linear viscoelasticity.³⁰ Isochronal temperature sweeps were conducted at heating rates of 1 and $5^\circ\text{C}/\text{min}$ at a frequency of 1 rad/s.

2.3 Results and Discussion

Scattering patterns acquired from the 9-46- A_2 copolymer series are displayed in Fig. 1, in which the A_2 block mass (M_{A_2} , in kDa) increases from 0 (the parent diblock copolymer) to 19.3, which corresponds to $\sim 2\times$ the mass of the A_1 block. A principal peak located at q_m is evident in each of these patterns. Close examination of the patterns beyond the resolution afforded in Fig. 1 reveals the existence of weak higher-order peaks positioned at $q_m\sqrt{3}$ and, in some cases, $q_m\sqrt{7}$, indicating that each of the copolymers in this series is microphase-ordered as A cylinders arranged on a hexagonal lattice in a B matrix. The absence of higher-order peaks confirms that these cylindrical morphologies do not exhibit long-range order, in agreement with results obtained from electron microscopy (to be reported elsewhere). An important feature of Fig. 1 is that q_m shifts to higher values, resulting in a reduction of the corresponding characteristic size, upon introduction of the A_2 block. A further increase in M_{A_2} , however, eventually promotes a decrease in q_m . Values of the microdomain period (D) extracted from the SAXS patterns in Fig. 1 and normalized with respect to D measured from the parent A_1B copolymer (D_0)

are provided as a function of M_{A_2} in Fig. 2. These results confirm that D/D_0 exhibits a minimum when the A_2 block is $\sim 70\%$ the mass of the A_1 block.

Although the molecular weights of the A_1BA_2 copolymers are larger than that of the parent diblock copolymer (depicted in Fig. 2a), the value of D/D_0 at this minimum is ~ 0.84 . A decrease in D/D_0 with increasing chain length is attributed to a reduction in interblock incompatibility (expressed in terms of χN , where χ is the Flory-Huggins interaction parameter and N is the number of statistical units along the copolymer backbone) between the A_1 and B blocks due to the presence of the A_2 block (Fig. 2b). Our earlier ODT analysis³⁰ of this copolymer series, in conjunction with previous SCFT predictions,³¹ asserts that the A_2 block remains mixed within the B matrix when it is short relative to the A_1 block. Accordingly, the B blocks relax due to the inclusion of dangling A_2 blocks. Although this molecular picture explains the initial reduction in D/D_0 with increasing M_{A_2} , it does not account for the minimum in Fig. 2. Once the A_2 block becomes sufficiently long (and incompatible with the B block) to likewise microphase-separate from the B matrix, however, it can co-locate within the A_1 microdomains so that an A_2 block resides within either the same microdomain as the A_1 block of the same molecule (the B block forms a loop) or a neighboring A_1 microdomain (the B block forms a bridge). This condition signifies the onset of bidisperse brushes composed of long A_1 and short A_2 blocks, illustrated in Fig. 2c, as the A_1BA_2 molecule effectively transforms from diblock to triblock copolymer with regard to its spatial arrangement within the copolymer nanostructure as the B midblock transitions from a tail to a bridge or a loop. As M_{A_2} is increased further, the A_2 block approaches M_{A_1} , at which point a

uniform brush develops (Fig. 2d), and then increases beyond M_{A1} , yielding bidisperse brushes consisting of short A_1 and long A_2 blocks (Fig. 2e) within the cylindrical microdomains.

Accounting for differences in density between the repeat units and using the temperature-dependent expression for χ reported by Lodge et al.³² yield the following estimates of χN for the parent A_1B diblock copolymer: 64 at 25°C and 53 at 75°C (near the upper T_g of the A_1B copolymer). The symmetric ABA triblock copolymer can be approximated as an $A(B/2)$ diblock copolymer, in which case the corresponding χN values are 36 and 30, respectively. These results reveal that all the copolymers examined here likely reside in the intermediate segregation regime ($\sim 20 < \chi N < \sim 100$), which is ideally suited for SCFT analysis. The SCFT employs a numerical procedure described elsewhere³³ to predict the morphologies of microphase-ordered triblock copolymers. Simulation of a prescribed system commences with a random arrangement of potential fields. Upon progressive iteration of coupled diffusion and field equations, the system is permitted to relax into an equilibrium nanostructure without prior knowledge of morphological symmetry, as previously proposed.³⁴ Following the initial relaxation of the free energy, the dimensions of the simulation box are iteratively changed to further minimize the free energy. The true free energy minimum is obtained when D is commensurate with the size of the simulation box. In this study, a hexagonal (cylindrical) morphology is predicted for all the copolymers, and values of D derived from these simulations and normalized with respect to D_0 are included for two different values of χN (36 and 60) in Fig. 2. The agreement between experimental data and SCFT predictions is

favorable. At low M_{A_2} , SCFT captures the observed dependence of D/D_0 on M_{A_2} . While the minimum in D/D_0 is also accurately predicted, the value of D/D_0 computed by SCFT is slightly lower than that measured by SAXS. Further increasing M_{A_2} promotes a monotonic increase in D/D_0 that likewise agrees with experimental results.

Segmental density distributions generated for each of the constituent blocks in six of the A_1BA_2 triblock copolymers investigated here are displayed over a distance (x) of one D in Fig. 3. In Fig. 3a, only the distributions corresponding to the A_1 and B blocks are shown for the case of the parent A_1B copolymer. Growth of relatively short A_2 blocks results in the distributions illustrated in Figs. 3b-c, which confirm that these A_2 blocks saturate along the A_1/B interface and likewise reside within the B matrix. A further increase in M_{A_2} results in localization of the A_2 blocks within the A_1 microdomains and concurrent purification of the B matrix in Figs. 3d-f. The double peak apparent in the A_2 distribution in Fig. 3d confirms the existence of a bidisperse brush composed of short A_2 blocks near the interface and longer A_1 blocks at the center of the A_1 microdomain, whereas the converse occurs when the A_2 block is longer than the A_1 block (*cf.* Fig. 3f). To facilitate further SCFT analysis and comparison with experimental data, the A_2 segmental density distributions evaluated at the core of the A_1 and B microdomains (at $x = 0$ and 0.5 , respectively, in Fig. 3) are presented as a function of M_{A_2} in Fig. 4a.

When the A_2 block is short relative to the A_1 block, the A_2 core density within the A_1 and B microdomains increases slowly. According to Fig. 2, D is observed and predicted to decrease over this M_{A_2} range. The SCFT simulation of the equilibrium nanostructure for the copolymer with $M_{A_2} = 3.4$ kDa (Fig. 4a inset) confirms the presence of A_2 blocks

along the A₁/B interface *and* within the B matrix. A further increase in M_{A2} promotes a pronounced increase of A₂ within the A₁ microdomain and a sharp reduction in the concentration of A₂ within the B matrix, thereby verifying co-location of the A₁ and A₂ blocks. When M_{A2} ≈ M_{A1}, the A₁BA₂ copolymer becomes molecularly symmetric and the A₂ core density within the A₁ microdomain approaches 0.5 (*cf.* Fig. 4a). Since the onset of brush bidispersity and, by inference, molecular bridging is anticipated to affect the mechanical properties of A₁BA₂ triblock copolymers, the dependence of the elastic modulus (G') on M_{A2} is provided in Fig. 4b. The initial decrease in G' with increasing M_{A2} in the melt (100°C is above the upper T_g and below the ODT³⁰ of each copolymer) is consistent with mixing between the A₂ and B blocks and chain relaxation. Once the A₂ block is sufficiently long to join the A₁ block and produce a bidisperse brush, the B midblock forms a loop or a bridge.

Thermodynamically-driven separation of the A₂ blocks from the B matrix, accompanied by the formation of permanently entangled loops or bridges, promotes a monotonic increase in G', as evidenced by the data shown in Fig. 4b when M_{A2} > 4 kDa. In the case of the molecularly symmetric triblock copolymer (which possesses an equilibrium fraction of bridged midblocks¹⁵), the interpolated value of G' is ~6.8x higher than that of the parent A₁B copolymer, which agrees well with observations reported elsewhere.¹⁹ This signature is consistent with our presumption that midblock bridging (looping) originates when the A₂ block separates from the B matrix to form an initially bidisperse brush (at M_{A2} < M_{A1}). Comparison of the microdomain periods and moduli in Figs. 2 and 4b, respectively, with the segmental densities in Fig. 4a unequivocally shows

that the block arrangement, morphological signature and mechanical properties of the A_1BA_2 copolymers undergo abrupt changes with increasing M_{A_2} . These results together indicate that A_2 blocks with $3.4 < M_{A_2} < 6.5$ co-locate with the A_1 blocks (9.4 kDa) and generate A_1+A_2 bidisperse brushes. When this occurs, the B midblocks transform from tails to bridges or loops.

2.4 Conclusions

Identification of the molecular-level conditions responsible for the formation of stratified brushes in block copolymers is necessary to better understand the underlying principles favoring the formation of nonclassical polymeric nanostructures, such as microemulsions²⁶ and vesicles.²⁸ In addition, Hashimoto and co-workers³⁵ have shown that entropically-driven localization effects in copolymer/homopolymers mixtures can be used to target the location of metal nanoparticles within the discrete microdomains of microphase-ordered block copolymers. This strategy complements more recent efforts³⁶ that employ nanoparticle surface functionality to control the positioning of nanoparticles in ordered copolymer matrices. Molecularly asymmetric triblock copolymers provide not only a single-molecule avenue by which to achieve brush bidispersity and, hence, intramicrodomain block stratification without resorting to physical copolymer mixtures, but also a facile experimental alternative to further elucidate the novel opportunities associated with constrained chain mixing and property development in nanoscale environments.

2.5 Acknowledgements

This work was supported, in part, by the Research Council of Norway under the NANOMAT Program and the Center for Integrated Nanotechnologies. Research at LANL is performed under the auspices of the U. S. Department of Energy (Contract No. W-7405-ENG-36).

2.6 References

1. Hamley, I. W. *The Physics of Block Copolymers*; Oxford University Press: New York, 1998.
2. Park, C.; Yoon, J.; Thomas, E. L. *Polymer* **2003**, *44*, 6725. Hamley, I. W. *Angew. Chem. Int. Ed.* **2003**, *42*, 1692.
3. Matsen, M. W.; Bates, F. S. *J. Chem. Phys.* **1997**, *106*, 2436.
4. Matsen, M. W.; Bates, F. S. *J. Polym. Sci. B: Polym. Phys.* **1997**, *35*, 945.
5. Chen, J. T.; Thomas, E. L.; Ober, C. K.; Mao, G. P. *Science* **1996**, *273*, 343.
6. Loo, Y. -L.; Register, R. A. In *Developments in Block Copolymer Science and Technology* (Hamley, I. W., ed.); Wiley: New York, 2004; pp. 213-244.
7. Stadler, R.; Auschra, C.; Beckmann, J.; Krappe, U.; Voigt-Martin, I.; Leibler, L. *Macromolecules* **1995**, *28*, 3080.
8. Bates, F. S.; Fredrickson, G. H. *Phys. Today* **1999**, *52*, 32.
9. Abetz, V. In *Encyclopedia of Polymer Science and Technology*, 3rd ed. (Kroschwitz, J. I., ed.); Wiley: Hoboken, NJ, 2003; Vol. 1, pp. 482-523.
10. Tyler, C. A.; Morse, D. C. *Phys. Rev. Lett.* **2005**, *94*, 208302.
11. Holden, G.; Legge, N. R.; Quirk, R.; Schroeder, H. E. (Eds.) *Thermoplastic Elastomers*, 2nd ed.; Hanser: Munich, 1996.
12. Laurer, J. H.; Hajduk, D. A.; Fung, J. C.; Sedat, J. W.; Smith, S. D.; Gruner, S. M.;

- Agard, D. A.; Spontak, R. J. *Macromolecules* **1997**, *30*, 3938.
13. Mayes, A. M.; Olvera de la Cruz, M. J. *J. Chem. Phys.* **1989**, *91*, 7228.
14. Dobrynin, A. V.; Erukhimovich, I. Ya. *Macromolecules* **1993**, *26*, 276.
15. Matsen, M. W.; Thompson, R. B. *J. Chem. Phys.* **1999**, *111*, 7139.
16. Ryu, C. Y.; Lee, M. S.; Hajduk, D. A.; Lodge, T. P. *J. Polym. Sci. B: Polym. Phys.* **1997**, *35*, 2811 (1997).
17. Lee, S. H.; Koberstein, J. T.; Quan, X.; Gancarz, I.; Wignall, G. D.; Wilson, F. C. *Macromolecules* **1994**, *27*, 3199.
18. Watanabe, H. *Macromolecules* **1995**, *28*, 5006. Karatasos, K.; Anastasiadis, S. H.; Pakula, T.; Watanabe, H. *Macromolecules* **2000**, *33*, 523. Watanabe, H.; Tan, H. *Macromolecules* **2004**, *37*, 5118.
19. Kane, L.; Norman, D. A.; White, S. A.; Matsen, M. W.; Satkowski, M. M.; Smith, S. D.; Spontak, R. J. *Macromol. Rapid Commun.* **2001**, *22*, 281.
20. Matsen, M. W.; Schick, M. *Macromolecules* **1994**, *27*, 187.
21. Drolet, F.; Fredrickson, G. H. *Macromolecules* **2001**, *34*, 5317.
22. Banaszak, M.; Woloszczuk, S.; Pakula, T.; Jurga, S. *Phys. Rev. E* **2002**, *66*, 031804.
23. Milner, S. T.; Witten, T. A. *J. Phys. (Paris)* **1988**, *49*, 1951. Milner, S. T.; Witten, T. A.; Cates, M. E. *Macromolecules* **1989**, *22*, 853.

24. Birshstein, T. M.; Lyatskaya, Y. V.; Zhulina, E. B. *Polymer* **1990**, *31*, 2185. Zhulina, E. B.; Liatskaya, Y. V.; Birshstein, T. M. *Polymer* **1992**, *33*, 332. Lai, P. Y.; Zhulina, E. B. *Macromolecules* **1992**, *25*, 5201.
25. Kane, L.; Satkowski, M. M.; Smith, S. D.; Spontak, R. J. *Macromolecules* **1996**, *29*, 8862.
26. Thompson, R. B.; Matsen, M. W. *Phys. Rev. Lett.* **2000**, *85*, 670.
27. Terzis, A. F. *Polymer* **2002**, *43*, 2435.
28. Discher, D. E.; Eisenberg, A. *Science* **2002**, *297*, 967. Lin, J. J.; Bates, F. S.; Hammer, D. A.; Silas, J. A. *Phys. Rev. Lett.* **2005**, *95*, 026101.
29. Court, F.; Hashimoto, T. *Macromolecules* **2001**, *34*, 2536; **2002**, *35*, 2566.
30. Hamersky, M. W.; Smith, S. D.; Gozen, A. O.; Spontak, R. J. *Phys. Rev. Lett.* **2005**, *95*, 168306.
31. Matsen, M. W. *J. Chem. Phys.* **2000**, *113*, 5539.
32. Lodge, T. P.; Pan, C.; Jin, X.; Liu, Z.; Zhao, J.; Maurer, W. W.; Bates, F. S. *J. Polym. Sci. B: Polym. Phys.* **1995**, *33*, 2289.
33. Rasmussen, K. Ø.; Kalosakas, G. *J. Polym. Sci. B: Polym. Phys.* **2002**, *40*, 1777.
34. Drolet, F.; Fredrickson, G. H. *Phys. Rev. Lett.* **1999**, *83*, 4317.
35. Tsutsumi, K.; Funaki, Y.; Hirokawa, Y.; Hashimoto, T. *Langmuir* **1999**, *15*, 5200.
36. Bockstaller, M. R.; Thomas, E. L. *Phys. Rev. Lett.* **2004**, *93*, 166106.

2.7 List of Figure Captions

Figure 2.1 SAXS patterns acquired at ambient temperature from the isomorphous A_1B diblock and molecularly asymmetric A_1BA_2 triblock copolymer series under investigation. The patterns have been shifted vertically to facilitate viewing, and the copolymers are identified by the listed value of M_{A_2} . The dashed line marks the principal peak position (q_m) of the parent A_1B copolymer.

Figure 2.2 The microdomain period (D) of A_1BA_2 triblock copolymers measured by SAXS, normalized with respect to that of the parent A_1B copolymer and presented as a function of M_{A_2} . The solid line corresponds to SCFT predictions, and the dotted horizontal line denotes $D/D_0 = 1$. The dashed vertical line shows where the A_1BA_2 copolymer becomes molecularly symmetric ($M_{A_1} = M_{A_2}$). Schematic cross-sections of the A-rich cylinders (a-e) show the arrangement of the A_1 (blue), B (red) and A_2 (yellow) blocks, as well as B/ A_2 (orange) and A_1/A_2 (green) mixtures.

Figure 2.3 Segmental density distributions generated by SCFT for six copolymers in the 9-46- A_2 series under investigation wherein M_{A_2} (in kDa) is systematically increased: (a) 0.0, (b) 2.0, (c) 3.4, (d) 6.5, (e) 8.2 and (f) 11.8. The A_1 , B and A_2 species are labeled in (a) and (b).

Figure 2.4 In (a), the A_2 core density evaluated from SCFT in the A_1 microdomain and B matrix (labeled) as a function of M_{A_2} . The dashed lines identify the condition of molecular symmetry ($M_{A_2} = M_{A_1}$), and the arrow shows where the core densities are

equal. The inset displays the density field of the A_2 block in the copolymer with $M_{A_2} = 3.4$ kDa. High and low concentrations are denoted by red and dark blue, respectively. The elastic modulus (G') is presented as a function of M_{A_2} at 100°C in (b). The solid lines are guides for the eye. The dotted line identifies the value of G' measured from the parent A_1B copolymer, and the dashed lines show where $M_{A_2} = M_{A_1}$.

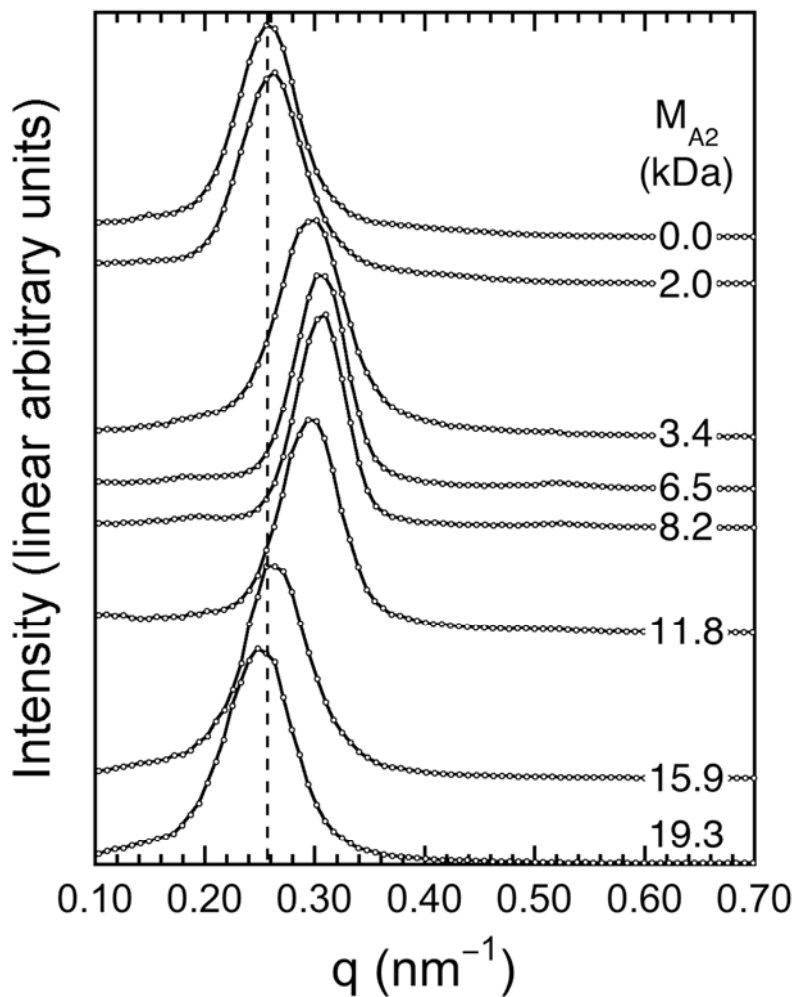


Figure 2.1. SAXS patterns acquired at ambient temperature from the isomorphous A_1B diblock and molecularly asymmetric A_1BA_2 triblock copolymer series under investigation. The patterns have been shifted vertically to facilitate viewing, and the copolymers are identified by the listed value of M_{A_2} . The dashed line marks the principal peak position (q_m) of the parent A_1B copolymer.

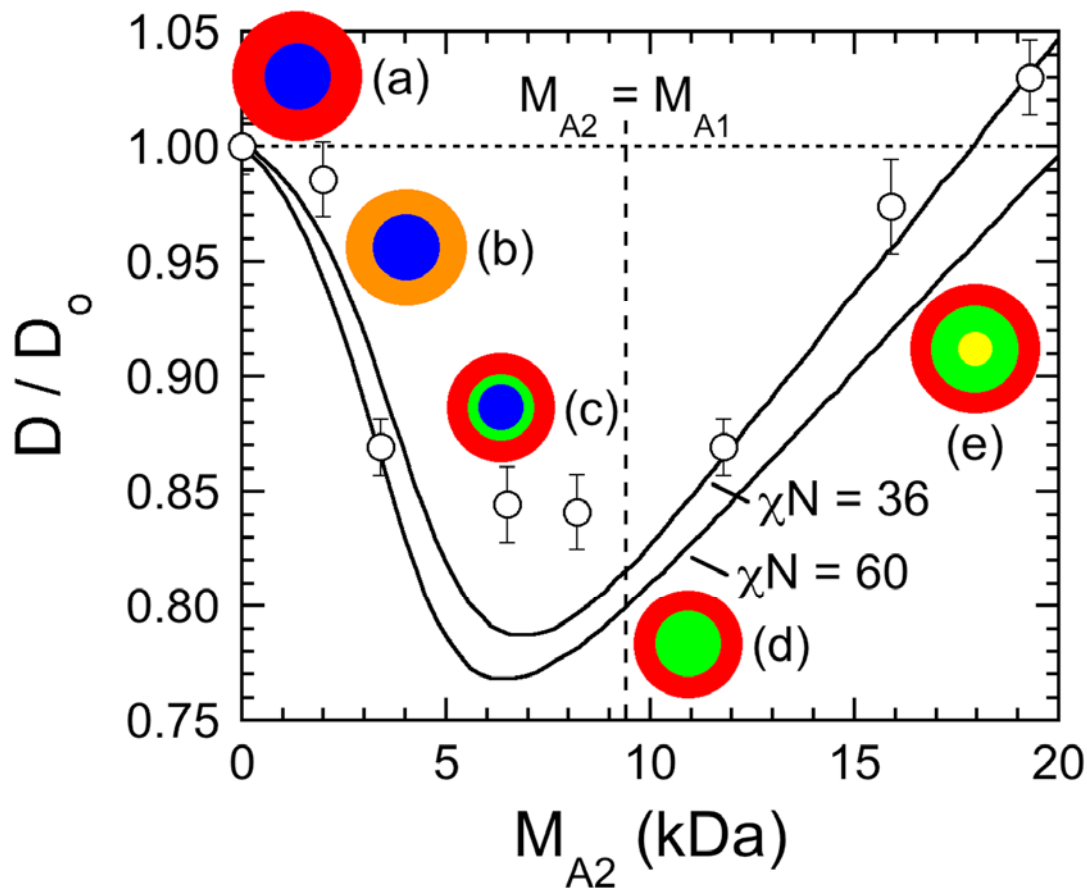


Figure 2.2. The microdomain period (D) of A_1BA_2 triblock copolymers measured by SAXS, normalized with respect to that of the parent A_1B copolymer and presented as a function of M_{A_2} . The solid line corresponds to SCFT predictions, and the dotted horizontal line denotes $D/D_0 = 1$. The dashed vertical line shows where the A_1BA_2 copolymer becomes molecularly symmetric ($M_{A_1} = M_{A_2}$). Schematic cross-sections of the A-rich cylinders (a-e) show the arrangement of the A_1 (blue), B (red) and A_2 (yellow) blocks, as well as B/ A_2 (orange) and A_1/A_2 (green) mixtures.

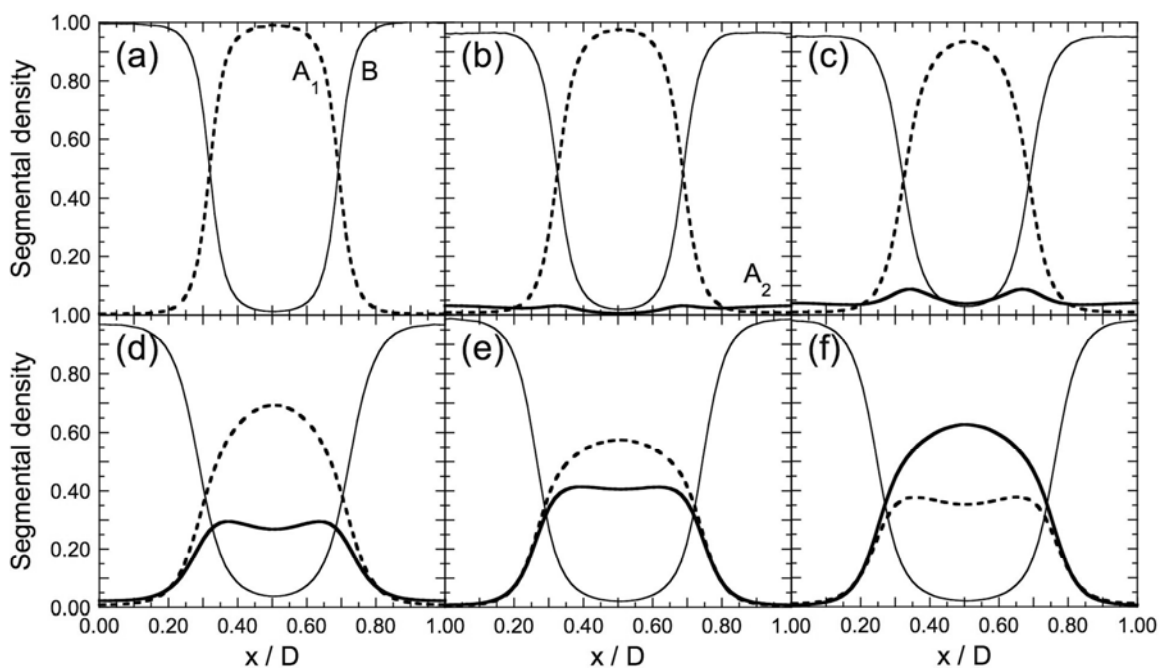


Figure 2.3. Segmental density distributions generated by SCFT for six copolymers in the 9-46- A_2 series under investigation wherein M_{A_2} (in kDa) is systematically increased: (a) 0.0, (b) 2.0, (c) 3.4, (d) 6.5, (e) 8.2 and (f) 11.8. The A_1 , B and A_2 species are labeled in (a) and (b).

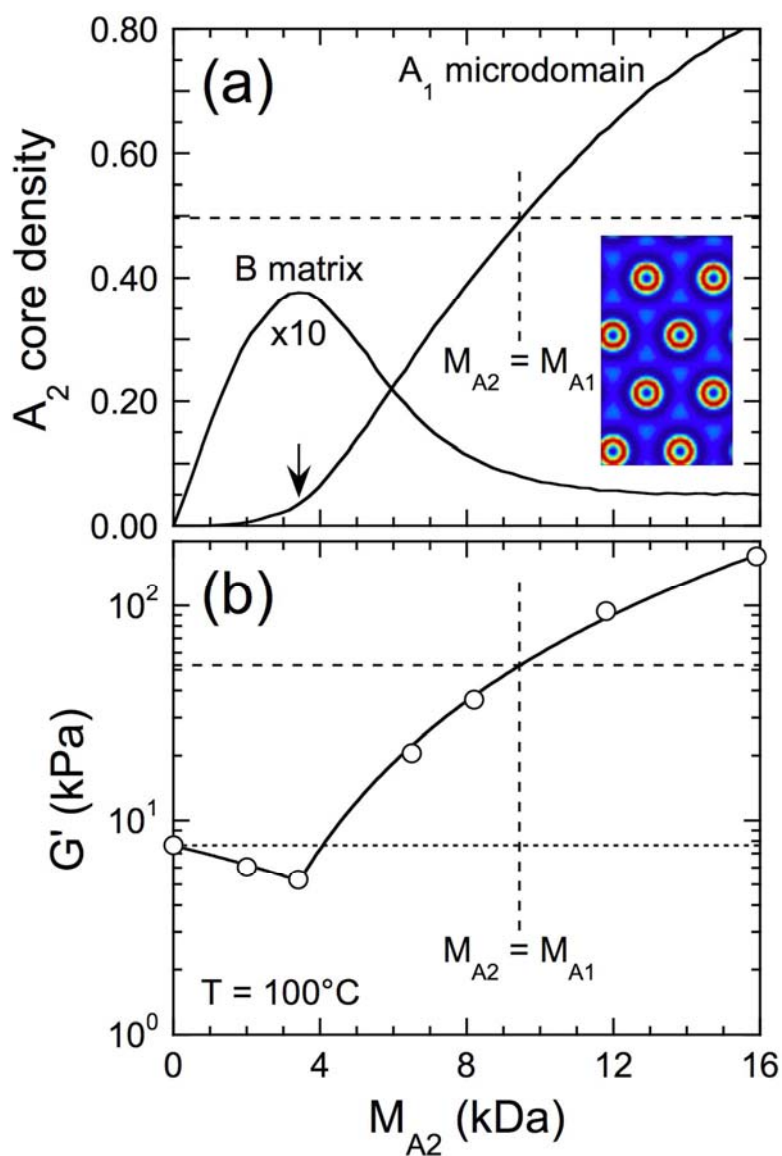


Figure 2.4. In (a), the A_2 core density evaluated from SCFT in the A_1 microdomain and B matrix (labeled) as a function of M_{A2} . The dashed lines identify the condition of molecular symmetry ($M_{A2} = M_{A1}$), and the arrow shows where the core densities are equal. The inset displays the density field of the A_2 block in the copolymer with $M_{A2} = 3.4$ kDa. High and low concentrations are denoted by red and dark blue, respectively. The elastic modulus (G') is presented as a function of M_{A2} at 100°C in (b). The solid lines are guides for the eye. The dotted line identifies the value of G' measured from the parent A_1B copolymer, and the dashed lines show where $M_{A2} = M_{A1}$.

CHAPTER 3

SELECTIVITY- AND SIZE-INDUCED SEGREGATION OF MOLECULAR AND NANOSCALE SPECIES IN MICROPHASE-ORDERED TRIBLOCK COPOLYMERS

Abstract

Microphase-ordered block copolymers serve as model systems to elucidate the potential of molecular self-assembly and organic templates to fabricate functionalized polymer materials. Both aspects are related to the incorporation of secondary species such as low-molar-mass compounds or nanoparticles within the copolymer matrices. Since the resulting properties of such functionalized copolymers critically depend on the morphology of the blend or composite, the nonrandom distribution of such inclusions within the copolymer matrix must be understood. Using a self-consistent field theoretical approach, we quantitatively evaluate the segregation and interfacial excess of low-molar-mass and nanoscale species in ordered triblock copolymers as functions of block selectivity and inclusion size. The predictions are found to agree with the morphology observed in a model triblock copolymer/nanoparticle composite, thereby demonstrating the generality of this approach.

Our results suggest a wide correspondence in the structure-forming effect of molecular and nanoscale inclusions that will have implications in the design and processing of functional nanostructured polymers.

(This chapter has been published in its entirety:
Spontak, R. J.; Shankar, R.; Bowman, M. K.; Krishnan, A. S.; Hamersky, M.W.; Samseth, J.; Bockstaller, M. R.; Rasmussen, K. Ø. Selectivity- and Size-Induced Segregation of Microphase-Ordered Triblock Copolymers. *Nano Lett.* **2006**, 22, 6465-6468).

3.1 Introduction

Due to their periodic nanostructures that spontaneously develop via molecular self-assembly, microphase-ordered block copolymers constitute a topic of immense contemporary interest. These copolymers, envisaged as two or more homopolymer chains covalently linked to generate a single macromolecule composed of long contiguous sequences ("blocks"), can, in the same fashion as low-molar-mass surfactants,^{1,2} order into a variety of periodic morphologies that depend on factors such as interblock incompatibility, composition and repeat unit asymmetry.³⁻⁵ Governing the enthalpic driving force promoting phase separation and the conformational entropy arising from interfacial chain packing, these factors can drive the formation of A(B) spheres or cylinders in a B(A) matrix, bicontinuous channels or alternating lamellae in incompatible AB diblock and ABA triblock copolymers. These morphologies can be furthermore altered in tunable fashion through the addition of low-molar-mass molecular species (a solvent),⁶⁻⁸ high-molar-mass species⁹ (one or two homopolymers^{10,11} or a second copolymer¹²) and discrete nanoscale particulates (organic nanogels¹³ or inorganic nanoparticles¹⁴⁻¹⁶). Since previous studies have established the localization effects of high-molar-mass species incorporated within miscible AB^{17,18} or ABA¹⁹ block copolymer blends, we turn our attention to non-chain-like additives with a wide range of characteristic length scales such as solvents and nanoparticles. Our studies focus on symmetric, lamella-forming ABA triblock copolymer architectures to facilitate comparison with experimental and previous theoretical studies.

While block copolymers in aqueous media have been exhaustively investigated and a rich assortment of ordered morphologies has been identified,^{6,7} only organic solvents are considered further to preclude chemical issues arising from hydrogen bonds or electrostatic interactions between copolymer and solvent molecules. Hashimoto and co-workers²⁰ have pioneered many of the early efforts to probe the morphologies and phase behavior of concentrated block copolymer solutions, with complementary mean-field calculations²¹ providing insight into the spatial distribution of the incorporated solvent molecules. Ongoing studies by Lodge and co-workers⁸ have elucidated the role of solvent selectivity on the phase behavior of concentrated block copolymer solutions. They have shown that toluene, a relatively neutral solvent for poly(styrene-*b*-isoprene) (SI) diblock copolymers, segregates to the S/I interfaces.²² Interfacial solvent segregation is consistent with calculations from self-consistent field theory (SCFT),²³ as well as gravimetric sorption analyses confirming that toluene-imbibed SI copolymers discharge solvent as they undergo microphase-disordering (and interfacial dissolution).²⁴ Thus, if ordered block copolymers are subjected to solvent sorption in sensory, separation or delivery technologies, or are annealed or otherwise processed in the presence of a solvent,²⁵ the nonrandom distribution of solvent within the copolymer matrix constitutes an important consideration. Similarly, the distribution of nanogels and nanoparticles, which are approximated here as large solvent molecules, in ordered block copolymers must be regulated for various nanotechnologies, especially those involving optics.²⁶

3.2 Methods

The objective of the present work is to establish, by use of SCFT, the effects of selectivity and size on the segregation of molecular and nanoscale species (S) in microphase-ordered ABA triblock copolymers. This copolymer architecture is chosen due to the ability of such macromolecules to form mechanically tough physical networks that can exhibit elastomeric (gel) behavior even at low copolymer fractions.²⁷ The SCFT employs a numerical procedure described elsewhere²⁸ to predict the equilibrium morphologies of microphase-ordered triblock copolymers. Simulation of a prescribed system begins with a random arrangement of potential fields for a symmetric copolymer (with $N_A = N_B$, where N_i is the number of repeat units of species i) of incompatibility α_{AB} ($= \chi_{AB}N$, where χ_{AB} is the Flory-Huggins interaction parameter between A and B, and $N = N_A + N_B$) and solvent volume fraction (Φ_S). The incompatibility between the A repeat units and the solvent S is similarly characterized by the parameter $\alpha_{AS} = \chi_{AS}N$, where χ_{AS} is the Flory-Huggins interaction parameter between A and S. Finally, we have chosen to compute the third incompatibility required (α_{BS}) from $\alpha_{AB} - \alpha_{AS}$. The solvent selectivity (ε) is defined as $\alpha_{AS}/\alpha_{AB} = \alpha_{AS}/(\alpha_{AS} + \alpha_{BS})$ and ranges from 0.5 (nonselective, $\alpha_{BS} = \alpha_{AS}$) to 2.0 in our case (highly B-selective, $\alpha_{BS} < 0$). Upon progressive iteration of coupled diffusion and field equations, the system is permitted to relax into a nanostructure without prior knowledge of morphological symmetry.²⁹ Following the initial free energy relaxation, the dimensions of the simulation box are iteratively changed to further minimize the free energy. The true free energy minimum is obtained

when the nanostructure period (D) is commensurate with the size of the simulation box. In this study, all reported predictions are restricted to the lamellar morphology.

Representative examples of solvent volume distributions generated for strongly-segregated ABA copolymers ($\alpha_{AB} = 100$) containing 5 – 15 vol% of a slightly B-selective solvent ($\varepsilon = 1.0$) are displayed over a distance (x) of one D in Fig. 1a. In the three distributions portrayed, as well as those discussed in the following section, the molar volume of the solvent relative to that of the copolymer (v_r) is arbitrarily set equal to 0.01. Two important features are evident in Fig. 1a: (i) the solvent selectively occupies the B lamella located in the center portion of the figure, and (ii) a fraction of the solvent (responsible for the visible peaks) segregates to the interfaces separating adjacent lamellae. The physical reason underlying interfacial solvent accumulation is that the solvent molecules screen energetically unfavorable A-B contacts. Such localization occurs, however, at the expense of solvent entropy, in which case the equilibrium interfacial solvent excess reflects the balance of these two competing effects. Since the entropic penalty depends on the volume of the solvent molecule, a change in v_r will clearly alter the balance and, hence, the solvent distribution, as demonstrated later. Half of each $\Phi_S(x)$ distribution (symmetric about $x/D = 0.5$) can be represented as the sum of a Gaussian profile (to account for interfacial excess) and a background that emulates the interfacial profile of the copolymer, *viz.*, $\Phi_S(x) = \phi(x) + \phi^*(x)$, where

$$\phi(x) = \frac{1}{2} \left[\Phi_{\max} + \Phi_{\min} + (\Phi_{\max} - \Phi_{\min}) \tanh \left(\frac{x - x_{c1}}{w_1} \right) \right] \quad (1)$$

and

$$\phi^*(x) = C e^{-(x-x_{c2})^2/w_2^2} \quad (2)$$

Here, Φ_{\max} and Φ_{\min} denote the minimum and maximum values of $\Phi_S(x)$ within the A and B lamellae, respectively, C is the background of the Gaussian profile, and x_{c_j} and w_j ($j = 1$ for the interfacial background and 2 for the interfacial excess) correspond to the center position and width, respectively, of the expressions given in Eqs. 1 and 2.

3.3 Results and Discussion

These decoupled contributions to a representative SCFT solvent distribution are provided for illustrative purposes in Fig. 1b and define the interfacial excess (ϕ^*) as $(2/D) \int_0^{D/2} \phi^*(x) dx$. Values of ϕ^* extracted in this fashion by nonlinear Levenberg-Marquardt regression analysis of $\Phi_S(x)$ are presented as functions of Φ_S and α_{AB} for nonselective solvents ($\varepsilon = 0.5$) in Fig. 2a, moderately B-selective solvents ($\varepsilon = 1.0$) in Fig. 2b and strongly B-selective solvents ($\varepsilon = 1.5$ and 2.0 in the inset) in Fig. 2c. It is important to note that increases in ϕ^* are due to convoluted increases in both C and interfacial width. In all cases, ϕ^* is predicted to increase initially with increasing Φ_S , and this increase is most pronounced for highly incompatible copolymers. In several cases a maximum in $\phi^*(\Phi_S)$ is apparent, while in other cases the predictions abruptly end as the swollen lamellae undergo an order-order transition into cylinders at high α_{AB} or complex morphologies (e.g., perforated lamellae) at low α_{AB} . These solvent-induced changes in interfacial chain packing and, hence, curvature becomes increasingly favored as α_{AB} and

ϵ increase. In fact, the results provided in Fig. 2 reveal that swollen lamellae are not stable under some of the solvent conditions examined, indicating that the phase diagram for solvated block copolymers is sensitive to changes in temperature (via α_{AB}) and solvent concentration/selectivity, in agreement with experimental observations.^{8,22} At constant Φ_s , the dependence of ϕ^* on solvent selectivity is evident in Fig. 3, which confirms that ϕ^* increases with increasing ϵ for a given α_{AB} and can, at sufficiently high ϵ , account for a nontrivial fraction of the solvent incorporated within the copolymer matrix.

As alluded to earlier, another consideration governing solvent distribution within an ordered block copolymer is the relative size of the solvent. This issue is encountered, for instance, when metal salts,³⁰ oligomeric aliphatic oils²⁷ or bulky aromatic compounds (e.g., asphaltenes³¹ or dyes) are incorporated into nanostructured polymers. As suggested earlier, relatively large "solvent" molecules are envisaged as discrete (non-chain-like) organic nanogels or inorganic nanoparticles. Previous experimental¹⁴⁻¹⁶ and theoretical^{32,33} treatments have demonstrated that the distribution of nanoparticles within nanostructured block copolymers can be controlled via selective surface treatment. Here, we address the importance of size under two different selectivity conditions. In Fig. 4a, small nonselective additives are uniformly distributed in the A- and B-lamellae comprising the copolymer nanostructure at a solvent concentration of 10 vol%. An order of magnitude increase in v_r is accompanied by interfacial segregation similar to that established in Fig. 1. A further increase in v_r promotes considerable interfacial segregation at the cost of reducing the solvent concentration in both lamellae, indicating

that it is possible to position nonselective nanogels or nanoparticles with precision along the interfacial regions of the copolymer matrix. An increase in B-selectivity, on the other hand, yields a very different distribution, as observed in Fig. 4b. One noteworthy feature of this distribution is that the concentration of additive in the A-lamellae decreases to nearly zero as v_r is progressively increased.

While the moderately B-selective additives in Fig. 4b continue to reside along the copolymer interfaces, they are also predicted to align along the center of each B-lamella, as evidenced by the third maximum in the B-lamella that has, until now, been marginal or absent altogether. The results displayed in Fig. 4 confirm that the size and selectivity of an added nanoscale species can drive either interfacial segregation, center alignment or a combination of the two. Earlier experimental studies³⁴ confirm that the incorporation of particle species differing in size and surface functionalization (Au and SiO₂) at comparable concentrations (~4 vol%) into a high-molecular-weight polystyrene-*b*-poly(ethylene-*co*-propylene) (PS-*b*-PEP) diblock copolymer promotes both modes of localization. Interestingly, relative particle size alone can dictate nanoparticle segregation behavior. Figure 5a depicts the equilibrium morphology of a blend containing poly-disperse gold nanocrystals coated with 900 Da oligostyrene sequestered within the PS domains of a PS-*b*-PEP-*b*-PS triblock copolymer (96 kDa molecular weight and 46 wt% PS).³⁵ The transmission electron micrograph reveals the segregation of larger particles (particle radius $R_p > 5$ nm) to the center of the PS lamellae, whereas small particles ($R_p < 3$ nm) uniformly distribute throughout the PS lamellae. Quantitative particle counting analysis performed on images similar to the one shown in Fig. 5a demonstrates that the

primary features of the particle distribution are correctly predicted by the SCFT model assuming weak block selectivity of the particles. Small particles uniformly distribute within the PS domains, but tend to localize along the interfaces (resulting in an interfacial excess, *cf.* Fig. 5b). Larger particles, on the other hand, preferentially segregate to the center of the PS domains (*cf.* Fig. 5c).

Although the experimental findings provided in Fig. 5 are not perfectly matched to the SCFT results reported in Fig. 4, they serve to verify that the size of nanoscale additives relative to the characteristic size of the copolymer nanostructure (which, in turn, reflects the size of the copolymer) can have a pronounced effect on nanoparticle segregation within the confines of a microphase-ordered block copolymer, as previously predicted³⁶ by SCFT in conjunction with density functional theory. Thus, we have demonstrated, through the use of SCFT alone, that the concentration, selectivity and size of molecular or nanoscale additives profoundly impact the segregation of these species in nanostructured block copolymer matrices. While such segregation can affect the phase behavior of concentrated block copolymer solutions during initial preparation or upon solvent-regulated annealing, knowledge of such segregation is also important in the development of (i) solvated block copolymers intended for sensory, separation or delivery applications, and (ii) block copolymer nanocomposites designed for nanotechnologies involving nonlinear optics.

3.4 Conclusions

The SCFT results reported here establish, in systematic and quantitative fashion, the relative importance of each of these considerations on segregation characteristics such as interfacial excess, and we provide limited experimental evidence to support our predictions. Nonrandom segregation of solvent molecules and particles at nanoscale dimensions in microphase-ordered block copolymers affords valuable insight into the molecular thermodynamics of self-organized media, as well as an attractive opportunity to tailor copolymer properties through the use of (in)organic additives varying in size and block selectivity.

3.5 Acknowledgements

This work was supported by the Research Council of Norway under the NANOMAT Program, the U. S. Department of Commerce through the National Textiles Center, the STC Program of the National Science Foundation under Agreement No. CHE-9876674, and the Center for Integrated Nanotechnologies (CINT). Research at Los Alamos National Laboratory is performed under the auspices of the National Nuclear Security Administration of the U. S. Department of Energy under Contract No. DE-AC52-06NA25396.

3.6 References

1. Discher, D. E.; Eisenberg, A. *Science* **2002**, *297*, 967. Falus, P.; Xiang, H.; Borthwick, M. A.; Russell, T. P.; Mochrie, S. G. J. *Phys. Rev. Lett.* **2004**, *93*, 145701.
2. Lin, J. J.; Bates, F. S.; Hammer, D. A.; Silas, J. A. *Phys. Rev. Lett.* **2005**, *95*, 026101. Jain, S.; Gong, X.; Scriven, L. E.; Bates, F. S. *Phys. Rev. Lett.* **2006**, *96*, 138304.
3. Hamley, I. W. *The Physics of Block Copolymers*; Oxford University Press: New York, 1998.
4. Bates, F. S.; Fredrickson, G. H. *Phys. Today* **1999**, *52*, 32.
5. Hadjichristidis, N.; Pispas, S.; Floudas, G. A. *Block Copolymers: Synthetic Strategies, Physical Properties, and Applications*; Wiley-Interscience: New York, 2003.
6. Alexandridis, P.; Spontak, R. J. *Curr. Opin. Colloid Interface Sci.* **1999**, *4*, 130.
7. Hamley, I. W. *Block Copolymers in Solution: Fundamentals and Applications*; John Wiley & Sons: Hoboken, NJ, 2005.
8. Hanley, K. J.; Lodge, T. P.; Huang, C.-I. *Macromolecules* **2000**, *33*, 5918. Lodge, T. P.; Pudil, B.; Hanley, K. J. *Macromolecules* **2002**, *35*, 4707. Lodge, T. P.; Hanley, K. J.; Pudil, B.; Alahapperuma, V. *Macromolecules* **2003**, *36*, 816.
9. Spontak, R. J.; Patel, N. P. In *Developments in Block Copolymer Science and Technology* (Hamley, I. W., ed.); Wiley: New York, 2004; pp. 159-212.
10. Winey, K. I.; Thomas, E. L.; Fetters, L. J. *Macromolecules* **1992**, *25*, 422, 2645.

11. Bates, F. S.; Maurer, W. W.; Lipic, P. M.; Hillmyer, M. A.; Almdal, K.; Mortensen, K.; Fredrickson, G. H.; Lodge, T. P. *Phys. Rev. Lett.* **1997**, *79*, 849.
12. Court, F.; Hashimoto, T. *Macromolecules* **2001**, *34*, 2536; **2002**, *35*, 2566.
13. Zhang, Q.; Remsen, E. E.; Wooley, K. L. *J. Am. Chem. Soc.* **2000**, *122*, 3642.
Hawker, C. J.; Bosman, A. W.; Harth, E. *Chem. Rev.* **2001**, *101* 3661. Gurr, P. A.; Qiao, G. G.; Solomon, D. H.; Harton, S. E.; Spontak, R. J. *Macromolecules* **2003**, *36*, 5650. Kuckling, D.; Vo, C. D.; Adler, H.-J. P.; Volkel, A.; Colfen, H. *Macromolecules* **2006**, *39*, 1585.
14. Jeng, U. S.; Sun, Y. S.; Lee, H. J.; Hsu, C. H.; Liang, K. S.; Yeh, S. W.; Wei K. H. *Macromolecules* **2004**, *37*, 4617.
15. Kim, B. J.; Chiu, J. J.; Yi, G. R.; Pine, D. J.; Kramer E. J. *Adv. Mater.* **2005**, *17*, 2618. Chiu, J. J.; Kim, B. J.; Kramer, E. J.; Pine, D. J. *J. Am. Chem. Soc.* **2005**, *127*, 5036.
16. Bockstaller, M. R.; Thomas, E. L. *Phys. Rev. Lett.* **2004**, *93*, 166106. Bockstaller, M. R.; Mickiewicz, R. A.; Thomas, E. L. *Adv. Mater.* **2005**, *17*, 1331.
17. Shull, K. R.; Winey, K. I.; Thomas, E. L.; Kramer, E. J. *Macromolecules* **1991**, *24*, 2748. Genzer, J.; Composto, R. J. *Macromolecules* **1998**, *31*, 870.
18. Matsen, M. W. *Macromolecules* **1995**, *28*, 5765; **2003**, *36*, 9647.
19. Kane, L.; Norman, D. A.; White, S. A.; Matsen, M. W.; Satkowski, M. M.; Smith, S. D.; Spontak, R. J. *Macromol. Rapid Commun.* **2001**, *22*, 281.

20. Hashimoto, T.; Shibayama, M.; Kawai, H. *Macromolecules* **1983**, *16*, 1093.
Shibayama, M.; Hashimoto, T.; Hasegawa, H.; Kawai, H. *Macromolecules* **1983**, *16*, 1427.
21. Hong, K. M.; Noolandi, J. *Macromolecules* **1981**, *14*, 727. Whitmore, M. D.;
Noolandi, J. *J. Chem. Phys.* **1990**, *93*, 2946. Banaszak, M.; Whitmore, M. D.
Macromolecules **1992**, *25*, 3406.
22. Lodge, T. P.; Hamersky, M. W.; Hanley, K. J.; Huang, C.-I. *Macromolecules* **1997**,
30, 6139.
23. Naughton, J. R.; Matsen, M. W. *Macromolecules* **2002**, *35*, 5688.
24. Hong, S.-U.; Laurer, J. H.; Zielinski, J. M.; Samseth, J.; Smith, S. D.; Duda, J. L.;
Spontak, R. J. *Macromolecules* 1998, **31**, 2174.
25. Kim, S. H.; Misner, M. J.; Russell, T. P. *Adv. Mater.* **2004**, *16*, 2119. Kiff, F. T.;
Richards, R. W.; Thompson, R. L. *Langmuir* **2004**, *20*, 4465. Hillmyer, M. A. *Adv.*
Polym. Sci. **2005**, *190*, 137.
26. Park, C.; Yoon, J.; Thomas, E. L. *Polymer* **2003**, *44*, 6725.
27. Laurer, J. H.; Khan, S. A.; Spontak, R. J.; Satkowski, M. M.; Grothaus, J. T.; Smith,
S. D.; Lin, J. S. *Langmuir* **1999**, *15*, 7947.
28. Tzeremes, G.; Rasmussen, K. Ø.; Lookman, T.; Saxena, A. *Phys. Rev. E* **2002**, *65*,
041806. Rasmussen, K. Ø.; Kalosakas, G. *J. Polym. Sci. B: Polym. Phys.* **2002**, *40*,
1777.
29. Drolet, F.; Fredrickson, G. H. *Phys. Rev. Lett.* **1999**, *83*, 4317; *Macromolecules*
2001, *34*, 5317.

30. Bronstein, L. M.; Chernyshov, D. M.; Valetsky, P. M.; Wilder, E. A.; Spontak, R. J. *Langmuir* **2000**, *16*, 8221.
31. Adedeji, A.; Grünfelder, T.; Bates, F. S.; Macosko, C. W.; Stroup-Gardiner, M.; Newcomb, D. E. *Polym. Eng. Sci.* **1996**, *36*, 1707.
32. Thompson, R. B.; Ginzburg, V. V.; Matsen, M. W.; Balazs A. C. *Science* **2001**, *292*, 2469. Thompson, R. B.; Ginzburg, V. V.; Matsen, M. W.; Balazs, A. C. *Macromolecules* **2002**, *35*, 1060. Thompson, R. B.; Rasmussen, K. Ø.; Lookman, T. *Nano Lett.* **2004**, *4*, 2455.
33. Haryono, A.; Binder, W. H. *Small* **2006**, *5*, 600.
34. Bockstaller, M. R.; Lapetnikov, Y.; Margel, S.; Thomas, E. L. *J. Am. Chem. Soc.* **2003**, *125*, 5276.
35. Gold nanocrystals with an approximately normal size distribution and a mean particle diameter ($\langle d \rangle$) of 4 ± 3 nm were obtained by blending nearly equal amounts of two particle fractions ($\langle d \rangle_1 = 3.5 \pm 1.5$ nm and $\langle d \rangle_2 = 4.5 \pm 1$ nm) synthesized according to a modified Brust-Schiffrin method as described elsewhere (Bockstaller, M.; Kolb, R.; Thomas, E. L. *Adv. Mater.* **2001**, *13*, 1783). Larger particle sizes were obtained by reducing the amount of sodium borohydride to 85% of the amount used previously. Thermogravimetric analysis confirmed that, within the experimental error, differences in the grafting density of both samples were negligible. The development of synthetic methods that facilitate concurrent control of both particle size and grafting density would be highly desirable.
36. Thompson, R. B.; Lee, J. Y.; Jasnow, D.; Balazs, A. C. *Phys. Rev. E* **2002**, *66*,

031801. Lee, J. Y.; Thompson, R. B.; Jasnow, D.; Balazs, A. C. *Faraday Disc.* **2003**,
123, 121.

3.7 List of Figure Captions

Figure 3.1 In (a), solvent volume-fraction distributions generated by SCFT of a highly incompatible ($\alpha_{AB} = 100$), compositionally and molecularly symmetric ABA triblock copolymer containing three different concentrations of a moderately B-selective solvent ($\epsilon = 1.0$). Variation in the copolymer interfacial width, which broadens with increasing solvent concentration, is not depicted here for simplicity. Half of one $\Phi_S(x)$ distribution (SCFT calculations as circles and the nonlinear regression as the solid line), along with its individual contributions generated by Eqs. 1 (dashed line) and 2 (heavy solid line) in the text, is depicted in (b). The interfacial excess (ϕ^*) is labeled.

Figure 3.2 Dependence of the interfacial excess (ϕ^*) on bulk solvent concentration (Φ_S) for systems differing in solvent selectivity (ϵ): (a) 0.5, nonselective; (b) 1.0, slightly B-selective; and (c) 1.5, strongly B-selective. Note the change in Φ_S range in (c). The inset in (c) with calculations for $\epsilon = 2.0$ has the same ϕ^* and Φ_S ranges as (c). The copolymer incompatibility (α_{AB}) values examined include 25 (solid line), 50 (dashed line), 75 (dotted line) and 100 (heavy solid line).

Figure 3.3 Interfacial excess (ϕ^*) as a function of solvent selectivity (ϵ) at $\Phi_S = 0.10$ for four copolymer incompatibility (α_{AB}) values (labeled). The solid lines are linear regressions to calculations at constant α_{AB} with three or more points.

Figure 3.4 Solvent volume-fraction distributions generated by SCFT of a microphase-ordered ABA triblock copolymer ($\alpha_{AB} = 50$) swollen with 10 vol% of a nonselective solvent ($\varepsilon = 0.5$) in (a) and a moderately B-selective solvent ($\varepsilon = 1.0$) in (b). The relative solvent volume (v_r) is varied by two orders of magnitude — 0.001 (dotted line), 0.01 (dashed line), 0.05 (solid line) and 0.1 (heavy solid line) — to illustrate the effect of solvent size on solvent segregation.

Figure 3.5 In (a), bright-field transmission electron microscopy (TEM) image of an unstained PS-PEP-PS/AuPS composite with ~ 2 vol% Au particles, which appear as dark dots within the PS domains. Shown in the inset is an enlargement that illustrates the enrichment of small particles along the lamellar interfaces. Imaging has been performed on a JEOL 2000FX electron microscope operated at 200 kV. The spatial distribution of Au particles with $R_p < 3$ nm measured along the [001] direction is provided in (b) and reveals that the particles uniformly distribute within the PS lamellae, but preferentially locate along the PS/PEP interfaces. The analogous distribution of particles with $R_p > 5$ nm measured along the [001] direction is included in (c) and confirms that these particles tend to segregate along the center plane of the PS domains, as observed in (a).

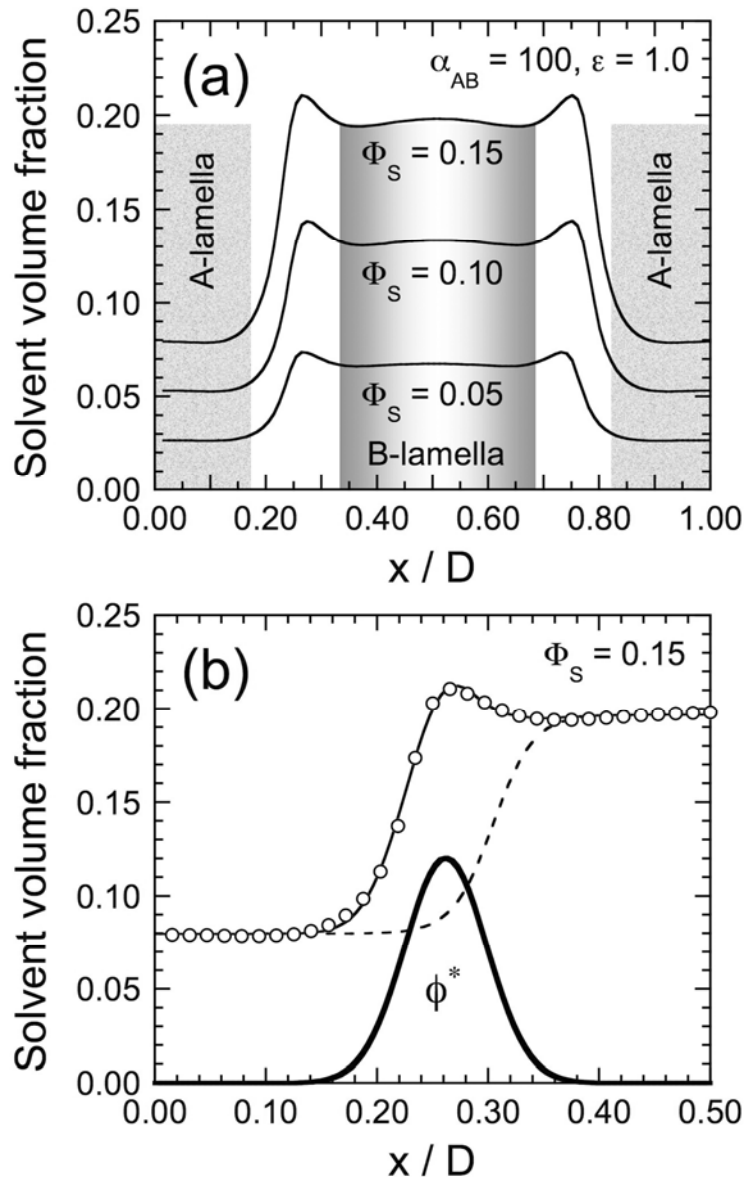


Figure 3.1. In (a), solvent volume-fraction distributions generated by SCFT of a highly incompatible ($\alpha_{AB} = 100$), compositionally and molecularly symmetric ABA triblock copolymer containing three different concentrations of a moderately B-selective solvent ($\epsilon = 1.0$). Variation in the copolymer interfacial width, which broadens with increasing solvent concentration, is not depicted here for simplicity. Half of one $\Phi_s(x)$ distribution (SCFT calculations as circles and the nonlinear regression as the solid line), along with its individual contributions generated by Eqs. 1 (dashed line) and 2 (heavy solid line) in the text, is depicted in (b). The interfacial excess (ϕ^*) is labeled.

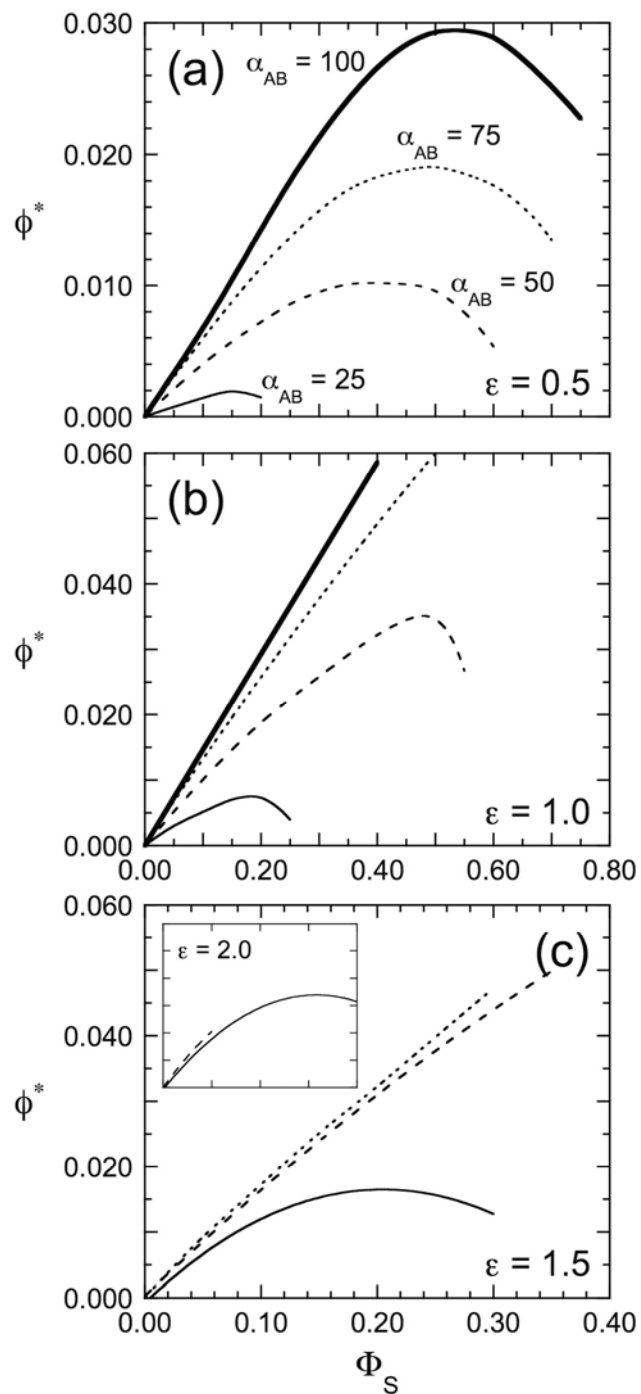


Figure 3.2. Dependence of the interfacial excess (ϕ^*) on bulk solvent concentration (Φ_S) for systems differing in solvent selectivity (ϵ): (a) 0.5, nonselective; (b) 1.0, slightly B-selective; and

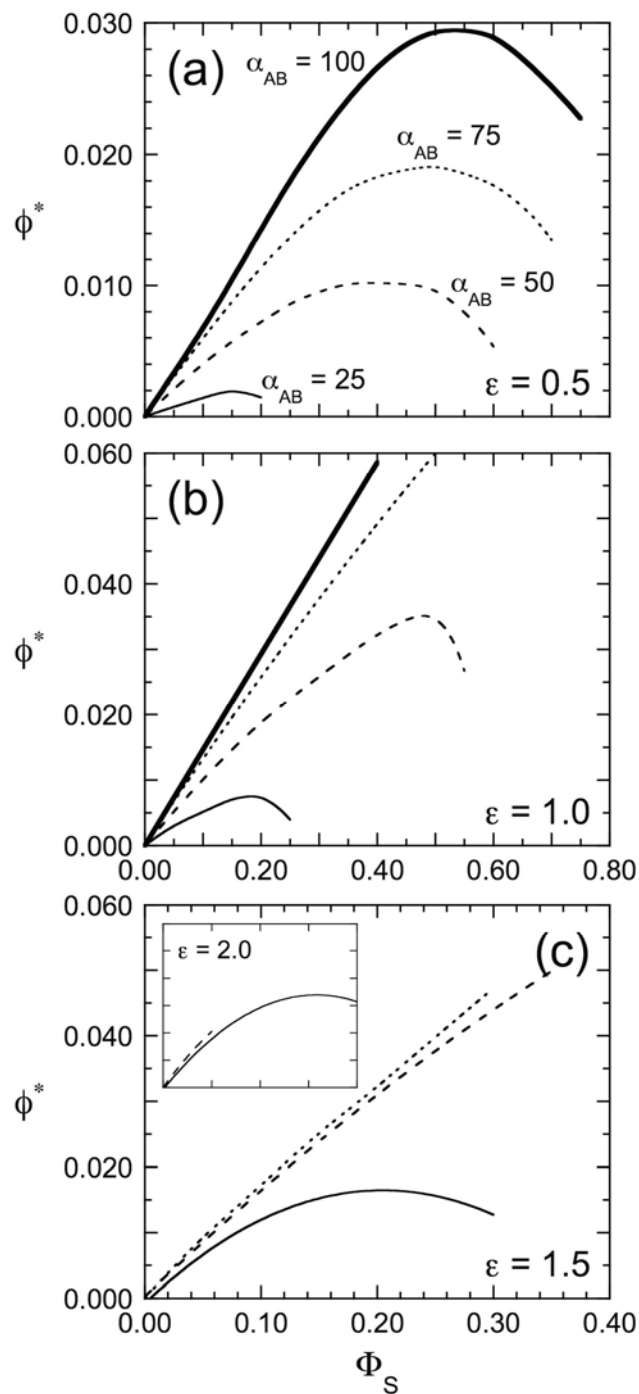


Figure 3.2c. 1.5, strongly B-selective. Note the change in Φ_S range in (c). The inset in (c) with calculations for $\epsilon = 2.0$ has the same ϕ^* and Φ_S ranges as (c). The copolymer incompatibility (α_{AB}) values examined include 25 (solid line), 50 (dashed line), 75 (dotted line) and 100 (heavy solid line).

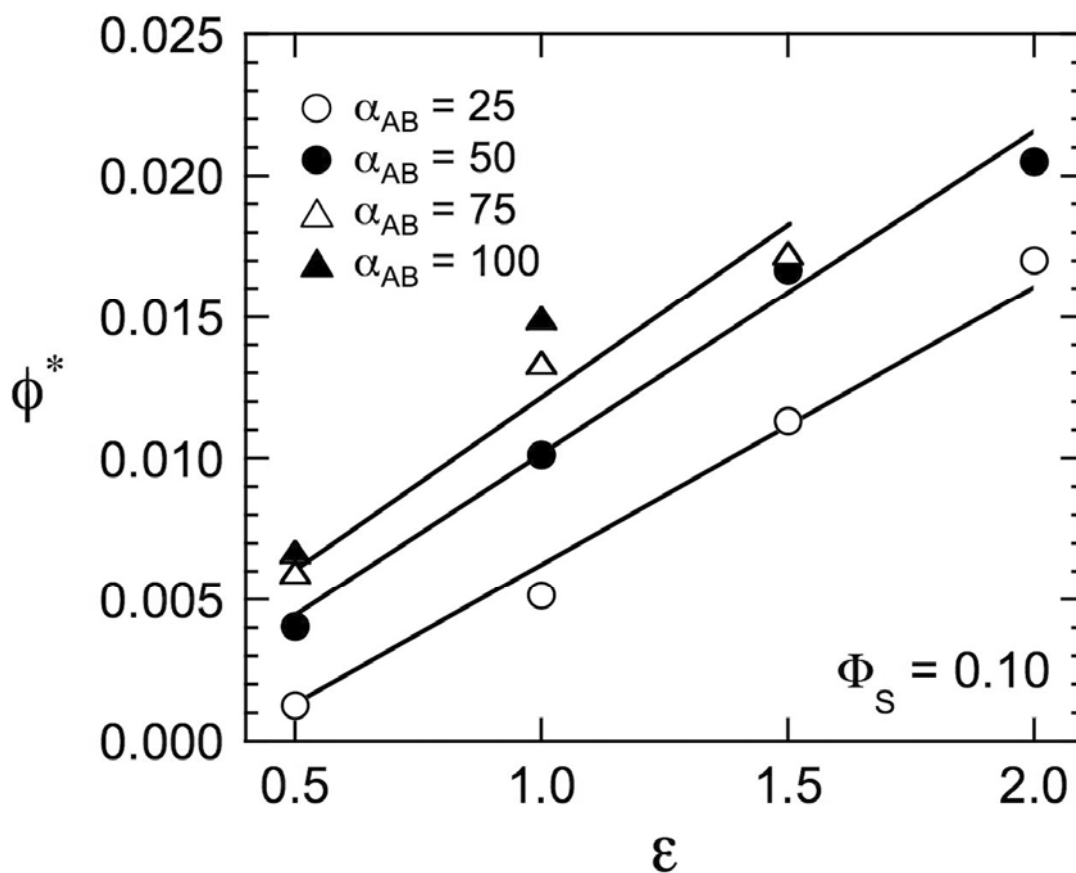


Figure 3.3. Interfacial excess (ϕ^*) as a function of solvent selectivity (ϵ) at $\Phi_S = 0.10$ for four copolymer incompatibility (α_{AB}) values (labeled). The solid lines are linear regressions to calculations at constant α_{AB} with three or more points.

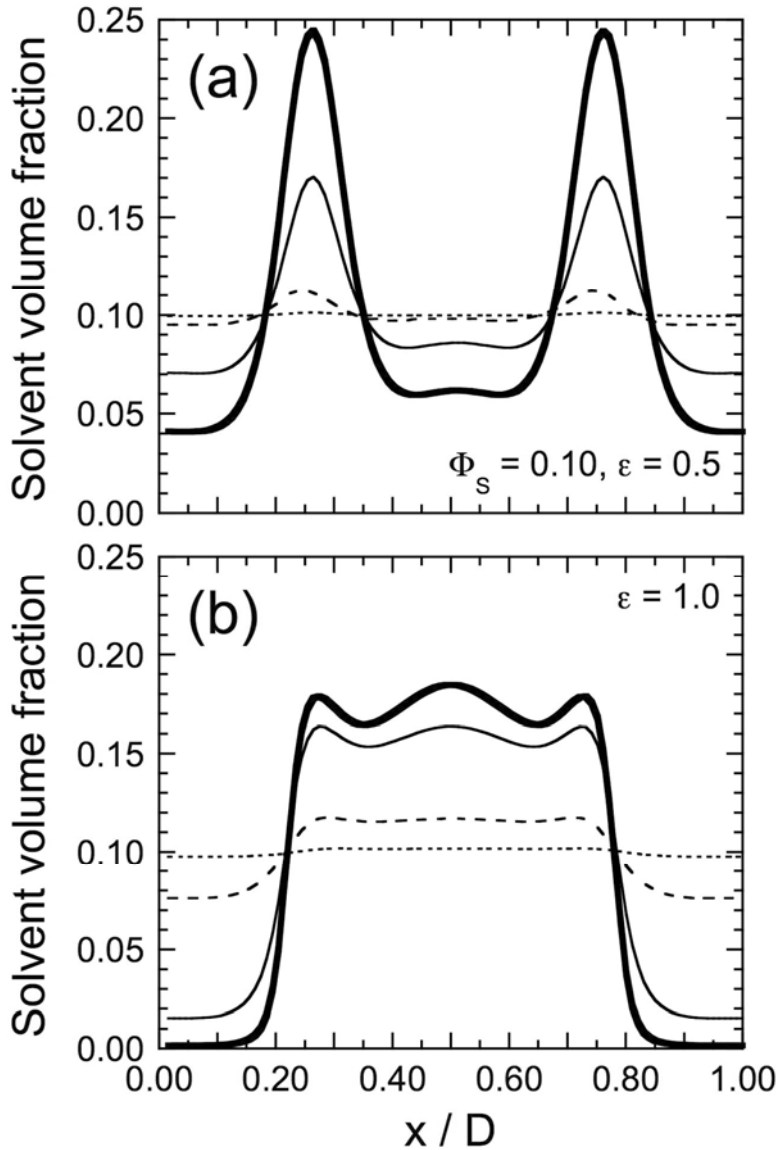


Figure 3.4. Solvent volume-fraction distributions generated by SCFT of a microphase-ordered ABA triblock copolymer ($\alpha_{AB} = 50$) swollen with 10 vol% of a nonselective solvent ($\epsilon = 0.5$) in (a) and a moderately B-selective solvent ($\epsilon = 1.0$) in (b). The relative solvent volume (v_r) is varied by two orders of magnitude — 0.001 (dotted line), 0.01 (dashed line), 0.05 (solid line) and 0.1 (heavy solid line) — to illustrate the effect of solvent size on solvent segregation.

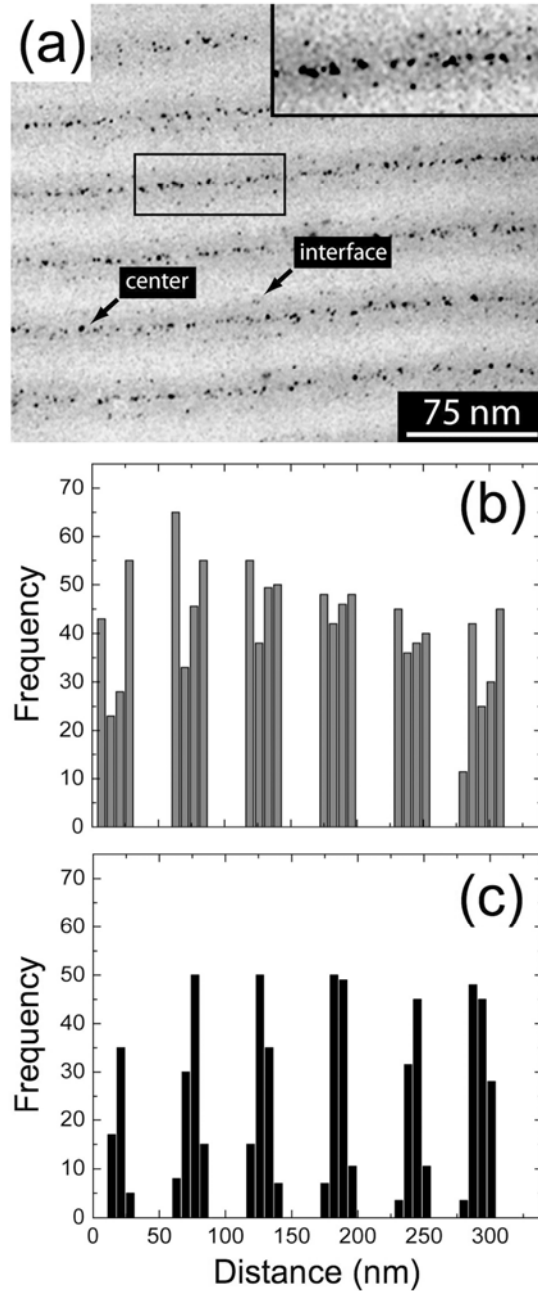


Figure 3.5. In (a), bright-field transmission electron microscopy (TEM) image of an unstained PS-PEP-PS/AuPS composite with ~ 2 vol% Au particles, which appear as dark dots within the PS domains. Shown in the inset is an enlargement that illustrates the enrichment of small particles along the lamellar interfaces.

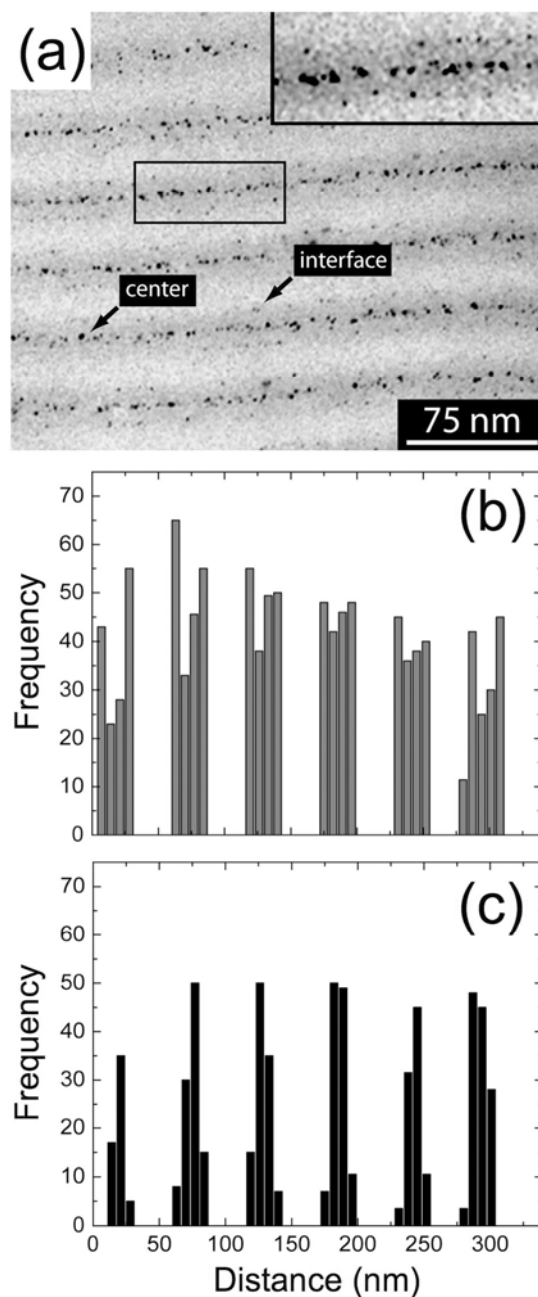


Figure 3.5b,c. Imaging has been performed on a JEOL 2000FX electron microscope operated at 200 kV. The spatial distribution of Au particles with $R_p < 3$ nm measured along the [001] direction is provided in (b) and reveals that the particles uniformly distribute within the PS lamellae, but preferentially locate along the PS/PEP interfaces. The analogous distribution of particles with $R_p > 5$ nm measured along the [001] direction is included in (c) and confirms that these particles tend to segregate along the center plane of the PS domains, as observed in (a).

CHAPTER 4

NANOPARTICLE-REGULATED PHASE BEHAVIOR OF ORDERED BLOCK COPOLYMERS

Abstract

Although block copolymer motifs have received considerable attention as supramolecular templates for inorganic nanoparticles, experimental observations of a nanostructured diblock copolymer containing inorganic nanoparticles – supported by theoretical trends predicted from a hybrid self-consistent field/density functional theory – confirm that nanoparticle size and selectivity can likewise stabilize the copolymer nanostructure by increasing its order-disorder transition temperature.

(This chapter will be published in its entirety:
Gaines, M.K.; Smith, S. D.; Samseth, J.; Bockstaller, M. R.; Thompson, R. B.;
Rasmussen, K. Ø.; Spontak, R. J. Nanoparticle-Regulated Phase Behavior of Ordered
Block Copolymers *Soft Matter* **2008** 4, 1-5.)

4.1 Introduction

Polymer nanocomposites remain at the forefront of advanced materials research due to the wide range of properties that can be realized by dispersing inorganic nanoparticles in a polymeric matrix at relatively low concentrations.¹ In addition to improving bulk thermo-mechanical properties,²⁻⁵ nanocomposites can be used in drug encapsulation,⁶ optics⁷ and microelectronics,⁸ as well as in the nanoscale design of Li batteries⁹ and gas-separation membranes.^{10,11} The spatial distribution of nanoparticles within the polymer constitutes a critically important consideration in nanotechnologies involving, for instance, photonic crystals,¹² and efforts to meet this challenge have relied on microphase-ordered block copolymers as mesoscale templates.^{3,13-16} Diblock copolymer molecules consist of two long, contiguous sequences that, if sufficiently incompatible, spontaneously self-assemble to produce ordered nanostructures, *viz.*, spheres on a body-centered (or face-centered¹⁷) cubic lattice, cylinders on a hexagonal lattice, bicontinuous channels and alternating lamellae.¹⁸ Because of their ability to self-organize, copolymers with specific morphologies, dimensions or phase behavior (expressed in terms of the order-disorder transition, ODT) continue to attract attention in emerging nanotechnologies.¹⁹⁻²¹ Such systems can be tailored by either (*i*) synthesizing molecules differing in composition or repeat unit attributes,²² or (*ii*) incorporating a miscible organic species (e.g., a selective solvent, parent homopolymer or second copolymer) that alters microdomain swelling and/or interfacial chain packing.²³

Previous studies of spherical nanoparticles templated by microphase-ordered block copolymers have established that the spatial distribution of the nanoparticles is sensitive

to factors such as concentration, selectivity and size.^{14,16,24} Related results that are central to the objective of the present study are summarized in Fig. 1 by segmental distributions generated from a hybrid self-consistent field (SCF) and density functional (DF) theory for an AB diblock copolymer (exhibiting a lamellar morphology of period D) containing spherical nanoparticles. If the nanoparticles are sufficiently small in radius (R) relative to the size of the copolymer morphology, which is dictated by the gyration radius of the copolymer molecule (R_g), they tend to distribute uniformly throughout the copolymer nanostructure and effectively behave as diluents irrespective of block selectivity (*cf.* Figs. 1a-b and the corresponding enlargements). When the magnitude of R/R_g is increased (Figs. 1c-d), however, block selectivity can be used to drive the nanoparticles either to the interface (neutral) or the lamellar midplane (selective), insofar as macrophase separation does not occur.^{25,26}

While we shall return to the density distributions displayed in Fig. 1 when we discuss the physical mechanism by which nanoparticles affect copolymer phase behavior, it is important to recognize at this juncture that the addition of selective nanoparticles to a block copolymer can likewise alter how block copolymer molecules self-organize.²⁶⁻²⁸ That is, by acting as impenetrable obstacles that affect system energy and translational entropy, nanoparticles can alter chain packing⁹ and direct copolymer assembly, thereby altering the stability of various copolymer morphologies. This observation qualitatively agrees with earlier SCF²⁹ studies wherein the copolymer ODT temperature (T_{ODT}) is predicted to decrease with increasing nanoparticle concentration. Discontinuous molecular dynamics simulations³⁰ suggest, however, that the dependence of T_{ODT} on

nanoparticle size and selectivity may be more complicated. The objectives of this study are to (i) probe the phase behavior of block copolymer nanocomposites containing nanoparticles varying in concentration and selectivity and (ii) explore the phase behavior of such systems predicted by a hybrid SCF/DF theory.¹³

4.2 Experimental

A poly(styrene-*b*-methyl methacrylate) (SM) diblock copolymer was synthesized via sequential living anionic polymerization of the S block in cyclohexane at 60°C, followed by the M block in tetrahydrofuran at -78°C, with *sec*-butyl lithium as the initiator. According to ¹H NMR and GPC analyses, the block masses were 13 kDa each, and the polydispersity index was 1.05. Three grades of functionalized fumed silica (FS), obtained in powder form from Degussa Corp. (Parsippany, NJ), represented clustered nanoparticles⁹ varying in surface selectivity: hydroxyl-terminated (OH), methacrylate-terminated (MA) and octyl-terminated (C8). In all cases, the primary particle size was ~12 nm. Native colloidal silica (CS-OH) particles with an average diameter of 10-15 nm were provided as a suspension (20% solids) in dimethylacetamide by Nissan Chemicals (Houston, TX). Oligostyrene-coated colloidal silica (CS-OS) particles with an average core diameter of ~20 nm were prepared by grafting oligostyrene (10 repeat units) onto colloidal silica by atom-transfer radical polymerization (ATRP).³¹ Specimens for rheometry were fabricated by first ultrasonicated the nanoparticles (at a mass fraction w_p relative to the copolymer) for 30 min in toluene, followed by copolymer dissolution and then air- and vacuum-drying, all performed at ambient temperature. No copolymer

degradation due to ultrasonication was detected according to GPC analysis of the resultant films. Dynamic rheology was performed on an ARES strain-controlled rheometer operated at 1 rad/s and 2% strain amplitude to ensure linear viscoelasticity. Discs measuring 8 mm in diameter and 1 mm thick were melt-pressed at 150°C from dried films and heated between parallel plates to 220°C under nitrogen. For each material, T_{ODT} was established from the inflection of a clearly discernible reduction in the dynamic elastic shear modulus (G') during isochronal temperature sweeps performed at a constant cooling rate of 1°C/min.

4.3 Results and Discussion

According to dynamic rheological measurements, T_{ODT} for the neat SM copolymer ($w_p = 0$) is $186 \pm 1^\circ\text{C}$. This temperature range is displayed as the shaded regions in Fig. 2 for both clustered (FS) and discrete (CS) nanoparticles. Measured values of T_{ODT} remain relatively constant within experimental uncertainty up to $w_p = 0.01$ for all the FS-based nanoparticle aggregates, of which only the FS-C8 is shown in Fig. 2 for the sake of clarity. At higher nanoparticle concentrations (up to $w_p = 0.1$), T_{ODT} generally decreases, with the FS-C8 series, wherein the nanoparticles are effectively neutral relative to the S and M repeat units of the copolymer, exhibiting the most pronounced reduction. Two important facts must be recognized regarding these data. The first is that, while their primary particle size is ~ 12 nm, FS-based nanoparticles exist for the most part (although not exclusively) as aggregate clusters that can measure up to hundreds of nanometers in size.⁹ At the concentrations of interest here, individual nanoparticles and small clusters

are observed. In addition, the size ratio R/R_g must be considered. The value of R_g discerned from $\sqrt{(\ell_S^2 N_S + \ell_M^2 N_M)}/6$, where ℓ_S and ℓ_M denote the statistical segment lengths of S and M (0.72 and 0.68 nm, respectively³²) and N_i ($i = S$ or M) is the degree of polymerization of block i , is about 4.6 nm, which translates into $R/R_g \approx 1.3$ relative to the primary FS nanoparticle size.

Although these cluster and size considerations complicate interpretation, the results displayed in Fig. 2 suggest one of two scenarios at play. In the first, the FS-based nanoparticles do not induce a measurable reduction in T_{ODT} at low w_p , with selective nanoparticles (MA- and OH-terminated) promoting a less pronounced decrease in T_{ODT} than neutral nanoparticles at high w_p . The second scenario is that the fused nanoparticle clusters aggregate⁹ or possibly macrophase-separate from the copolymer, thereby leaving the copolymer matrix and its phase behavior (including T_{ODT}) largely unaffected at low w_p . At high w_p , however, entropically-unfavorable confinement effects³³ adversely influence the stability of ordered copolymer molecules and lower T_{ODT} to marginally different extents based on selectivity. The complication of fused FS clustering is altogether eliminated in the case of discrete (CS) nanoparticles, for which T_{ODT} is included as a function of w_p in Fig. 2. As with the FS-based nanoparticles, the CS-OH nanoparticles eventually induce a reduction in T_{ODT} with increasing w_p . Addition of the CS-OS nanoparticles, however, promotes a slight, but measurable, increase in T_{ODT} up to $w_p = 0.01$, followed by a decrease thereafter. While aggregation of CS-OH nanoparticles may again explain the reduction in T_{ODT} apparent in Fig. 2, the maximum in T_{ODT} indicates that CS-OS nanoparticles can, under favorable experimental conditions,

improve microphase stability. The nanoparticle characteristics capable of inducing this possibility are examined below within the framework of a hybrid SCF/DF theory.¹³ It must be recognized, however, that the following analysis is intended to provide general physical trends and, while motivated by experimental observation, is not to be quantitatively compared to the data provided in Fig. 2.

A symmetric AB diblock copolymer with $N_A = N_B$ is chosen to complement the experimental systems investigated here. Simulation of a copolymer/nanoparticle system commences with a random arrangement of potential fields for a copolymer of sufficiently high copolymer incompatibility $\chi_{AB}N$ (where χ_{AB} is the Flory-Huggins interaction parameter between A and B repeat units, and $N = N_A + N_B$) to ensure microphase ordering into a lamellar morphology. The system is then modified with nanoparticles at a volume fraction ϕ_p . Incompatibility between the copolymer repeat units and nanoparticles is prescribed by assigned values of $\chi_{Ap}N$ and $\chi_{Bp}N$ ($= 25$). For a non-selective (neutral) nanoparticle, $\chi_{Ap}N = \chi_{Bp}N$. If $\chi_{Ap}N < \chi_{Bp}N$, then the nanoparticle is considered A-selective. Upon iteration of coupled diffusion and field equations,³⁴ the system relaxes into a nanostructure without prior knowledge of morphological symmetry. Once the copolymer nanostructure at its initially high $\chi_{AB}N$ is known, the value of χ_{AB} is systematically reduced until a periodic nanostructure no longer develops. At this set of conditions, $\chi_{AB}N = (\chi_{AB}N)_{ODT}$. Determination of the ODT in this fashion is somewhat non-standard. Usually, the free energy of the disordered state at a given $\chi_{AB}N$ and ϕ_p would be compared to the free energy of the ordered morphology to determine the precise location of the ODT. However, the hybrid SCF/DF theory employed here is not capable

of rigorously resolving the ODT since the excluded volume of the particles with respect to the polymer matrix becomes increasingly inaccurate as the ODT is approached.³⁵ Since it is not worthwhile to perform laborious free energy calculations for this reason, we have elected instead to employ the simpler procedure described above as it does yield the key variations that elucidate the effect of nanoparticles on block copolymer phase behavior.

The dependence of $(\chi_{AB}N)_{ODT}$ on ϕ_p for an AB diblock copolymer modified with nanoparticles ($R/R_g = 0.40$) at varying levels of nanoparticle selectivity ($\chi_{Ap}N$) is presented in Fig. 3 and reveals several important features. The first is that $(\chi_{AB}N)_{ODT}$ increases to a limit as the nanoparticles become less selective and $\chi_{Ap}N$ increases (*cf.* the inset in Fig. 3). The second is that, for highly selective nanoparticles with $\chi_{Ap}N \rightarrow 0$, $(\chi_{AB}N)_{ODT}$ decreases with increasing ϕ_p to a selectivity-dependent minimum and then increases thereafter. This minimum, which corresponds to a maximum in T_{ODT} (*cf.* Fig. 2) and shifts to lower ϕ_p with increasing $\chi_{Ap}N$, signifies the condition at which the energy responsible for a reduction in $(\chi_{AB}N)_{ODT}$ is matched by the translational entropy that favors microphase disorder. These results most importantly establish that, if the nanoparticles are sufficiently selective, they can induce an increase in T_{ODT} , which is consistent with our experimental findings. Complementary predictions for $(\chi_{AB}N)_{ODT}$ as a function of ϕ_p for A-selective nanoparticles ($\chi_{Ap}N = 0$) varying in size (R/R_g) are included in Fig. 4, and confirm that a reduction in $(\chi_{AB}N)_{ODT}$ is only achieved in the limit of relatively large nanoparticles (conditions corresponding to copolymer/nanoparticle macrophase separation are not considered here). In this limit, the nanoparticles tend to

locate along the lamellar midplane (illustrated in Fig. 4) and stabilize the microdomains. As R/R_g decreases, $(\chi_{AB}N)_{ODT}$ increases (*cf.* the inset in Fig. 4) to different extents depending on ϕ_p . Minima in $(\chi_{AB}N)_{ODT}(\phi_p)$ are again predicted, indicating that the selectivity-induced trade-off between energetic and entropic driving forces evident in Fig. 3 is also manifested by changing the size of highly selective nanoparticles.

At a fixed ϕ_p , numerous small nanoparticles possess greater translational entropy than fewer large nanoparticles. As a result, the smaller nanoparticles spread to maximize their entropy. This gives rise to the segmental distributions shown in Figs. 1a and 1b, wherein the nanoparticles are almost uniformly distributed throughout the matrix. Opposing this spreading tendency is the energetic tendency for neutral nanoparticles to localize along the interface¹⁶ to relieve interfacial tension (Fig. 1a). By doing so, neutral nanoparticles screen out A/B contacts, thereby diluting the segregation and promoting an increase in $(\chi_{AB}N)_{ODT}$ (decrease in T_{ODT}) with increasing ϕ_p . When nanoparticles are sufficiently large, however, they possess lower translational entropy and less spreading tendency, in which case energetic considerations dominate. As seen in Fig. 1c, large neutral nanoparticles aggregate at interfaces^{14,16} to reduce interfacial tension by decreasing A/B contacts and the driving force for copolymer demixing so that T_{ODT} decreases. If small nanoparticles are selective (Fig. 1b), their translational entropy continues to dominate, and the result is that T_{ODT} again decreases with increasing ϕ_p . Energy effects only prevail if selective nanoparticles are sufficiently large and limited in translational entropy. In this limit (Fig. 1d), the nanoparticles localize within microdomain cores¹⁶ (*cf.* the illustration

in Fig. 4) rather than at interfaces and act as "seeds," not diluents, for the copolymer by promoting demixing and an increase in T_{ODT} .

4.4 Conclusions

Contrary to the widely accepted influence of nanoparticles on ordered block copolymers, nanoparticles of appropriate size and selectivity can effectively serve as heterogeneous nucleation sites to improve the formation and stability of copolymer nanostructures that would ordinarily rely on homogeneous nucleation³⁶ during microphase ordering. This attribute, which distinguishes such nanoparticles from small nanoparticles or simple low-molar-mass molecules that interact only by van der Waals forces, is experimentally observed and theoretically predicted. In this spirit, we note that independent studies have shown that the stability of block copolymer nanostructures can likewise be enhanced through the incorporation of selective³⁷ or functional³⁸ homopolymers that remain mixed within (and do not macrophase-separate from) the copolymer nanostructure. Addition of selective nanoparticles to ordered block copolymers may therefore not only yield novel, spatially-modulated hybrid materials via nanoparticle assembly³⁹ for a wide variety of growing nanotechnologies, but also provide an alternative physical means by which to promote polymeric nanostructure development.

4.5 Acknowledgements

This work was supported by the Research Council of Norway under the NANOMAT

Program. Research at LANL is performed under the auspices of the National Nuclear Security Administration of the U. S. Department of Energy at Los Alamos National Laboratory under Contract No. DE-AC52-06NA25396. R. B. T. thanks the NSERC of Canada for financial support, and M. K. G. expresses her gratitude for a GEM Fellowship and a NOBCCChE Procter & Gamble Fellowship.

4.6 References

1. R. Krishnamoorti and R. A. Vaia (eds.), *Polymer Nanocomposites: Synthesis, Characterization and Modeling*, American Chemical Society, Washington, D. C., 2001.
2. P. Podsiadlo, A. K. Kaushik, E. M. Arruda, A. M. Waas, B. S. Shim, J. D. Xu, H. Nandivada, B. G. Pumplin, J. Lahann, A. Ramamoorthy and N. A. Kotov, *Science* 2007, **318**, 80.
3. M. R. Bockstaller, R. A. Mickiewicz and E. L. Thomas, *Adv. Mater.* 2005, **17**, 1331.
4. A. C. Balazs, *Nat. Mater.* **2007**, *6*, 94.
5. S. C. Warren, F. J. Disalvo and U. Weisner, *Nat. Mater.* 2007, **6**, 156.
6. R. Savić, L. Luo, A. Eisenberg and D. Maysinger, *Science* 2003, **300**, 615.
7. L. L. Beecroft and C. K. Ober, *Chem. Mater.* 1997, **9**, 1302.
8. D. Y. Godovsky, *Adv. Polym. Sci.* 2000, **153**, 165.
9. F. Croce, G. B. Appetecchi, L. Persi and B. Scrosati, *Nature* 1998, **394**, 456.
10. T. C. Merkel, B. D. Freeman, R. J. Spontak, Z. He, I. Pinnau, P. Meakin and A. J. Hill, *Science* 2002, **296**, 519.
11. R. J. Hill, *Phys. Rev. Lett.* 2006, **96**, 216001.
12. M. J. Fasolka, L. S. Goldner, J. Hwang, A. M. Urbas, P. DeRege, T. Swager and E. L. Thomas, *Phys. Rev. Lett.* 2003, **90**, 016107.
13. R. B. Thompson, V. V. Ginzburg, M. W. Matsen and A. C. Balazs, *Science* 2001, **292**, 2469.
14. M. R. Bockstaller, Y. Lapetnikov, S. Margel and E. L. Thomas, *J. Am. Chem. Soc.* 2003, **125**, 5276.
15. A. C. Balazs, T. Emrick and T. P. Russell, *Science* 2006, **314**, 1107.

16. R. J. Spontak, R. Shankar, M. K. Bowman, A. S. Krishnan, M. W. Hamersky, J. Samseth, M. R. Bockstaller and K. Ø. Rasmussen, *Nano Lett.* 2006, **6**, 2115.
17. T. P. Lodge, J. Bang, M. J. Park and K. Char, *Phys. Rev. Lett.* 2004, **92**, 145501.
18. I. W. Hamley, *The Physics of Block Copolymers*, Oxford University Press, New York, 1998.
19. C. Park, J. Yoon and E. L. Thomas, *Polymer* 2003, **44**, 6725.
20. I. W. Hamley, *Angew. Chem. Int. Ed.* 2003, **42**, 1692.
21. M. Lazzari, G. Liu and S. Lecommandoux (eds.), *Block Copolymers in Nanoscience*, Wiley-VCH, Weinheim, 2006.
22. A. K. Khandpur, S. Förster, F. S. Bates, I. W. Hamley, A. J. Ryan, W. Bras, K. Almdal and K. Mortensen, *Macromolecules* 1995, **28**, 8796.
23. R. J. Spontak and N. P. Patel, in *Developments in Block Copolymer Science and Technology* (I. W. Hamley, ed.), Wiley, New York, 2004, pp. 159-212.
24. V. Pryamitsym and V. Ganesan, *Macromolecules* 2006, **39**, 8499.
25. S. W. Sides, B. J. Kim, E. J. Kramer and G. H. Fredrickson, *Phys. Rev. Lett.* 2006, **96**, 250601.
26. C.-T. Lo, B. Lee, V. G. Pol, N. L. Dietz Rago, S. Seifert, R. E. Winans and P. Thiagarajan, *Macromolecules* 2007, **40**, 8302.
27. B. J. Kim, J. J. Chiu, G. R. Yi, D. J. Pine and E. J. Kramer, *Adv. Mater.* 2005, **17**, 2618.
28. B. J. Kim, G. H. Fredrickson, C. J. Hawker and E. J. Kramer, *Langmuir* 2007, **23**, 7804.
29. A. I. Chervanyov and A. C. Balazs, *J. Chem. Phys.* 2003, **119**, 3529.
30. A. J. Schultz, C. K. Hall and J. Genzer, *Macromolecules* 2005, **38**, 3007.

31. L. Bombalski, H. Dong, J. Listak, K. Matyjazewski and M. R. Bockstaller, *Adv. Mater.* 2007, **19**, 4486.
32. F. Rodriguez, C. Cohen, C. K. Ober and L. A. Archer, *Principles of Polymer Systems, 5th Ed.*, Taylor & Francis, New York, 2003, p. 264.
33. P. Rittigstein, R. D. Priestley, L. J. Broadbelt and J. M. Torkelson, *Nat. Mater.* 2007, **6**, 278.
34. K. Ø. Rasmussen and G. Kalosakas, *J. Polym. Sci. B: Polym. Phys.* 2002, **40**, 1777.
35. M. W. Matsen and R. B. Thompson, *Macromolecules* 2008, **41**, 1853.
36. W. G. Kim, M. Y. Chang, B. A. Garetz, M. C. Newstein, N. P. Balsara, J. H. Lee, H. Hahn and S. S. Patel, *J. Chem. Phys.* 2001, **114**, 10196.
37. M. W. Matsen, *Macromolecules* 2003, **36**, 9647.
38. V. R. Tirumala, A. Romang, S. Agarwal, E. K. Lin and J. J. Watkins, *Adv. Mater.* 2008, DOI: 10.1002/adma.200701577.
39. A. J. Rahedi, J. F. Douglas and F. W. Starr, *J. Chem. Phys.* 2008, **128**, 024902.

4.7 List of Figure Captions

Figure 4.1 Segmental density profiles of the A block (solid line), B block (dotted line) and nanoparticle (ρ , bold solid line) as a function of distance (x) perpendicular to the lamellar microdomains in an ordered block copolymer and normalized with respect to the microdomain period (D). These results are generated by a hybrid SCF/DF theory for AB diblock copolymers ($\chi_{AB}N = 25$, $N_A = N_B$) modified with (a,b) small ($R/R_g = 0.05$) and (c,d) large ($R/R_g = 0.50$) nanoparticles varying in selectivity: (a,c) neutral ($\chi_{Ap}N = \chi_{Bp}N$) and (b,d) A-selective ($\chi_{Ap}N = 0$). The enlargements below (a) and (b) show the corresponding nanoparticle density profiles.

Figure 4.2 The order-disorder transition temperature (T_{ODT}) measured by isochronal dynamic rheology as a function of nanoparticle mass fraction (w_p) and block selectivity (i.e., nanoparticle surface chemistry, labeled) for clustered (FS) and discrete (CS) nanoparticles. The solid lines serve as guides for the eye, and the shaded region corresponds to the experimental uncertainty in the measured T_{ODT} of the neat copolymer.

Figure 4.3 Predicted dependence of $(\chi_{AB}N)_{ODT}$ from SCF/DF analysis on the volume fraction of nanoparticles (ϕ_p), which vary in block selectivity (values of $\chi_{Ap}N$ are labeled) at $R/R_g = 0.40$. The dashed line identifies $(\chi_{AB}N)_{ODT}$ for the neat copolymer, and the arrowheads denote minima in the curves. The inset shows the explicit effect of nanoparticle selectivity on copolymer phase behavior at two different concentrations ($\phi_p = 0.05$ and 0.10).

Figure 4.4 Predicted dependence of $(\chi_{AB}N)_{ODT}$ from SCF/DF analysis on ϕ_p for A-selective nanoparticles ($\chi_{Ap}N = 0$) varying in R/R_g (in 0.04 intervals, labeled). The inset shows the explicit effect of nanoparticle size on copolymer phase behavior at two different concentrations ($\phi_p = 0.05$ and 0.10), and the illustration depicts the observed¹⁶ localization of nanoparticles in the large R/R_g limit.

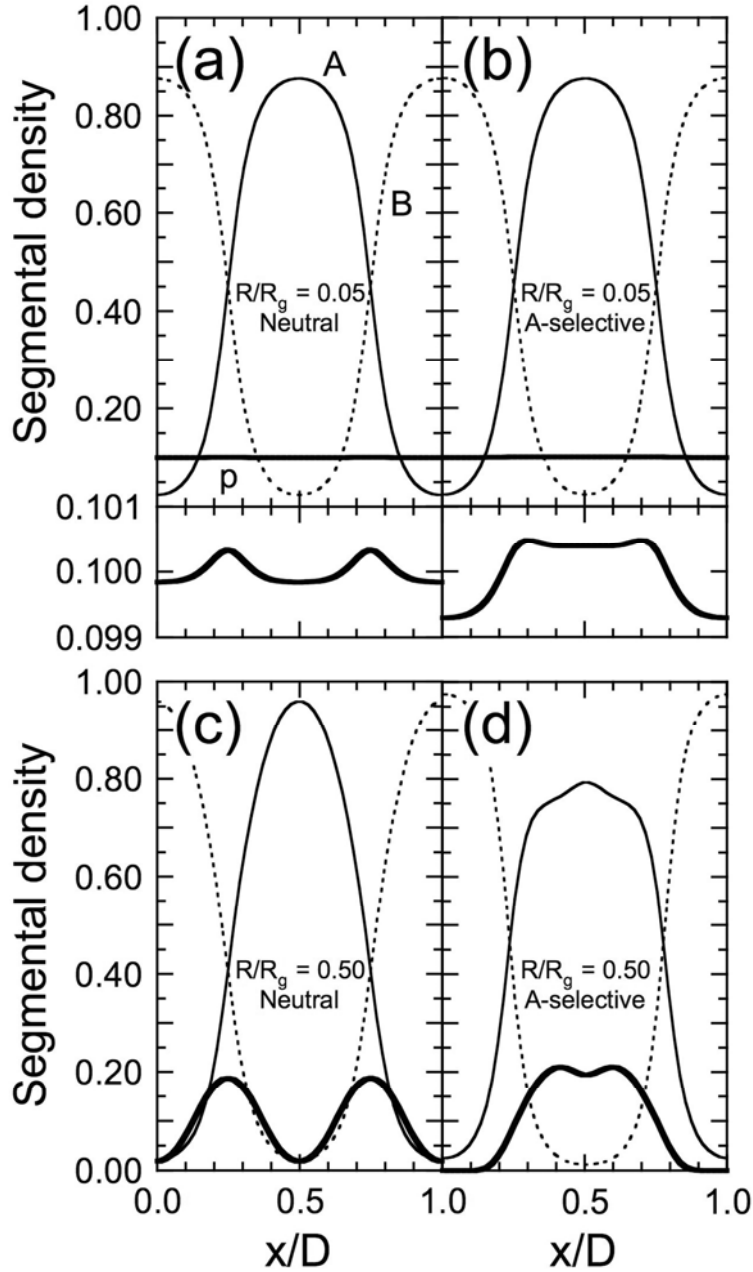


Figure 4.1. Segmental density profiles of the A block (solid line), B block (dotted line) and nanoparticle (p, bold solid line) as a function of distance (x) perpendicular to the lamellar microdomains in an ordered block copolymer and normalized with respect to the microdomain period (D). These results are generated by a hybrid SCF/DF theory for AB diblock copolymers ($\chi_{AB}N = 25$, $N_A = N_B$) modified with (a,b) small ($R/R_g = 0.05$) and (c,d) large ($R/R_g = 0.50$) nanoparticles varying in selectivity: (a,c) neutral ($\chi_{Ap}N = \chi_{Bp}N$) and (b,d) A-selective ($\chi_{Ap}N = 0$). The enlargements below (a) and (b) show the corresponding nanoparticle density profiles.

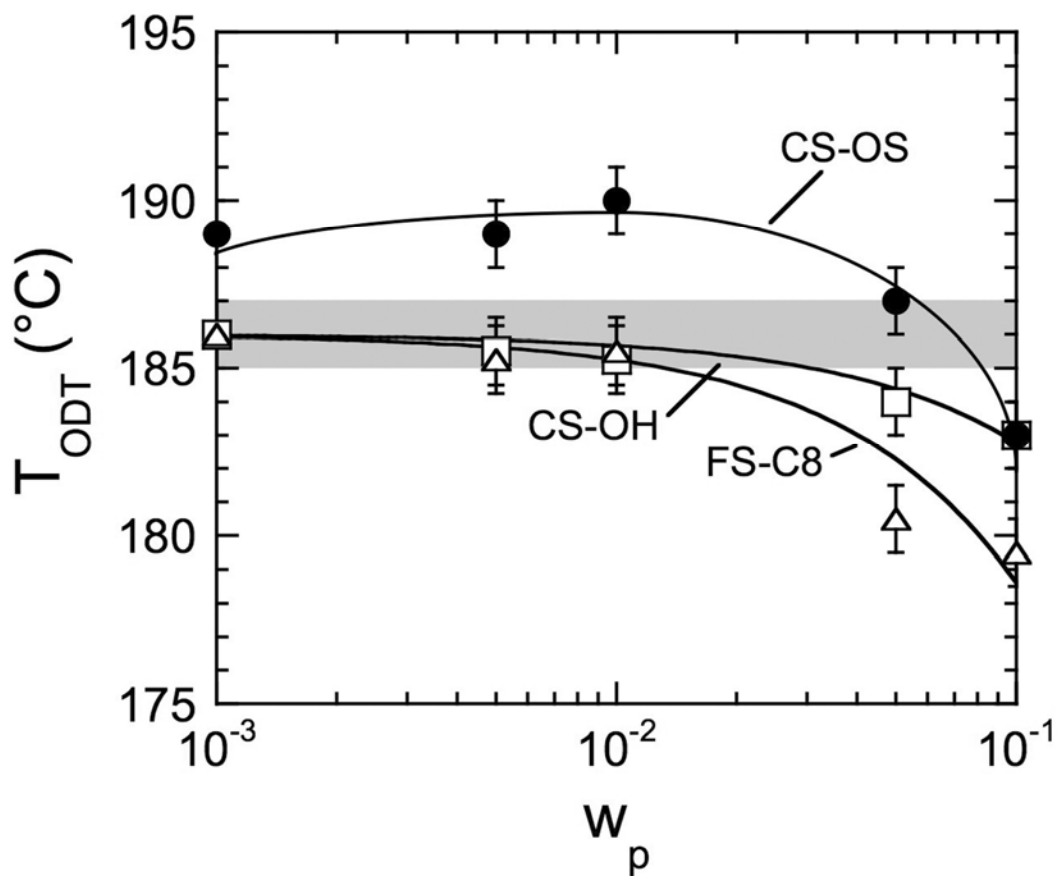


Figure 4.2. The order-disorder transition temperature (T_{ODT}) measured by isochronal dynamic rheology as a function of nanoparticle mass fraction (w_p) and block selectivity (i.e., nanoparticle surface chemistry, labeled) for clustered (FS) and discrete (CS) nanoparticles. The solid lines serve as guides for the eye, and the shaded region corresponds to the experimental uncertainty in the measured T_{ODT} of the neat copolymer.

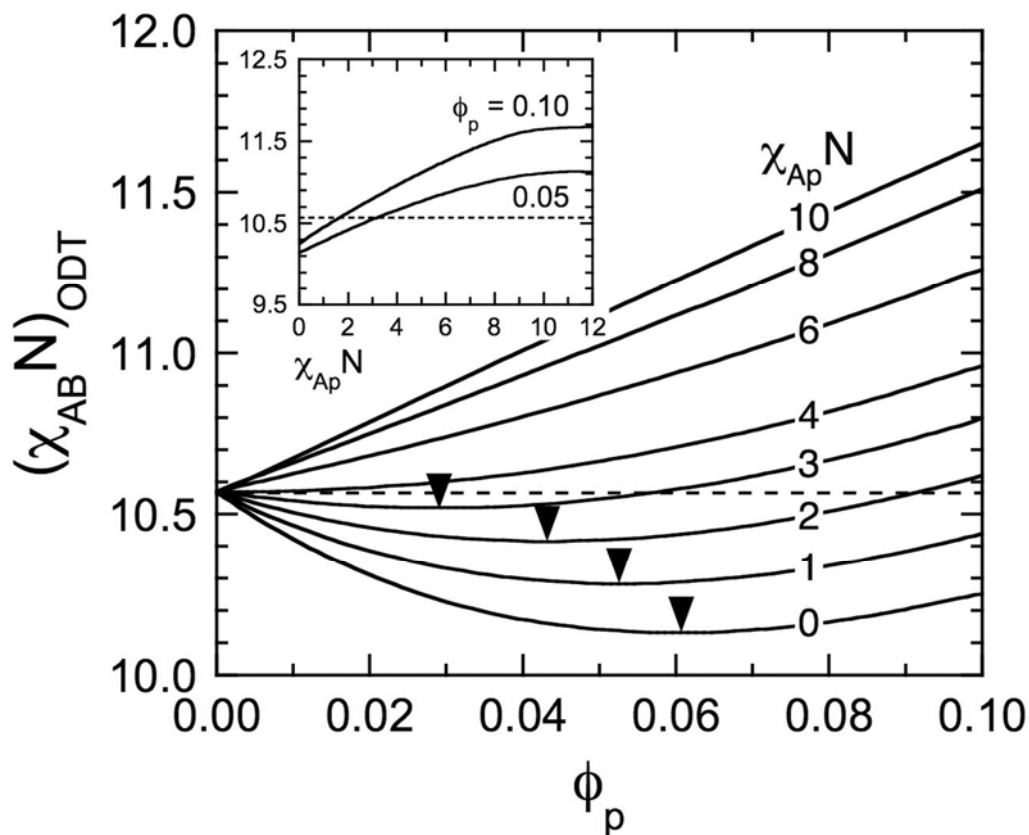


Figure 4.3. Predicted dependence of $(\chi_{AB}N)_{ODT}$ from SCF/DF analysis on the volume fraction of nanoparticles (ϕ_p), which vary in block selectivity (values of $\chi_{Ap}N$ are labeled) at $R/R_g = 0.40$. The dashed line identifies $(\chi_{AB}N)_{ODT}$ for the neat copolymer, and the arrowheads denote minima in the curves. The inset shows the explicit effect of nanoparticle selectivity on copolymer phase behavior at two different concentrations ($\phi_p = 0.05$ and 0.10).

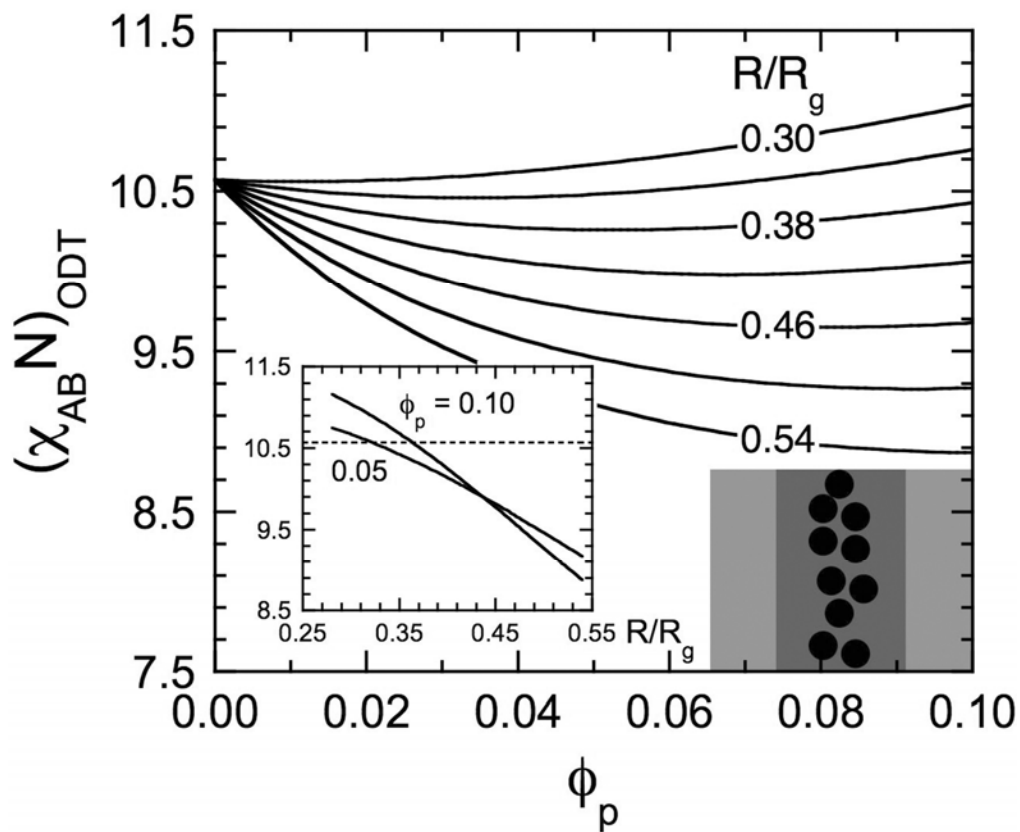


Figure 4.4. Predicted dependence of $(\chi_{AB}N)_{ODT}$ from SCF/DF analysis on ϕ_p for A-selective nanoparticles ($\chi_{Ap}N = 0$) varying in R/R_g (in 0.04 intervals, labeled). The inset shows the explicit effect of nanoparticle size on copolymer phase behavior at two different concentrations ($\phi_p = 0.05$ and 0.10), and the illustration depicts the observed¹⁶ localization of nanoparticles in the large R/R_g limit.

CHAPTER 5

COLLOIDAL NETWORK FORMATION IN NANOSTRUCTURED POLYMER MATRICES

Abstract

Incorporation of nanoparticles composed of surface-functionalized fumed silica (FS) or native colloidal silica (CS) into a nanostructured block copolymer yields hybrid nanocomposites whose mechanical properties can be tuned by nanoparticle concentration and surface chemistry. In this work, dynamic rheology is used to probe the frequency and thermal responses of nanocomposites composed of a symmetric poly(styrene-*b*-methyl methacrylate) (SM) diblock copolymer and varying in nanoparticle concentration and surface functionality. At sufficiently high loading levels, FS nanoparticle aggregates establish a load-bearing colloidal network within the copolymer matrix. Transmission electron microscopy images reveal the morphological characteristics of the nanocomposites under these conditions.

(This chapter has will be published in its entirety:
Gaines, M.K.; Smith, S. D.; Samseth, J.; Khan, S. A.; Spontak, R. J. *submitted to Langmuir*)

5.1 Introduction

Block copolymers continue to remain one of the most extensively studied classes of polymers due to their intrinsic ability to infuse the dissimilar properties of homopolymers into a single material by spontaneously self-organizing at the molecular level. Molecular self-assembly is a direct consequence of thermodynamic incompatibility between the long, contiguous sequences comprising block copolymers and results in the formation of (a)periodic nanoscale morphologies.^{1,2} Ordered morphologies observed in simple AB diblock copolymers include A(B) spheres on a body- or face-centered cubic lattice in a B(A) matrix, A(B) cylinders on a hexagonal lattice in a B(A) matrix, triply periodic bicontinuous (gyroid) channels or alternating lamellar sheets. Targeted addition of a selective low-molar-mass solvent or relatively low-molecular-weight homopolymer to an ordered block copolymer can be used to preferentially swell one of the domains comprising the copolymer nanostructure and ultimately yield tunable transitions to morphologies with specific mechanical or optical properties.³⁻⁸ Recent studies have extended this general design paradigm by modifying ordered block copolymers with surface-functionalized inorganic nanoparticles to achieve hybrid nanocomposites. Unlike conventional nanocomposites prepared from homopolymers, block copolymer nanocomposites rely on the existing copolymer nanostructure to template – that is, spatially modulate – the nanoparticles.

Previous experimental studies⁸⁻¹² of block copolymer nanocomposites have focused on precise positioning of nanoparticles within the copolymer nanostructure for use in optics, such as waveguides. Such efforts have demonstrated that, if sufficiently small

with respect to the host copolymer molecules (i.e., the characteristic size of the copolymer nanostructure), nonselective nanoparticles tend to distribute uniformly throughout the copolymer matrix in much the same fashion as nonselective solvent molecules. Selective nanoparticles, on the other hand, tend to locate along the interface separating adjacent domains within the copolymer nanostructure due to interfacial energy considerations, which result in fewer contacts between A and B repeat units. Larger selective nanoparticles are enthalpically driven to the core of the compatible domains to minimize repulsive contacts with incompatible blocks. Surface-functionalized nanoparticles have likewise been incorporated into ordered block copolymers to promote changes in morphology,¹³⁻¹⁵ as well as changes in phase behavior¹⁶⁻¹⁸ discerned from the order-disorder transition (ODT). We have recently demonstrated¹⁸ that the ODT of a poly(styrene-*b*-methyl methacrylate) (SM) diblock copolymer modified with surface-functionalized fumed silica (FS) or native (hydroxyl-terminated) colloidal silica (CS) decreases monotonically with increasing nanoparticle loading. If, however, oligostyrene-functionalized CS is added to the copolymer, the ODT increases slightly before dropping, in qualitative agreement with self-consistent field predictions.

The objective of the present work is to examine how the mechanical properties of such block copolymer nanocomposites evolve as the concentration of surface-functionalized FS and native CS is systematically increased. Dynamic melt rheology is employed to investigate the mechanical properties, and transmission electron microscopy (TEM) is used to examine the morphology of one of the nanocomposites.

5.2 Experimental

The SM copolymer was synthesized via sequential living anionic polymerization of the S block in cyclohexane at 60°C, followed by the M block in tetrahydrofuran at -78°C, with *sec*-butyl lithium as the initiator. According to proton nuclear magnetic resonance (¹H NMR) spectroscopy and size-exclusion chromatography (SEC), the block masses measured 13,000 each, with an overall polydispersity of 1.05. Three grades of functionalized FS were obtained in powder form from Degussa Corp. (Parsippany, NJ) and probed the effects of hydrophilicity *vs.* hydrophobicity and block selectivity: hydroxyl-terminated (OH), methacrylate-terminated (MA) and octyl-terminated (C8). According to the manufacturer, the primary particle size in each case was ~12 nm. The CS nanoparticles with an average diameter of 10-15 nm were provided as a suspension (20% solids) in dimethylacetamide by Nissan Chemicals (Houston, TX). Specimens for dynamic melt rheology were produced by ultrasonication the nanoparticles (at a specimen-specific concentration relative to the copolymer) for 30 min in toluene to achieve a satisfactory dispersion, followed by copolymer dissolution and further ultrasonication, and then air- and vacuum-drying, all performed at ambient temperature. No copolymer degradation due to ultrasonication was detected according to SEC analysis of the resultant films.

Dynamic rheology was performed on an ARES strain-controlled rheometer equipped with serrated 8 mm parallel plates and operated at 2% strain amplitude to ensure linear viscoelasticity. Discs measuring 8 mm in diameter and 1 mm thick were melt-pressed at 150°C and heated to 220°C under nitrogen. Frequency (ω) spectra were acquired at

discrete temperatures above and below the ODT, while isochronal temperature sweeps were performed at $\omega = 1$ rad/s and a cooling rate of 1°C/min under a nitrogen purge to avoid oxidative degradation. Specimens for TEMT were prepared by sectioning the glassy nanocomposites at ambient temperature. Electron-transparent sections measuring *ca.* 150 nm thick were subjected to the vapor of 0.5% RuO₄(aq) to selectively stain the styrenic units. Serial TEM tilt images were collected on a Gatan UltraScan 4000 CCD camera at a resolution of 0.76 nm/pixel and tilt angles ranging from -69 to +69° at an angular interval of 1.5° on a Technai T20 microscope operated at 200 kV. While the full tilt series was aligned using a pre-calibrated geometric model based on a high-precision goniometer stage,¹⁹ only representative images acquired at 0°, 15° and 30° are reported herein.

5.3 Results and Discussion

According to the discontinuous change in the dynamic storage modulus (G') encountered during an isochronal temperature sweep (upon cooling),²⁰ the ODT of the neat copolymer is determined to be 186±1°C. Addition of FS or CS nanoparticles up to 10 wt% reduces the ODT by as much as ~7°C, depending on surface functionality. This change in ODT is markedly different from that observed in block copolymer nanocomposites composed of a poly(styrene-*b*-isoprene) diblock copolymer modified with C₆₀ buckyballs.²¹ In that case, the ODT is found by dynamic rheology to decrease by 21°C upon incorporation of only 0.04 wt% C₆₀. At higher concentrations of C₆₀ nanoparticles (up to 0.5 wt%), the ODT does not change further but it does progressively

broaden. Such sensitivity is indicative of chemical interactions between the copolymer molecule (specifically, the unsaturated isoprenic units) and the carbonaceous nanoparticles,²² thereby generating a cross-linked material. Such interactions are not expected in the present systems, although we suspect that hydroxyl-terminated silica nanoparticles may bind with the acrylic units upon thermal treatment. To discern the effect of siliceous nanoparticles on mechanical properties at higher concentrations, temperature sweeps are presented in Fig. 1 for SM nanocomposites containing 20 wt% of the FS-OH, FS-C8 and CS additives.

These results immediately indicate that the fumed nanoparticles, which exist as branched aggregates commonly measuring on the order of hundreds of nanometers, have a more pronounced effect on the SM copolymer than do the CS nanoparticles. Specifically, the magnitude of G' for the nanocomposites with FS consistently exceeds the dynamic loss modulus (G'') over the entire temperature interval examined, even though the copolymer exists as a structureless melt. In contrast, G' increases beyond G'' only at low temperatures. Close examination of $G'(T)$ for the SM/CS nanocomposite also reveals that (i) the ODT of the copolymer persists in the vicinity of 172°C, which constitutes a 14°C reduction in the ODT of the copolymer, and (ii) a second transition appears to occur at *ca.* 204°C. This second transition is likewise apparent in the data collected from the SM/FS-OH nanocomposite, but is absent in the case of the system containing FS-C8. Neither of the FS-containing nanocomposites appears to exhibit an ODT. Similar disappearance of the ODT is observed²¹ in the case of nanocomposites modified with C₆₀ buckyballs. Over the range from 160 to 200°C, the dynamic moduli

measured from the SM-based nanocomposites described in Fig. 1 are well-behaved and permit direct assessment of modulus enhancement and nanocomposite rigidity as functions of nanoparticle concentration and surface chemistry below and above the copolymer ODT, if one exists.

The variation of the dynamic storage modulus (G') and dissipation factor ($\tan\delta = G''/G'$) with nanoparticle concentration is provided at a temperature below the block copolymer ODT (at 160°C) in Figs. 2a and 2b, respectively, and above the ODT (at 200°C) in Figs. 2c and 2d, respectively. In Fig. 2a, values of G' measured from FS-containing nanocomposites do not vary substantially (within experimental scatter, denoted by the shaded region) up to 5 wt% and then increase sharply. In contrast, G' from the SM/CS nanocomposite does not exhibit an abrupt rise until 20 wt%, indicating that single nanoparticles are less effective at improving the rigidity of the nanocomposite than the aggregated FS nanoparticles. Within the family of FS nanoparticles examined here, the FS-MA variant appears to be the most effective, while the FS-C8 nanoparticles are the least effective, at improving the mechanical properties of the copolymer. This is most likely due to the presumably nonselective nature of the FS-C8 nanoparticles. The FS-MA and FS-OH nanoparticles, on the other hand, can preferentially interact with the PMMA units of the copolymer and therefore distribute more uniformly. The solid and dashed lines included in the figure are meant as guides for the eye, but correspond to exponential regressions and fit the data surprisingly well. Similar behavior is also observed at 200°C (cf. Fig. 2c) when the copolymer is at a temperature above its ODT and disordered. It is

interesting that the onset of the increase in G' occurs at about the same concentration of both FS and CS nanoparticles.

In Fig. 2b, $\tan\delta$, a direct measure of liquid- versus solid-like behavior, is provided as a function of nanoparticle concentration and shows that, up to the concentration where G' suddenly increases in Fig. 2a, $\tan\delta$ is, for the most part, greater than unity. Since $\tan\delta = G''/G'$, this observation indicates that the nanocomposite behaves liquid-like. At higher nanoparticle concentrations, $\tan\delta$ decreases below unity, and the material behaves more solid-like. While there is little systematic variation among the three surface-functionalized FS grades, the SM/CS nanocomposites exhibit the greatest liquid-like tendency, marginally behaving solid-like at 20 wt% CS. The solid and dashed curves constitute exponential regressions to the data and again fit the data well. As before, similar results are seen in Fig. 2d, which displays $\tan\delta$ as a function of nanoparticle concentration at 200°C, above the copolymer ODT. Solid-like behavior becomes evident at nanoparticle loading levels that correspond to the sharp rise in G' . The one series that deviates from the data previously discussed with regard to Fig. 2b consists of SM/FS-C8 nanocomposites. According to Fig. 2d, $\tan\delta$ for this series attains the highest $\tan\delta$ value measured (15.5 at 0.1 wt%) in this study and thus exhibits the greatest liquid-like behavior of all the nanocomposites investigated. As the concentration of FS-C8 is increased, however, values of $\tan\delta$ for this series become comparable to those measured for the other FS, as well as CS, series.

Of all the additives considered here, the discrete CS nanoparticles appear to be the least effective in improving the mechanical properties of the SM copolymer (due to the

formation of discrete, rather than interconnected, aggregate structures) and are not considered further. The FS-C8 nanoparticles likewise appear ineffective at low nanoparticle concentrations and temperatures above the copolymer ODT, but their efficacy progressively improves as the nanoparticle concentration increases. Since this series of nanocomposites represents the worst case of FS-based nanoparticles in terms of property-enhancing attributes, it is used here to probe the ability FS nanoparticles to form colloidal networks within the nanostructured copolymer matrix. Figure 3a shows the frequency spectra for G' and G'' at 140°C and a nanoparticle concentration of 0.5 wt% FS-C8. Typical viscoelastic behavior is observed wherein G'' exceeds G' at low ω , but G' grows larger than G'' at high ω .²³ The crossover point at ω_c , where G' and G'' intersect, yields a characteristic relaxation time (τ) for the material. In this case, $\tau = 1/\omega_c$ is about 1.67 s. At 200°C, similar behavior is observed, but τ decreases by an order of magnitude to 0.13 s. When the concentration of FS-C8 is increased to 10 wt%, the frequency spectra change dramatically from the one displayed in Fig. 3a. In Fig. 3b, G' is greater than and nearly parallel to G'' over the entire ω range examined. This signature feature establishes that the nanocomposite responds to shear as a gel wherein the FS-C8 forms a continuous, load-bearing network within the nanostructured copolymer melt.²⁴ Analysis of the data in Fig. 3b reveals that both G' and G'' scale as $\omega^{0.21}$ over the full ω range so that $\tan\delta$ remains constant, which satisfies the Winter-Chambon rheological criterion²⁵ for a gel possessing infinite relaxation time. In the disordered SM copolymer matrix at 200°C, (Fig. 3c), G' continues to exceed G'' , remaining parallel at high ω (with G' and G'' scaling as $\omega^{0.35}$) and starting to show evidence of a plateau at low ω . Since this is the least

effective modifier of the FS family, it immediately follows that the other additives exhibit comparable, if not more pronounced, network behavior at nanoparticle concentrations of 10 wt% or more.

We now turn our attention to the most promising network-forming nanoparticle grade: FS-MA. Conventional TEM images acquired from relatively thick stained sections of two nanocomposites containing 5 and 20 wt% FS-MA are provided at 0°, 15° and 30° tilt in the top and bottom rows, respectively, of Fig. 4. In the case of the material with 5 wt% FS-MA, the lamellar morphology of the SM copolymer is evident and possesses a period of 20 ± 2 nm. Existence of lamellae confirms that the copolymer molecules are capable of self-organizing (albeit under frustrating conditions) and that an ODT should be observed, which it is according to dynamic rheology.¹⁸ Discrete clusters of FS-MA nanoparticles are likewise visible and measure from ~ 10 to 35 nm across (which is on the same scale as the primary FS-MA nanoparticles). Recall that, of all the FS nanoparticles investigated here, the FS-MA nanoparticles are expected to be the most uniformly dispersed throughout the copolymer matrix because they generally promote the greatest and most consistent property enhancement. Since the nanoparticles are located throughout the specimen in the z direction (parallel to the electron beam) and TEM images provide 2D projections of 3D objects, the precise effect of these nanoparticles (as well as nanoparticle clusters) on copolymer nanostructure cannot be directly deduced without the use of 3D transmission electron microtomography,^{26,27} which will be provided in a forthcoming publication.

It is apparent, however, from the tilt images corresponding to the nanocomposite with 5 wt% FS-MA that the copolymer lamellae are not highly oriented due, in large part, to the presence of the nanoparticles. Moreover, in several locations throughout the field of view, the lamellae appear distorted or even discontinuous (cf. the circled region at 30° tilt), which is consistent with our previous phase study¹⁸ indicating that the stability of the copolymer nanostructure (discerned from the magnitude of the ODT) in this nanocomposite is lower than that of the neat copolymer. In the case of the nanocomposite containing 20 wt% FS-MA, however, the lamellar nanostructure of the copolymer is altogether eliminated, replaced by a continuous background of nearly constant optical density, whereas the FS-MA nanoparticles form a continuous network that extends throughout the material. These results agree with our findings from dynamic rheology: (i) no ODT is discernible from isochronal temperature sweeps of this nanocomposite, and (ii) this nanocomposite exhibits solid-like behavior at both low and high temperatures in the melt. Thus, we provide experimental evidence to demonstrate that incorporation of nanoparticles in block copolymer melts can induce sufficient molecular frustration via nanoscale confinement to completely thwart the ability of the copolymer molecules to form a periodic nanostructure.

5.4 Conclusions

Addition of native and surface-functionalized siliceous nanoparticles varying in hydrophobicity and inherent aggregation to a nanostructured block copolymer melt has little effect on the rheological properties at low nanoparticle concentrations, but promotes

an abrupt increase in G' and a corresponding decrease in $\tan\delta$ (below unity) at high nanoparticle loading levels. In this latter regime, the nanocomposite melt behaves solid-like at temperatures above and below the copolymer ODT, suggesting that a colloidal network composed of nanoparticles develops. Existence of such a network is confirmed from mechanical frequency spectra acquired at different nanoparticle concentrations and temperatures. Transmission electron microscopy provides direct visual evidence of the colloidal network within the ordered copolymer nanostructure and demonstrates that two dissimilar nanostructures, both capable of imparting solid-like behavior to soft materials, can coexist in block copolymer nanocomposite melts.²⁸

5.5 Acknowledgements

This work was supported by the Research Council of Norway under the NANOMAT Program. M. K. G. expresses her gratitude for a GEM Fellowship and a NOBCCHE Procter & Gamble Fellowship.

5.6 References

1. Hamley, I. W. *The Physics of Block Copolymers*; Oxford University Press: New York, 1998.
2. Bates, F. S.; Fredrickson, G. H. *Physics Today* **1999**, *52*, 32-38.
3. Alexandridis, P. *Amphiphilic Block Copolymers: Self-Assembly and Applications*; Elsevier: Amsterdam, 2000.
4. Alexandridis, P.; Spontak, R. J. *Curr. Opin. Colloid Interface Sci.* **1999**, *4*, 130.
5. Lodge T. P.; Blazey, M. A.; Lui, Z. *Macromol. Chem. Phys.* **1997**, *198*, 983-995.
6. Spontak, R. J.; Patel, N. P. In *Developments in Block Copolymer Science and Technology* (Hamley, I. W., ed.); Wiley: New York, 2004; pp. 159-212.
7. Hamley, I. W. *Introduction of Soft Matter: Polymers, Colloids, Amphiphiles, and Liquid Crystals*; Wiley: New York, 2000.
8. Spontak, R. J.; Shankar, R.; Bowman, M. K.; Krishnan, A. S.; Hamersky, M. W.; Samseth, J.; Bockstaller, M. R.; Rasmussen, K. Ø. *Nano Lett.* **2006**, *6*, 2115.
9. Tsutsumi, K.; Funaki, Y.; Hirokawa, Y.; Hashimoto, T. *Langmuir* **1999**, *15*, 5200.
10. Bockstaller, M. R.; Lapetnikov, Y.; Margel, S.; Thomas, E. L. *J. Am. Chem. Soc.* **2003**, *125*, 5276.
11. Bockstaller M. R.; Mickiewicz, R. A.; Thomas, E. L. *Adv. Mater.* **2005**, *17*, 1331-1349.

12. Bockstaller, M. R.; Thomas, E. L. *Phys. Rev. Lett.* **2004**, *93*, 166106.
13. Göltner, C. G.; Berton, B.; Krämer, E.; Antonelli, M. *Adv. Mater.* **1999**, *11*, 395-398.
14. Kim, B.J.; Chiu, J. J.; Yi, G. -R.; Pine, D. J.; Kramer, E. J. *Adv. Mater.* **2005**, *17*, 2618-2622.
15. B. J.; Fredrickson, G. H.; Hawker, C. J.; Kramer, E. J. *Langmuir* **2007**, *23*, 7804-7809.
16. Lee, K. M.; Han, C. D. *Macromolecules* **2003**, *36*, 804-815.
17. Warren, S. C.; Disalvo, F. J.; Wiesner, U.; *Nature Materials* **2007**, *6*, 156-161.
18. Gaines, M. K.; Smith, S. D.; Samseth, J.; Bockstaller, M. R., Thompson, R. B., Rasmussen, K. Ø., Spontak, R. J. submitted to *Soft Matter*.
19. Fung, J. C.; Kane, L. Smith, S. D.; Sedat, J.W.; Agard, D. A.; Spontak, R. J.; *Mater. Sci. Forums* **1997**, 239-241, 179-184.
20. Rosedale, J. H.; Bates, F. S. *Macromolecules* **1990**, *23*, 2329-2338.
21. Zhao, Y.; Hashimoto, T.; Douglas, J. F.; Gaines, M. K.; Spontak, R. J. *manuscript in preparation for submission to Nature Materials*.
22. Biglova, Yu. N.; Sigaeva, N. N.; Talipov, R. F.; Monakov, Yu. B. *Oxidation Communications* **2005**, *4*, 753-798.

23. Dealy, J. M.; Larson, R. G. *Structure and Rheology of Molten Polymers: from Structure to Flow Behavior and Back Again*; Hanser Gardner Publications: Cincinnati, 2006.
24. Khan, S. A.; Prud'homme, R. K.; Larson, R. G. *Rheol. Acta* **1987**, 26, 144-151.
25. Winter, H. H.; Mours, M. *Adv. Polym. Sci.* **1997**, 134, 165-234.
26. Dohi, H.; Kimura, H.; Kotani, M.; Kaneko, T.; Kitaoka, T.; Nishi, T.; Jinnai, H. *Polym. J.* 2007, 39, 749-758.
27. Abetz, V., Spontak, R.J., and Talmon, Y., "Determination of Bulk and Solution Morphologies by Electron Microscopy," in *Macromolecular Engineering: Precise Synthesis, Materials Properties, Applications* (K. Matyjaszewski, Y. Gnanou and L. Leibler, eds.), Wiley-VCH, Weinheim, 2007, Vol. 3, Chap. 7, pp. 1649-1685.
28. Thompson, R. B.; Ginzburg, V. V.; Matsen, M. W.; Balazs, A. C. *Science* **2001**, 292, 2469-2472.

5.7 List of Figure Captions

Figure 5.1. Temperature dependence of the dynamic shear moduli (G' , open; G'' , filled) for SM nanocomposites containing 20 wt% of three different nanoscale additives: hydroxyl-terminated colloidal silica (CS, circles), hydroxyl-terminated fumed silica (FS-OH, triangles) and octyl-terminated fumed silica (FS-C8, squares). The dotted vertical line identifies an abrupt change in G' that occurs in the case of the hydroxyl-terminated nanoparticles.

Figure 5.2. Dependence of G' (a,c) and $\tan\delta$ (b,d) on nanoparticle concentration for three nanoparticle species — CS (●), FS-OH (△), FS-C8 (□) and FS-MA (○) — at two temperatures (in °C): 160 (a,b) and 200 (c,d). The solid and dashed lines serve as guides for the eye for the FS-MA and CS data, respectively; whereas the shaded region shows the range in G' over which nanoparticle concentration generally has little effect on nanocomposite mechanical properties. The vertical dotted line identifies the concentration vicinity beyond which the nanocomposites behave solid-like, and the horizontal dotted line (c,d only) signifies where $\tan\delta = 1$.

Figure 5.3. Isothermal frequency spectra acquired for G' (○) and G'' (●) at the following conditions: (a) 0.5 wt% FS-C8 at 140°C, (b) 10 wt% FS-C8 at 140°C and (c) 10 wt% FS-C8 at 200°C.

Figure 5.4. TEM images acquired at three different tilt angles (labeled) from SM/FS-MA nanocomposites containing 5 and 20 wt% FS-MA (top and bottom rows,

respectively). In each case, the FS-MA nanoparticles appear as electron-opaque (dark) aggregate features, whereas the styrenic lamellae of the SM copolymer are likewise dark due to selective staining. The arrow shows the location of lamellae comprising the copolymer nanostructure, whereas the circled region highlights copolymer lamellae that appear distorted or partially discontinuous.

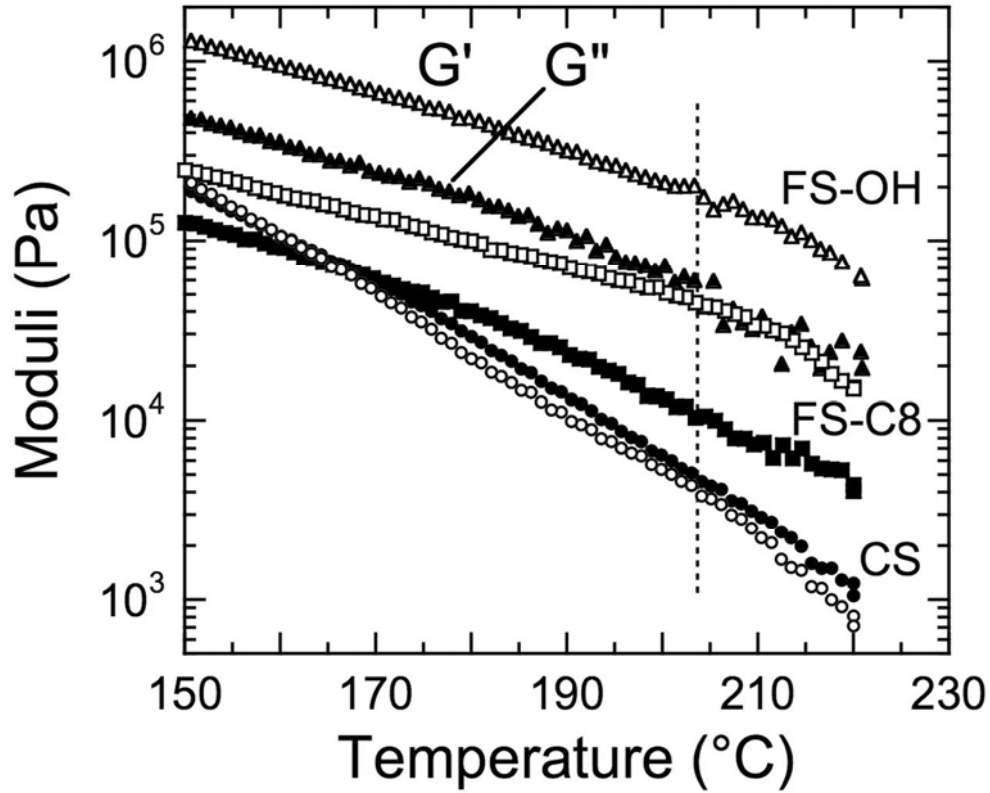


Figure 5.1. Temperature dependence of the dynamic shear moduli (G' , open; G'' , filled) for SM nanocomposites containing 20 wt% of three different nanoscale additives: hydroxyl-terminated colloidal silica (CS, circles), hydroxyl-terminated fumed silica (FS-OH, triangles) and octyl-terminated fumed silica (FS-C8, squares). The dotted vertical line identifies an abrupt change in G' that occurs in the case of the hydroxyl-terminated nanoparticles.

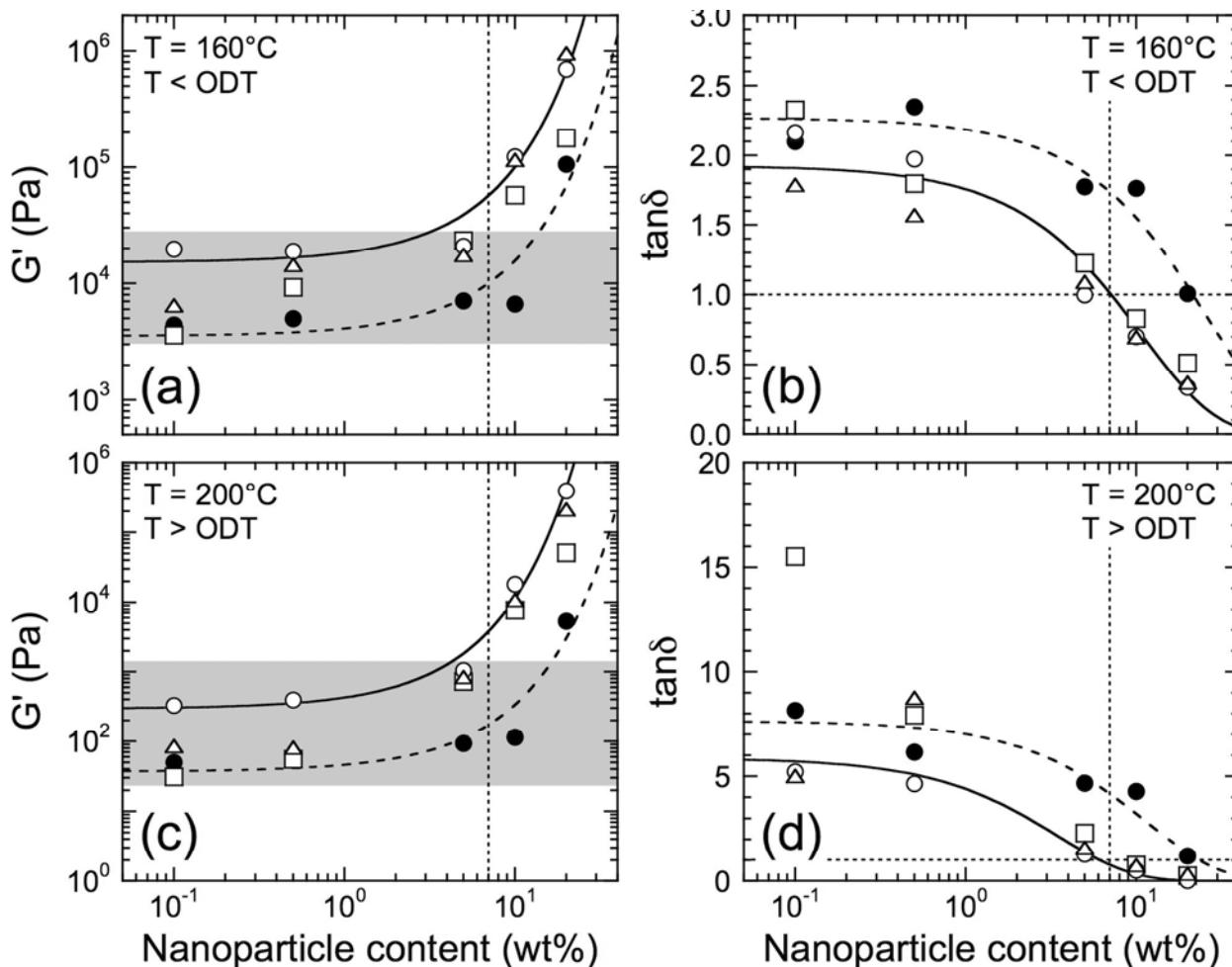


Figure 5.2. Dependence of G' (a,c) and $\tan\delta$ (b,d) on nanoparticle concentration for three nanoparticle species — CS (●), FS-OH (△), FS-C8 (□) and FS-MA (○) — at two temperatures (in $^\circ\text{C}$): 160 (a,b) and 200 (c,d). The solid and dashed lines serve as guides for the eye for the FS-MA and CS data, respectively; whereas the shaded region shows the range in G' over which nanoparticle concentration generally has little effect on nanocomposite mechanical properties. The vertical dotted line identifies the concentration vicinity beyond which the nanocomposites behave solid-like, and the horizontal dotted line (c,d only) signifies where $\tan\delta = 1$.

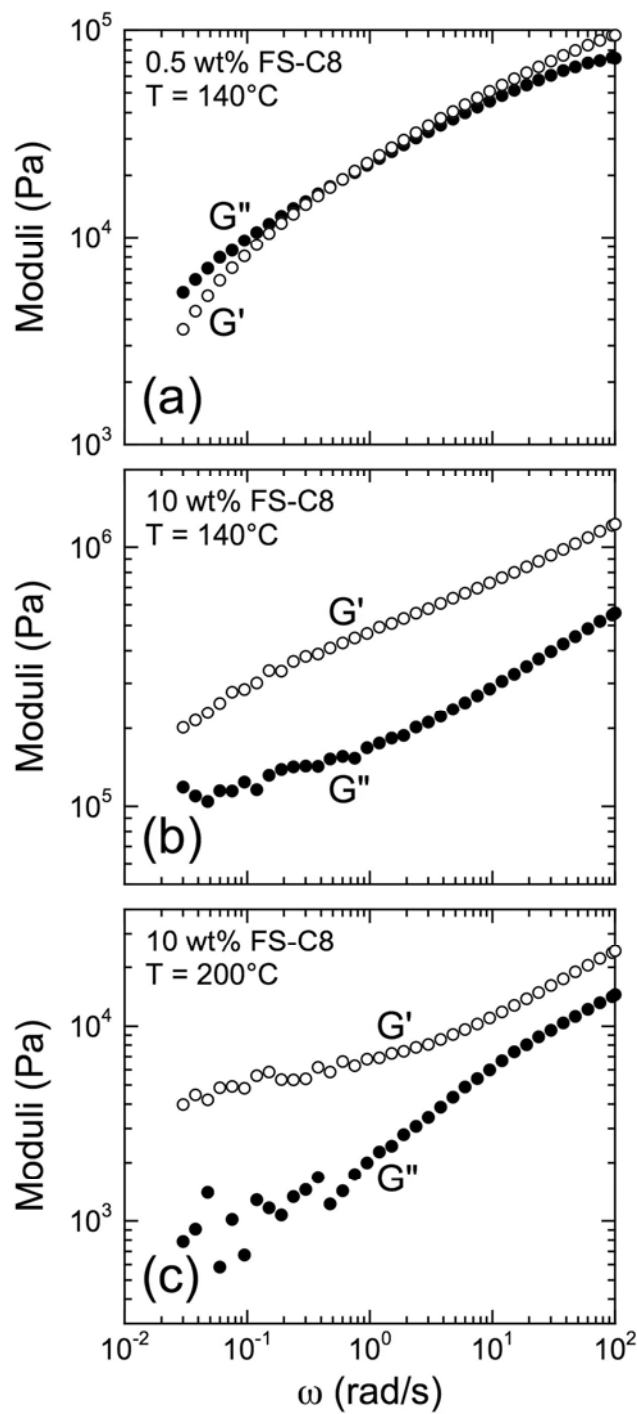


Figure 5.3. Isothermal frequency spectra acquired for G' (○) and G'' (●) at the following conditions: (a) 0.5 wt% FS-C8 at 140°C , (b) 10 wt% FS-C8 at 140°C and (c) 10 wt% FS-C8 at 200°C .

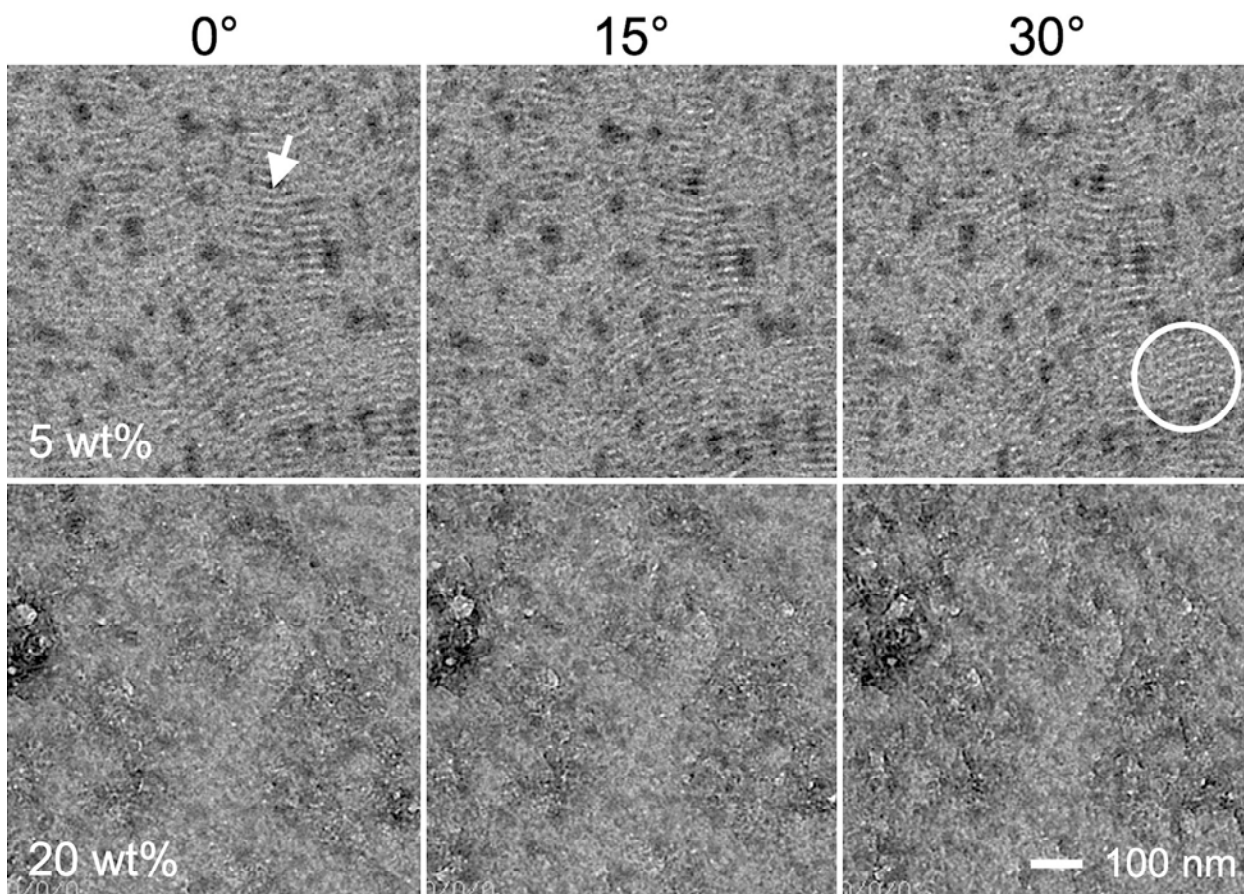


Figure 5.4. TEM images acquired at three different tilt angles (labeled) from SM/FS-MA nanocomposites containing 5 and 20 wt% FS-MA (top and bottom rows, respectively). In each case, the FS-MA nanoparticles appear as electron-opaque (dark) aggregate features, whereas the styrenic lamellae of the SM copolymer are likewise dark due to selective staining. The arrow shows the location of lamellae comprising the copolymer nanostructure, whereas the circled region highlights copolymer lamellae that appear distorted or partially discontinuous.

CHAPTER 6

FRUSTERATING THE LAMELLAR ORDERING TRANSITION OF POLYSTYRENE-*BLOCK*- POLYISOPRENE WITH C₆₀ BUCKYBALLS

Abstract

Thermal fluctuations in block copolymer (BCP) materials characteristically drive the ordering transition from a second-order phase transition, as predicted by mean-field theory, to a first-order phase transition by the well known Brazovskii mechanism. Many observations of a sharp jump in X-ray and neutron scattering intensity, as well as rheological properties, at the order-disorder transition (ODT) temperature (T_{ODT}) signal this phenomenon. However, introduction of "quenched disorder," as might be expected from the introduction of associating nanoparticles (NPs) and cross-links into the BCP material, is theoretically predicted to either *eliminate* the ODT or, more dramatically, *restore* the second-order nature of the phase transition. The present paper considers the dispersion of C₆₀ ("buckyballs") into a symmetric diblock copolymer [polystyrene-*block*-polyisoprene); PS-*b*-PI] to see how this NP additive alters the character of BCP ordering. Numerous previous experiments have established that C₆₀ tends to aggregate in PS and other polymer matrices and possesses oxidative properties that might serve to create effective "cross-links" so that these particles can induce quenched disorder at the scale of

the BCP ordering. A significant perturbation of the BCP ordering process is thus anticipated. Our small-angle X-ray scattering observations indicate that the addition of a relatively small amount of C₆₀ (~0.4 wt%) lowers T_{ODT} appreciably (by $\approx 15^{\circ}\text{C}$) relative to the neat BCP, and the temperature range of the ordering process and the characteristic period of the lamellae both increase significantly. More impressively, the addition of ~1 wt% C₆₀ causes the BCP to remain in a disordered state over a wide temperature range so that T_{ODT} apparently *disappears* altogether. These results confirm that incorporation of NPs to BCP materials can have a significant effect on even the *qualitative* nature of the ordering process, offering both challenges and opportunities.

6.1 Introduction

Nanohybrid materials, more generally referred to as "nanocomposites," composed of a block copolymer (BCP) and a dispersed nanoparticle (NP) additive have attracted much attention recently because BCPs are materials that self-organize into diverse and tunable multiphase structures with nanoscale periodicity and widespread commercial interest.¹⁻¹⁴ Independent studies generally recognize that the mechanical, thermal, optical, and interfacial properties¹⁵⁻¹⁷ of even ordinary polymers can strongly benefit from the addition of NPs. Fullerenes constitute particularly attractive NP additives because of the numerous proposed applications of fullerene nanocomposites in electronics, laser engineering, optics, and pharmaceuticals,^{18,19} as well as the relative simplicity of characterizing and working with these materials. The investigation of NP additives, such as fullerenes, to BCP materials is scientifically interesting because of their potential for perturbing the very nature of the phase transitions that occur in these materials, an effect that may by itself lead to new applications. In particular, first-order phase transitions, such as those encountered in neat BCP materials, are sensitive to the introduction of quenched disorder from impurities and other constraints (e.g., mechanical perturbations such as stretching) that can either eliminate the ordering transition altogether or drive the phase transition to become second-order.²⁰⁻²⁴ The extraordinary prediction of an ordering conversion from first-order to second-order has been confirmed in inorganic materials,²⁵⁻²⁸ and the present work considers the possible existence of this phenomenon in BCP materials.

While a precise description of quenched disorder in the context of BCP materials is

somewhat vague from a theoretical standpoint, it is intuitively clear that such impurity-drive disorder should have dimensions on the scale of ordering in the BCP material (e.g., the lamellar spacing) to be effective at perturbing the ordering process. On the other hand, if the additive is much larger than this scale, such as in the case of conventional micron-sized filler particles, then the BCP molecules will primarily encounter only macroscopic interfaces. Thus, we judge NPs to be optimal for studies aimed at perturbing the very nature of the ordering transition in BCP materials. Apart from the fact that fullerenes are true NPs with the obvious advantage of having a well-characterized geometry and surface chemistry, they are known to form clusters in polymer matrices at low particle concentrations. In this case, the size of the clusters can be *tuned* by varying the NP concentration.²⁹⁻³¹ Moreover, molecular dynamics simulations have explored the fundamental nature of NP self-assembly,³²⁻³⁴ which is interesting in its own right. Such clustering allows for controllable variation in the scale of heterogeneities within the BCP material and thus provides a viable means of by which to alter the extent of quenched disorder to effect a change in BCP ordering.

While some simulation studies aimed at understanding the influence of NPs on ordering in BCP materials have been based on mesoscopic simulation methods (dynamical density functional³⁵ and cell dynamical theories^{36,37}), these mean-field computational methods do not explicitly consider the role of composition fluctuations on the ordering process. Indeed, the effect of such fluctuations can not be realistically simulated for BCP materials in the absence of NPs, and the long timescales involved make large-scale molecular dynamics simulations unfeasible for such investigations.

However, existing mean-field simulations³⁵⁻³⁸ have revealed a tendency for NPs possessing idealized interactions to localize either at the interface of the BCP components or to within one of the blocks, depending on the selective nature of the NP-BCP interaction. These results, which have been experimentally verified,^{38,39} are most likely robust tendencies and the omission of fluctuations probably does not compromise these qualitative conclusions. However, the NP size, shape and surface interactions are often assumed to be completely wetting or non-wetting by the polymer matrix, and the interactions leading to self-assembly are completely neglected in these simplified mean-field simulations. These assumptions can be difficult to realize in practice. One must consequently be prepared for new phenomena to emerge in these systems that simulations have not yet revealed. Recent self-consistent field calculations have also strongly suggested that the dynamic heterogeneity associated with the glass-forming nature of the components can influence ordering in BCP materials,⁴⁰ providing yet another source of disorder to be considered in relation to understanding and controlling BCP ordering.

Prior experimental studies have elucidated the effect of NP additives on the phase behavior of polymers. For example, Wiesner *et al.*⁴¹ report that adding silica-like NPs measuring 12 to 18 nm in diameter and possessing a surface layer of grafted polyisoprene into a BCP matrix composed of polystyrene-*block*-polyisoprene (PS-*b*-PI) at 0.5 wt% decreased the order-disorder transition temperature (T_{ODT}). Han *et al.*⁴² have shown that the addition of Cloisite 30B (synthetic exfoliated clay sheets) increased T_{ODT} of a functionalized polystyrene-*block*-hydroxylated polyisoprene BCP relative to the neat BCP material. This observation is attributed to varying defect energy density in the BCP

material upon addition of these NPs. More recently, Gaines *et al.*⁴³ have demonstrated that T_{ODT} increases for polystyrene-coated silica NPs (20 nm diameter), but decreases for hydroxyl-terminated native silica NPs (12 nm diameter), in a polystyrene-*block*-methyl methacrylate BCP. Their accompanying self-consistent field simulations indicate that increases in T_{ODT} can occur under favorable conditions of NP concentration, selectivity and size. In general terms, these shifts of the ordering temperature, either up or down depending on the preferential affinity of the additive for the polymer components, are completely normal upon addition of solvent additives to small molecule mixtures, polymer blends or even magnets for that matter.⁴⁴ Apart from the qualitative nature of the phenomenon, there are outstanding questions relating to how additive morphology and interaction strength *quantitatively* affect the magnitude and sign of these temperature shifts. We also note at this juncture that Sanz *et al.*⁴⁵ have utilized inelastic incoherent neutron scattering to quantify the effect of C_{60} NP additives on the amplitude of local chain motion in glassy polystyrene and found an appreciably increased amplitude of atomic motion upon addition of the NPs, an effect that has significant potential ramifications for influencing ordering processes involving glassy polymeric materials.

In the present study, we present an experimental study of the influence of C_{60} on T_{ODT} of lamellae-forming symmetric PS-*b*-PI BCP materials. The organization of this paper is as follows: First, small-angle X-ray scattering (SAXS) profiles for the specimens with and without C_{60} are presented over a wide temperature range traversing T_{ODT} . This range is investigated to determine how the nature of the transition is altered upon incorporation of the NP additive. Secondly, we address how the ODT and breadth of the

ordering transition become modified by the presence of C₆₀ and how these changes are manifested in the dynamic rheological behavior of the nanocomposites. Finally, we discuss the implications of our observations.

6.2 Experimental

Materials

Given the unexpected nature of our preliminary results, we synthesized two block copolymer samples, one at the ASRC in Japan (BCP1) and the other at Procter & Gamble in the United States (BCP2). Both PS-*b*-PI materials were synthesized by living anionic polymerization with *sec*-butyllithium as the initiator according to standard methods.⁴⁶ The molecular weight characteristics of BCP were $M_n = 21500$ g/mol and $M_w/M_n = 1.02$, whereas those for BCP2 were $M_n = 16000$ g/mol and $M_w/M_n = 1.02$. The volume fraction of PS (f_{PS}) in each copolymer was 0.55 and 0.50, respectively. The fullerene NPs (≈ 1 nm in diameter) incorporated into BCP1 were purchased from Aldrich, while those in BCP2 were obtained from Alpha Aesar.⁴⁷

Sample preparation

Since the solubility of C₆₀ in organic solvents is limited (e.g., the saturated concentration of C₆₀ in benzene is reported⁴⁸ to be ≈ 1.44 mg/g at 30°C) and to avoid excessive clustering, small amounts of NPs were added to the BCP materials. Films of BCP1 without and with 0.4 wt% C₆₀ (referred to as films BCP1*a* and BCP1*b*, respectively) were prepared for SAXS by slowly evaporating a benzene solution with

5.15 wt% BCP1 at ambient temperature in air for one week and then under vacuum for one week. In the case of the nanocomposite, special care was exercised to obtain, as much as possible, a homogeneous dispersion of C₆₀ in the as-cast films. The BCP1 and C₆₀ were first separately dissolved in benzene at concentrations of 10.3 and 0.04 wt%, respectively. The C₆₀ solution was further subjected to ultrasound for 30 min before the two solutions were subsequently mixed in a 1:1 volume ratio. Film BCP1_c, wherein the C₆₀ concentration in the film was increased to a value near 1 wt%, was formed in the same way as film BCP1_b. The thickness of the as-cast films after drying was ≈ 0.43 mm. Nanocomposites of BCP2 and C₆₀ were fabricated for dynamic rheology in similar fashion as those produced with BCP1. The C₆₀ was dispersed in toluene at concentrations ranging from 0 to 0.5% w/v under sonication for ≈ 1 h. Clear, purple solutions were obtained in this fashion, indicating that the NPs were relatively well-dispersed. The BCP2 material was then added to each solution at a concentration of 3% w/v and dissolved while being stirred. The solutions were cast in Teflon molds, and the toluene was allowed to evaporate slowly at ambient temperature. Dried films measured ≈ 1 mm thick and varied in color from purple to brown with increasing C₆₀ content, but consistently remained optically clear.

Sample characterization

The scattering intensity was measured *in situ* with a SAXS diffractometer described elsewhere.⁴⁹ To suppress thermal degradation as much as possible, each specimen, consisting of a stack of six films so that the total thickness was ≈ 2.6 mm, was placed in a

chamber filled with nitrogen, and the temperature was controlled to an uncertainty of $\pm 0.03^\circ\text{C}$. Acquired scattering profiles were desmeared for slit-height and slit-width smearing and corrected for absorption, air scattering and thermal diffuse scattering as described elsewhere.⁴⁹ The thermal history for the SAXS experiments performed on BCP1 films is depicted in Fig. 1. Each sample was cooled starting from an initial temperature 180°C , corresponding to the disordered state. The temperature was then reduced in 1°C decrements through T_{ODT} . Samples were held at temperature for ≈ 60 min before each ≈ 30 min measurement. Dynamic shear rheology was performed on BCP2 films to discern T_{ODT} as a function of C_{60} concentration. Isochronal temperature sweeps were conducted at a fixed oscillatory frequency and strain amplitude of 1 rad/s and 1%, respectively, to ensure linear viscoelasticity on an ARES strain rheometer outfitted with 25 mm parallel plates and operated under a nitrogen purge to prevent oxidative degradation. Specimens were heated from 80 to 150°C at a constant heating rate of $1^\circ\text{C}/\text{min}$. The value of T_{ODT} was deduced from the midpoint of the discontinuous reduction in the dynamic storage modulus (G') with increasing temperature.

6.3 Results

Figure 2 shows the corrected SAXS scattering profiles acquired *in situ* from film BCP1a as a function of temperature according to the thermal protocol provided in Fig. 1. Here, the scattering intensity is plotted against the magnitude of the scattering vector q , where $q \equiv (4\pi/\lambda) \sin(\theta/2)$, $\lambda = 0.154$ nm and θ represents the scattering angle. As in former SAXS studies of the same BCP material,⁵⁰ an abrupt change in scattering intensity

(quantified below) is observed in Fig. 2a at a temperature between 165 and 160°C. Moreover, a second-order Bragg peak is evident for $T < T_{\text{ODT}}$ (not shown). This is caused by the slightly asymmetric composition ($f_{\text{PS}} = 0.55$) and is characteristic of a lamellar morphology.^{51,52} The scattering data for the neat BCP film shows a continuous increase in the scattering intensity maximum and a decrease of the peak width upon cooling. These features constitute "normal" behavior and provide a reference point for our observations below for the NP-modified BCP.

Corrected SAXS profiles from the BCP1*b* film possessing a relatively low concentration of C_{60} (0.4 wt%) again according to the thermal protocol in Fig. 1 are displayed in Fig. 3. In this case, the scattering intensity presented as function of q changes abruptly from a broad maximum to a sharp peak over a narrow temperature range between 150 and 146°C, implying an appreciable shift of T_{ODT} for such a small amount of additive. Profiles collected above T_{ODT} are highlighted in Fig. 3b. In addition to the apparent shift in T_{ODT} upon fullerene addition, the shape of the scattering maximum changes: it is lower and the peak width is broader than the virgin BCP1*a*. We elaborate further on these differences below. Corrected SAXS data for the BCP1*c* film modified with a relatively large amount of C_{60} (≈ 1 wt%) are included for comparison in Fig. 4, in which the thermal protocol is again described by Fig. 1. In this case, the peak SAXS scattering intensity never becomes large (note the different ordinate scales in Figs. 3 and 4), despite the large temperature range investigated.

The first-order scattering peak is normally analyzed in terms of the maximum intensity (I_m), the peak position (q_m) and the full width at half maximum (σ_q) of the

scattering intensity. This latter quantity is the inverse of the correlation length describing the BCP in the ordered and disordered states, $\xi \equiv 1/\sigma_q$. Characteristically, a plot of I_m^{-1} or σ_q^2 vs T^{-1} reveals a discontinuous change at T_{ODT} ,^{50,53,54} as a consequence of thermal fluctuation-induced first-order transition.⁵⁵ Both I_m^{-1} and σ_q^2 are plotted as a function of T^{-1} or $\Delta = T^{-1} - T_{\text{ODT}}^{-1}$ for all the films discussed above in Fig. 5. As expected, I_m^{-1} and σ_q^2 exhibit similar temperature dependence in films BCP1a and BCP1b, with each exhibiting a temperature discontinuity over a narrow temperature range. Thus, these films exhibit well-defined first-order phase transitions, which occur between 163 and 161°C for BCP1a and 149 and 146°C for BCP1b (cf. Figs. 5a and 5b). Moreover, T_{ODT} is depressed by about 15°C for BCP1b relative to the neat BCP1a film. Normally, three distinct temperature regimes are evident in such plots and correspond to the temperature ranges above, near and below the transition point. In each regime, I_m^{-1} vs. T^{-1} and σ_q^2 vs. T^{-1} are nearly linear and the temperature range of the ODT indicated above is determined from the intersection of these three lines. The temperature window of the ordering transition also becomes broader in the C_{60} -modified (BCP1b) film. The situation is strikingly different in BCP1c with the highest C_{60} concentration, however, where *no* discernible transition, first-order or otherwise, is observed. As the temperature is varied, the change in scattering intensity and correlation length appear continuous.

In Figs. 5c and 5d, I_m^{-1} and σ_q^2 are compared as functions of Δ for films BCP1a and BCP1b. Here, Δ is related to an effective segregation power of PS and PI blocks: $\chi_T - \chi_{\text{ODT}}$, where χ_T and χ_{ODT} are the thermodynamic interblock interaction parameters evaluated at T and T_{ODT} , respectively. The temperature dependence of I_m^{-1} and σ_q^2 for

films BCP1*a* and BCP1*b* become almost identical when I_m^{-1} and σ_q^2 are plotted in terms of Δ , which implies that the change in scattering observed in these two films is due to a change in the interaction parameter χ_T through the addition of C₆₀ NPs. Incorporation of the NPs at low concentrations yields an effect that is similar to that of BCP materials upon addition of solvent, i.e., a simple change in χ_T . However, a subtle difference in the scattering data arises upon addition of the fullerene NPs: I_m^{-1} for a given Δ is somewhat smaller in BCP1*a* than in BCP1*b* (cf. Fig. 5c). This difference will be discussed later. We next consider the nature of the ordering transition of BCP2 with C₆₀ ascertained on the basis of dynamic rheological measurements.

As in the crystallization of molten polymeric materials, the ordering transition of BCP materials is accompanied by the formation of structure that endows the BCP with solid-like character through a first-order phase transformation. Rheological measurements thus provide a method for locating and characterizing the nature of the ordering transition that is complementary to small-angle scattering. While rheological measurements require finite deformation of samples subjected to very low strains that in some cases perturb the material (even in the linear viscoelasticity limit), this approach is nonetheless useful for measuring the temperature corresponding to this ordering transition.^{62,63} Determination of T_{ODT} in a BCP by dynamic melt rheology is achieved by examining the temperature dependence of the dynamic storage modulus G' , since this quantity best characterizes the elastic nature of the polymer melt.⁶⁷ Figure 6 shows representative temperature scans for BCP2 films with and without the C₆₀ NPs. The

rheological order-disorder transition is identified by the inflection point in the discontinuous drop of G' as a function of temperature.

In the case of the neat BCP2 (BCP2*a*), T_{ODT} is measured as $117 \pm 1^\circ\text{C}$.⁶⁷ (The uncertainty includes the range of temperatures associated with data points collected at $\Delta T \approx 0.3$.) Table 1 lists values of T_{ODT} measured for BCP2 nanocomposites varying in NP concentration. Introduction of 0.02 wt% C_{60} in BCP2*b*, for instance, reduces T_{ODT} by almost 17°C relative to BCP2*a*. Increasing the concentration of C_{60} to 0.04 wt% (an order of magnitude lower concentration compared to BCP1*b*) in BCP2*c* results in $\approx 21^\circ\text{C}$ decrease in T_{ODT} , which quantitatively agrees with the results obtained for the BCP1 series by SAXS. This change in T_{ODT} is accompanied by an 8 % increase in the magnitude of G' evaluated at 80°C . The glass transition temperature (T_g) of the PS block in this BCP material is 58°C according to differential scanning calorimetry and is nearly independent of C_{60} concentration. Increases in NP loading up to 0.08 wt% promote little, if any, further reduction in T_{ODT} , suggesting that the mechanism responsible for the observed change in T_{ODT} reaches a limit. The temperature range over which G' decreases due to disordering (ΔT_{ODT} in Table 1) is likewise useful to describe self-assembly transitions that often exhibit transition rounding⁶²⁻⁶⁵ and generally broadens progressively with increasing C_{60} concentration. At 0.50 wt% C_{60} , existence of an unequivocal inflection point in G' becomes questionable, which is consistent with an apparent disappearance of the first-order phase transition according to SAXS.

Figure 7 shows the repeat period (D) determined from the position of the wavevector corresponding to the scattering maximum (q_m) from Bragg's law ($D = 2\pi/q_m$) as a

function of T^{-1} for the three BCP1 films. No profound change in D occurs near T_{ODT} , which is consistent with previous reports by Bates *et al.*⁶⁶ and Hashimoto *et al.*⁴⁷ In contrast, D progressively changes in the order $D_a < D_b < D_c$, where the subscript denotes the relevant material. Specifically, D_b is found to be larger than D_a by about 0.5 nm at a given temperature, while D_c is larger by about 5 nm than the neat BCP material at high temperatures. The presence of the C_{60} influences the effective thickness of the ordered lamellae, as well as the intensity and scale of the composition fluctuations in the BCP. At 1 wt% C_{60} , no ODT is apparent over the wide temperature investigated. This observation, coupled with the low peak scattering intensity, indicates that the BCP remains in what can reasonably be called a disordered state, in which case we propose that the ODT simply disappears.

To determine how the addition of such a small amount of C_{60} to the BCP matrix can cause such a significant suppression of the T_{ODT} and such a large increase in D , we plot the scattering profiles near the first-order peak for the three films at the same temperature (180°C) in Fig. 8. The plots reveal the following: (i) The scattering maximum I_{mi} decreases in the order of $I_{ma} > I_{mb} > I_{mc}$, whereas (ii) the peak width σ_{qi} increases in the order of $\sigma_{qa} < \sigma_{qb} < \sigma_{qc}$, and (iii) the peak position decreases (or, conversely, D increases) upon increasing the C_{60} concentration. According to these results, the Fourier modes of concentration fluctuations at large q ($q > 0.3 \text{ nm}^{-1}$) are suppressed, while those at small q ($q < 0.3 \text{ nm}^{-1}$) are enhanced. All these findings reflect the downward shift in T_{ODT} upon incorporation of C_{60} . Results (i) and (ii) naturally arise from changes in the magnitude of the thermodynamic interaction parameter χ_T between the PS and PI blocks, as discussed

above. However, result (iii) wherein q_m depends on NP concentration is not a consequence of a simple change in χ_T . Thus, the observations to be elucidated here are the origin of the T_{ODT} shift and the meaning of result (iii).

6.4 Discussion

Our investigation of two neat BCP materials indicates a canonical behavior of a fluctuation-induced first-order phase transition. From this baseline, we can discuss how the presence of C_{60} changes the order–disorder transition in these materials. The introduction of a relatively small concentration (0.4 wt%) of C_{60} into either BCP profoundly reduces the T_{ODT} , an effect that by itself is unremarkable. The breadth of the transition temperature, on the other hand, is increased, which is intuitively anticipated, but not predicted, from the presence of NPs altering molecular packing and thus the entropic, as well as the enthalpic, contributions to the thermodynamic parameter χ_T , which effectively governs the degree of block segregation.⁵⁰ An interesting feature of the reduction of T_{ODT} is the magnitude of the shift in comparison to small-molecule diluents.⁵¹⁻⁵³ In small-molecule liquid mixtures or even magnetic systems, the concentration-dependent shift of the phase boundary is often linear in the volume of additive, with a slope that is on the order of unity or smaller. The 15-21°C reduction measured in T_{ODT} in the BCP films containing 0.02-0.4 wt% C_{60} corresponds to a change that is about an order of magnitude larger than normal relative to small-molecule additives. Although theoretical investigations are severely limited with respect to this problem, we note that large critical temperature (χ_T) shifts have been reported^{55,56} when

highly extended polymers are added to small-molecule critical mixtures. In particular, Siano and Bock⁵⁵ find that cloud point shifts correlate with the intrinsic viscosity of the additive times the additive concentration. An order of magnitude increase in the aspect ratio of the additive is typically sufficient to promote an order of magnitude shift in the intrinsic viscosity,^{57,58} in which case NP clustering provides a potential explanation for the transition shift observed here.

The possibility of C₆₀ clustering in the BCP matrices is consistent with ample other evidence in polymeric materials. This C₆₀ particle clustering phenomenon has been nicely illustrated by Kropka *et al.*²⁹ in studies where poly(methyl methacrylate) (PMMA) constitutes the matrix, whereas others^{30,31} have considered the equivalent case of polystyrene. The electron microscopy observations of Kropka *et al.*²⁹ confirm the presence of C₆₀ aggregates measuring on the order of 10 to 20 nm at a C₆₀ concentration on the order of 1 wt%. Such NP clustering provides an obvious source of structural order that is responsible for changes in the scattering and rheological data, as well as in the nature of the ordering transition in the C₆₀-modified BCP materials described above.

Another basic finding of several theoretical studies relating to quenched disorder effects on first-order phase transitions is the existence of a critical concentration in three dimensions, where the phase transition *either* transforms to a second-order phase transition *or* disappears altogether (i.e., no critical concentration exists in two dimensions).⁵⁵⁻⁵⁸ An infinitesimal amount of disorder can destabilize a first-order phase transition, which perhaps has some significance for ultrathin quasi-2D BCP films by transforming into some glass-like state where ordering is so frustrated that only a highly

rounded remnant of the original phase transition exists. Observations of the BCP1c film containing 1 wt% C₆₀ are consistent with these general expectations. In particular, the heterogeneity in the BCP material arising from C₆₀ clusters at the higher fullerene concentrations so disrupts the BCP ordering that a phase transition *does not exist*. Only limited local ordering occurs, which is revealed in the weak BCP interchain correlations that are reflected in the broad peaks in Fig. 4 and the broadening of the discontinuity in G' in Fig. 6. It would be interesting to see if other types of additives are capable of making the ordering transition second order, an effect that is *certainly not* observed in our measurements. Unfortunately, theory offers little guidance on this question.

The C₆₀ NPs appear to exhibit little selective affinity for either block or the interblock interface in our measurements. The Flory-Huggins interaction parameters between the blocks of PS-*b*-PI and C₆₀ have been calculated^{73,74} as $\chi_{f,PS} = 0.015$ and $\chi_{f,PI} = 0.026$, respectively. Although $\chi_{f,PI}$ is nearly twice as large as $\chi_{f,PS}$, the interaction parameters between C₆₀ and both of the blocks are relatively small, in which case the NPs can be expected to exhibit comparable miscibility within both blocks, but with a marginally higher affinity for the PS block. Because the C₆₀ has not been functionalized with any surface-grafted polymer chains to induce block-selective interaction, its ability to interact with each of the copolymer blocks is dictated solely by the magnitudes of $\chi_{f,PS}$ and $\chi_{f,PI}$. In the event that the NPs were functionalized, the microphase separation behavior could be considerably different. For example, Schmaltz and coworkers⁸³ have studied C₆₀ functionalized with long grafted PS chains ranging from 10,000 to 105,000 g/mol and report that the NP localized within the PS-rich microdomains of the copolymer

structure⁷⁹, as one might expect. Their observations, however, show no evidence that the nanoparticles disrupt the ability of the BCP to order. Another consideration that influences the localization of NPs within a structured BCP material,⁸¹ as well as the stability of the BCP structure itself,⁸² is the primary size of the NP relative to the size of a BCP molecule, often expressed in terms of its gyration radius (R_g), which is given by $\sqrt{(l_{PS}^2 N_{PS} + l_{PI}^2 N_{PI})/6}$. Here, l_{PS} and l_{PI} denote the statistical segment lengths of PS and PI (0.71 and 0.83 nm, respectively⁷⁴), and N_i ($i = PS$ or PI) is the number of statistical segment lengths comprising block i . The characteristic NP/BCP size ratio (R_{C60}/R_g), where R_{C60} is the radius of the C_{60} NPs, for both systems is about 0.1.

A shift in phase-transition temperature upon incorporation of an additive to a polymeric matrix is a rather universal phenomenon that exhibits common trends.⁸⁰ In particular, the enthalpy and entropy governing the thermodynamics of the nanocomposite govern what sort of critical temperature shifts will be observed. According to Timmerman's rule, the addition of an additive with a high selectivity towards one of the components in a mixture tends to destabilize the critical point (i.e., raise the temperature for an upper critical solution temperature, UCST, blend), whereas the addition of a non-selective additive (equally incompatible or compatible) stabilizes the mixture (lowers the critical point). Recent observations by Gaines *et al.*⁴³ have demonstrated a tendency for T_{ODT} in a block copolymer to shift upward to marginally higher temperatures upon addition of highly selective (surface-functionalized) silica NP, which is in agreement with the Timmerman's simple rule extended to BCP materials. Previous observations by Wiesner *et al.*³⁹ have likewise established that a functionalized NP induces a downward

shift of T_{ODT} , again a result qualitatively expected from Timmerman's rule. However the Flory-Huggins interaction parameter provides only the enthalpic contribution of the free energy for the polymer system. In order to fully understand the equilibrium phase behavior and resulting copolymer morphology, the entropic contribution must also be considered. Several groups use theoretical calculations⁷⁵⁻⁷⁸ to explain the ability of highly selective, small NPs to localize at/near the interface between the two blocks of the BCP. In this case, T_{ODT} decreases dramatically because the polymer chains are now required to stretch around single or clustered NPs. Greater chain stretching causes the T_{ODT} to decrease, and the BCP equilibrium morphology to become less stable.

There is another source of quenched disorder other than C_{60} particle clustering that must, however, be considered. Nanoparticles intrinsically possess high surface area relative to other additives, and, as such, they are often highly reactive species, in which case we need to explore effects of a chemical, as well as a physical, nature when such nanomaterials are mixed with organic polymers. In particular, C_{60} has been found to exhibit a powerful oxidizing effect on cell membranes, a primary factor implicated in the toxicity of this class of materials.^{68,69} Underivatized fullerenes behave as both electron donors and electron acceptors, and their numerous electrophilic double bonds can spontaneously couple to nucleophiles, free radicals and conjugated double bonds.⁸⁴⁻⁸⁷ The likelihood that this reaction proceeds increases with increasing temperature. As the number of polymer-particle contacts increases with C_{60} loading, the NPs can easily form chemical cross-links with either the double bonds along the PI block or the phenyl rings

of the PS block or both, recognizing that double bonds are more electron-donating than phenyl rings.

There is direct evidence for chemical alteration in both series of BCP nanocomposites arising from active fullerene chemistry. First, the Fourier modes of concentration fluctuations at large q values are suppressed, while those at small q are enhanced. Second, the BCP1 c and BCP2 films with 1 wt% C₆₀ after thermal treatment would only swell, and not dissolve, upon immersion in either THF or toluene. Third, FTIR analysis of BCP2 films after heat treatment during rheological analysis confirms changes in chemistry, especially at high wavenumbers where molecular vibrations due to hydrogen bonding becomes important. Chemical interaction of C₆₀ with the double bonds of the PI blocks in the BCP films may promote cross-linking of the PI blocks, either physically or chemically, both in regions rich in PI blocks (ordered state) and in the regions containing PS blocks (disordered state). Cross-linking generally suppresses concentration fluctuations and therefore stabilizes the disordered state and reduces scattering intensity particularly at $q \geq q_m$. Heterogeneous cross-linking, wherein more cross-linking occurs in spatial regions rich in PI (upon ordering) than in the regions also containing PS, accounts for enhancement of thermal concentration fluctuations at large length scales and, hence, $I(q)$ at small q ($< q_m$). Fullerene-induced cross-linking apparently provides yet another source of heterogeneity that could disrupt BCP ordering, thereby affecting the order-disorder transition. Cross-linking, as well as NP clustering, can thus account for the experimentally observed augmentation of large-length scale thermal concentration fluctuations at small q .

6.5 Conclusions

We have prepared two series of nanocomposites composed of a symmetric PS-*b*-PI BCP material and C₆₀, and studied the impact of this NP on the thermodynamic nature of the lamellar ordering transition. Results from SAXS analysis of one BCP series indicate a large downward shift of T_{ODT} at a relatively low concentration (0.4 wt%) of the C₆₀ additive, an effect readily rationalized by the tendency of these NPs to form clusters within the polymer matrix even at relatively low NP concentrations. Nearly identical results are observed by dynamic rheology performed independently on the second BCP series. Although the phase transition was reduced and broadened in both instances, it remained first order, according to SAXS measurements. Increasing the concentration further (≈ 1 wt% C₆₀) proves to be sufficient to frustrate altogether the occurrence of the phase transition. This observation, which most likely reflects the combined effects of NP clustering and NP cross-linking of the polymer matrix, is consistent with the general expectation that the introduction of a sufficient amount of heterogeneity should *eliminate* the first-order phase transition observed in the bulk material. Evidently, the addition of surface-active NPs to BCP materials can lead to new and unintended effects, but these property changes also afford opportunities for the development of *new* materials that exploit new types of thermodynamic transition phenomena that arise from simply blending NPs with polymeric media.

6.6 Acknowledgments

This work has been supported by the Research Council of Norway under the NANOMAT Program. M.K.G. would also like to express her gratitude for a GEM Fellowship and a NOBCCHE Procter & Gamble Graduate Fellowship.

6.7 References and Notes

1. Park, M.; Harrison, C.; Chaikin, P. M.; Register, R. A.; Adamson, D. H. *Science* **1997**, 276, 1401-1404.
2. Spatz, J. P.; Eibeck, P.; Mossmer, S.; Moller, M.; Herzog, T.; Ziemann, P. *Adv. Mater.* **1998**, 10, 849-852.
3. Hamley, I. W. *The Physics of Block Copolymers*; Oxford University Press: New York, 1998.
4. Khandpur, A. K.; Forster, S.; Bates, F. S.; Hamley, I. W.; Ryan, A. J.; Bras, W.; Almdal, K. and Mortensen, K. *Macromolecules* **1995**, 28, 8796-8806.
5. Sakamoto, N.; Hashimoto, T. *Macromolecules* **1998**, 31, 3292-3302.
6. Van Oene, H. in *Polymer Blends* **1978**, 1, chap. 7, edited by Paul, D. R.; Newman, S., Academic Press, Orlando.
7. Fried, J. R. *Polymer Science and Technology* **1995**, Prentice-Hall, Englewood Cliffs, NJ.
8. Usuki, A.; Kawasumi, M.; Kojima, Y.; Fukushima, Y.; Okada, A.; Kurauchi, T.; Kamigaito, O. *J. Mater. Res.* **1993**, 8, 1174.
9. Templin, M.; Frank, A.; Chesne, A. D., Leist, H.; Zang, Y. Ulrich, R.; Schadler, V.; Wieser, U. *Science* **1997**, 278, 1795-1798.
10. Zao, D.; Feng, J.; Huo, Q.; Melosh, N.; Fredrickson, G. H.; Chmelka, B. F.; Stucky, G. *D. Science* **1998**, 279, 548-552.
11. Thompson, R. B.; Ginzburg, V. V.; Matsen, M. W.; Balazs, A. C. *Science* **2001**, 292, 2469-2472.

12. Edrington, A. C.; Urbas, A. M.; DeRege, P.; Chen, C. X.; Swager, T. M.; Hadjichristidis, N.; Xenidou, M.; Fetters, L. J.; Joannopoulos, J. D.; Fink, Y.; Thomas, E. L. *Adv. Mater.* **2001**, *13*, 412-425.
13. Lopes, W. A.; Jaeger, H. M. *Nature* **2001**, *414*, 735-738.
14. Fendler, J. H. *Nanoparticles and Nanostructured Films* Ed. Wiley-VCH: Weinheim, 1998.
15. Kojima, Y.; Usuki, A.; Kawasumi, M.; Okada, A.; Kurauchi, T.; Kamigaito, O. *J. Polym. Sci.: Part A: Polym. Chem.* **1993**, *31*, 983.
16. Krishnamoorti, R.; Vaia, R. A.; Giannelis, E. P. *Chem. Mater.* **1996**, *8*, 1728.
17. Yano, K.; Uzuki, A.; Okada, A.; Kurauchi, T.; Kamigaito, O. *J. Polym. Sci.: Part A: Polym. Chem.* **1993**, *31*, 2493.
18. Kroto, H.W.; Allaf, A.W.; Balm, S.P. *Chem. Rev.* **1991**, *91*, 1213.
19. Hirsch, A. *The Chemistry of the Fullerenes*; Georg Thieme Verlag: Stuttgart, 1994.
20. Hoston, W.; Berker, A. N. *J. Appl. Phys.* **1991**, *70*, 6101-6103.
21. Berker, A. N. *Physica A* **1993**, *194*, 72-76.
22. Aizenman, M.; Wehr, J. *Phys. Rev. Lett.* **1989**, *62*, 2503-2506.
23. Kerszberg, M; Mukamel, D. *Phys. Rev. Lett.* **1979**, *43*, 293-296.
24. Imry, Y.; Wortis, M. *Phys. Rev. B* **1979**, *19*, 3850-3855.
25. Cox, U. J.; Gibaud, A.; Cowley, R. A. *Phys. Rev. Lett.* **1988**, *61*, 982-985.
26. Bloch, D.; Hermann-Ronzaud, D.; Vettier, C.; Yelon, W. B.; Alben, R. *Phys. Rev. Lett.* **1975**, *35*, 963-697.
27. Aharony, A.; Bruce, A. D. *Phys. Rev. Lett.* **1979**, *42*, 462-465.

28. Buzaré, J. Y.; Fayet, J. C.; Berlinger, W.; Müller, K. A. *Phys. Rev. Lett.* **1979**, *42*, 465-468.
29. Kropka, J. M.; Putz, K. W.; Pryamitsyn, V.; Ganesan, P. F. *Macromolecules* **2007**, *40*, 5424-5432.
30. Gladchenko, S. V.; Polotskaya, G. A.; Griбанov, A. V.; Zgonnik, V. N. *Tech. Phys.* **2002**, *47*, 102-106.
31. Peng, H.; Leung, F. S. M.; Wu, A. X.; Dong, Y. R.; Dong, Y. Q.; Yu, N. T.; Feng, X. D.; Tang, B. Z. *Chem. Mat.* **2004**, *16*, 4790-4798.
32. Starr, F. W.; Douglas, J. F.; Gloter, S. C. *J. Chem. Phys.* **2003**, *119*, 1777-1788.
33. Rahedi, A. J.; Douglas, J. F.; Starr, F. W. *J. Chem. Phys.* **2008**, *128*, 024902.
34. Knauert, S. T.; Douglas, J. F.; Starr, F. W. *J. Polym. Sci. B* **2007**, *45*, 1882-1887.
35. Sevink, G. J. A.; Zvelindovsky, A. V.; van Vlimmeren, B. A. C.; Maurits, N. M.; Fraaije, J. G. E. M. *J. Chem. Phys.* **1999**, *110*, 2250.
36. Balazs, A. C.; Ginzburg, V. V.; Qiu, F.; Peng, G.; Jasnow, D. *J. Phys. Chem. B* **2000**, *104*, 3411-3422.
37. Ginzburg, V. V.; Gibbons, C.; Qiu, F.; Peng, G.; Balazs, A. C. *Macromolecules* **2000**, *33*, 6140-6147.
38. Spontak, R. J.; Shankar, R.; Bowman, M. K.; Krishnan, A. S.; Hamersky, M. W.; Samseth, J.; Bockstaller, M. R.; Rasmussen, K. Ø. *Nano Lett* **2006**, *6*, 2115-2120.
39. Bockstaller, M. R.; Lapetnikov, Y.; Margel, S.; Thomas, E. L. *Journal of American Chemical Society* **2003**, *125*, 5276-5277.
40. Bosse, A. W.; Douglas, J. F.; Berry, B. C.; Jones, R. L.; Karim, A. *Phys. Rev. Lett.*

- 2007**, *99*, 216101.
41. Jain, A.; Gutmann, J. S.; Garcia, C. B. W.; Zhang, Y.; Tate, M. W.; Gruner, S. M.; Wiesner, U. *Macromolecules* **2002**, *35*, 4862-4865.
42. Lee, K. M.; Han, C. D. *Macromolecules* **2003**, *36*, 804-815.
43. Gaines, M. K.; Smith, S. D.; Samseth, J.; Bockstaller, M. R., Thompson, R. B., Rasmussen, K. Ø., Spontak, R. J. submitted to *Soft Matter*
44. Dudowicz, J.; Freed, K. F.; Douglas, J. F. *Macromolecules* **1995**, *28*, 2276-2287.
45. Sanz, A.; Ruppel, M.; Douglas, J. F.; Cabral, J. T. *J. Phys.: Condens. Matter* **2008**, *20*, in press.
46. Szwarc, M.; Van Beylen, M. *Ionic Polymerization and Living Polymers*, Chapman & Hall: N.Y., 1993.
47. Certain equipment, instruments, or materials are identified in this paper in order to adequately specify the experimental details. Such identification does not imply recommendation by the NIST, nor does it imply the materials are necessarily the best available for the purpose.
48. Sivaraman, N.; Dhamodaran, R.; Kaliappan, I. *J. Org. Chem.* **1992**, *57*, 6077-6079.
49. Hashimoto, T.; Suehiro, S.; Shibayama, M.; Saijo, K.; Kawai, H. *Polym. J.* **1981**, *13*, 501.
50. Sakamoto, N.; Hashimoto, T. *Macromolecules* **1995**, *28*, 6825-6834.
51. Hashimoto, T.; Nagatoshi, K.; Todo, A.; Hasegawa, H.; Kawai, H. *Macromolecules* **1974**, *7*, 364.
52. Hasegawa, H.; Hashimoto, T.; Kawai, H.; Lodge, T. P.; Amis, E. J.; Glinka, C. J.;

- Han, C. C. *Macromolecules* **1985**, *18*, 67.
53. Hashimoto, T. *Macromol. Symp.* **2001**, *174*, 69-86.
54. Dudowicz, J.; Freed K. F., Douglas, J. F. *Phys. Rev. Lett.* **2002**, *88*, 095503.
55. Lodge, T. P.; Pudil, B.; Hanley, K. J. *Macromolecules* **2002**, *35*, 4707-4717.
56. Lodge, T. P.; Hanley, K. J.; Pudil, B.; Alahapperuma, V. *Macromolecules* **2003**, *36*, 816-822.
57. Sakamoto, N.; Hashimoto, T.; Han, C. D.; Kim, D.; Vaidy, N. Y. *Macromolecules* **1997**, *30*, 5321-5330.
58. Lai, C.; Russell, W. B.; Register, R. A. *Macromolecules* **2002**, *35*, 841-849.
59. Siano, D. B.; Bock, J. J. *J. Coll. Interface Sci.* **1982**, *90*, 359.
60. Kline, R. J.; Ihde, A. J. *J. Coll. Polym. Sci.* **1958**, *13*, 163.
61. Douglas, J. F.; Garboczi, E. J. *Adv. Chem. Phys.* **1995**, *91*, 85.
62. Bicerono, J.; Douglas, J. F.; Brune, D. A. *Rev. Macromol. Chem. Phys. C*, **1999**, *39*, 561.
63. Wolff, T.; Burger, C.; Ruland, W. *Macromolecules* **1993**, *26*, 1707.
64. Floudas, G.; Pakula, T.; Fischer, E. W.; Hadjichristidis, N.; Pispas, S. *Acta Polym.* **1994**, *45*, 176.
65. Fredrickson, G. H.; Helfand, E. *J. Chem. Phys.* **1987**, *87*, 697-705.
66. Han C. D.; Kim, J. *Macromolecules* **1987**, *25*, 1741-1764.
67. Rosedale, J. H.; Bates, F. S. *Macromolecules* **1990**, *23*, 2329-2338
68. Lee, K. M.; Han, C. D. *Macromolecules* **2003**, *36*, 804-815.
69. Rosedale, J. H.; Bates, F. S.; Almdal, K.; Mortensen, K.; Wignall, G. D.

- Macromolecules* **1995**, 28, 1429-1443.
70. Bates, F. S.; Rosedale, J. H.; Fredrickson, G. H. *J. Chem. Phys.* **1990**, 92, 6255-6270.
71. The Goodyear Tire & Rubber Company, US Patent 5750615.
72. Chen, X. L.; Jenekhe, S. A. *Langmuir*, **1999** 15, 8007-8017.
73. Zolotukhin, I. V.; Yanchenko, L. I.; Belonogov, E. K. *JETP Lett.* **1998**, 67, 720-722.
74. Saye, C. M.; Gobin, A. M.; Ausman, K. D.; Mendoz, J.; West, J.L.; Colvin, V. L. *Biomaterials* **2005**, 26, 7587-7595.
75. Kamat, J. P.; Devasagayam, T. P. A.; Priyadarsini, K. I.; Mohan, H. *Toxicology* **2000**, 155, 55.
76. Lo, C. -T.; Lee, B.; Pol, V. G.; Rago, N. L. D.; Seifert, S.; Winans, R. E.; Thiagarajan, P. *Macromolecules* **2007**, 40, 8302-8310.
77. Mountrichas, G.; Pispas, S.; Xenogiannopoulou, E.; Aloukos, P.; Couris, S. *J. Phys. Chem. B.* **2007**, 111, 4315-4319.
78. F. Rodriguez, C. Cohen, C. K. Ober and L. A. Archer, *Principles of Polymer Systems*, 5th Ed., Taylor & Francis, New York, 2003, p. 40 & 264.
79. Thompson, R. B.; Ginzberg, V. V.; Matsen, M. W.; Balazs, A. C. *Science* **2001**, 292, 2469-2472.
80. Balazs A. C. *Nature Materials* **2007**, 6, 94-95.
81. Tadd, E.; Bradley, J. Tannenbaum, R. *Langmuir* **2002**, 18, 2378-2384.
82. Chervanyov, A. I.; Balazs, A. C. *J. Chem. Phys.* 2003, 119, 3529-2534.

83. a) Schmaltz, B.; Brinkmann, M.; Mathis, C. *Macromolecules* **2004** 37, 9056-9063. b)
Schmaltz, B.; Brinkmann, M.; Mathis, C. *Fullerenes, Nanotubes, and Carbon Nanostructures* **2005**, 13, 225-227.
84. Laiho A.; Ras, R. H. A.; Valkama, S.; Ruokolainen, J.; Österbacka, R.; Ikkala, O. *Macromolecules* **2006**, 39, 7648-7653.
85. Zeynalov, E.B.; Friedrich, J. F. *Polymer Materials* **2007** 49, 265-270.
86. Ginzburg, B. M.; Shibaev, L. A.; Kireenko, O. F.; Shepelevskii, A.A.; Melenevskaya, E. Yu.; Ugolkov, V. L. *Polymer Science Ser. A* **2005**, 47, 160-174.
87. Biglova, Yu. N.; Sigaeva, N. N.; Talipov, R. F.; Monakov, Yu. B. *Oxidation Communications* **2005**, 4, 753-798.

6.8 List of Table Captions

Table 6.1 Measured values of T_{ODT} from BCP2 materials modified with C_{60} nanoparticles according to dynamic shear rheology.

Table 6.1. Measured values of T_{ODT} from BCP2 materials modified with C_{60} nanoparticles according to dynamic shear rheology.

wt% C_{60}	T_{ODT} Inflection ($^{\circ}\text{C}$)	T_{ODT} Onset ($^{\circ}\text{C}$)	T_{ODT} Offset ($^{\circ}\text{C}$)	ΔT_{ODT} ($^{\circ}\text{C}$)
0.00	116.6	115.4	117.8	2.4
0.02	99.3	92.6	106.1	13.6
0.04	95.8	89.1	102.7	13.5
0.06	94.8	86.6	103.0	16.4
0.08	94.4	85.8	102.9	17.0
0.50	98.5	86.6	110.2	23.4

6.9 List of Figure Captions

Figure 6.1 Thermal treatment protocols adopted in the SAXS measurements for: (a) BCP1a (neat PS-*b*-PI); (b) BCP1b with 0.387 wt% C₆₀; (c) BCP1c with 1 wt% C₆₀. The arrows marked in *a* and *b* denote the corresponding values of T_{ODT}: 163-161°C and 149-146°C, respectively.

Figure 6.2 Temperature dependence of the SAXS profiles near the first-order peaks for BCP1a at various temperatures (a) and at T > T_{ODT} (b).

Figure 6.3 Temperature dependence of the SAXS profiles near the first-order peaks for BCP1b at various temperatures (a) and at T > T_{ODT} (b).

Figure 6.4 Temperature dependence of the SAXS profiles near the first order peaks for BCP1c at various temperatures.

Figure 6.5 I_m^{-1} and (b) σ_q^2 presented as functions of T⁻¹ for BCP1a, BCP1b and BCP1c. (c) I_m^{-1} and (d) σ_q^2 plotted as functions of T⁻¹-T_{ODT}⁻¹ for BCP1a and BCP1b.

Figure 6.6 Isochronal temperature sweeps of the dynamic storage modulus (G') for the BCP2 series varying in C₆₀ concentration from 0 to 0.5 wt% (see key).

Figure 6.7 Variation of *D* with T⁻¹ for BCP1a, BCP1b and BCP1c.

Figure 6.8 Scattering profiles near the first-order peak for BCP1a, BCP1b and BCP1c evaluated at 180°C.

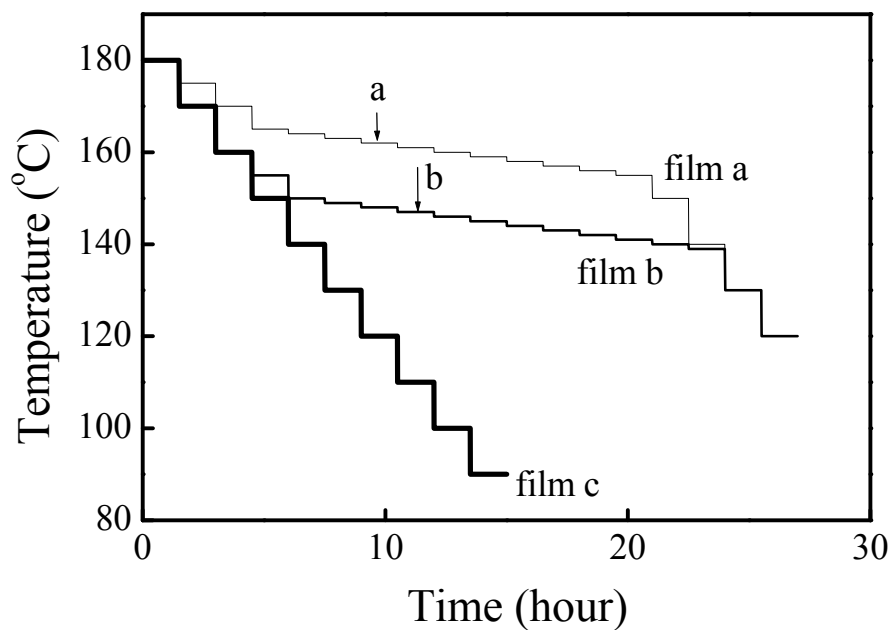


Figure 6.1. Thermal treatment protocols adopted in the SAXS measurements for: (a) BCP1*a* (neat PS-*b*-PI); (b) BCP1*b* with 0.387 wt% C₆₀; (c) BCP1*c* with 1 wt% C₆₀. The arrows marked in *a* and *b* denote the corresponding values of T_{ODT}: 163-161°C and 149-146°C, respectively.

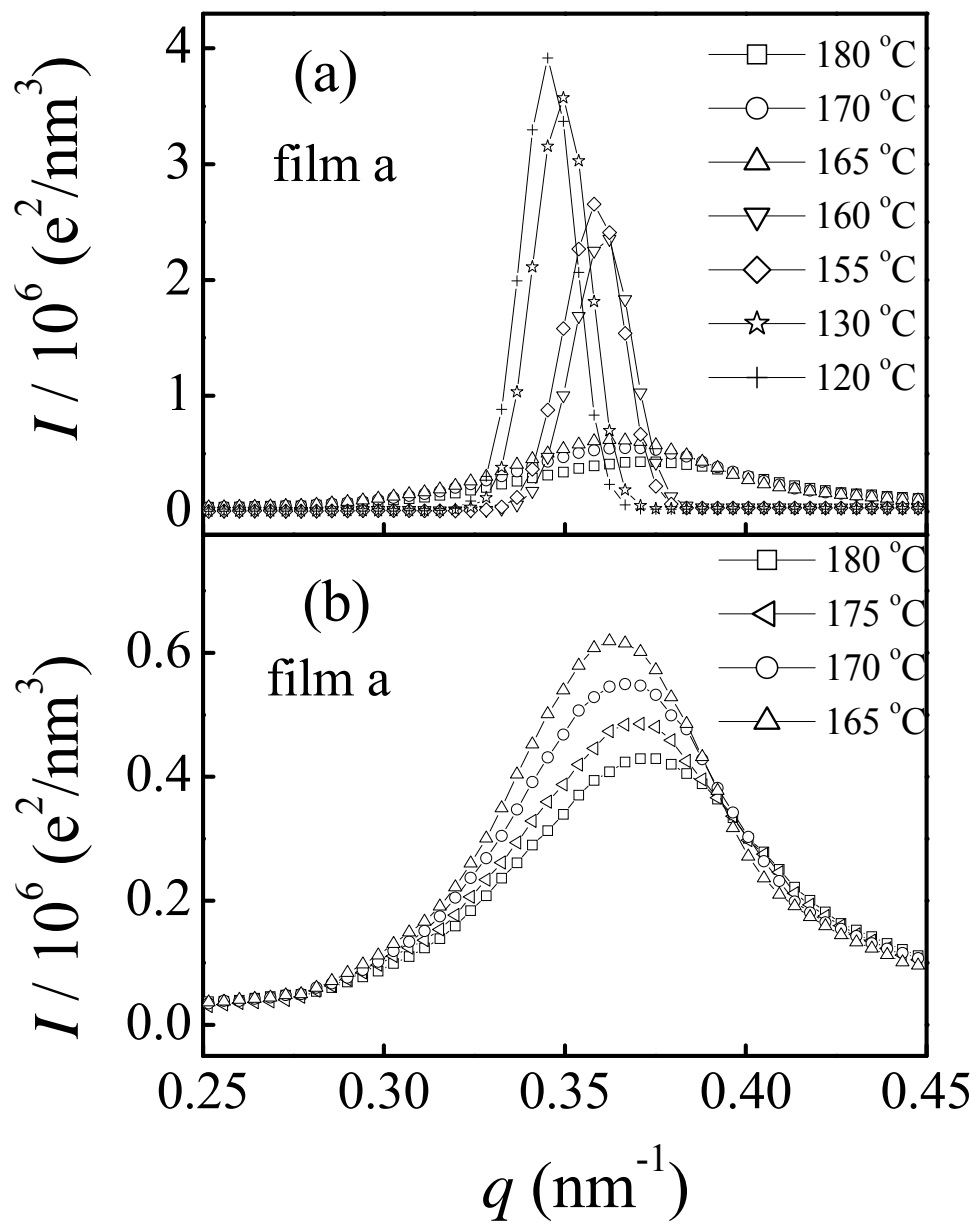


Figure 6.2. Temperature dependence of the SAXS profiles near the first-order peaks or BCP1a at various temperatures (a) and at $T > T_{ODT}$ (b).

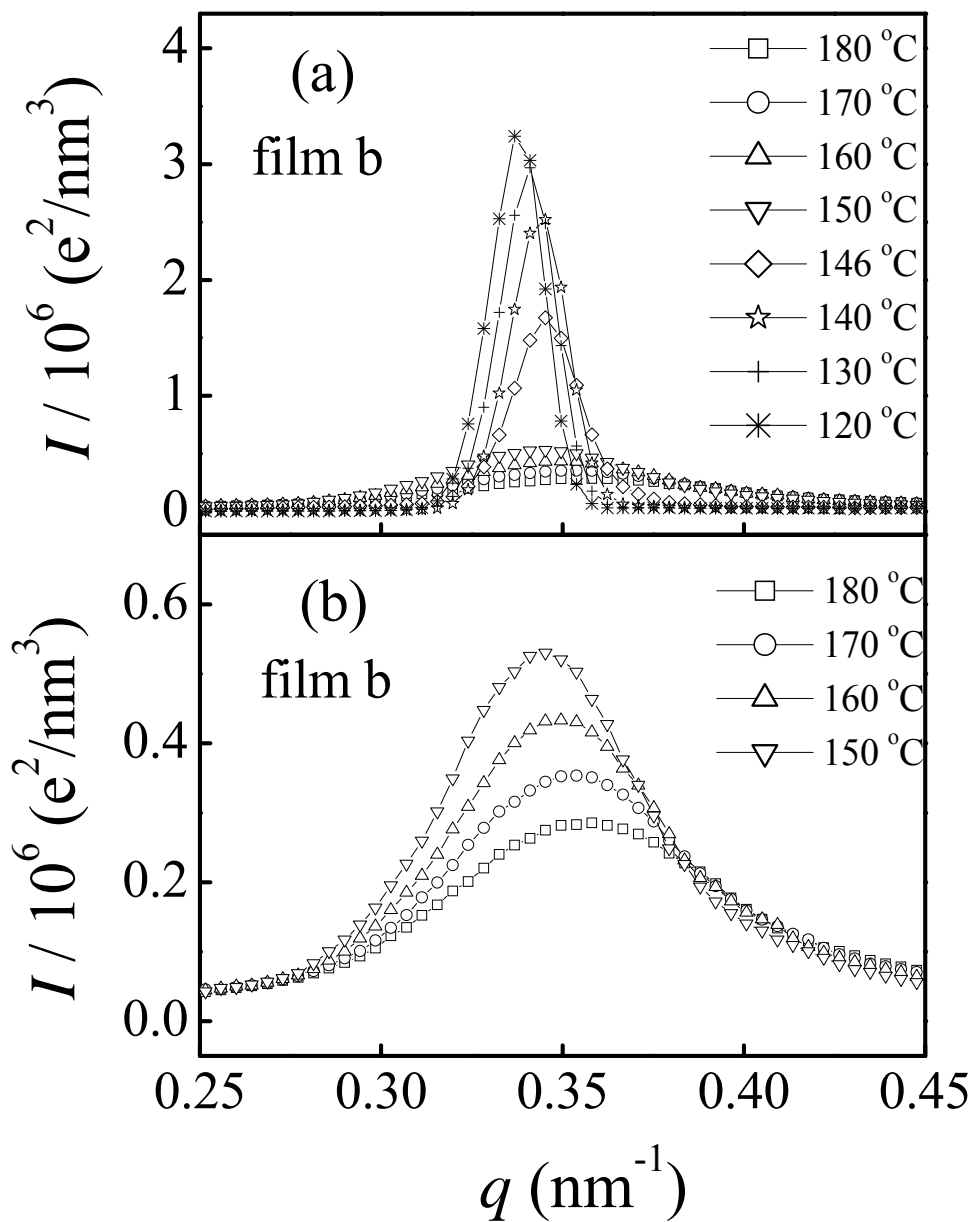


Figure 6.3. Temperature dependence of the SAXS profiles near the first-order peaks for BCP1*b* at various temperatures (a) and at $T > T_{\text{ODT}}$ (b).

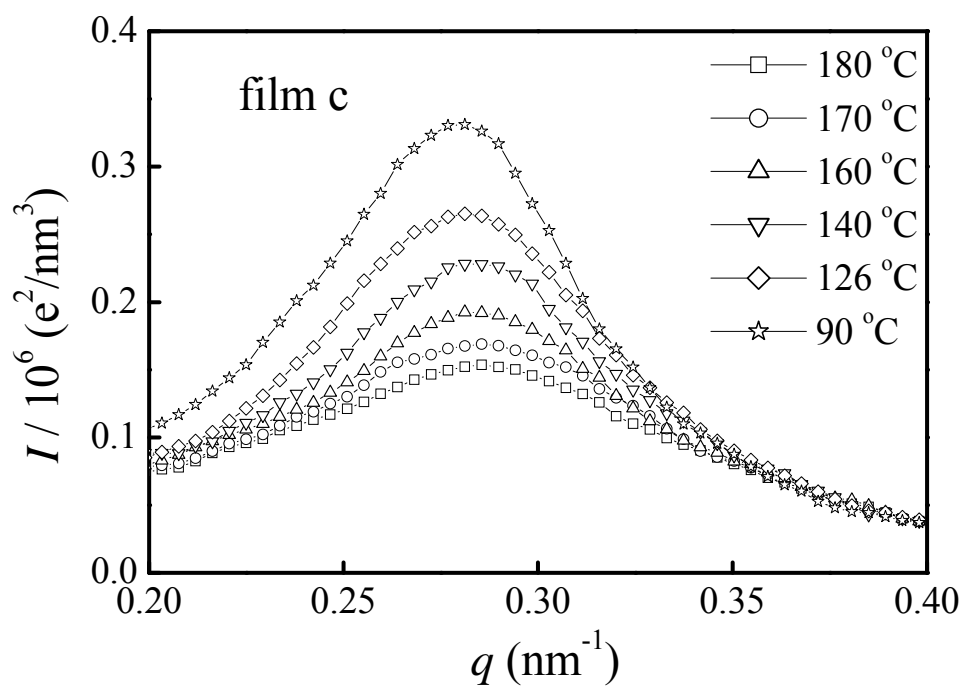


Figure 6.4. Temperature dependence of the SAXS profiles near the first order peaks for BCP1c at various temperatures.

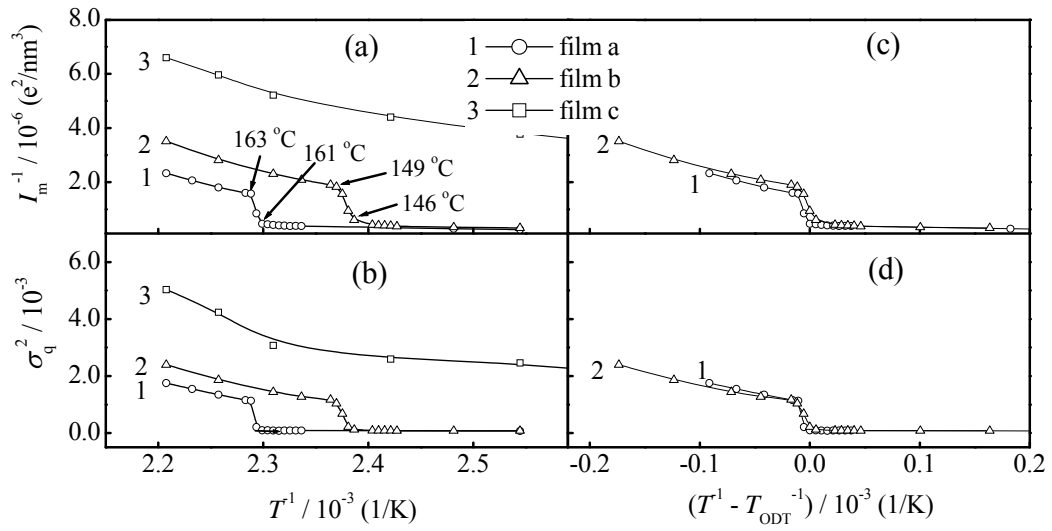


Figure 6.5. I_m^{-1} and (b) σ_q^2 presented as functions of T^{-1} for BCP1a, BCP1b and BCP1c. (c) I_m^{-1} and (d) σ_q^2 plotted as functions of $T^{-1} - T_{\text{ODT}}^{-1}$ for BCP1a and BCP1b.

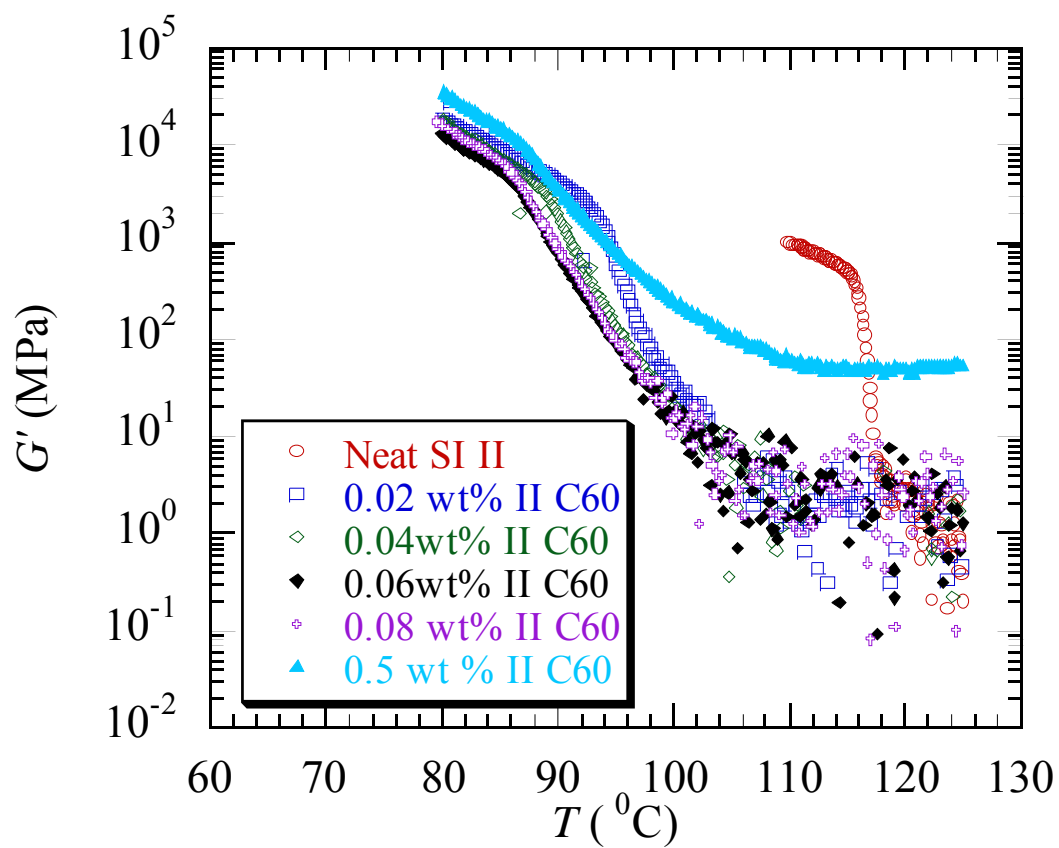


Figure 6.6. Isochronal temperature sweeps of the dynamic storage modulus (G') for the BCP2 series varying in C_{60} concentration from 0 to 0.5 wt% (see key).

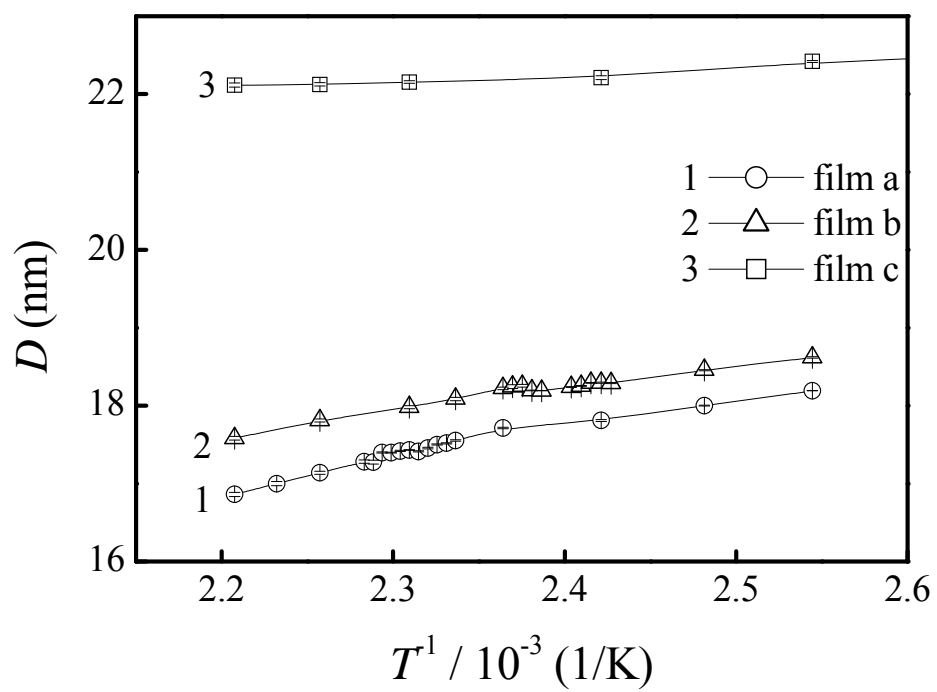


Figure 6.7. Variation of D with T^{-1} for BCP1a, BCP1b and BCP1c

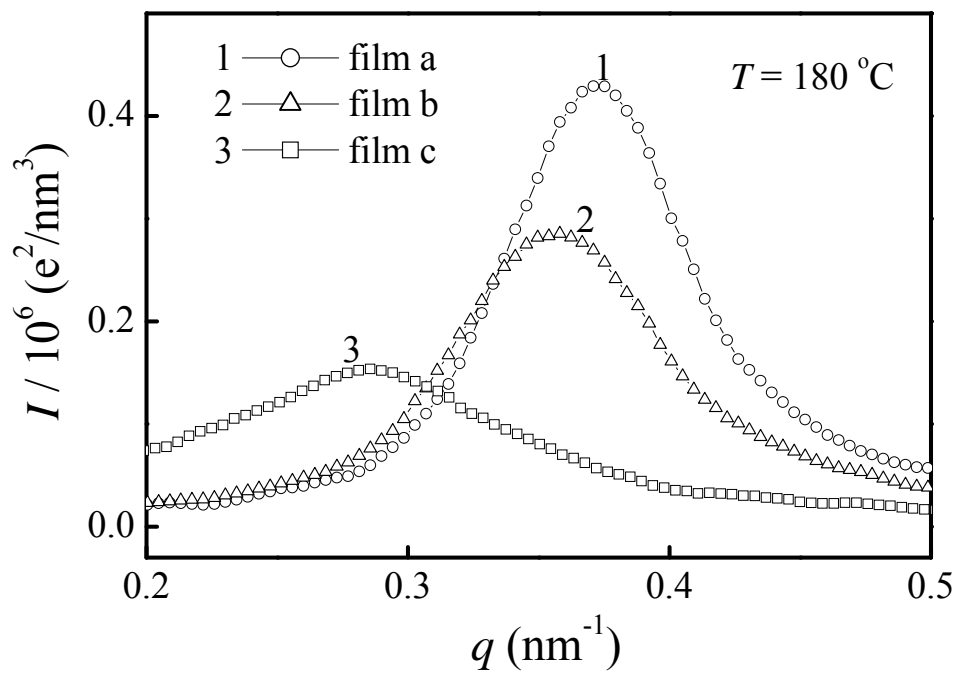


Figure 6.8. Scattering profiles near the first-order peak for BCP1*a*, BCP1*b* and BCP1*c* evaluated at 180°C

CHAPTER 7

CONCLUSIONS AND FUTURE WORK

This work has shown that block copolymer microphase-ordering behavior is influenced by the block composition as well as the presence of large solvent molecules and nanoparticles.

7.1 A₁BA₂ Asymmetric Triblock Copolymers

The microphase-ordering in asymmetric A₁BA₂ triblock copolymers showed two trends as A₂ grew on the end of the B-block: 1) A decrease in microphase stability at low molecular weight A₂ and 2) An increase in microphase stability, once MW_{A1} ~ MW_{A2}. When low molecular weight A₂ (MW_{A1} < MW_{A2}) was added to the end of the B-block, it phase-mixed with the B-blocks and formed a *tail*. Its phase behavior resulted from a reduction in χ_{eff} (evidenced by a decrease in T_{ODT}, $\chi \sim 1/T$) between itself and the B chains. A₂'s small length caused entropy to be the driving force in decreasing the T_{ODT}, causing less microphase stability from enthalpically unfavorable A₂. This reduction in interaction parameter caused the d-spacing to decrease, due to reduced molecular chain stretching. As A₂ continued to grow (MW_{A1} ~ MW_{A2}), χ_{eff} increased and caused A₂ to phase-separate from the B-phase and join the same phase as the chemically-similar A₁

block, forming a *bi-disperse polymer brush* with one macromolecule. The enthalpy became the driving force for improving microphase stability and increased the T_{ODT} . In order to accommodate the phase separation, the chains in the B-block became stretched. The d-spacing also increased and evidenced the same trends exhibited by strongly segregated block copolymers.¹ Finally, as A_2 continued to grow, the phase behavior transitioned to a *symmetric ABA triblock copolymer* ($A_2 = A_1$) and then eventually another *bi-disperse polymer brush* ($A_2 > A_1$). The phase segregation continued to increase as A_2 increased.

The future work for this project entails understanding more about predicting the phase-separation behavior of these block copolymers. More SCF calculations will explain more on the polymer physics. They will allow us to understand how varying the composition of A_1 also tunes the phase behavior of the B-block. It is expected that as A_1 decreases, phase-segregation will decrease, and it would eventually behave as a tail. With the addition of low molecular weight A_2 , the polymer molecules will remain disordered and phase-mixed in all environments (pH, temperature, electric field).²

Other factors could also influence the phase behavior. For example, when A_1 and A_2 are short tails and are homogeneously phase-mixed with in the B-phase, adding cross-links, solvent, or nanoparticles are all avenues that could modify the polymers' phase behavior and can be experimented upon. Adding a cross-linking agent to some of the A-blocks could cause phase-segregation and micelles to form among short A_1 and A_2 tails.³ Strongly affinitive solvent molecules or nanoparticles may also have the ability to behave as cross-linkers to the short A_1 and A_2 tails, allowing them to form micelles around the

additives and allow phase-separation. If one of these additives could cause a blend that would have normally remained disordered to microphase-separate, it would also be interesting to monitor the changes in the ordering behavior (d-spacing and T_{ODT}). These materials would be useful in the development of photovoltaics and hydrogels, where electromagnetic radiation or changing pH could influence the phase segregation.

Asymmetric triblock copolymers may be used for a variety of applications. One of the main advantages of materials with bi-disperse polymer brushes is reduced confinement in one of the microphases. More space is present and may be occupied by any sort of additive. Nanoparticles could be placed within one of the phases, depending on their size, interaction, and geometry. Based on the interactions and size-ratio, they could be arranged in any desired manner. Large pockets of solvent molecules could also reside within one of the phases, gathering in another location than the interface. Polymer brushes are ideal materials for the coating industry, where surface chemistry becomes important. These asymmetric polymer brushes could be used to spontaneously absorb molecules/particles in one environment and then release the molecules/particles in another, for biomedical applications (anti-microbial wound dressings) or the electronics industry.

7.2 Block Copolymer Molecular-Composites

From the work done on tuning the phase behavior of a triblock (ABA) copolymer by adding large-molecule solvent, we observed a gathering of solvent molecules at the interface between A- and B-blocks. The degree of clustering was quantified as a function

of A-B segregation ($\chi_{AB}N$), selectivity (ϵ), and solvent volume fraction (Φ_s) and recognized as the interfacial excess, ϕ^* . Reported in Chapter 3, the most influential parameter causing ϕ^* to increase was A-B segregation, $\chi_{AB}N$. Selective and nonselective solvent molecules were entropically driven to the A-B interface, causing the number of A-B contacts to decrease (reducing the enthalpic contribution) and also causing the incompatibility to favorably reduce in the copolymer. Overall, these behaviors are expected to improve microphase stability of the copolymer microphases. Also highlighted, was the influence of molecular-penetrant size on the microphase stability. Smaller molecules dispersed more uniformly than larger molecules, despite the unfavorable enthalpic χ_{AS} interactions.⁴ Entropy governs the phase behavior here, where smaller molecules' possession of high translational entropy governs their desire to spread. Larger molecules have less translational entropy and tend to still gather at the A-B interface, reducing the number of A-B contacts. They also gather at the midplane of the B-block and reduce chain stretching around the molecules. Their strong selectivity to the B-block and low translational entropy causes the system's enthalpy to drive the molecules to the center of the favored B-block. Similar behaviors were observed in PS-*b*-PEP copolymer with surface functionalized Au NP, however two different sized NP had to be incorporated to achieve the same affect.⁴ This study precludes methods to specify NP for tailoring the phase behavior of block copolymer nanocomposite systems.

Further work for this project includes gaining more understanding on how Φ_s influences the BCP phase behavior via ϕ^* . In particular, inducing phase transitions from increased ϕ^* must be understood in order to fully predict BCP phase behavior in selective

or nonselective solvent environments. It is expected that as the A- and B- blocks become more segregated ($\chi_{AB}N = 50, 75, \text{ or } 100$) and the solvent molecules become partially ($\epsilon = 1.0$) or highly selective ($\epsilon = 1.5, 2.0$), phase transitions from lamellae, cylinders, and spheres can be induced.⁵ ϕ^* and selective solvent molecules to the B-block cause a change in interfacial curvature, resulting in a phase transition. More SCF calculations were conducted, by modifying the $\chi_{AB}N$ and the ϵ , in an effort to determine if phase transitions were induced, as Φ_S increased. Figure 1 shows a partially selective system, where the $\chi_{AB}N = 50$ and $\epsilon = 1.0$. At 10% solvent, a lamellar morphology is observed. As the solvent volume increases to 66%, the d-spacing increases slightly but the lamellar morphology remains in tact. At 67%, however, a phase transition to cylinders occurs. Selective solvent molecules gathering in the B-block and at the interface cause the interfacial curvature to increase and for cylinders to form. At 69% solvent, a metastable morphology emerges before disordering the copolymer, at 70% partially selective solvent.

Nonselective solvent molecules are expected to gather at the interface and also swell the A- & B-blocks, eventually causing the copolymer to disorder. The nonselective solvent molecules are not particular to either of the blocks and should merely dilute the system, while also causing the lamellar d-spacing to increase. Figure 2 shows a nonselective solvent system, where the $\chi_{AB}N = 50$ and $\epsilon = 0.5$. Now at 10% nonselective solvent, an interfacial excess is observed as well as solvent segregation from the A- and B- blocks. The morphology of the copolymer is lamellar, as depicted earlier in Chapter 3. However as nonselective solvent volume fraction increases, so does the lamellar spacing

allowing the lamellar morphology to remain at 62% solvent. A phase transition to cylinders appears at 63% nonselective solvent, but it does not remain stable. At 64%, the same metastable structure remains until the system disorders at 65% nonselective solvent. Regardless of selectivity, the microphase stability of the copolymer decreases with increasing Φ_s . However, as solvent selectivity and segregation increases, more solvent is required before disordering can be induced.

More SCFT will be necessary to observe the phase behavior of more segregated copolymer systems. It is expected that higher values of χ_{ABN} and highly selective solvent may cause cylindrical and spherical morphologies to appear and become more stable. Others have demonstrated that mechanical properties of a block copolymer can improve with the addition of a selective solvent.⁶ The next phase of the project will be linking mechanical integrity to physical gel formation as the volume fraction of selective solvent is modified. Verifying microphase stability is necessary for these systems, so they may be developed for practical applications.

7.3 Block Copolymer Nanocomposites

In the nanoparticle/block copolymer systems, the ODT either increased with nanoparticle loading, or increased and decreased. As the concentration of nanoparticles became high, the eventual disappearance of the ODT was observed in both the PS-*b*-PM and the PS-*b*-PI nanocomposites, resulting in an absence of lamellar block copolymer ordering. The reason the PS-*b*-PM lamellar morphology did not form was because silica agglomerates obstructed block copolymer microphase ordering. High FS concentrations,

eventually lead to colloidal network formation. CS formed smaller aggregates and interacted more with the block copolymer. The large size-ratio of the CS-OS in the copolymer contributed to its improvement in microphase stability at low concentrations, resulting from seeding polymer chains at the NP surface. These observations convey the importance in tailoring particle-polymer interactions, size-ratio, concentration, and surface roughness, to control nanoscale block copolymer microphase stability.

The PS-*b*-PI nanocomposite series, containing C₆₀, showed different phase behavior. The smaller-sized C₆₀ was expected to attract to the PS benzene rings and have a different affect on the block copolymer's ODT. Small concentrations of NP demonstrated a large decrease in the T_{ODT}. The decrease in microphase stability resulted from the entropic contribution, where the NP behaved as diluents and spread throughout the blocks. The polymer chains had to stretch around the NP, causing the polymer chains to remain less ordered. The decrease in T_{ODT} was predicted accurately by SCFT calculations. The theory also verified the effect of larger selective NP's ability to increase the ODT and microphase stability, due to their interaction and failure to spread.

Cross-linking or strong interactions also occurred in the PS-*b*-PI/C₆₀ nanocomposites, which resulted in the disappearance of the first-order ODT. Figure 3 illustrates temperature sweeps of nanocomposites, containing up to 4 wt% C₆₀. The ODT disappears and the storage shear modulus (G') begins to increase at temperatures above 110 °C. This up-swing in the data evidences possible cross-linking. In order to verify this speculation, further characterization is required. Fourier Transform Infra-Red Spectroscopy (FTIR) and Differential Scanning Calorimetry (DSC) were conducted on

four samples, before and after thermal treatment. Figure 4 evidences the presence of water at about 3440 cm^{-1} and a C–O bond at 1068 cm^{-1} , for the 1 wt% and 4 wt% nanocomposites. The hydrogen atoms in water vapor are highly attracted to carbon⁷, causing hydrolysis and new bonds to form in the copolymers. 904 cm^{-1} illustrates the presence of an *R* group bonded to the CH=CH double bonds, which depicts cross-linking of strong interactions between PI or PS benzene rings and the C₆₀ nanoparticles. Figure 5 shows how heating the samples cause the water to evaporate and reduce the hydrolysis bonds and C₆₀–double bond cross-linking/interactions. Figure 6 shows the behavior of the glass-transition temperatures (*T_g*) for PS and PI. The C₆₀ does not seem to affect the *T_g* for PS, but PI's *T_g* increases dramatically with increasing C₆₀. The fullerenes are serving as an anti-plasticizer, reducing the free volume and the mobility of the PI polymer chains. The C₆₀ molecules are interacting with both the PS blocks as well as the PI blocks. More characterization is required to identify more information on the cross-linking/interaction behavior.

There are new questions that emerge from this project. One inquiry involves understanding how block copolymer nanocomposite phase behavior and stability is linked to material properties. In the case of C₆₀ nanoparticles in PS-*b*-PI block copolymer, the fullerenes are able to conduct electricity in an otherwise insulating material. A useful parameter would include knowledge of the necessary concentration to meet a percolation threshold, while remaining a stable microphase-separated block copolymer. Also intriguing, would be to enhance the functionality of the material by being electrically conductive *and* chemically and thermally resistant. When incorporated

in an integrated circuit, the composite escalates to very high temperatures and a stable non-degraded nanocomposite is necessary. The microphase stability of bi-disperse NP systems must be understood. The last important piece to this puzzle is to fully understand and predict the kinetics of these materials. We must understand if the NP govern block copolymer segregation or if the block copolymer chains dictate the spatial distribution of the NP. Most likely, the kinetic behavior is dependent on the parameters of the system. Trends must be realized in order to gain a full perspective on how NP influence block copolymer phase behavior and morphology.

7.4 References

1. Fredrickson, G. H.; Helfand, E. *J. Chem. Phys.* **1987**, 87, 697-705.
2. Sumpter, B. G.; Noid, D. W.; Barnes, M. D. *Polymer* **2003**, 44, 4389-4403.
3. Gomez, E. D.; Das, J.; Chakraborty, A. K.; Pople, J. A.; Balsara, N. P. *Macromolecules* **2006**, 39, 4848-4859.
4. Lee, J. -Y.; Thompson, R. B.; Jasnow, D.; Balazs, A. C. *Phys. Rev. Lett.* **2002**, 89, 155503
5. Hanley, K. J.; Lodge, T. P.; Huang C-I *Macromolecules* **2000**, 33, 5918-5931.
6. Shankar, R.; Ghosh, T. K.; Spontak, R. J. *Soft Matter* **2007**, 3, 1116-1129.
7. Zeynalov, E. B.; Azerbaijan, B.; Friedrich, J. F. *Polymer Materials* **2007**, 49, 265-270.

7.5 List of Figure Captions

Figure 7.1 Two-dimensional probability density profiles of selective solvent in an ABA triblock copolymer. The images show that with increasing Φ_S , phase transitions can be induced. a) $\Phi_S = 0.10$ – lamellae, b) $\Phi_S = 0.66$ – lamellae, c) $\Phi_S = 0.67$ – cylinders, d) $\Phi_S = 0.68$ – cylinders, e) $\Phi_S = 0.69$ – spheres, $\Phi_S = 0.70$ – disorders. ($\chi_{AB}N = 50$; $\varepsilon = 1.0$)

Figure 7.2 Two-dimensional probability density profiles of nonselective solvent in an ABA triblock copolymer. The images show that with increasing Φ_S and less solvent–B-block interaction, fewer phase transitions can be induced. a) $\Phi_S = 0.10$ – lamellae, b) $\Phi_S = 0.62$ – lamellae, c) $\Phi_S = 0.63$ – cylinders, d) $\Phi_S = 0.68$ – swollen lamellae, e) $\Phi_S = 0.69$ – disorders. ($\chi_{AB}N = 50$; $\varepsilon = 0.5$)

Figure 7.3 Dynamic temperature sweeps of PS-*b*-PI diblock copolymer (sample II) nanocomposites, with increasing C_{60} concentration. These show evidence of first order ODT disappearance at high C_{60} concentrations, and cross-linking/strong-interaction behavior occur at temperatures past 110°C.

Figure 7.4 FTIR data of Neat, 0.02 wt%, 1 wt%, & 4 wt% nanocomposites before thermal treatment, to investigate the source of cross-linking behavior. The 1wt% and 4 wt% samples show evidence of –OH groups ($\sim 3440 \text{ cm}^{-1}$), the emergence of C–O bonds (1068 cm^{-1}), and presence of CH=CH-R bonds ($\sim 904 \text{ cm}^{-1}$). These peaks describe the

nanocomposite's interaction with water, causing alcohols to form and bonding to occur between either the PI double bond and/or the PS benzene ring.

Figure 7.5 FTIR data of Neat, 0.02 wt%, 1 wt%, & 4 wt% nanocomposites after thermal treatment, to continue investigating the source of cross-linking/interaction behavior. 1 wt% and 4 wt% samples show a reduction in the [2990-2850] cm^{-1} triplet, indicating a reduced signal for the aliphatic groups in PI. The $-\text{OH}$ peak and the $\text{C}-\text{O}$ peaks reduced and the $\text{CH}=\text{CH}$ peak ($\sim 680 \text{ cm}^{-1}$) remained the strongest peak. Heating the nanocomposites may have reduced the number of cross-links or interactions between molecules formed between the C_{60} NP and the PI and PS double bonds.

Figure 7.6 DSC traces of Neat, 0.02 wt%, 1 wt%, & 4 wt% nanocomposites before thermal treatment. These data show the nanoparticles' affect on the glass-transition temperature, T_g . The fullerenes show no influence on PS, but cause PI's T_g to increase with C_{60} concentration. The fullerenes act like an anti-plasticizer, reducing in mobility of the PI blocks.

Figure 7.7 DSC traces of Neat, 0.02 wt%, 1 wt%, & 4 wt% nanocomposites after thermal treatment. These data so no evidence of change compared to the non-thermally treated samples.

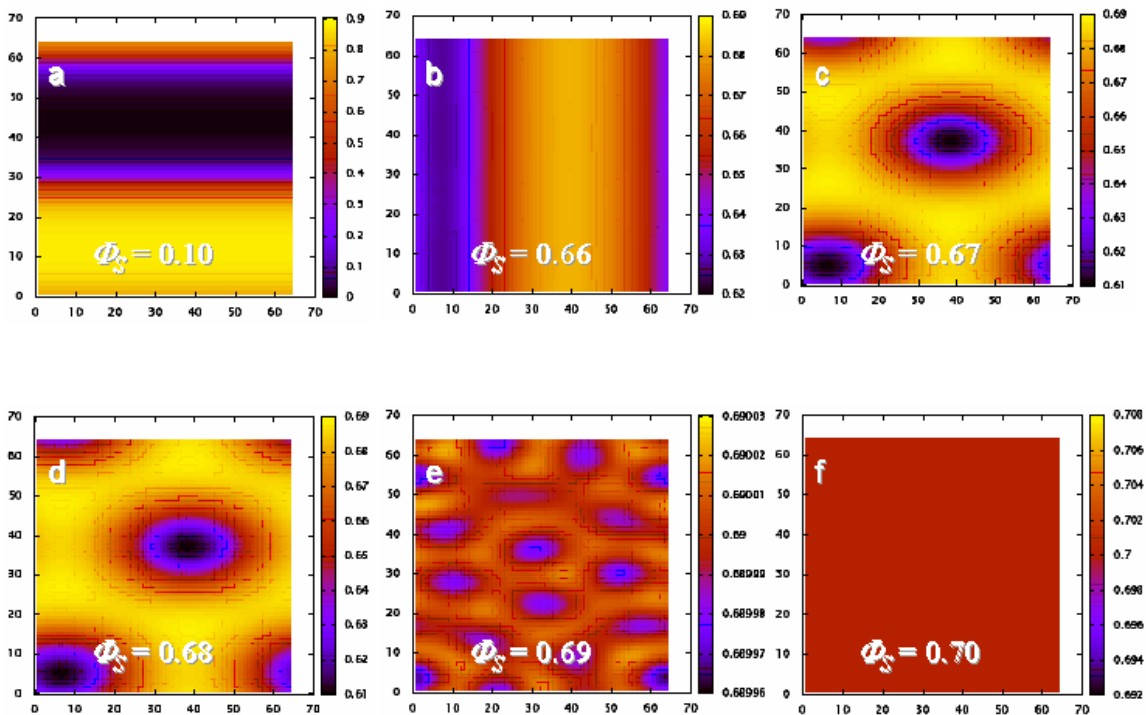


Figure 7.1. Two-dimensional probability density profiles of selective solvent in an ABA triblock copolymer. The images show that with increasing Φ_S , phase transitions can be induced. a) $\Phi_S = 0.10$ – lamellae, b) $\Phi_S = 0.66$ – lamellae, c) $\Phi_S = 0.67$ – cylinders, d) $\Phi_S = 0.68$ – cylinders, e) $\Phi_S = 0.69$ – spheres, $\Phi_S = 0.70$ – disorders. ($\chi_{AB}N= 50$; $\varepsilon = 1.0$)

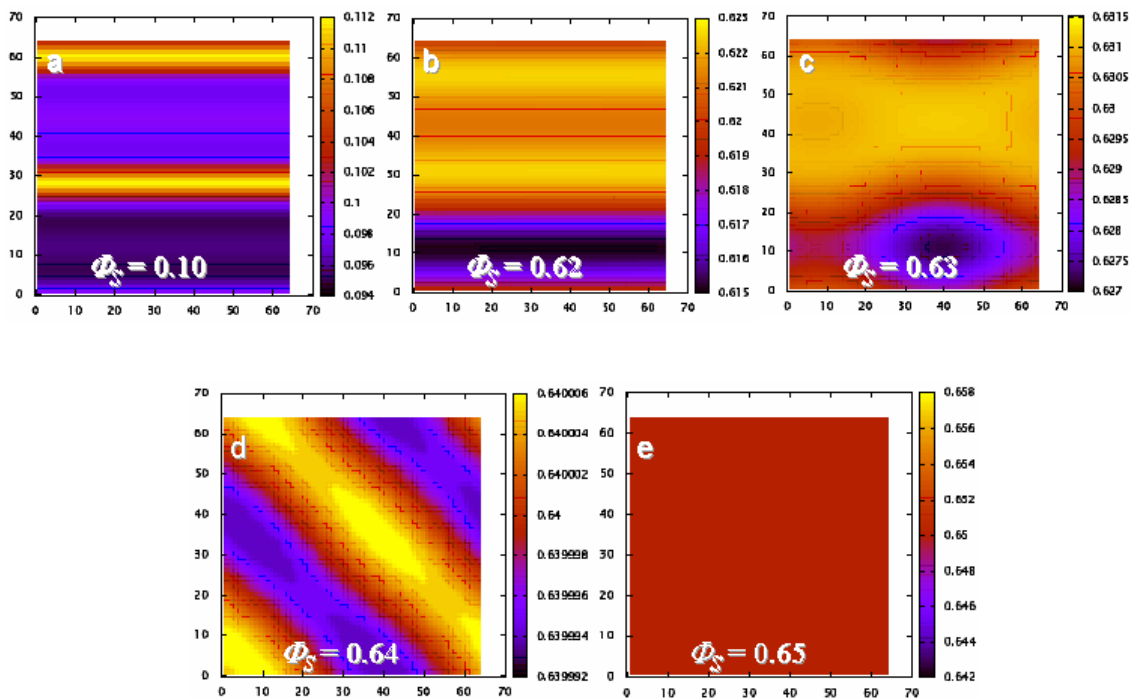


Figure 7.2. Two-dimensional probability density profiles of nonselective solvent in an ABA triblock copolymer. The images show that with increasing Φ_S and less solvent–B-block interaction, fewer phase transitions can be induced. a) $\Phi_S = 0.10$ – lamellae, b) $\Phi_S = 0.62$ – lamellae, c) $\Phi_S = 0.63$ – cylinders, d) $\Phi_S = 0.68$ – swollen lamellae, e) $\Phi_S = 0.69$ – disorders. ($\chi_{AB}N = 50$; $\varepsilon = 0.5$)

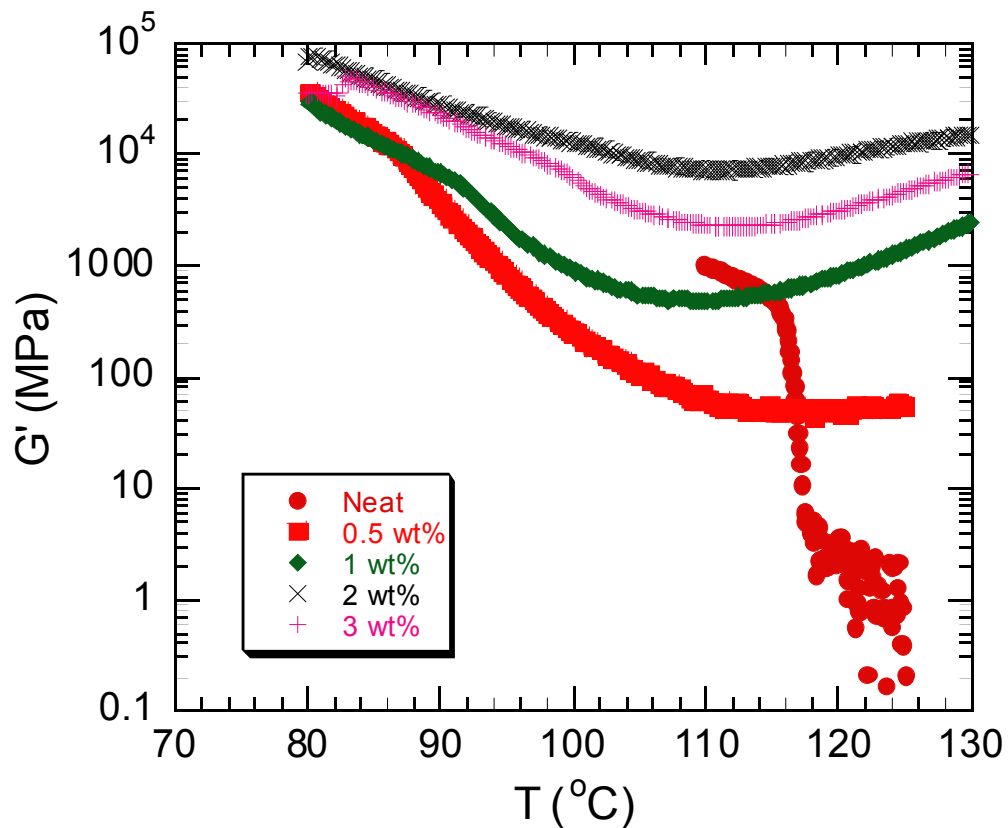


Figure 7.3. Dynamic temperature sweeps of PS-*b*-PI diblock copolymer (sample II) nanocomposites, with increasing C_{60} concentration. These show evidence of first order ODT disappearance at high C_{60} concentrations, and cross-linking/strong-interaction behavior occur at temperatures past 110°C.

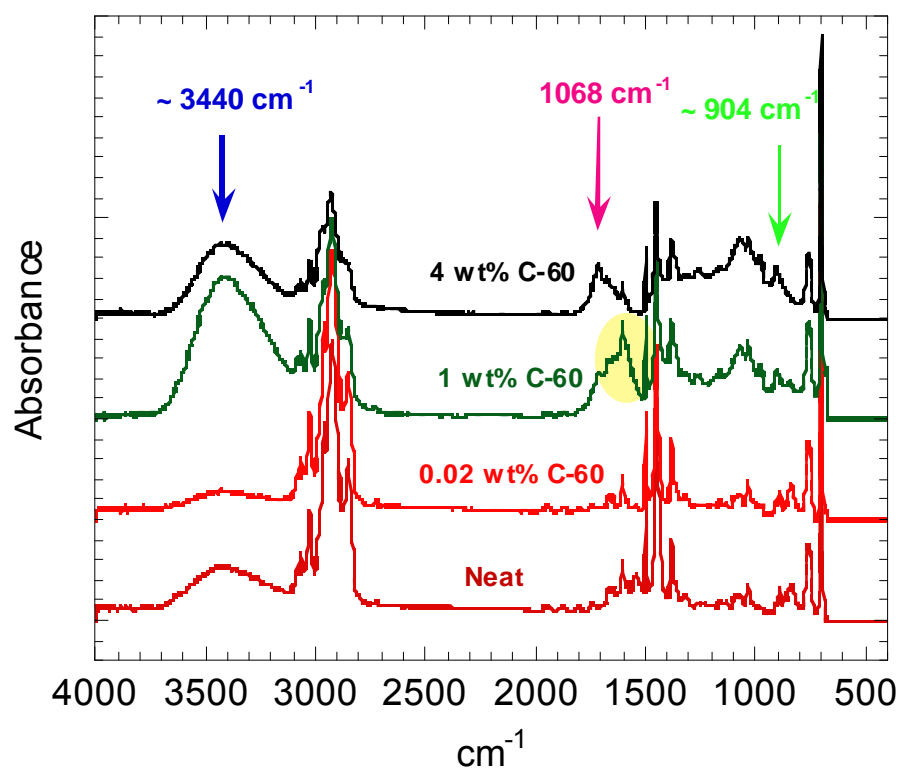


Figure 7.4. FTIR data of Neat, 0.02 wt%, 1 wt%, & 4 wt% nanocomposites before thermal treatment, to investigate the source of cross-linking behavior. The 1wt% and 4 wt% samples show evidence of -OH groups ($\sim 3440 \text{ cm}^{-1}$), the emergence of C-O bonds (1068 cm^{-1}), and presence of CH=CH-R bonds ($\sim 904 \text{ cm}^{-1}$). These peaks describe the nanocomposite's interaction with water, causing alcohols to form and bonding to occur between either the PI double bond and/or the PS benzene ring.

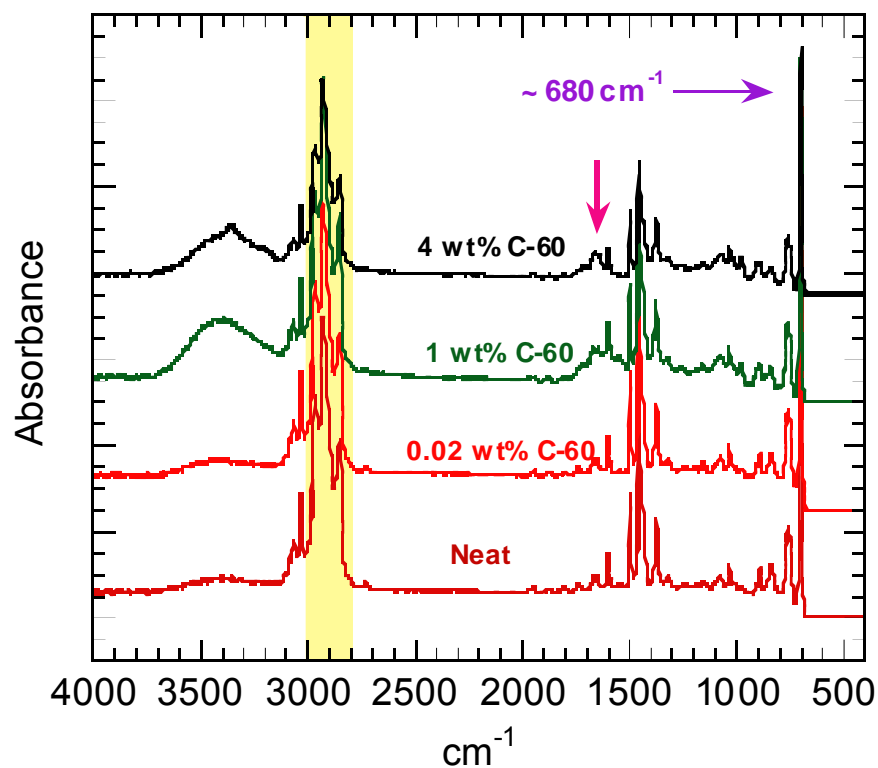


Figure 7.5. FTIR data of Neat, 0.02 wt%, 1 wt%, & 4 wt% nanocomposites after thermal treatment, to continue investigating the source of cross-linking/interaction behavior. 1 wt% and 4 wt% samples show a reduction in the [2990-2850] cm^{-1} triplet, indicating a reduced signal for the aliphatic groups in PI. The $-\text{OH}$ peak and the $\text{C}-\text{O}$ peaks reduced and the $\text{CH}=\text{CH}$ peak ($\sim 680 \text{ cm}^{-1}$) remained the strongest peak. Heating the nanocomposites may have reduced the number of cross-links or interactions between molecules formed between the C_{60} NP and the PI and PS double bonds.

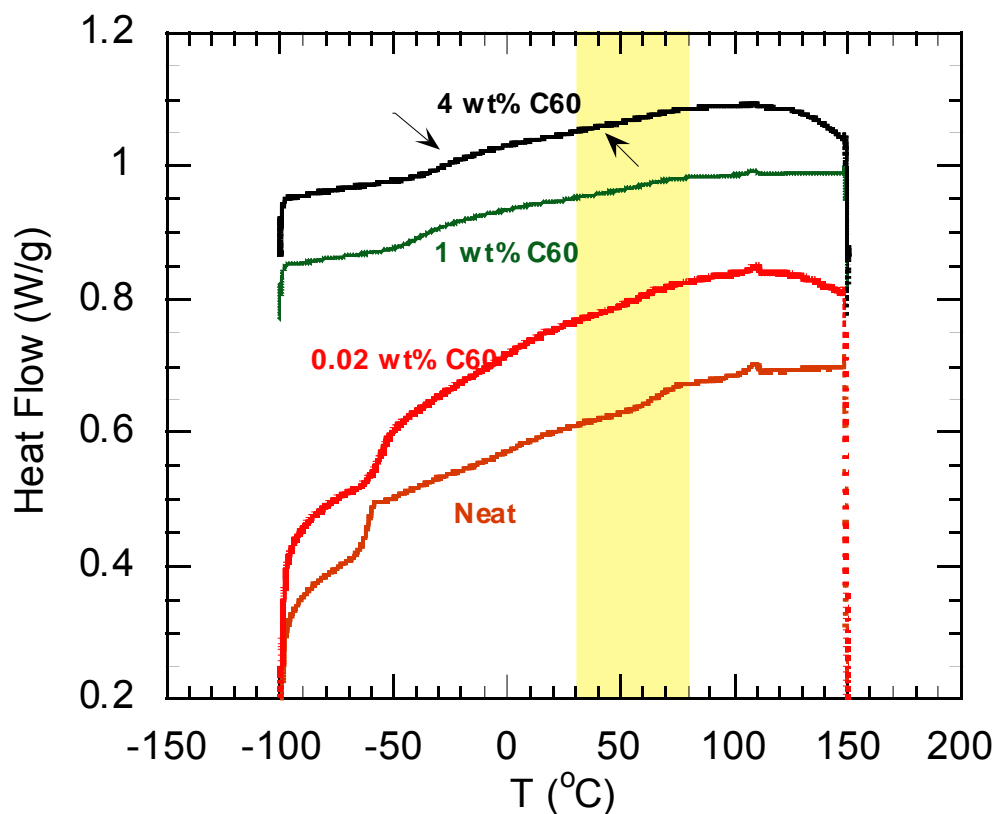


Figure 7.6. DSC traces of Neat, 0.02 wt%, 1 wt%, & 4 wt% nanocomposites before thermal treatment. These data show the nanoparticles' affect on the glass-transition temperature, T_g . The fullerenes show no influence on PS, but cause PI's T_g to increase with C_{60} concentration. The fullerenes act like an anti-plasticizer, reducing in mobility of the PI blocks.

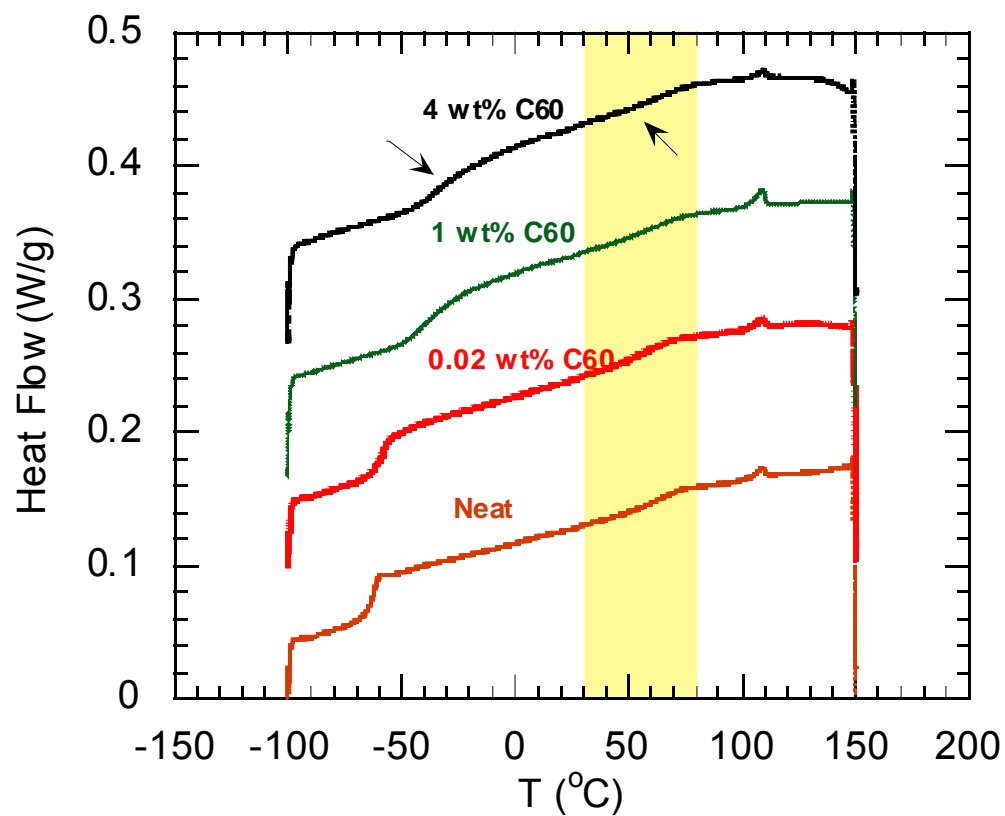


Figure 7.7. DSC traces of Neat, 0.02 wt%, 1 wt%, & 4 wt% nanocomposites after thermal treatment. These data show no evidence of change compared to the non-thermally treated samples.